Synthesis and Characterization of Ternary Magnesium-Based Selenide Spinels for the Application as Solid Electrolytes in Magnesium Batteries

dem Fachbereich Biologie und Chemie

der Justus-Liebig-Universität Gießen vorgelegte

Dissertation

zur Erlangung des akademischen Grades

Doktor der Naturwissenschaften

– Dr. rer. nat. –

von

Clarissa Simon (geb. Glaser)

———— Juni 2025 ————

Dekan/Dean:	Prof. Dr. Holger Zorn
1. Gutachter / 1st Reviewer:	Prof. Dr. Dr. h.c. Jürgen Janek (Justus-Liebig-Universität Gießen)
2. Gutachter / 2nd Reviewer:	Prof. Dr. Bernd M. Smarsly (Justus-Liebig-Universität Gießen)
Eingereicht/Submitted	26.06.2025
Disputation/Disputation	26.09.2025

Eidesstattliche Erklärung

Die vorliegende Arbeit wurde im Zeitraum vom 01.11.2020 bis 26.06.2025 am Physikalisch-Chemischen Institut der Justus-Liebig-Universität Gießen unter Betreuung von Prof. Dr. Dr. h.c. Jürgen Janek angefertigt.

Ich erkläre: Ich habe die vorgelegte Dissertation selbstständig und ohne unerlaubte fremde Hilfe und nur mit den Hilfen angefertigt, die ich in der Dissertation angegeben habe. Alle Textstellen, die wörtlich oder sinngemäß aus veröffentlichten Schriften entnommen sind, und alle Angaben, die auf mündlichen Auskünften beruhen, sind als solche kenntlich gemacht. Ich stimme einer evtl. Überprüfung meiner Dissertation durch eine Antiplagiat-Software zu. Bei den von mir durchgeführten und in der Dissertation erwähnten Untersuchungen habe ich die Grundsätze guter wissenschaftlicher Praxis, wie sie in der „Satzung der Justus-Liebig-Universität Gießen zur Sicherung guter wissenschaftlicher Praxis“ niedergelegt sind, eingehalten.

_____ _____

Ort, Datum Unterschrift

Zusammenfassung

Um angesichts der begrenzten Lithiumverfügbarkeit den steigenden Bedarf an Energiespeichern für Lithiumionen-Batterien zu decken, ist die Entwicklung ressourcenschonender, lithiumfreier Batterien der nächsten Generation unerlässlich. Magnesiumbatterien gelten derzeit aufgrund der potentiellen Vorteile der Magnesiummetallanode, wie etwa der hohen volumetrischen Kapazität, dem reichlichen Vorkommen und der niedrigeren Kosten von Magnesium, als eine vielversprechende Option. Zur Gewährleistung einer höheren Sicherheit und um einer Passivierung der wertvollen Metallanode durch Flüssigelektrolyte vorzubeugen, führt dabei der Weg in Richtung Festkörperbatterien. Hierin liegt jedoch eine zentrale Herausforderung in der Ionenleiterentwicklung, da die hohe Ladungsdichte der Mg^{2+}-Ionen deren Transport in Festkörpern oft stark hindert.

Computergestützten Berechnungen zufolge wird insbesondere MgB_2Se_4-Spinellen (B = Sc, Y, Ln) ein hohes Potential als Raumtemperaturionenleiter zugesprochen, weshalb am Beispiel von $MgSc_2Se_4$ bereits erste elektrochemische Studien durchgeführt wurden. Diese erbrachten allerdings weder einen eindeutigen Nachweis für einen makroskopischen Mg^{2+}-Transport, noch einen belastbaren Ansatz zur Bestimmung der ionischen Leitfähigkeit des zugleich elektronenleitenden Spinels. Darüber hinaus ist auch der Einfluss der Spinellzusammensetzung auf die Mg^{2+}-Ionenleitfähigkeit und -Migrationsbarriere noch weitgehend unerforscht.

Diese Doktorarbeit befasst sich folglich mit der umfangreichen Untersuchung von MgB_2Se_4-Spinellen als potentielle Magnesiumionenleiter. Hierzu wurde zunächst $MgSc_2Se_4$ als Prototyp in verschiedenen Mg^{2+}-Überführungszellen eingesetzt und dabei stellvertretend die Ionenleitfähigkeit der Spinelle durch reversible und kathodische Magnesiumabscheidung belegt. Um die ionischen Transporteigenschaften der gemischtleitenden Spinelle präziser zu charakterisieren, wurde ein Zellkonzept entwickelt, das durch ausschließlich ionenleitende Zwischenschichten den Elektronentransport blockiert. So ließen sich unter Anwendung von Impedanzspektroskopie hohe ionische Raumtemperaturleitfähigkeiten und niedrige Mg^{2+}-Migrationsbarrieren bei allen untersuchten MgB_2Se_4-Spinellen (B = Sc, Y, Er, Tm) identifizieren. Die gute Übereinstimmung zwischen den experimentellen und theoretischen Migrationsbarrieren diente dabei als Basis für weiterführende Dichtefunktionaltheorie-Berechnungen zur B^{3+}-Ionenabhängigkeit der zugrundeliegenden Energiebeiträge. Diese erlaubten die Aufstellung erster Leitlinien zum Erreichen niedriger Migrationsbarrieren im MgB_2Se_4-System, welche später durch die Berücksichtigung der Magnesiuminsertionsenergie erweitert wurden. Dadurch war es möglich, $MgYb_2Se_4$ unter den Spinellen als bisher stärksten Kandidaten für den Einsatz als Magnesiumfestelektrolyt auszumachen, was zugleich experimentell durch eine besonders niedrigere Migrationsbarriere und eine noch höhere Ionenleitfähigkeit des Spinells von über 10^{-4} S cm^{-1} bestätigt werden konnte.

Diese Dissertation ist derzeit die umfangreichste der Autorin bekannte Studie zu Mg^{2+}-ionenleitenden Spinellen. Die präsentierten elektrochemischen Strategien ermöglichen es zukünftig die partiellen Ionenleitfähigkeiten der MgB_2Se_4-Spinelle, sowie anderer ionisch-elektronisch-leitender Magnesiumverbindungen, eindeutig nachzuweisen und präzise zu bestimmen. Darüber hinaus vertiefen die computergestützten Ergebnisse das Verständnis über den Ionentransport der Spinelle und bieten einen fundierten Ausgangspunkt für weitere Untersuchungen am MgB_2Se_4-System.

Abstract

To meet the growing demand for energy storage systems and the limited lithium availability for today's lithium-ion batteries, it is essential to develop resource-saving, lithium-free next-generation battery cells. One promising option is the magnesium battery which stands out due to the potential advantages of the magnesium metal anode, such as the high magnesium earth abundance, low costs, and the high theoretical volumetric energy density. In order to ensure a high level of safety and circumvent the drawbacks of passivation/corrosion of the magnesium metal anode in liquid cells, solid-state cells are often the concept of choice. However, the high charge density of the Mg^{2+}-ion leads to strong Coulomb interactions in the solid host-framework, making the development of magnesium-ion-conducting solid electrolytes quite challenging.

Among considered classes of magnesium ion conductors, MgB_2Se_4 spinels (B = Sc, Y, Ln) are predicted to enable high magnesium ion mobility even at room-temperature. To date, a handful of electrochemical studies have been conducted on a single spinel, $MgSc_2Se_4$, while unequivocal evidence for magnesium ion transport beyond short-range motion as well as an approach to accurately determine the ionic conductivity in the mixed-conducting spinels are still missing. Apart from that, the nature of the electronic conductivity and the influence of the spinel composition on the magnesium ion conductivity and migration barrier are yet not well understood.

This doctoral thesis focuses on a systematic investigation of MgB_2Se_4 spinels as potential magnesium ion conductors. $MgSc_2Se_4$ was used as a pioneer material to study the magnesium ion transport by two independent electrochemical methods, namely reversible magnesium plating/ stripping cycling and electrochemical deposition of magnesium metal. After proving the Mg^{2+}-ion transport, a cell concept with electron blocking interlayer-electrodes was developed to tackle the challenge of determining the partial ionic conductivity of the mixed-conducting spinel from impedance spectroscopy. Thus, a high room-temperature magnesium ion conductivity of $MgSc_2Se_4$ and, later on, of three further synthesized spinels (MgY_2Se_4, $MgEr_2Se_4$, $MgTm_2Se_4$) was confirmed. Driven by the good accordance of the experimental and computational magnesium ion migration barriers, systematic theoretical periodic density calculations of the static and kinetic energy contribution were performed dependent on the B^{3+}-ion. In this context, general guidelines for achieving small migration barriers in the MgB_2Se_4 spinel system could be identified, which were later extended by the consideration of the magnesium insertion energy, suggesting an outstanding high magnesium ion mobility in $MgYb_2Se_4$. This was finally confirmed by an experimentally high ionic conductivity exceeding 10^{-4} S cm^{-1} and a low migration barrier, making the $MgYb_2Se_4$ spinel to a strong candidate for a magnesium ion solid electrolyte.

Overall, this doctoral thesis is the most comprehensive work on magnesium-ion-conducting selenide spinels so far. Approaches for accurate electrochemical characterization of spinels with mixed ionic-electronic character were developed, which will not only advance the research on MgB_2Se_4 phases but also pave the way for exploring other magnesium-based mixed conductors. Moreover, the computational studies in this work provide a deeper understanding of the magnesium ion transport in the chalcogenide spinels and could therefore serve as a starting point for further studies on the MgB_2Se_4 system.

Table of Contents

1 Introduction

Today, global warming, driven primarily by the accumulation of greenhouse gases in the earth's atmosphere, has become one of the most important environmental issues on our planet. The Paris Climate Agreement of 2015 therefore calls for restricting the rise in global temperature to 1.5 °C by 2050 relative to the pre-industrial level.[1] According to estimates, this corresponds to a remaining CO_2 budget of 500 Gt, which cannot be met if the current annual record high of 37 Gt set in 2023 is maintained.[2,3]

A key element in reducing CO_2 emission is the transport sector, which contributes a fifth of the total.[4] Here, the change from a traditional combustion engine to a battery electric vehicle (BEV) is the cleaner, more sustainable option. For this comprehensive electrification of vehicles as well as for the storage of renewable energy from sources such as wind and photovoltaics, energy storage systems are required.[5]

Since their commercialization in 1991, lithium-ion batteries (LIBs) dominate the market in energy storage technologies for portable electrical devices and BEVs.[6,7] However, to extend the present driving range of BEVs and to make them more affordable, the research community is targeting a specific energy density of more than 400 Wh kg^{-1} and costs of 100 USD per kWh.[8,9] Due to the fact that the theoretical energy density of LIBs (~300 Wh kg^{-1}) is insufficient for this goal, efforts on additional Li-based batteries like Li-S batteries are underway, while the dwindling amount of lithium resources from salt lakes and mines is a cause of concern.[9,10] It is therefore essential to develop next-generation battery systems based on low-cost and earth-abundant materials.

A promising option for post-lithium energy storage system are multivalent (MV) ion batteries that utilize charge carriers such as Mg^{2+}, Ca^{2+}, and Zn^{2+}, resulting in potentially high volumetric energy densities.[11] Among them, Mg-based batteries have attracted the most research interest in the years 1985 to 2015, accounting for about 80% of the publications on MV-ion batteries, mainly attributed to the excellent characteristics of the Mg metal anode (MMA).[12] These include the magnesium's much lower standard potential (–2.37 V vs. standard hydrogen electrode (SHE)) compared to the Zn metal (–0.76 V vs. SHE) and its high theoretical volumetric capacity of 3833 mAh cm^{-3}, almost double the amount of Ca and Li and three times as much as for Na metal.[13] Moreover, magnesium is with a content of 2.9% (10^3 times higher than that of lithium) highly abundant in the earth's crust and also suspected to have a low tendency for dendrite formation during electrodeposition.[13,14]

Despite these advantages related to the Mg metal anode, the development of competitive rechargeable magnesium batteries (RMBs) is still hindered by the availability of suitable Mg-ion electrolytes, as analogues from LIBs cannot be simply transferred. That is because conventional liquid electrolyte (LE) analogues from LIBs either form a Mg^{2+} impermeable passivation layer on the Mg metal anode or have a practical limit on their anodic stability, resulting in irreversible electrodeposition of Mg.[15,16] To overcome these shortcomings, efforts have been made on the investigation of novel electrolytes based on Grignard reagents or fluorinated magnesium alkoxyborates, which in turn are highly flammable due to their ether-based solvents.[17–19] For these

reasons, to ensure higher levels of safety and to circumvent the drawbacks of passivation/ corrosion as well as the limited low electrochemical stability, solid electrolyte (SE) concepts are pursued.[20] Nevertheless, the development of Mg-ion SEs with sufficient room-temperature ionic conductivity ($\sigma_{ion} \approx 10^{-4}$-$10^{-3}$ S cm) is quite challenging, as the high charge density of the Mg^{2+}-ion results in strong Coulomb interactions in the solid state, associated with a typically sluggish ion mobility.[18,21] The most Mg-ion SE classes adapted from Li and Na monovalent ion SEs, such as NASICON-type oxides ($Mg_{0.5}Zr_2(PO_4)_3$ and modifications), thiophosphates (MgS-P_2S_5-MgI_2), and halides ($MgAl_2Cl_{8-y}Br_y$), cannot exceed a conductivity of $\sigma_{ion} = 3 \cdot 10^{-5}$ S cm^{-1} at ambient conditions.[22–28] An exception of them are the both magnesium borohydride derivates β-$Mg(BH_4)_2 \cdot CH_3NH_2$ and $Mg(BH_4)_2 \cdot 1.5NH_3$-60wt%TiO_2, which exhibit room-temperature ionic conductivities slightly above 10^{-4} S cm^{-1}.[29,30] However, their generally low electrochemical stability (≤1.3 V vs. Mg^{2+}/Mg) makes pairing with potential cathodes difficult.[31]

A groundbreaking discovery regarding Mg-ion SEs was made in the computational study by Canepa et al., which predicted low theoretical migration barriers [E_a(th) = 0.36-0.53 eV] in MgB_2X_4 (B = Sc, Y, In; X = S, Se) chalcogenide spinels.[32] Consistent with that theory, Canepa et al. demonstrated by ^{25}Mg nuclear magnetic resonance (NMR) experiments a low Mg-ion migration barrier of $E_a = 370 \pm 90$ meV, referred to short-range motion, for their synthesized $MgSc_2Se_4$.[32] For the long-range motion, important for the performance of a solid electrolyte, electrochemical impedance spectroscopy (EIS) on a Ta|$MgSc_2Se_4$|Ta cell was performed. However, the electrochemical estimated room-temperature ionic conductivity ($\sigma_{ion} \approx 10^{-4}$ S cm^{-1}) is yet not sufficiently evidenced as the way of evaluation is not considered reliable. There is a limited resolution in the high-frequency region of the impedance spectra, that does not allow satisfactory fitting and accurate determination of the ionic conductivity according to the used Jamnik and Maier model for mixed ionic-electronic conductors (MIECs).[32–34] Therefore, it is crucial to find new strategies to verify and determine the ionic conductivity reliably, even if the electron-conducting character of $MgSc_2Se_4$ makes this quiet challenging.

Apart from that, the high electronic conductivity of $MgSc_2Se_4$ is also of concern as it is $4 \cdot 10^{-4}$ times of the estimated ionic conductivity and hence significantly higher than for current alkali SEs (10^{-8}-10^{-6}).[18,32] This drastically reduces the efficiency of a battery by self-discharge.[35] Thus, attempts have been made to minimize the electronic conductivity, which is attributed to manipulatable causes, including point defects neutralized by electrons or the presence of electron-conducting secondary phases.[36] Wang et al. focused on the reduction of point defects by compositional tuning, while Kundu et al. used an electric field-assisted synthesis route to increase the phase purity.[37–39] However, only the latter method demonstrated a reduced, but still high, electronic fraction of $5 \cdot 10^{-6}$ when assuming that their ionic conductivity determined similar to Canepa et al. is true.[39]

Although electron conduction remains an unsolved issue, there has recently been a surge in computational studies aimed at improving the understanding of Mg^{2+} migration in spinels. For example, the Groß group studied the influence of different A-cations (including Mg^{2+}) on the migration barrier of ASc_2Se_4 and ASc_2S_4 compounds as well as the electrochemical stability of

Mg sulfide spinels.[40,41] Moreover, the Mg^{2+} migration and structural stabilities of several $MgLn_2X_4$ (Ln = lanthanide; X = S, Se) spinels were investigated by Koettgen et al.[42] In this work, the authors revealed that a balance between a stable spinel phase (with respect to competing $MgLn_2X_4$-type phases) and a low theoretical migration barrier E_a(th) is primarily given for selenide spinels with an ionic radius r_{Ln} of the lanthanides ranging from Lu to Er [$r_{Lu\text{-}Er}$ = 0.861-0.890 Å; $E_a(th)_{Lu\text{-}Er}$ = 0.369-0.358 eV]. Therefore, this selection of Ln-based spinels is considered as quite attractive for the investigation as Mg-ion SEs, especially due to the smaller migration barriers compared to their pioneer $MgSc_2Se_4$ [E_a(th) = 0.375 eV].[32]

To the best of the author's knowledge, this dissertation presents the most comprehensive study on MgB_2Se_4 (B = Sc, Y, Ln) spinels as potential candidates for Mg-ion SEs. Several magnesium selenide spinels are synthesized and structurally characterized by techniques such as X-ray diffraction (XRD) and NMR spectroscopy as well as novel cell concepts for a reliable and accurate electrochemical investigation are developed. Paired with detailed density functional theory (DFT) calculations on the MgB_2Se_4 system conducted by a collaboration partner, this work provides a better understanding for the Mg-ion migration in this class of magnesium compounds.

The publication 1 of this dissertation, titled "To be or not to be – Is $MgSc_2Se_4$ a Mg-Ion Solid Electrolyte?", addresses the question of whether Mg-ion transport really occurs in $MgSc_2Se_4$.[43] Therefore, electrochemical magnesium plating experiments were performed, to provide the first unequivocal evidence for Mg-ion conduction in $MgSc_2Se_4$ beyond short-range motion. Moreover, a transference cell, including purely Mg^{2+}-conducting interlayer-electrodes, is presented. This special cell design effectively suppresses electron transport, allowing accurate determination of the partial ionic conductivity and thus the Mg^{2+} migration barrier of the mixed-conducting $MgSc_2Se_4$ spinel.

In publication 2 of this dissertation, titled "MgB_2Se_4 Spinels (B = Sc, Y, Er, Tm) as Potential Mg-Ion Solid Electrolytes – Partial Ionic Conductivity and the Ion Migration Barrier", a combined experimental and computational study on magnesium selenide spinels is presented.[44] Three new MgB_2Se_4 (B = Y, Er, Tm) spinels were synthesized and investigated electrochemically according to the previous work (publication 1). Compared to $MgSc_2Se_4$, these compounds (MgY_2Se_4 excepted) showed a higher ionic conductivity as well as lower Mg^{2+} migration barriers, which were found to be in excellent agreement with the values derived from the DFT calculations in this study. Moreover, the detailed computational investigation on the MgB_2Se_4 system provides a deeper understanding of how the variation of B^{3+}-cations influences the static and kinetic contributions to the overall migration barrier.

The publication 3 of this dissertation, titled "High Room-Temperature Magnesium Ion Conductivity in Spinel-Type $MgYb_2Se_4$ Solid Electrolyte", deals with the investigation of $MgYb_2Se_4$ and two further multicationic/multianionic spinel compounds.[45] Among them, $MgYb_2Se_4$ exhibits a very high room-temperature ionic conductivity exceeding 10^{-4} S cm^{-1} and a low Mg^{2+} migration barrier (E_a = 364 meV), which is attributed to its lower magnesium insertion energy determined by DFT calculations. Furthermore, the lower electronic transference number ($t_{el} = 7 \cdot 10^{-6}$) compared to the previous studied compounds, coupled with the spinel's generally

high electrochemical stability window, makes $MgYb_2Se_4$ a highly attractive candidate as a Mg-ion SE.

Collectively, this dissertation represents a major milestone in the investigation of magnesium selenide spinels as Mg-ion conductors. For the first time, Mg^{2+}-ion conduction beyond short-range was unequivocally evidenced as well as high ionic conductivities of the MgB_2Se_4 spinels could be precisely determined by a specially developed cell concept. These findings not only increase the attractiveness of the spinel compounds in terms of Mg-ion SEs but also open the door for exploring other magnesium-based mixed ionic-electronic conductors. Furthermore, the computational studies in this work expand the understanding of the magnesium ion transport in the MgB_2Se_4 system and guide to find spinels with low experimental Mg^{2+} migration barriers, as demonstrated in the case of $MgYb_2Se_4$.

2 Fundamentals

This chapter provides a summary of the fundamental knowledge from the research on inorganic key materials for magnesium-based solid-state batteries, with a main focus on SEs. Besides a general overview on the challenges and recent progress on anode, cathode, and solid electrolyte materials, special attention is given to the ionic transport in SEs as well as the structural effect on multivalent ion conduction. Moreover, the determination of the partial conductivities of mixed ionic-electronic conductors (MIECs) is considered, which is not that trivial for magnesium-based materials due to a lack of suitable and compatible electrodes.

2.1 Challenges and Recent Progress on Inorganic Key Materials for Magnesium-Based Solid-State Batteries

Although solid-state batteries (SSBs) with higher energy density and safety compared to liquid cells have gained prominence in research, the development process of Mg-based SSBs is still accompanied by many challenges.[46] These challenges and the recent progress toward obtaining suitable electrode materials with acceptable kinetics as well as electrolytes compatible with both cathode and anode are summarized below.

2.1.1 Anodes

Rechargeable magnesium batteries (RMBs) are considered the post-lithium battery technology with most potential for commercial applications, not least due to the excellent characteristics of the magnesium metal anode (MMA).[46] These include the high volumetric energy density (3833 mAh cm^{-3}) and the low standard potential (–2.37 V vs. SHE) of the magnesium metal, as well as the high abundance of Mg resources in the earth's crust, which directly reduces the production cost of a battery. Moreover, unlike alkali metals, Mg metal exhibits a low reactivity in the atmosphere and tends to form a smooth and uniform deposition layer during the charging process, allowing the use as a metallic Mg anode. The homogenous Mg deposition behavior avoids in principle the formation of dendrites, as reported for several tested electrolyte solutions, although individual cases prove that the electrodeposition of Mg metal is not totally free of dendrite formation.[47–50]

Solid electrolytes are believed to prevent or delay the formation of metal dendrites by their high mechanical strength and high ionic transference number, crucial for the direct use of the MMA in SSBs.[51,52] However, the development of a functional and efficient Mg SSB faces a major challenge based on the low ductility of the Mg metal.[53] The high Young's modulus of Mg (44 GPa) compared to lithium (4.9 GPa) and sodium (10 GPa) not only leads to a poor physical contact between the SE and the MMA in a practical SSB, but also to a reduced "true" energy density.[53,54] This is because most Mg foils used as anodes in research are too thick (usually >100 µm) in relation to the given capacities of the cathodes, which results in a lower specific capacity and thus lower energy density of the battery.[55] Apart from that, further drawbacks such as fast capacity fading, uneven heat generation and distribution, and battery packaging issues are

associated with the use of surplus Mg foils. It is therefore very important to manufacture MMAs with an adequate thickness (<100 µm), which is already possible through processes such as melt-spinning, rapid solidification, and hot-rolling.[56–58] However, those processes are not suitable for practical applications due to issues of easy oxidation, low efficiency, and the difficulty to control accuracy.[55]

Another aspect to be considered in SSBs concerns the rarely studied interface reactions of Mg-ion solid electrolytes with the MMA.[53] The nature of the metal|electrolyte interface is crucial for the functionality of a SSB. When considering the contact between a MMA and a Mg-ion SE, four different types of interface/interphase formation analogues to Li SSBs are conceivable (Figure 1),[59] although not all of them have been proven in case of Mg SSBs so far.[60–62]

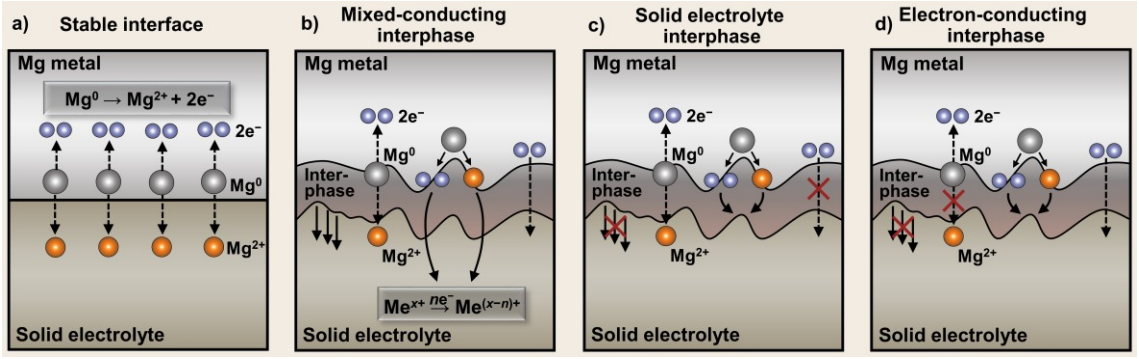

Figure 1: Four conceivable types of interface formation between the MMA and a Mg-ion SE. a) A thermodynamically stable interface, b) a growing, mixed-conducting interphase (MCI), c) a solid electrolyte interphase (SEI) with self-limiting growth, and d) an electron-conducting interphase with self-limiting growth. Me^{x+} refers to a metal cation of the SE involved in the interphase formation by reacting with Mg^{2+} and electrons from the MMA. The interphase growth is indicated by solid arrow lines. The transport of Mg^{2+} and electrons is represented by dashed arrows. Panels a-c) modified from publication Wenzel et al.[59], Copyright 2015, with permission from Elsevier.

If the SE is thermodynamically stable in contact with the MMA (Figure 1a), no interfacial degradation reactions occur and a sharp 2D interface is formed.[59] This basically enables stable cell operation. In the case that the SE is thermodynamically unstable in contact with the MMA (Figure 1b-d), both materials form a 3D interphase by chemical reactions. Depending on the transport properties of the formed interphase, three reported types can be distinguished:[59,63] A mixed-conducting interphase (MCI) with sufficient ionic and electronic conductivity that steadily grows "into" the SE, resulting sooner or later in a failure of the battery (Figure 1b). Secondly, an ionically conducting interphase in which the electronic conductivity is low enough to self-limit the growth of the interphase to a thin layer (Figure 1c). This layer is then named as stable solid electrolyte interphase (SEI) and can influence the performance of a battery depending on its ion-conducting properties. And lastly, an interlayer in which the electronic conductivity surpasses the ionic conductivity (Figure 1d). In this case, the growth of the interphase is self-limiting, analogues to the SEI, but due to low ionic conductivity.[63] Obviously, this latter case is the worst because the final interphase will not be Mg-ion conductive, similar to the passivation layer formed on the Mg metal electrode with the most common liquid electrolytes (LEs).[13] Therefore, to prevent such undesired chemical reactions between MMA and electrolyte, research on modified and alternative

anodes is already underway, however, primarily studied in the field of liquid cells. These types of anodes are classified as i) modified Mg metal anodes, ii) low-potential insertion-type materials, and iii) alloy-based conversion-type materials.

i) Modified Mg Metal Anodes

Among the alternatives to the plain Mg metal foil electrode, modified Mg metal anodes are the ones that retain a Mg metal anode. A possible strategy here is to change the form or texture of the Mg metal. For instance, it is proposed to replace the Mg metal foil with ultra-small Mg nanoparticles pretreated with a $Ti(TFSI)_2Cl_2$ titanium complex.[64–66] This novel type of anode not only has an adjustable thickness but also significantly decreases the binding affinity between Mg and O and thus ensures an effective removal of the Mg oxide layer. Other options include coatings and artificial membranes on the surface of the MMA. Li et al. reported a magnesium fluoride (MgF_2) layer that enables the transport of Mg-ions and was formed by the controlled reaction of hydrofluoric acid with the Mg metal surface.[67] Moreover, a Mg^{2+} conductive artificial polymer interphase based on Mg powder, carbon black, polyacrylonitrile, and $Mg(CF_3SO_3)_2$ was presented by Son et al.[68] This interlayer has been shown to effectively prevent the electrochemical reduction of the used electrolyte. Nevertheless, it is worth to mention that these approaches also bring drawbacks such as the handling of easily oxidizing Mg nanoparticles or a reduced capacity of the electrode due to additives.

ii) Low-Potential Insertion-Type Materials

Inspired by the already commercialized graphite anode for LIBs, alternative insertion-type anodes at low potentials have been largely studied to circumvent interfacial issues.[55] To name a few, $Li_4Ti_5O_{12}$ (LTO) in nanoparticle size (7-8 nm) was found to achieve a high reversible capacity of 175 mAh g^{-1} (corresponding to 1.5 Mg atoms per formula unit) and a superior cycling performance over 500 cycles, benefiting from its zero-strain spinel framework structure.[10,69] Moreover, $Na_2Ti_6O_{13}$ nanowires exhibit a good structural stability during Mg-ion insertion/ extraction process, although its capacity (discharge: 165.8 mAh g^{-1}, charge: 147.7 mAh g^{-1}) cannot compete with that of LTO.[70] Li_3VO_4/carbon hollow spheres, instead, still delivered a much higher specific capacity of ~195 mAh g^{-1} after 15 cycles, attributed to enhanced Mg^{2+} insertion kinetics and a shortened Mg^{2+} diffusion path by the high surface area of the mesoporous structure.[10,71] These anodes are in general known to be compatible with Mg-salt electrolytes in polar aprotic solvents, but are accompanied by challenges including low Mg insertion/extraction kinetics, high volume changes, and low specific capacities.[55,66]

iii) Alloy-Based Conversion-Type Materials

Compared with insertion-type materials, alloy-type electrodes work through a conversion process. During electrochemical alloying, the reaction of Mg^{2+} and another active element M creates compounds with new atomic organization, while in the dealloying process the pristine materials are formed again:[10]

$$x\mathrm{Mg}^{2+} + 2x\mathrm{e}^{-} + \mathrm{M} \rightleftharpoons \mathrm{Mg}_x\mathrm{M} \quad (2.1.1)$$

Among the alloy-type electrodes made from p-block elements, Bi-based anodes are the most studied, since the intermediate phase MgBi formed by the two-step alloying reaction ($\mathrm{Bi} \xrightarrow{\mathrm{Mg}} \mathrm{MgBi} \xrightarrow{\mathrm{Mg}} \mathrm{Mg_3Bi_2}$) greatly reduces the volume expansion and promotes the Mg storing kinetics.[10,46,66] In addition, as demonstrated by Shao et al., state of the art Bi anodes exhibit a high specific capacity of 350 mAh g^{-1} (theoretical: 385 mAh g^{-1}), excellent cycling stability, and a high Coulombic efficiency over 200 cycles.[72] Beside bismuth, Sn anodes with a higher remarkable theoretical capacity (900 mAh g^{-1}) are regarded as possible option, although crack formation during demagnesiation represents a major challenge.[10,73] It is therefore proposed to combine the high capacity of Sn and the stable reversibility of Bi in bimetallic Bi-Sn anodes.[66] Hence, further research into alloy-based anodes as an alternative to the MMA is required, not least due to their promising high capacity.

2.1.2 Cathodes

In recent years, to realize RMBs, extensive research work has been conducted on the development of cathode materials, which should ideally fulfill the following characteristics: high operating potential and specific capacity, fast and reversible kinetics for Mg-ion migration, and good cycling stability.[66] So far, however, investigations into the cathode material have been limited to the more advanced liquid cells. To get started with SSBs, it is therefore suggested to first study them with common and well-characterized cathodes from liquid cells before starting with novel materials specifically for SSBs.[74] For this reason, the most developed Mg cathode materials for liquid cells are discussed below.

i) Layered Oxides

Among the well-characterized cathode materials, layered oxides such as V_2O_5, MoO_3, and MnO_2 turned out to be rather difficult for their application in RMBs.[10,31,75–81] Although layered oxides are successfully developed host structures in monovalent systems, they do not show comparable storage capability in RMBs.[53] This is because the high charge density of Mg^{2+} induces a strong interaction with the O^{2-}-based framework, resulting in a significantly higher kinetic barrier than required for Li^{+} migration. Moreover, the strong interaction leads to severe structural distortion, accompanied by undesirable conversion reactions that can thermodynamically dominate over the intercalation process.[53,81] Due to these drawbacks, the development of cathodes for RMBs is largely restricted to soft and highly polarizable anion frameworks based on sulfur and selenium, which enable smoother Mg^{2+} migration and thus improve the intercalation kinetics.[14,53]

ii) Chevrel Phase

The sulfide-based Chevrel phase (CP) with the formula $Mg_xMo_6S_8$ is considered as the earliest Mg^{2+} intercalation cathode material when it was used in the first prototype magnesium battery by Aurbach et al. in 2000.[82,83] In combination with a MMA and a $Mg(AlCl_2BuEt)_2$/tetrahydrofuran electrolyte, the CP achieved a capacity of ~70 mAh g^{-1} at an operating voltage of ~1.1 V (vs.

Mg^{2+}/Mg) over more than 2000 cycles. This capacity was set as a benchmark, but still offered room for improvement, since after the initial magnesiation 20% to 25% of the Mg^{2+}-ions were irreversibly trapped in the crystal structure by a ring-trapping mechanism, thereby reducing the theoretical capacity to 75% to 80%.[84] In this context, theoretical studies revealed that increasing the lattice size distorts the geometry of the structure and thus disrupts the ring-trapping mechanism.[85,86] Accordingly, attempts have been made to replace the S^{2-}- by larger Se^{2-}-ions in the CP structure, whereby $Mg_xMo_6S_6Se_2$ has been developed so far as the best compound of this cathode class with an initial capacity of 110 mAh g^{-1}.[82,84] However, due to the limited theoretical capacity (<150 mAh g^{-1}) and low operational voltage (<1.5 V vs. Mg^{2+}/Mg), CP compounds can only be regarded as medium or low energy density cathode materials.[66]

iii) Spinel, Layered, and Nanostructured Chalcogenides

Compared to the Chevrel phase, spinel, layered, and nanostructured chalcogenide compounds were found to achieve equivalent or even higher capacities in a similar voltage window. Among a variety of $Mg_xB_2X_4$ spinels ($0 < x < 1$; B = transition metal; X = O, S) studied so far, $Mg_xTi_2S_4$ is reported with the most promising electrochemical performance.[82] The spinel achieved a capacity of 190 mAh g^{-1}, corresponding to 80% of the theoretically capacity (239 mAh g^{-1}), at an elevated temperature of 60 °C and an average voltage of 1.1 V (vs. Mg^{2+}/Mg).[87] Moreover, reversible Mg^{2+} intercalation has been demonstrated in both layered Mg_xTiS_2 and layered Mg_xTiSe_2 ($0 < x < 0.5$) with capacities of 115 mAh g^{-1} (at 60 °C and 1.2 V) and 110 mAh g^{-1} (at 25 °C and 0.9 V), respectively.[88,89] Even higher capacities within chalcogenide compounds could only be realized by nanostructured materials such as expanded VS_4 nanodendrites (268 mAh g^{-1} at 1.2 V), CuS nanospheres (477 mAh g^{-1} at 1.1 V), and WSe_2 nanowires (203 mAh g^{-1} at 1.6 V), although the low working voltage is still a concern.[31,90–92]

iv) Other Mg Battery Cathodes

In addition to layered oxides, Chevrel phase, and chalcogenide compounds, several other Mg battery cathode materials have been studied since the demonstration of the first RMB prototype. To name a few, polyanionic compounds such as the NASICON-type $Mg_{0.5}Ti_2(PO_4)_3$ and $Na_3V_2(PO_4)_3$ as well as open framework structures like the Prussian Blue analogues $NiFe(CN)_6$, $Na_{0.69}Fe_2(CN)_6$, and $KNi[Fe(CN)_6]$ have been introduced as high voltage cathode materials for RMBs.[93–97] These cathode material classes offer operating voltages up to 2.5 V and 3.0 V (vs. Mg^{2+}/Mg), respectively, but present major challenges due to their sluggish electrode kinetics and insufficient, poor electronic conductivity.[31] Moreover, several organic materials with redox-active groups attracted interest, such as 2,5-dimethoxy-1,4-benzoquinone,[31,98] which, however, will not be discussed further in this dissertation, as it is restricted to inorganic materials.[31,95]

2.1.3 Solid Electrolytes

Electrolytes play the crucial role in transferring certain ions between the anode and cathode of a battery. In order to get rid of issues associated with liquid electrolytes (LEs) such as undesired anion migration and polarization effects, passivation, corrosion, and dendrite growth at the MMA

as well as the high flammability of organic solvents, solid electrolytes (SEs) are considered as an effective solution.[20] However, the typically sluggish mobility of the Mg^{2+}-ion in solid-state frameworks, induced by its high charge density, makes the development of a Mg-ion SE with sufficient ionic conductivity at room-temperature quite challenging. The ionic conductivity of the reported Mg-ion SEs is not yet comparable to that of LEs (>10^{-3} S cm^{-1}), although significant progress has already been made in the recent years.[7,99]

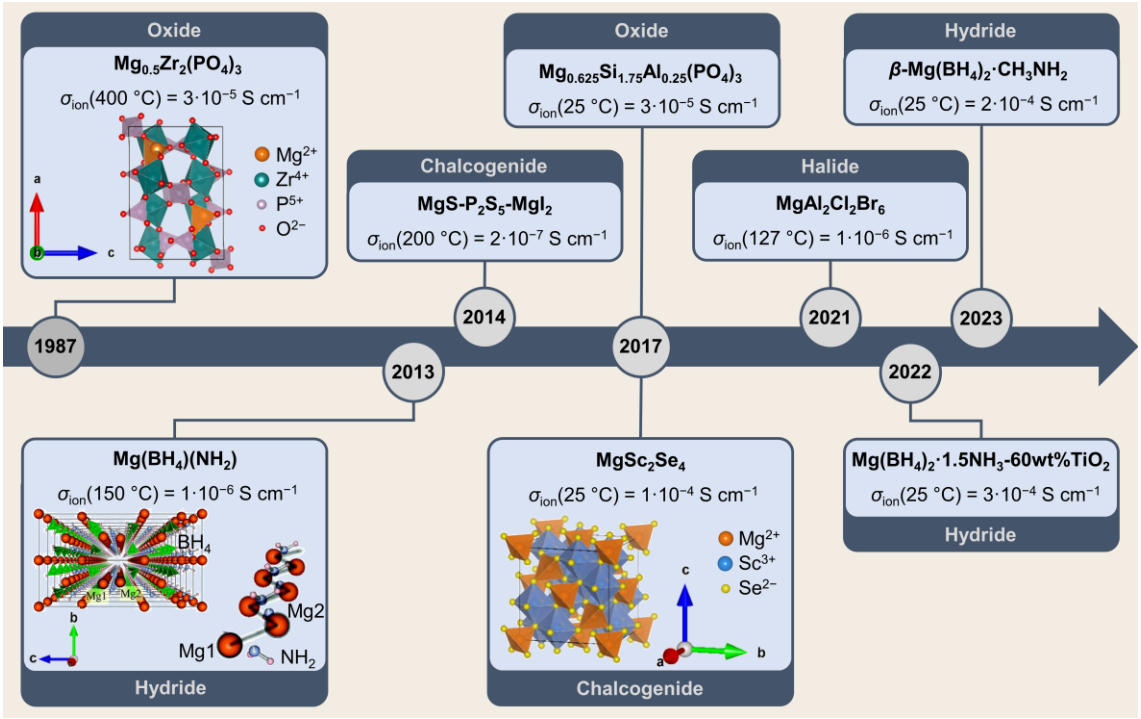

Figure 2: Timeline of major breakthroughs in the search for Mg-ion SEs. The Mg-ion SEs classified in oxides, hydrides, chalcogenides, and halides exhibit Mg-ion conductivities σ_{ion} up to 10^{-4} S cm^{-1} at room-temperature. The σ_{ion} values are based on the references [22,26–30,32,100] and the simulated $Mg(BH_4)(NH_2)$ structure was used with permission of The Royal Society of Chemistry, from Higashi et al.[100]; permission conveyed through Copyright Clearance Center, Inc. The crystal structures of $Mg_{0.5}Zr_2(PO_4)_3$ and $MgSc_2Se_4$ were generated from crystallographic data of the Inorganic Crystal Structure Database (ICSD 250452 and ICSD 642814).[101]

Figure 2 illustrates the timeline of important milestones in the search for Mg-ion SEs, which can be classified in oxides, hydrides, chalcogenides, and halides. These SE compounds are discussed below in terms of their ionic conductivity and other properties (if published) that need to be fulfilled by an ideal SE, such as negligible electronic conductivity, excellent oxidative stability, compatibility with the MMA and high voltage cathodes, and ease of processing.

i) Oxides

The earliest work on Mg-ion SEs appeared in the late 80's, in which Ikeda et al. reported an observed Mg-ion conduction in an oxide material, $Mg_{0.5}Zr_2(PO_4)_3$, validated by Tubandt's method (discussed in section 2.4.1).[22] The material with β-$Fe_2(SO_4)_3$-type structure – similar to the superionic-conducting NASICON-type – achieved ionic conductivities σ_{ion} of $6·10^{-3}$ S cm^{-1} and $3·10^{-5}$ S cm^{-1} at 800 °C and 400 °C, respectively, with an activation energy of E_a = 0.82 eV. To

improve the around ten orders of magnitude lower room-temperature ionic conductivity, several studies for substituting aliovalent ions at the Zr-site followed.[26,102–104] Lower charged aliovalent cations such as Fe^{3+}, Zn^{2+}, and Al^{3+} were used to increase the concentration of Mg^{2+} interstitial ions for an enhanced Mg^{2+} migration amount, whereas larger radii cations like Nb^{5+} should widening the ion channels to reduce the activation energy. Nevertheless, all attempts exhibited too low room-temperature Mg-ion conductivity, with the highest of $\sigma_{ion} = 3 \cdot 10^{-5}$ S cm^{-1} reported for $Mg_{0.625}Si_{1.75}Al_{0.25}(PO_4)_3$, which at the same time possess a large anodic stability up to 2.51 V vs. Mg^{2+}/Mg.[26]

ii) Hydrides

Magnesium borohydrides emerged as another potential group of Mg-ion SEs, when Matsuo et al. investigated the high-temperature diffusion in $Mg(BH_4)_2$ by *ab initio* calculations in 2013.[105,106] In their study, they proposed that the general low Mg-ion mobility in $Mg(BH_4)_2$, originated due to strong Coulomb interactions with the BH_4^--ions, can be accelerated by partial replacing the anions with larger ions or neutral molecules such as AlH_4^-, NH_3BH_3, or NH_2^-. Following the hypothesis, one year later Higashi et al. reported an increased ionic conductivity of $\sigma_{ion} = 1 \cdot 10^{-6}$ S cm^{-1} at 150 °C for $Mg(BH_4)(NH_2)$, which is three orders of magnitude higher than that of $Mg(BH_4)_2$ and suggest to be partly a result of the shorter Mg-Mg distance along the Mg^{2+} zigzag chain in the cavity structure (see Figure 2).[100] This initial progress was followed by several approaches with more complex magnesium borohydrides derivates to further increase the ionic conductivity, even at ambient temperature.[29,30,107–110] Among them, the β-$Mg(BH_4)_2 \cdot CH_3NH_2$ polymorph ($\sigma_{ion} = 1.5 \cdot 10^{-4}$ S cm^{-1}) and the $Mg(BH_4)_2 \cdot 1.5NH_3$-60wt%TiO_2 composite ($\sigma_{ion} = 3.0 \cdot 10^{-4}$ S cm^{-1}) turned out to exhibit record-breaking Mg-ion conductivities at room-temperature, exceeding 10^{-4} S cm^{-1}.[29,30] However, the high ionic conductivity in these compounds was found to be accompanied by a lower electrochemical stability of ≤1.3 V (vs. Mg^{2+}/Mg) compared to the 3 V of $Mg(BH_4)(NH_2)$, making them incompatible with high-voltage cathodes.[100]

iii) Chalcogenides

Due to the superionic Li^+ and Na^+ conductivity of several chalcogenide-based (in particular sulfide-based) phases, such as argyrodites and glass-ceramics, also, Mg chalcogenide materials are considered as promising class of SEs.[111–116] As its first representatives, Yamanaka et al. studied MgS-P_2S_5-MgI_2 glass ceramics inspired by the highly conductive Li_2S-P_2S_5-LiI system (σ_{ion} = 10^{-4}-10^{-3} S cm^{-1} at 25 °C).[27,117] By tuning the Mg-based system with different amounts of MgI_2, the authors observed the highest ionic conductivity of $\sigma_{ion} = 2.1\ 10^{-7}$ S cm^{-1} at 200 °C with the composition $48MgS \cdot 32P_2S_5 \cdot 20MgI_2$, far less than that of the Li^+ analogues. Therefore, since this is not yet the case, follow-up work is waiting to improve the conductivity and also uncover the still unexplored migration barrier and transport mechanism.[53]

Compared to the glass ceramic, MgB_2X_4 (B = Sc, Y, In; Ln, X = S, Se) chalcogenide spinels have already achieved a major breakthrough within the Mg-ion SEs, as result of their low Mg^{2+} migration barriers [E_a(th) < 0.53 eV] predicted by DFT calculations of Ceder and co-workers.[32,42] The spinel's low migration barriers are attributed to the features of the spinel-type crystal structure

such as 3D conduction pathways, weak cation-cation repulsion, and a favorable coordination environment (discussed in section 2.3). However, despite this promising prediction, only one of the spinels, $MgSc_2Se_4$ (see Figure 2), has been successfully synthesized and electrochemically investigated to date. The authors estimated an outstanding room-temperature ionic conductivity of ~10^{-4} S cm^{-1}, which, however, was not unequivocal evidenced (discussed in section 2.4.4) and accompanied by a relatively high electronic conductivity ($4 \cdot 10^{-4}$ times the ionic conductivity). This is higher than of the common SEs (10^{-8}-10^{-6}) and a concern as it is suggested to result in significant self-discharge of a battery and dendrite formation in the material itself.[35,51] As possible origin of the electronic conduction, Ceder et al. identified point defects, in particular intrinsic Mg/Sc anti-site and Mg-vacancy defects, in selenium-poor phases and the presence of undesired electron-conducting secondary phases.[32,36] Accordingly, Wang et al. applied two strategies for mitigating the intrinsic defects, including the synthesis of Se excess phases and aliovalent doping of Sc^{3+} by Ti^{4+} and Ce^{4+}.[37] Moreover, Kundu et al. used a room-temperature electric field-assisted synthesis to reduce the evaporation of volatile Mg and Se and thus prevent the formation of electronically conductive phases such as Sc and ScSe.[39] Compared to Wang et al.'s strategies, this method significantly lowered the electronic conductivity to $5 \cdot 10^{-6}$ times the ionic one, although still not sufficiently enough. Nevertheless, this work demonstrates that the electronic conductivity can generally be reduced and, moreover, that the spinel probably possesses a high electrochemical stability, as indicated by the stable direct current (DC) polarization at 3 V (vs. Mg^{2+}/Mg) of the Au|$MgSc_2Se_4$|Au cell used for the electrochemical study.

iv) Halides

As the latest group of Mg-ion SEs, halide materials have been published in two recent works. The first deals with the investigation of a series of $MgAl_2Cl_{8-y}Br_y$ compounds, where the highest ionic conductivity of $\sigma_{ion} = 1.3 \cdot 10^{-6}$ S cm^{-1} at 127 °C was found for $MgAl_2Cl_2Br_6$.[28] In the second, a much higher conductivity of $\sigma_{ion} = 4.7 \cdot 10^{-4}$ S cm^{-1} at room-temperature was reported for the magnesium gallium halide $x$$MgCl_2$-$GaF_3$ ($x = 1$).[118] Herein, the authors attributed the fast ion conduction to the undercoordinated Mg^{2+}-ions in a chlorine-rich chemical environment, although the determined conductivity cannot be unequivocally assigned to the Mg-ions as both the cations and anions are mobile. Moreover, a poor interfacial stability of the halide material with the MMA was found. Calculations indicate that the stability ranges from 1.9 V to 3.9 V (vs. Mg^{2+}/Mg), making the novel compound more suitable as a catholyte than an electrolyte.

In light of the material classes presented, borohydrides and chalcogenide spinels have so far proven to be the most promising candidates for room-temperature Mg-ion SEs with ionic conductivities of $\sigma_{ion} \geq 10^{-4}$ S cm^{-1} (cf. Figure 2). In particular, the latter are expected to own low migration barriers and a sufficient large electrochemical stability window to be compatible with high-voltage cathodes. Thus, inspired by these predicted properties, the study of MgB_2Se_4 spinels became the focus of this dissertation, although a way to effectively lower or suppress the electronic conductivity has not yet been found.

2.2 Ionic Transport in Inorganic Solid Electrolytes

The transport of ions within inorganic solid electrolytes is typically considered as a multiscale process from the atomic scale up to the macroscopic device scale.[119] While on the larger scale of macroscopic samples (often SE pellets) contributions of components such as grain boundaries, amorphous phases, and impurities to the ionic transport are distinguished, the atomic scale is limited to mechanisms in the crystal lattice. These mechanisms are very important to understand the principle of ionic transport in crystalline SEs like $MgSc_2Se_4$ and are based on an ionic hopping process introduced by defects: an ion hops from its occupied site to an adjected site – mostly a vacancy or interstitial defect site – in the lattice by overcoming a migration activation energy.[120] In this regard, the migration event can occur via one of the mechanisms shown in Figure 3a: i) vacancy diffusion where an ion migrates from its lattice site into a neighboring vacant lattice site, ii) direct interstitial diffusion in which the ion hops from an interstitial site to the next interstitial site, and iii) correlated or concerted interstitial (or knock-on) migration where the migrating interstitial ion displaces a neighboring lattice ion into an adjacent interstitial site.[119]

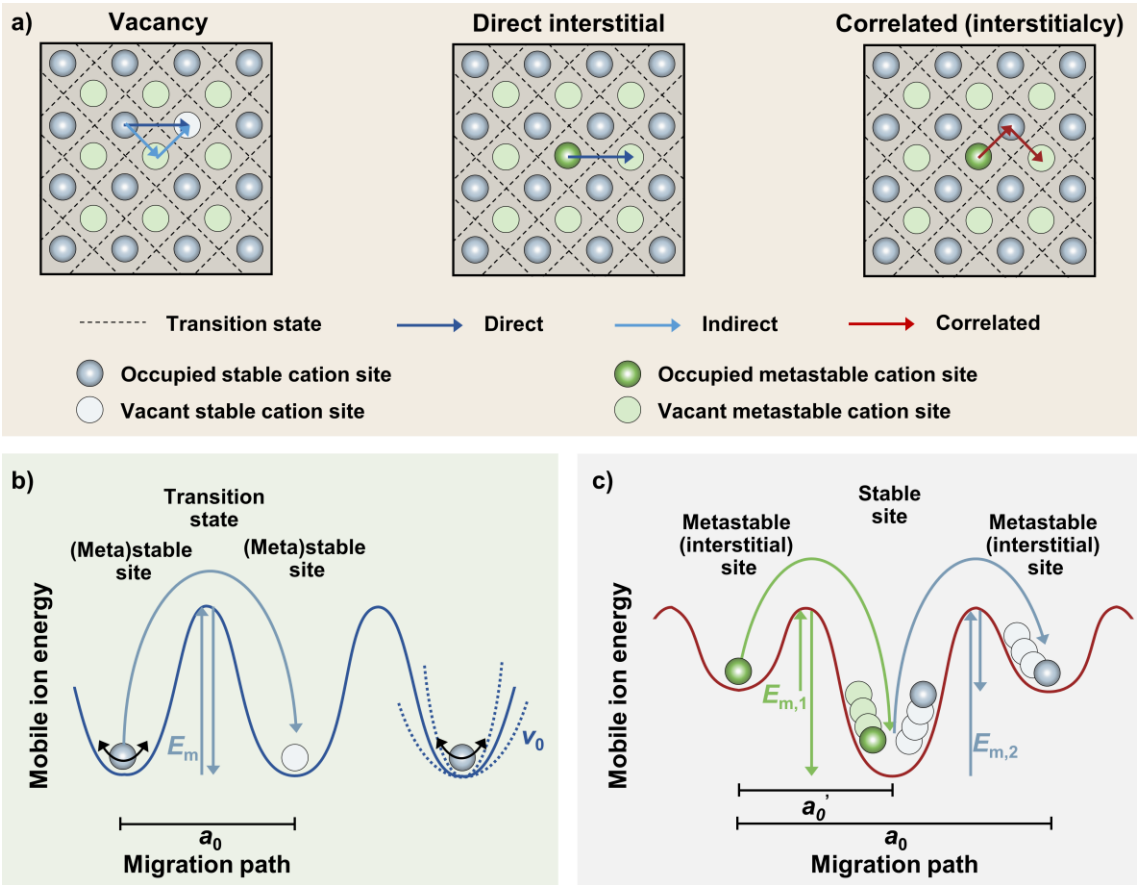

Figure 3: a) Three types of ion migration mechanisms: vacancy diffusion (left), direct interstitial diffusion (center), and correlated diffusion (right). The direction of (in)direct and correlated diffusion in the host lattice is indicated by arrows. b-c) Energy profiles associated with the ion migration. The energy profile of direct vacancy or interstitial hopping is depicted with a blue line in b), while the landscape of correlated hopping is shown with a red line in c). Dashed lines indicate exemplarily the broadness of the potential well related to the hopping frequency v_0. The

hopping distance of the (half) migration pathway is denoted by (a_0') a_0 and the hopping energy E_m is represented by upward arrows. Reproduced with permission from Springer Nature.[119]

Depending on the number of involved ions (single-ion migration or multi-ion correlated migration) and the jump count / passed sites during the mechanism, different landscape geometries arise for the hopping event.[119] As two examples, Figure 3b-c illustrates the landscape of a single-ion migration with one jump and a correlated migration of two ions having one jump each, respectively. Here, the flatness and width of the energy profile is largely determined by individual parameters, such as the hopping energy E_m, hopping distance a_0, and hopping frequency v_0, based on the host structure and the kind of migrating defect. Assuming a homogenous material without chemical potential gradient, these parameters generally correlate with the random-walk diffusion coefficient D_R of the hopping ion:[120,121]

$$D_R = \frac{1}{2d}\, a_0{}^2 v_0 \exp\left(\frac{\Delta S_a}{k_B}\right) \exp\left(-\frac{\Delta H_a}{k_B T}\right) \tag{2.2.1}$$

where d is the number of dimensions considered for ion diffusion, ΔS_a is the activation entropy, and ΔH_a is the activation enthalpy. Note that the defect formation enthalpy $\Delta_f H$ often is neglected as a component of ΔH_a in heavily defective superionic conductors, meaning that only the migration enthalpy $\Delta_m H$ (conventionally E_m) applies, which is then referred to as activation barrier/energy E_a.[120]

However, D_R only applies if diffusion is completely random and uncorrelated.[121] If changing ion-ion interactions (correlations) and self-correlations come into play, constraints to the diffusion occur.[122] Therefore, a measured tracer- or self-diffusion coefficient D_T is often smaller than D_R, which is described by the following relationship:

$$D_T = f\, D_R \tag{2.2.2}$$

where f ($0 \leq f \leq 1$) is a correlation factor as the measure of randomness of successive jumps.[121]

By changing to the transport of ions in a concentration gradient or an electric field, the macroscopic long-range diffusivity D_σ is considered. This is linked to D_T by the Haven ratio H_R ($H_R = D_T/D_\sigma$), which indicates the discrepancy between microscopic ionic diffusion and macroscopic ionic conductivity.[121,122] According to the Nernst-Einstein relation, D_σ relates to the electrical mobility u of the ionic charge carrier and thus also to its ionic conductivity σ_{ion}:

$$D_\sigma = \frac{u k_B T}{q} = \frac{\sigma_{ion} k_B T}{n q^2} \tag{2.2.3}$$

where n is the charge carrier density and q is the quantity of electric charge per charge carrier.

Combining the equations (2.2.1), (2.2.2), and (2.2.3) by considering H_R, the ion conduction can be finally expressed as thermally activated process by the modified Arrhenius-type relationship:

$$\sigma_{\text{ion}} = \frac{\sigma_0}{T} \exp\left(-\frac{E_a}{k_B T}\right) \tag{2.2.4}$$

$$\sigma_0 = \frac{f}{H_R} \frac{nq^2}{k_B} \frac{1}{2d} a_0^2 \nu_0 \exp\left(\frac{\Delta S_a}{k_B}\right) \tag{2.2.5}$$

with σ_0 representing the pre-exponential factor.[121]

Considering this Arrhenius-type relationship, it can be deduced that there are general requirements to achieve high ionic conductivity in SEs, namely: i) The pre-exponential factor σ_0 should be high. This results, on the one hand, from a high charge carrier density n, whose migration requires a heavily defective material and thus a low defect formation enthalpy $\Delta_f H$.[121] On the other hand, σ_0 can be easily affected by ΔS_a and ν_0. However, while there is still no thorough study of ΔS_a in terms of ionic conductivity, it has been shown that a similar landscape of the initial and final site along the migration path increases the probability of a jump and thus the hopping frequency ν_0.[122,123] ii) There should be a low activation barrier E_a. This is particularly important for multivalent (MV) ion conduction, where the high charge density of the mobile ions results in stronger Coulomb interactions with the anion sublattice and, hence, in a high E_a value.[121] For this reason, and due to the fact that the migration barrier of several fast Li-ion conductors such as garnets and LISICON ranges from E_a = 200 meV to 500 meV, a similarly low value is likely promising for MV-ion SEs candidates.[124,125] In order to achieve this, structural impacts on E_a must be considered, including the lattice polarizability and the geometry of the migration pathway.[122] These and other structural effects on the MV-ion conduction are discussed in the following section.

2.3 Structural Effects on Multivalent Ion Conduction in Inorganic Solid Electrolytes

To mitigate the strong Coulomb interactions experienced by the high charge density of MV ions such as Mg^{2+} in the solid-state framework, and thus to find a SE with sufficient multivalent ion conductivity at room-temperature, several structural criteria must be considered. Therefore, the following sections discuss structural effects on the MV-ion conduction based on the structure type, coordination environment, and structural flexibility, with particular attention to MgB_2X_4 (B = Sc, Y, In; Ln, X = S, Se) spinel SEs, which are the focus of this dissertation.

2.3.1 Favourable Structure Types

In general, crystal structures owning exclusively interconnected 3D conduction pathways are considered to be favorable for SEs.[121] They provide a better platform for fast ion diffusion over long-range, since 1D and 2D conduction pathways are more easily blocked completely by intrinsic anti-site and extrinsic defects.[126] However, to finally realize smooth ion diffusion further certain requirements need to be fulfilled. A wide bottleneck size is mandatory along the migration path, which weakens the Coulomb interaction between the mobile ion and the surrounding anions at the transition state (TS).[121,127] This is achieved, for instance, with "open" structures like NASICON-type compounds, where the corner sharing of $[ZrO_6]$ and $[PO_4]$ polyhedra enables a wide bottleneck for the 3D channels. Moreover, it is crucial to mitigate the cation-cation repulsion at the transition state.[128] In this context, a promising example is the AB_2X_4 spinel structure, that offers beside wide 3D conduction channels a relatively large distance between the mobile A-cation in its activated state and the neighboring B-cations compared to other crystal structures. As illustrated in Figure 4 for a layered ($LiCoO_2$) compound vs. a spinel ($LiCo_2O_4$) of the same elements, there is an immense difference in that distance (2.0 Å vs. 2.9 Å) depending on the structure type.[121] The larger distance in the spinel structure inherently reduces the cation-cation repulsion, especially important to enable MV-ion conduction at ambient temperature.

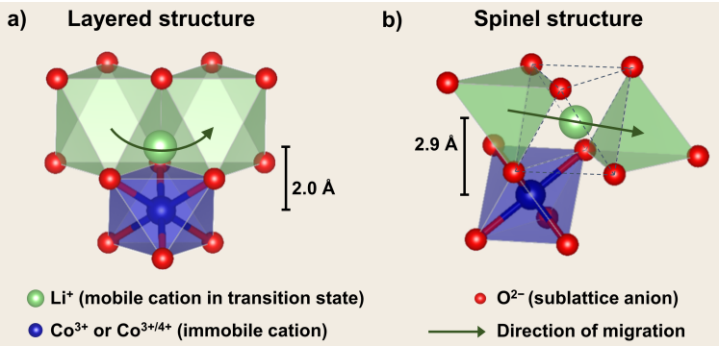

Figure 4: The distance between the mobile ion (Li^+) in the activated state and the nearest immobile cation (Co^{3+} or $Co^{3+/4+}$) is smaller in a) a layered structure ($LiCoO_2$) than in b) a spinel structure ($LiCo_2O_4$). Data for $LiCoO_2$ (mp-22526) and $LiCo_2O_4$ (mp-25383) retrieved from the Materials Project database version v2022.10.28.[129] Adapted with permission from Iton et al.[121] Copyright 2022 American Chemical Society.

Apart from that, to circumvent the strong Coulombic interactions of MV ions in a rigid inorganic anion sublattice, crystalline complex compounds with weak covalent bonds are considered as

favorable structure types.[121] As presented in section 2.1.3, Mg borohydrides are an excellent example in which the addition of neutral molecules results in a weakening of the covalent bonding character, which significantly improves the ionic conductivity.

2.3.2 Coordination Environment

It has also been suggested that the coordination environments that the mobile ion experiences along its migration path play a meaningful role for the E_a value.[121] According to the computational study by Rong et al., significantly lower E_a values are predicted when the MV ion occupies a stable lattice site with an "unfavorable" and an activated site with a "favorable" coordination environment.[130] "Favorable" means in this context the statistically most often found coordination environment, which is for the MV ions Zn^{2+}, Mg^{2+}, and Ca^{2+} the tetrahedral (*tet*), octahedral (*oct*), and 8-coordinate site, respectively. Later on, Canepa et al. supported the hypothesis of Rong et al. by calculating Mg/Zn sulfide and selenide spinels in which both MV ions occupy a stable tetrahedral site, with the Mg compounds consistently exhibiting lower E_a values.[32] In these MgB_2X_4 (B = Sc, Y, In; Ln, X = S, Se) spinels, the Mg-ions hop from their unfavorable tetrahedrally coordinated stable site across a favorable octahedral activated site to reach the next tetrahedral site along the *tet-oct-tet* migration path (Figure 5a). Since the activated *oct* site is favourable, its energy level decreases, while the energy level of the unfavourable initial and final *tet* sites increases. This leads to a flattening of the migration path's energy profile (Figure 5b) and thus to a low migration barrier.[32,35,131] The magnitude of this migration barrier E_a is defined by the relative energy difference between the stable site and the transition state TS (here: trigonal face (*tri*) between *tet* and *oct*), representing the bottleneck of the migration path, and is composed of a kinetic and a static component.[32,35] In this regard, the kinetic contribution is referred to as kinetically resolved activation barrier E_{KRA}, while the static contribution is descripted by the site preference energy ΔE, i.e., the stability difference between the activated (here: *oct*) and the stable site (here: *tet*).[35,132]

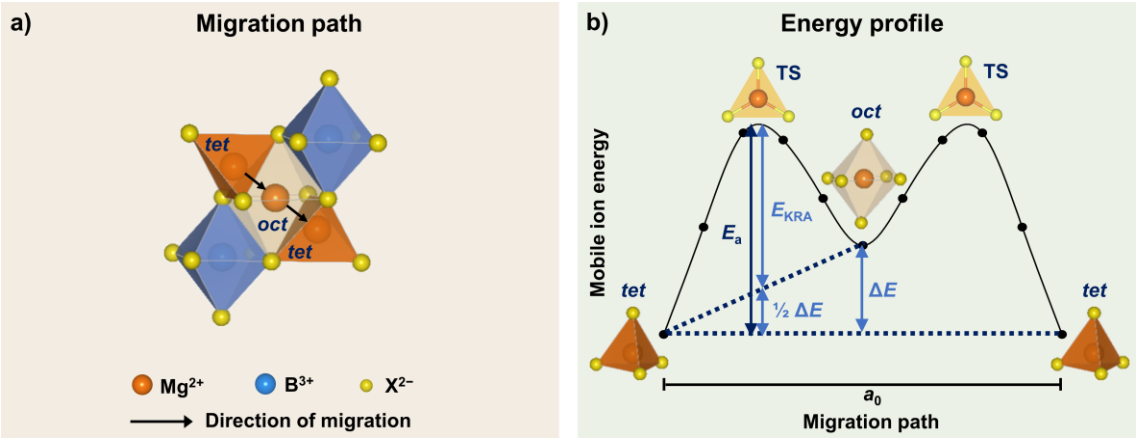

Figure 5: a) The tet-oct-tet migration path in MgB_2X_4 spinels. Mg^{2+} is tetrahedrally coordinated at the initial and final sites (orange) and migrates though an empty octahedral (light orange) site. b) Schematic of the energy profile along the migration path a_0. The migration barrier E_a and the contributions of the kinetically resolved activation barrier E_{KRA} and the site preference energy ΔE are indicated by arrows. Figures adapted with permission from Glaser et al.[44] Copyright 2024 Advanced Energy Materials, Wiley-VCH.

However, given the migration profile in Figure 5b, in addition to a low Δ*E* between the *oct* and *tet* site, stabilization of the transition state is obviously crucial for low E_a values. This can be typically realized by choosing larger anions ($O^{2-} < S^{2-} < Se^{2-} < Te^{2-}$), which increase the area of the transition state, the trigonal face in the spinel structure, and thus facilitate the MV-ion migration.[32,133] Moreover, the volume increase of the divalent anions also leads to a softer, more polarizable anion framework.[134] This weakens the binding interaction of the mobile ion and the framework, meaning the local jump mode achieved a broad oscillation, whereby E_a is reduced (Figure 6a). Therefore, selenide-based compounds can have even higher MV-ion mobility than sulfides, but usually at the expense of electrochemical stability.[121]

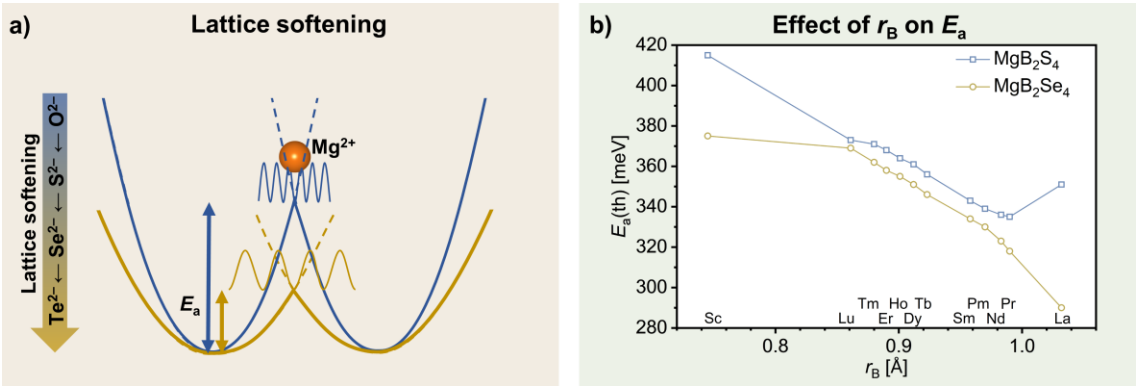

Figure 6: a) Effect of anion lattice softening on the migration energy landscape and the Mg^{2+} migration barrier. The Mg^{2+} migration barriers are indicated by solid arrows. b) Effect of the radius r_B of the B^{3+}-ion on the Mg^{2+} migration barrier in sulfide and selenide spinels. Ionic radii are taken from Shannon.[135] Data for E_a(th) retrieved from Canepa et al.[32] and Koettgen et al.[42] Figure in panel a) is adapted with permission from Kraft et al.[136] Copyright 2017 American Chemical Society.

Another way to stabilize the transition state through a larger bottleneck is to substitute the immobile cation in the lattice for a larger cation. According to the computational study by Koettgen et al., in the MgB_2X_4 spinel structure the unit cell volume and thus the bottleneck increases with the ion radius r_B of the B^{3+}-ion (Figure 6b).[42] A 40% increase of r_B from 0.745 Å (Sc^{3+}) to 1.032 A (La^{3+}) leads to an ~30% increase of the unit cell volume. Thus, a decrease in E_a(th) from 375 meV ($MgSc_2Se_4$) to 290 meV ($MgLa_2Se_4$) is predicted, which is certainly also due to a reduced cation-cation repulsion (see section 2.3.1) in the expanded structure. Practically, such a concept has more or less already been applied to the NASICON-type $Mg_{0.5}Zr_2(PO_4)_3$ SE. By replacing $Zr_2(PO_4)_3$ with the larger $HfNb(PO_4)_3$ unit, a decrease of E_a from 0.82 eV to 0.66 eV was reported, which is at least partly due to the expansion of the conduction pathway.[22,121,137]

Nevertheless, it should be noted that compositional tuning of a material not only affects the unit cell volume, but can also have other effects, such as structural distortion or even a change in the structure type. This may lead to a different migration pathway or at least have further influence on the kinetic and static contributions to the migration barrier. In the MgB_2X_4 spinel structure, for example, the trigonal distortion of the octahedra changes by varying the B^{3+}-ion. The influence of trigonal distortion on the migration path geometry and the energetic contributions to E_a has not

yet been investigated and is therefore discussed in detail as part of the second publication (section 3.2) of this doctoral thesis.

2.3.3 Structural Flexibility

Another non-negligible positive effect on the ion conduction results from the structural flexibility. This means that flexible components in the structure distort or rotate in response to ion transport and thus facilitating the migration.[121] Such phenomenon has been reported for many structures with covalent bonds in polyanions (e.g., NO^{2-}, PO_4^{3-}, SO_4^{2-}).[134,138–140] A rare example of a MV-ion conductor with flexible components is the electronically insulating $ZnPS_3$.[121,141] In this compound, the Zn^{2+}-ion conduction is facilitated by the distortion of $[P_2S_6]^{2-}$ polyanions, which widens the bottleneck along the migration path and thus reduces the Coulomb interaction. This results in a low E_a value of 350 meV, comparable to many superionic Li^+ conductors. Beyond distortion, dynamic rotational disorder of polyanions through the so-called paddlewheel mechanism has been observed in high volume crystalline phases, typically stabilized in glassy, disordered materials or at high temperatures.[142] A prominent example with a high temperature "rotor phase" is Li_3PS_4.[134] While in the stable low-temperature γ-Li_3PS_4 phase the $[PS_4]^{3-}$ tetrahedra are arranged along the *c* axis, a particular disorder arrangement occurs in the high-temperature β-Li_3PS_4 phase, allowing polyanion rotation. Interestingly, this β-phase could recently be stabilized at room-temperature by partial substitution of Si^{4+} at the P^{5+} site, thereby reducing the migration barrier of the compound.[143,144] It can therefore be summarized that in addition to an advantageous coordination environment with large bottlenecks, 3D conduction paths, and a high polarizability of the anion sublattice, structural flexibility should also be considered when searching for novel MV-ion conductors with high room-temperature ionic conductivity.

2.4 How to Determine Partial Conductivities of Mixed Ionic-Electronic Conductors

Although simultaneous ionic and electronic conductivity play an important role for cathode materials, in SEs electronic transport is undesired as it leads to battery self-discharge and dendrite formation.[35,51] However, if the material is a so-called mixed ionic-electronic conductor (MIEC), it is in any case crucial to know the partial conductivities. To this end, the following chapter presents four methods which are widely suitable for the determination of partial conductivities or transference numbers. The working principles along with the shortcomings/requirements of these methods are discussed, especially with focus on the investigation of novel magnesium compounds such as the mixed conductor $MgSc_2Se_4$, whose partial conductivities have not yet been clearly determined.

2.4.1 Electrolysis Method

The electrolysis method, often known as Tubandt's method, describes basically a transference measurement in which the amount of substance transported through a solid (e.g., SE, MIEC) is compared with the charge that was flown through.[145] An early example of this method dates back to 1920, when Tubandt evaluated the ionic fraction of the total electrical conductivity in AgI using the galvanic cell depicted in Figure 7.[146,147]

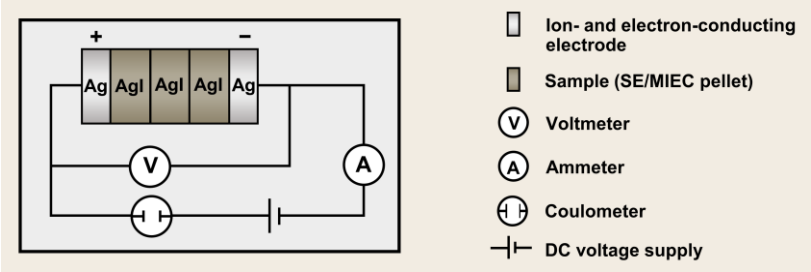

Figure 7: Schematic illustration of the Tubandt's method for determining ionic and electronic transference numbers of solids, exemplified for AgI. Modified with permission of IOP Publishing, Ltd., from Takahashi et al.[148]; permission conveyed through Copyright Clearance Center, Inc.

In principle, the cell design of this method requires the use of non-blocking electrodes (here: Ag) for either the mobile ions or electrons, three pellets of the MIEC (or SE, here: AgI) lined up between the electrodes, and the imposition of a direct current j_{DC} of known time and magnitude.[149] Due to the applied direct current, substance (Ag) can be transferred from one electrode|MIEC interface (positive side) through the MIEC to the other (negative side) by ionic (Ag^+) transport.[145] Consequently, one electrode|MIEC pair is getting lighter, while the other is getting heavier. Applying the Faraday's law on the weight change of one electrode|MIEC pair, the partial ionic current j_{ion} results. If the value of j_{ion} is not identical to that of j_{DC}, this indicates that an electronic current j_{el} must also have flowed through the pellets. The ratio between j_{ion} and $j_{DC.}$ gives the value of the ionic transference number t_{ion} and thus also of the electronic transference number t_{el} according the following equations:[149]

$$t_{ion} = \frac{j_{ion}}{j_{DC}} = \frac{j_{ion}}{j_{ion} + j_{el}} \tag{2.4.1}$$

$$t_{\text{ion}} + t_{el} = 1 \tag{2.4.2}$$

In the last decades, modifications of the Tubandt's method have been widely applied for the investigation of oxide-based materials such as tungstates, glasses, and phosphates, including even NASICON-type Mg-ion conductors.[22,137,150–154] What most of these modifications have in common is the use of ion-blocking Pt electrodes, between which ion transport is only ensured due to oxygen redox chemistry at the electrodes.[22] This proves to be very beneficial for the study of oxide Mg-ion conductors, since this modification eliminates the need for stiff and oxidizing Mg electrodes, which may lead to poor contact with the MIEC pellet. In fact, these properties of the magnesium electrode are probably one of the reasons why no other classes of Mg-ion conductors have been studied by the Tubandt's method so far. Other reasons may be related to the requirements of the method that address the Mg-ion conductor. These include a maximum of two mobile species in ionic or ionic-electronic transport, the compressibility into stable pellets, a sufficient pellet-pellet contact, and electrochemical stability against the electrodes.[145,153,154]

2.4.2 Stationary Polarization Method

The second method is the stationary polarization method in which either the electronic or ionic current is suppressed by appropriate choice of electrodes and polarity.[145] This allows the direct measurement of the non-blocked current and hence the determination of the corresponding partial conductivity. In order to perform the stationary polarization method three meaningful electrode combination are possible, in which the MIEC is i) between electron-blocking electrodes, ii) between ion-blocking electrodes, or iii) between a reversible and an ion-blocking electrode. These combinations are illustrated as examples for the MIEC Ag_2S in Figure 8 and are discussed below.

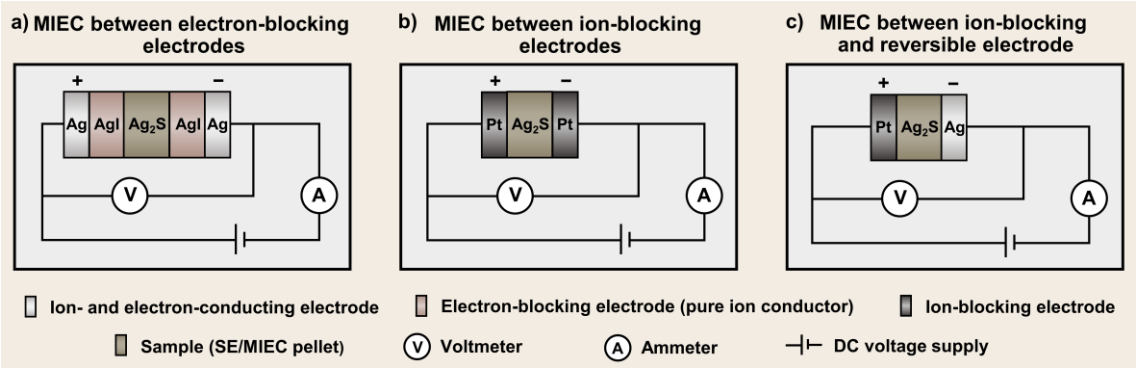

Figure 8: Experimental set-ups of electrode combinations and polarities used in the stationary polarization method to suppress either a) the electronic or b-c) the ionic current of a MIEC. Depending on the suppressed current, the partial conductivity of the respective unblocked charge carrier can be determined. Panel a-b) modified with permission from Springer Nature.[145] Panel c) modified from publication Riess[155], Copyright 1996, with permission from Elsevier.

i) Mixed Conductor between Electron-Blocking Electrodes

The combination of electron-blocking electrodes is used when the partial ionic conductivity of a MIEC (here: Ag_2S) is to be determined.[145] In this case, the electron-blocking electrodes consist of a pure ion conductor (AgI), whose mobile species (Ag^+) corresponds to that of the MIEC. This

means that under an applied potential difference only an ionic current flows through the cell at steady-state, while the transport of electrons is suppressed. At this point it is worth noting that the measurement of the ionic current may be accompanied by polarization phenomena at the current-carrying electrodes (Ag).[145] These polarization effects are eliminated by including separate electron-blocking probes of a pure ion conductor that measure the electrochemical potential difference of the mobile ions over a certain distance in the MIEC. With regard to the application of this sub-method to Mg-based MIECs, this means that for such electron-blocking electrodes a pure Mg-ion-conducting solid must be found which is compatible with the MIEC and the external electrodes. However, this is currently quite difficult due to the still very limited selection of Mg-ion SEs. Moreover, the external electrodes, which must in turn be ion- and electron-conducting, present another challenge for the application. Although Mg electrodes appear here to be obviously a reasonable choice, their reported overpotential, which is caused by passivation and poor physical contact due to low deformability, raises concerns about their suitability.[62]

ii) Mixed Conductor between Ion-Blocking Electrodes

This second stationary polarization sub-method is used to determine the partial electronic conductivity of a MIEC.[145] By applying a constant DC polarization to a MIEC between ion-blocking (Pt) electrodes, the (Ag^+) ion current is completely blocked after reaching stationary state conditions and thus the residual current is solely from electronic contribution.[156] However, it should be mentioned that this approach can lead to an overestimation of the electronic conductivity. Based on the fact that the activity of the mobile species is not defined for each electrode, it is unclear in which activity range the electronic conductivity is being measured.[157] Therefore, it is assumed that the measured steady-state current (SSC) is the maximum current allowed to flow under the given potential voltage, which can be considered as the upper limit of the electronic conductivity. In addition, electrolytic decomposition of the MIEC due to a limited electrochemical stability window can occur, whereby a resulting decomposition current can contribute to the measured SSC.[157] Nevertheless, aside from the overestimation of the SSC, this sub-method appears to be applicable to Mg-based MIECs/SEs with a sufficient stability window, not least due to wide availability of ion-blocking electrodes, such as Au, Ag, C, Pt, and Ta.[32]

iii) Mixed Conductor between Ion-Blocking Electrode and Reversible Electrode

The last sub-method, also called Hebb-Wagner approach, is based on an asymmetric electrode arrangement consisting of an ion-blocking and a reversible electrode.[158] In this approach, the chosen polarity (see Figure 8c) allows only electrons to flow through the MIEC in the steady-state, thus ensuring the determination of the partial electronic conductivity.[145] Since, in contrast to the second sub-method, a reversible electrode is used, the chemical potential μ_i of one component *i* (e.g., Ag) at a particular activity of *i* is exactly defined on one side of the MIEC.[157] Instead, at the ion-blocking electrode on the other side of the cell, the chemical potential varies depending on the voltage applied to the cell.[145] This enables the measurement of the electronic current as a function of the chemical potential and thus an even more precise evaluation of the partial electronic conductivity. However, despite this advantage, some inaccuracies are also

reported for the Hebb-Wagner approach concerning the interphase formation at the electrodes induced by electrochemical instability of the SE/ MIEC.[155,157] The interphase formation can cause a potential variation at the reversible electrode or an ionic current at the ion-blocking electrode.[157] For that reason, it ultimately influences the given chemical potential and the measured SSC, but also induces overpotentials at the electrodes. If the overpotential is not small enough to be neglected, it is suggested to use two additional inner probes with the Hebb-Wagner approach to determine the real potential difference within the SE/MIEC.[155,159] These inner probes should be electron-conducting but ion-blocking to the MIEC, meaning that there is likely a wide availability of probe materials for studying Mg^{2+} mixed conductors, whereas finding a reversible ion- and electron-conducting electrode, as discussed above, is rather challenging.

2.4.3 Open Circuit Potential Method / emf Method

The open circuit potential method, also called as emf (electromotive force) method, is applied like the Tubandt's method to determine the ionic and electronic transference number. In this approach, the MIEC (or SE) is studied between two electrodes with different chemical potential μ_i of the mobile species i using a galvanic cell, as shown in Figure 9.[145]

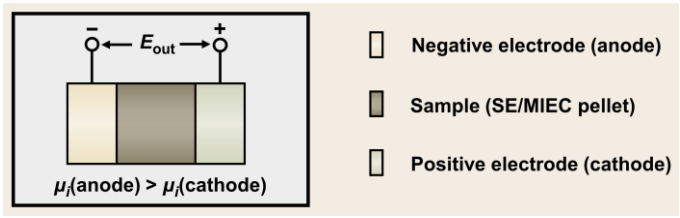

Figure 9: Simple model of an electrochemical cell used for the emf method to determine the ionic and electronic transference numbers. Reproduced with permission from Springer Nature.[160]

Due to the chemical potential difference of the cathode μ_i(cathode) and anode μ_i(anode), a corresponding output voltage E_{out} is expected under open circuit conditions when neither ions nor electron can be transported externally from one electrode to the other.[149] Under those conditions, the measured E_{out} value is assumed to be equal to the electromotive force emf, meaning the electrical equivalent of the chemical driving force, which is given by[145,149,161]

$$E_{out} = -\frac{\mu_i(\text{cathode}) - \mu_i(\text{anode})}{zF} = -\frac{\Delta_r G}{zF} = \text{emf} \tag{2.4.3}$$

where $\Delta_r G$ is the change in molar Gibbs free energy of the theoretical cell reaction, z is number of transferred electrons per mobile ion and F is the Faraday constant. If the solid electrolyte has an electronic leakage or in other words is a MIEC, the resulting voltage is then given by[149]

$$E_{out} = t_{ion} \cdot \text{emf} = \frac{R_{el}}{R_{ion} + R_{el}} \cdot \text{emf} \tag{2.4.4}$$

where t_{ion} is the ionic transference number, which can also be expressed by a ratio of internal resistances associated with the mobile ion transport (R_{ion}) and the electronic leakage (R_{el}). This equation basically demonstrates the simple concept of the emf method to determine transference

numbers by measuring the E_{out} value of a galvanic cell with defined emf. However, as the method requires well-defined and known thermodynamic conditions at each of the electrodes, it can be quite difficult to find suitable electrode materials, especially in the case of less advanced technologies such as MV systems, where the choice is still relatively limited.

2.4.4 Variable Frequency Small Signal AC Method

The variable frequency small signal alternating current (AC) method is based on impedance measurements and has proven to be an alternative option to the DC methods for determining partial conductivities and transference numbers of solids.[162] Its most common arrangement (Figure 10a) uses ion-blocking but electron-conducting electrodes on either side of the solid being investigated.

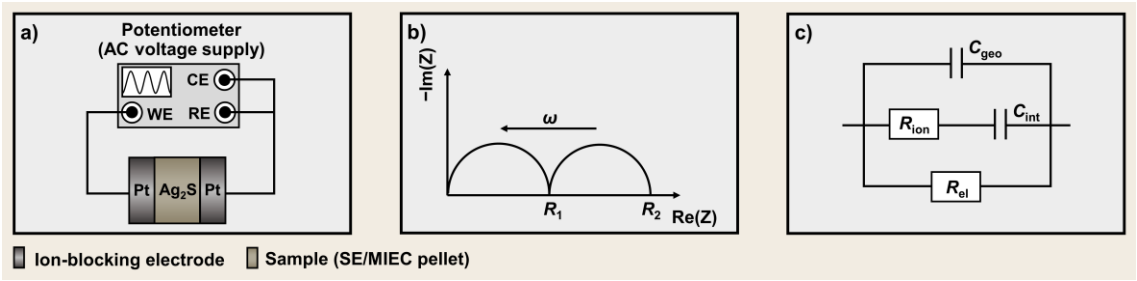

Figure 10: a) Common experimental set-up used for the variable frequency small signal AC method to determine partial conductivities of solids, exemplified for Ag_2S. WE, CE, and RE represent the working, counter, and reference electrode of the potentiometer, respectively, which are connected to the ion-blocking electrodes of the electrochemical cell. b) Sketch of the resulting Nyquist plot of the impedance spectrum of a solid with significant ionic and electronic conductivity (MIEC), whose corresponding equivalent circuit is depicted in c). Figures modified from Huggins.[149] Reproduced with permission from Springer Nature.

If the solid between the electrodes is a MIEC with a substantial ionic transport as well as an electronic contribution, this results in an impedance spectrum with two semicircles, as shown in the Nyquist plot in Figure 10b.[149,162] The semicircle at low frequencies represents the parallel combination of the electronic resistance R_{el} and the geometrical capacitance C_{geo}, while the high-frequency semicircle corresponds to the parallel combination of the ionic resistance R_{ion} and C_{geo}. This can also be described by the physically meaningful equivalent circuit in Figure 10c, in which the blockage of the ionic transport at low frequencies due to ion-blocking electrodes is expressed by an interfacial capacitance C_{int} in the ionic conduction pathway. As instead the electronic conduction pathway is unblocked, there is no interfacial capacitance and thus no blocking-tail appears for the low frequency semicircle in the impedance spectrum. Moreover, due to the ion blockage, the real axis intercept of this semicircle, denoted as R_2, is merely the electronic resistance R_{el}, which corresponds to the DC resistance of the cell. At higher frequency, however, the resulting intercept R_1 is a combination of the two parallel resistances R_{el} and R_{ion} and is described as follows:

$$\frac{1}{R_1} = \frac{1}{R_{ion}} + \frac{1}{R_{el}} \tag{2.4.5}$$

Hence, these relationships to the axis intercepts R_2 and R_1 allow the determination of R_{el} and R_{ion}, and thus the partial electronic and ionic conductivity, σ_{el} and σ_{ion}, which in turn define the transference numbers t_{el} and t_{ion}:[149,162]

$$t_{ion} = \frac{\sigma_{ion}}{\sigma_{ion} + \sigma_{el}} = \frac{R_{el}}{R_{ion} + R_{el}} \tag{2.4.6}$$

$$t_{el} = \frac{\sigma_{el}}{\sigma_{ion} + \sigma_{el}} = \frac{R_{ion}}{R_{ion} + R_{el}} \tag{2.4.7}$$

Considering the case of $t_{ion} >> t_{el}$ (meaning $R_{el} >> R_{ion}$), as desired for a solid electrolyte, the higher frequency semicircle is generally the smaller one in the impedance spectrum.[149,162] Moreover, it is even possible that this semicircle completely disappears. If so, only R_{el} (R_2) and thus the electronic conductivity can be unequivocally derived from the single lower frequency semicircle. This is obviously a shortcoming of the AC method, which needs always to be considered. Disregard, however, may lead to misinterpretations, such as in the recent studies of $MgSc_2Se_4$ by the groups of Ceder and Fichtner.[32,37] Here, the authors simply neglected that the high-frequency semicircle did not appear and used the left-hand offset of the lower frequency semicircle as a substitute to calculate the ionic conductivity, without proof of validity. For this reason, the evaluation of the ionic conductivity in this way must be regarded as unreliable, so that so far there is no unequivocal evidence for Mg-ion transport in $MgSc_2Se_4$.

However, to still be able to determine the ionic conductivity of compounds such as $MgSc_2Se_4$, the AC method can alternatively be conducted in the less common electron-blocking version.[163] In this variant, the setup usually consists of one central MIEC pellet to be characterized, sandwiched between a double layer of an ion conductor (inner layer = electron-blocking) and a reversible reservoir electrode (outer layer), analogues as descript for the first DC sub-method (cf. Figure 8a). If in this variant t_{ion} is much larger than t_{el}, the opposite case as before is observed and the higher frequency semicircle is the larger or even the only one that appears. Thus, an accurate determination of the ionic conductivity is possible.

Overall, this comprehensive method overview demonstrates that the determination of partial conductivities as well as transference numbers is not always trivial, especially in the case of MV-ion materials, where the search for suitable and compatible electrodes is a challenge. With regard to the investigation of $MgSc_2Se_4$, both the DC polarization and the AC method using conventional ion-blocking electrodes such as Ta and Au have so far proved to be appropriate for the analysis of the partial electronic conductivity.[32,37] The determination of the partial ionic conductivity is, however, hindered by the lack of compatible reversible and pure Mg-ion-conducting electrodes, whose overpotentials / interface resistances should be negligible or well-defined in order to be suitable for DC methods (electrolysis, stationary polarization, and open circuit method).[149,155] Therefore, the electron-blocking AC method, which also allows revealing the interfacial contributions,[149] currently appears as the most promising way for determining the partial ionic conductivity. Accordingly, in the first publication of this work, a cell concept was developed for

the AC method to accurately determine the partial ionic conductivity of $MgSc_2Se_4$ and other mixed-conducting MgB_2Se_4 spinels.

3 Results

At the beginning of this doctoral thesis in 2020, there was uncertainty whether MgB_2Se_4 spinels are Mg-ion conductors and thus suitable as potential Mg-ion SEs. Although there had been a handful of electrochemical studies on one of the spinels, $MgSc_2Se_4$, unequivocal evidence for Mg-ion transport in this class of materials was still missing. Moreover, the compositional influence on the transport properties of the MgB_2Se_4 spinels was exclusively investigated to a very limited extent by DFT calculations, not allowing detailed insights. Therefore, the objectives of this dissertation were to provide reliable evidence for Mg-ion transport in the MgB_2Se_4 spinels and to gain deeper understanding of how the variation of B^{3+}-cations influences the ionic transport properties.

This chapter presents three publications that address the objectives of this dissertation and serve as its basis. Publication 1 deals with the proof of Mg-ion transport in $MgSc_2Se_4$ and introduces a special cell concept, allowing the accurate determination of the partial ionic conductivity of mixed-conducting Mg-based compounds. The second publication provides a comprehensive experimental and computational study on the MgB_2Se_4 system, which contributes to a better understanding of how to reach small migration barriers in magnesium chalcogenide spinels. This study was further modified in publication 3 by considering the magnesium insertion energy, whereby a magnesium selenide spinel with exceptional high magnesium ion mobility was identified.

3.1 Publication 1: "To be or not to be – Is $MgSc_2Se_4$ a Mg-Ion Solid Electrolyte?"

This first publication addresses in the initial part the open scientific question of whether $MgSc_2Se_4$ is a magnesium ion conductor, crucial for further research into its use as a Mg-ion SE. To reliably clarify this question, a Mg metal deposition experiment was conducted under DC conditions using a Mg|$MgSc_2Se_4$|Au cell. With this approach, the formation of Mg deposits at the Au electrode was observed by energy-dispersive X-ray spectroscopy (EDS) during scanning electron microscopy (SEM) measurements, suggesting that Mg-ion transport through the spinel must have occurred. In line with that, cycling experiments based on plating/stripping and full cells demonstrated reversible Mg^{2+} cycling and served therefore as another unequivocal evidence for Mg-ion conduction in the $MgSc_2Se_4$ spinel.

Based on these conclusions – identifying $MgSc_2Se_4$ as a Mg-ion SE – the following section of the study focused on determining the partial ionic conductivity of the spinel. To overcome the difficulty of extracting the ionic contribution of the mixed ionic-electronic conductor $MgSc_2Se_4$, a transference cell was developed that contains purely Mg-ion-conducting interlayers. This special cell design effectively suppressed the electron transport during the EIS measurements and thus enabled an accurate determination of the high partial ionic conductivity (σ_{ion} = $4 \cdot 10^{-5}$ S cm^{-1} at 25 °C) and the low Mg^{2+} migration barrier (E_a = 386 meV) of $MgSc_2Se_4$.

Overall, this first publication provides the foundation for considering $MgSc_2Se_4$ and the compounds of its material class as potential Mg-ion solid electrolytes. For the first time, long-

range Mg-ion transport in the $MgSc_2Se_4$ spinel was unequivocally evidenced as well as a simple strategy for the precise determination of ionic conductivities of magnesium-based MIECs was developed. These achievements, in combination with the outstanding ionic transport properties of $MgSc_2Se_4$, pave the way for further research on ternary magnesium selenide spinel SEs, and with that of the following publications 2 and 3.

The experiments were designed and planned by the first author with the assistance of Dr. Z. Wei under supervision of Prof. M. Rohnke and Prof. J. Janek. The $MgSc_2Se_4$ SE was synthesized by C. Glaser and the $Mg[B(hfip)_4]_2$ LE was provided by Dr. Z. Zhao-Karger. C. Glaser performed all electrochemical experiments as well as the SEM, EDS, and X-ray diffraction measurements. The first author was supported by Prof. H. Ehrenberg in the Rietveld refinements based on the XRD patterns and assisted by Dr. Z. Wei in the interpretation of the electrochemical data. Dr. S. Indris conducted and interpreted the NMR measurements. Absorption and photoluminescence spectroscopy were carried out by Dr. P. Klement from the group of Prof. S. Chatterjee. The manuscript was written by the first author and revised by eight co-authors.

This study was part of the research within POLiS – Post Lithium Storage Cluster of Excellence.

RESEARCH ARTICLE

ADVANCED ENERGY MATERIALS
www.advenergymat.de

To Be or Not to Be – Is $MgSc_2Se_4$ a Mg-Ion Solid Electrolyte?

*Clarissa Glaser, Zhixuan Wei, Sylvio Indris, Philip Klement, Sangam Chatterjee, Helmut Ehrenberg, Zhirong Zhao-Karger, Marcus Rohnke, and Jürgen Janek**

Magnesium batteries offer promising potential as next-generation sustainable energy-storage solutions due to the high theoretical capacity of the magnesium metal anode. Facilitating dendrite-free operation of metal anodes necessitates the development of solid electrolytes with high magnesium-ion conductivity. While the chalcogenide spinel $MgSc_2Se_4$ is predicted to exhibit high magnesium ion mobility, unequivocal experimental evidence for magnesium ion conduction beyond short-range motion is still missing. This study confirms magnesium-ion transport in $MgSc_2Se_4$ through two independent electrochemical methods: electrochemical deposition of magnesium metal and reversible magnesium plating/stripping cycling. To overcome the difficulty of measuring the ionic conductivity of the mixed conducting $MgSc_2Se_4$ spinel, a pure ion conducting interlayer is employed in a symmetric transference cell. This approach effectively suppresses the electron transport, allowing accurate characterization of the ionic conductivity. The experimental results confirm a low migration barrier of (386 ± 24) meV for magnesium ion transport in $MgSc_2Se_4$ and demonstrate one of the best performances at room temperature among the reported inorganic magnesium solid electrolytes. The findings open a new door for exploring additional mixed magnesium ion conductors and highlight the potential of magnesium chalcogenide spinels as a promising class of magnesium solid electrolytes.

1. Introduction

Lithium-ion batteries (LIBs) have emerged as the most promising energy storage systems for portable and smart electronic devices.[1] However, the limited lithium availability and safety issues of LIBs combined with the growth of the human demand for energy increased the interest in developing next-generation battery cells.[2–4] Recently, sodium-ion batteries (SIB) have emerged as a serious new storage concept, with commercialization efforts already underway.[5] While potassium ion cells may appear as a natural progression, cell concepts utilizing multivalent ions such as Mg^{2+}, Ca^{2+} and Zn^{2+} offer the potential for higher volumetric energy densities compared to cells utilizing monovalent ions. Furthermore, these multivalent ion-based cells are expected to achieve lower cost, making them an attractive option.[6] As a result, research activity on calcium and zinc has grown rapidly, albeit not to the same extent as magnesium. The discrepancy is probably due to the fact that the suitability of calcium and zinc as safe anode materials has not been studied as extensively. In alkaline aqueous solutions, zinc notoriously plates into tree-like dendrites, while calcium exhibits various morphologies, including the desired dense and thick bulk structures that are widely documented for magnesium.[3] In addition to this, magnesium-ion batteries (MIBs) are an attractive avenue for further development alongside the alkali-ion technology. This is primarily due to the outstanding characteristics of the magnesium metal anode, which include an almost

C. Glaser, Z. Wei, M. Rohnke, J. Janek
Institute of Physical Chemistry
Justus Liebig University Giessen
Heinrich-Buff-Ring 17, D-35392 Giessen, Germany
E-mail: Juergen.Janek@phys.chemie.uni-giessen.de

C. Glaser, Z. Wei, P. Klement, S. Chatterjee, M. Rohnke, J. Janek
Center for Materials Research (ZfM)
Justus Liebig University Giessen
Heinrich-Buff-Ring 16–17, D-35392 Giessen, Germany

The ORCID identification number(s) for the author(s) of this article can be found under https://doi.org/10.1002/aenm.202301980

DOI: 10.1002/aenm.202301980

S. Indris, H. Ehrenberg
Institute for Applied Materials - Energy Storage Systems (IAM-ESS)
Karlsruhe Institute of Technology (KIT)
Hermann-von-Helmholtz-Platz 1, D-76344 Eggenstein-Leopoldshafen, Germany

P. Klement, S. Chatterjee
Institute of Experimental Physics I
Justus Liebig University Giessen
Heinrich-Buff-Ring 16, D-35392 Giessen, Germany

Z. Zhao-Karger
Institute of Nanotechnology (INT)
Karlsruhe Institute of Technology (KIT)
Hermann-von-Helmholtz-Platz 1, D-76344 Eggenstein-Leopoldshafen, Germany

Z. Zhao-Karger
Helmholtz Institute Ulm (HIU) Electrochemical Energy Storage
Helmholtzstrasse 11, D-89081 Ulm, Germany

ADVANCED SCIENCE NEWS
www.advancedsciencenews.com

ADVANCED ENERGY MATERIALS
www.advenergymat.de

double volumetric capacity of $q_V = 3833$ mAh cm^{-3} and 10^4 times higher earth-abundance compared to lithium, and a low potential of magnesium ($E_H = -2.37$ V vs SHE). Furthermore, the Mg metal anode is predicted to be less reactive and less prone to dendrite formation, making MIBs a more secure energy storage option.[2,7] Despite these theoretical advantages of magnesium, there are several key challenges that need to be addressed in the development of electrolytes and cathodes before MIBs can be practically implemented. The knowledge gained from the research on LIBs and SIBs cannot be directly transferred to MIBs due to the significant differences in the electrochemistry of monovalent and multivalent ions in various aspects. For instance, an ion-blocking passivation layer forms on Mg metal when it comes into contact with conventional carbonate-based electrolyte solvents that are widely used in LIBs and SIBs.[8,9] Consequently, novel electrolytes based on Grignard reagents have been developed. However, safety concerns associated with their ether-based solvents, such as high vapor pressure and flammability, arise.[9,10] Alternatively, non-flammable ionic liquids (ILs) can be used as solvents to dissolve magnesium salts, provided that they possess a sufficient reductive stability against the Mg metal.[7] In light of this, solid electrolytes (SEs) can be viewed as a safe alternative, where the most challenging factor is to achieve sufficient conductivity at room temperature due to the typically low ion mobility resulting from the high charge density of the Mg^{2+} ion.[10]

The earliest work on Mg-ion SEs dates back to 1987, when Ikeda et al. reported an ionic conductivity of $\sigma_{ion} = 6 \times 10^{-3}$ S cm^{-1} at 800 °C for $Mg_{0.5}Zr_2(PO_4)_3$.[11] The conductivity at room temperature is ten orders of magnitude lower. To improve the room temperature conductivity, several studies on the substitution of aliovalent ions on the Zr- and P-lattice sites have been performed. However, so far the reported conductivities are still limited to values below $\sigma_{ion} = 3 \times 10^{-5}$ S cm^{-1}.[12] Borohydrides, another class of Mg-ion conductors, benefit from the Mg-ion zigzag chains in the tunneling crystal structure that allows fast Mg-ion diffusion. Recently, the nanocomposite $Mg(BH_4)_2$·1.5THF-MgO(75 wt%) achieved an ionic conductivity of $\sigma_{ion} \approx 10^{-4}$ S cm^{-1} at mildly elevated temperature of 70 °C. However, the presence of inactive MgO, which is necessary for mechanical stabilization, limits the ionic conductivity of the material.[13] Therefore, in order to improve conductivity and stability, and expand the operating potential window, additional modifications are necessary.[10] In addition to these materials, Yamanaka et al. synthesized MgS-P_2S_5-MgI_2[14], a sulfide-based SE analogous to the lithium SE found in the quasi-binary and -ternary systems Li_2S-P_2S_5 and Li_2S-P_2S_5-LiX (X = Cl, Br, I).[15] The glass-ceramic SE achieved an ionic conductivity of $\sigma_{ion} = 2 \times 10^{-7}$ S cm^{-1} at 200 °C as the framework was expanded by the large iodine anions. However, there is still a need for optimization strategies to further improve the performance.

The computational studies of Canepa et al., which predict low migration barriers (0.36–0.53 eV) in MgZ_2X_4 (Z = In, Y, Sc and X = S, Se) spinel chalcogenides, can be considered as a major breakthrough in the search for inorganic Mg-ion SEs.[16] In the spinel structure (**Figure 1**a), the Mg-ions occupy an unfavorable tetrahedrally coordinated stable site (*tet*) and hop across a favorable octahedral activated site (*oct*) to reach the next tetrahedral site along the migration path. Thereby, the magnitude of the migration barrier is determined by the shared triangular face (*tri*) between tetrahedra and octahedra, namely the bottleneck of the energy landscape, which can be widened by increasing the volume per anion. After successful synthesis of one of the spinels, $MgSc_2Se_4$, Canepa et al. performed ^{25}Mg static variable temperature spin lattice relaxation nuclear magnetic resonance (SLR NMR) measurements and determined a Mg^{2+} migration barrier of (370 ± 90) meV, consistent with their computed data. However, this experimental evidence of Mg^{2+} mobility only corresponds to short-range motion/local jumps, while the long-range motion is of particular importance for the electrochemical performance of a solid electrolyte. Hence, they carried out impedance measurements with ion-blocking Ta electrodes and estimated an ionic conductivity of $\approx 1 \times 10^{-4}$ S cm^{-1} at room temperature. In their equivalent circuit, two Jamnik-Maier elements were utilized,[17] representing bulk and grain boundary contributions in the high frequency range. The total ionic resistance was determined by the Re(Z) axis intercept at the offset of the observed semicircle. However, we consider the results are yet not sufficiently evident due to lack of data points in the high-frequency range, which are necessary for accurately determining the intercept and obtaining a satisfactory fit of the spectrum (see Figure S1, Supporting Information). We consider it fortuitous as that the evaluated conductivity coincides with the true conductivity. However, from a critical perspective, the reported impedance data do not provide clear evidence for Mg-ion conduction in the $MgSc_2Se_4$ spinel. The authors determined an electronic conductivity of $\sigma_{el} = 4 \times 10^{-8}$ S cm^{-1}, which could potentially be attributed to point defects, neutralized by electrons, or the presence of electron conducting secondary phases. This high electronic conductivity poses a challenge for its practical application as it leads to significant self-discharge.[16] In our earlier work, we estimated the self-discharge for a charged $Mg|MgSc_2Se_4|Mo_6S_8$ battery and found that 10% of the total charge capacity would be lost within a short duration of 16 h.[18] Due to the promising ionic conductivity of $MgSc_2Se_4$ reported by Canepa et al., follow-up works have been carried out to gain a more comprehensive understanding. Wang et al. employed two routes of compositional tuning to suppress the electronic conductivity of $MgSc_2Se_4$, but neither method was successful.[19] It is worth mentioning that the impedance analysis by both, Wang et al. and by Canepa et al., is unreliable. In their work, Kundu and co-workers focused more on the synthesis parameters. On one hand, they proposed avoiding high energy precursor ball milling before the solid-state reaction since it can cause the formation of an electron conducting ScSe phase.[20] On the other hand, they reported an electric field-assisted synthesis route, including a subsequent low thermal treatment (500 °C for 40 h), to obtain a more phase pure spinel with less electron conducting impurity phases. Given the doubts surrounding the impedance analysis by both, Canepa et al. and Wang et al., it is crucial to prioritize the definitive verification of the partial ionic conductivity of $MgSc_2Se_4$ as prototype Mg-ion conducting spinel. This step is essential before spending more efforts to reduce the partial electronic conductivity. We like to add that the well-established strategies to determine the partial ionic conductivity of mixed ionic/electronic conductors (electrolysis method,[21] emf of galvanic cells,[21,22] 4-point stationary polarization method[21,23]) are not applicable

ADVANCED SCIENCE NEWS
www.advancedsciencenews.com

ADVANCED ENERGY MATERIALS
www.advenergymat.de

due to the lack of suitable and compatible electrodes with low overpotential. In view of all these challenges, it is the key target of this work to demonstrate unequivocally the relatively high Mg-ion conductivity of the $MgSc_2Se_4$ spinel, even over a long range.

To address this challenge, we successfully synthesized nearly phase pure $MgSc_2Se_4$ using a solid-state synthesis in a quartz glass ampule. We present reliable evidence for Mg-ion conduction in $MgSc_2Se_4$ through an electrochemical Mg plating experiment. Furthermore, we establish a universally applicable procedure to determine the partial ionic conductivity of the spinel. The Mg-ion migration barrier E_a results as (386 ± 24) meV, determined through temperature-dependent impedance measurements using the same electrochemical cell. We anticipate that these findings will advance the research on $MgSc_2Se_4$ and pave the way for exploring other mixed conducting MgZ_2X_4 spinels as potential Mg-ion solid electrolytes.

2. Results and Discussion

2.1. Structure and Morphology Information of $MgSc_2Se_4$

$MgSc_2Se_4$ powder was prepared via one- and two-step solid-state reaction routes. By performing Rietveld refinement based on the X-ray diffraction (XRD) data of both types of $MgSc_2Se_4$ samples (Figure 1a; Figure S2, Supporting Information), we identified a cubic spinel structure within the Fd-3m space group, where the Mg-ions are positioned on the 8*b* sites (tetrahedra), while the 16*c* sites (octahedra) are occupied by the Sc-ions for both samples. The detailed crystallographic data of these refinements, which are in good agreement with previously published results by Canepa et al.[16] and Wang et al.,[19] can be found in the Tables S1 and S2 (Supporting Information). Furthermore, the refined data confirm almost phase pure samples with a comparably small fraction of MgSe impurity (4.4 and 5.1 wt% for one-step and two-step synthesis, respectively). Since the one-step synthesized $MgSc_2Se_4$ shows slightly higher purity, it was chosen for all subsequent investigations. From the additional characterization by energy-dispersive X-ray spectroscopy (EDS) during scanning electron microscopy (SEM) measurements, as shown in Figure 1b, uniform distributions of the elements Mg, Sc, and Se were obtained. The atomic ratio of 1:2.3:3.6 confirms the spinel stoichiometry, whereby the small deficit of Mg and Se is due to vapor loss from the pellet surface at the high synthesis temperature. In addition to the particle size in the agglomerates indicated by the SEM image (1–5 µm), transmission electron microscopy (TEM) images (Figure S3a,b, Supporting Information) also demonstrate that the as-prepared $MgSc_2Se_4$ shows a typical particle size from 1–3 µm. Furthermore, the selected area electron diffraction (SAED) pattern performed during TEM measurements confirms the spinel structure as well (diffraction image depicted in Figure S3c, Supporting Information). To obtain information on the Mg and Sc positions in the sample, ^{25}Mg and ^{45}Sc magic-angle spinning nuclear magnetic resonance (MAS NMR) spectroscopy was carried out (see Figure 1c,d). The ^{25}Mg MAS NMR spectrum shows a single peak at 53.2 ppm, which agrees with the results of Canepa et al., indicating the presence of Mg exclusively on the tetrahedral sites. The strong peak at 429 ppm in the ^{45}Sc MAS NMR spectrum confirms the presence of Sc predominantly on the octahedral sites, while the small peak at 400 ppm (area fraction 1.3%) might arise from a secondary phase or from a small fraction of Sc-ions on the tetrahedral sites. The latter is quite likely, since the sample shows a Sc excess according to the EDS results. This excess Sc tends to occupy Mg sites, forming the $Sc^{\bullet}_{Mg}$ anti-site defect (n-type defect) which is probably charge-balanced by electrons.[24] These can cause increased electronic conductivity when the conduction band minimum is reached in terms of energy. The semiconducting nature of $MgSc_2Se_4$, as suggested in the literature,[25] is confirmed through absorption and photoluminescence spectroscopy. Linear absorption measurements (Figure 1e) yield a band-gap energy of E_g = 2.3 eV, and a direct allowed transition by the Tauc method (Figure 1f). This is consistent with the light-brown translucent appearance of the samples (Figure 1b). Additionally, a much more prominent absorption band is observed at higher energies, with a second absorption edge around $E_{g'}$ = 2.8 eV, in agreement with previous reports of a band-gap energy of approximately 3 eV for the corresponding sulfide-based spinel $MgSc_2S_4$.[26] Furthermore, $MgSc_2Se_4$ exhibits a spectrally broad photoluminescence centered at 1.93 eV and a full width at half maximum (FWHM) of 0.44 eV. Notably, the photoluminescence is Stokes-shifted by 0.37 eV from the absorption edge. These findings provide further evidence for the semiconducting nature of $MgSc_2Se_4$.

2.2. Electronic Conductivity

The room temperature partial electronic conductivity of the semi-conductor $MgSc_2Se_4$ was determined by electrochemical impedance spectroscopy (EIS) and chronoamperometry (CA) measurements. In both cases, symmetric cells (Me|$MgSc_2Se_4$|Me) with ion-blocking metal (Me) electrodes were used. Initially, to find out the best cell configuration, Nyquist plots using different ion-blocking electrodes (stainless-steel punches (SS), Ta foil and Au foil) were compared. For this purpose, homemade press cells were used,[28] consisting of a PEEK housing in which the $MgSc_2Se_4$ powder was pressed in between two stainless-steel punches, with the punches serving directly as ion-blocking electrodes. In the case of Ta or Au blocking electrodes, the metal foils were subsequently placed between the cold-pressed $MgSc_2Se_4$ pellet and the stainless-steel punches. As shown in Figure S4 (Supporting Information), application of this cold-pressing procedure with ion-blocking electrodes results in noisy impedance spectra, which can be attributed to poor physical contact at the electrode|SE interface. Among them, the Au foil comparatively shows the best physical contact, and a semicircle was detected in the Nyquist plot. To further improve the contact, with the consideration that foils are mostly stiff and therefore difficult to adapt to bumps on the rough SE surface, a smoothing Au layer was evaporated onto both sides of a sintered spinel pellet. Then, the pellet was placed between Ni arrestors as current collectors in a pouch cell and the EIS measurements were performed again. As can be seen in the corresponding Nyquist plot in **Figure 2**a, the gas phase deposition significantly improves the physical contact. A noiseless spectrum results, showing a characteristic depressed semicircle without low-frequency tail. The missing tail may be explained by an imperfect ion-blocking electrode. An ideal ion-blocking

ADVANCED SCIENCE NEWS
www.advancedsciencenews.com

ADVANCED ENERGY MATERIALS
www.advenergymat.de

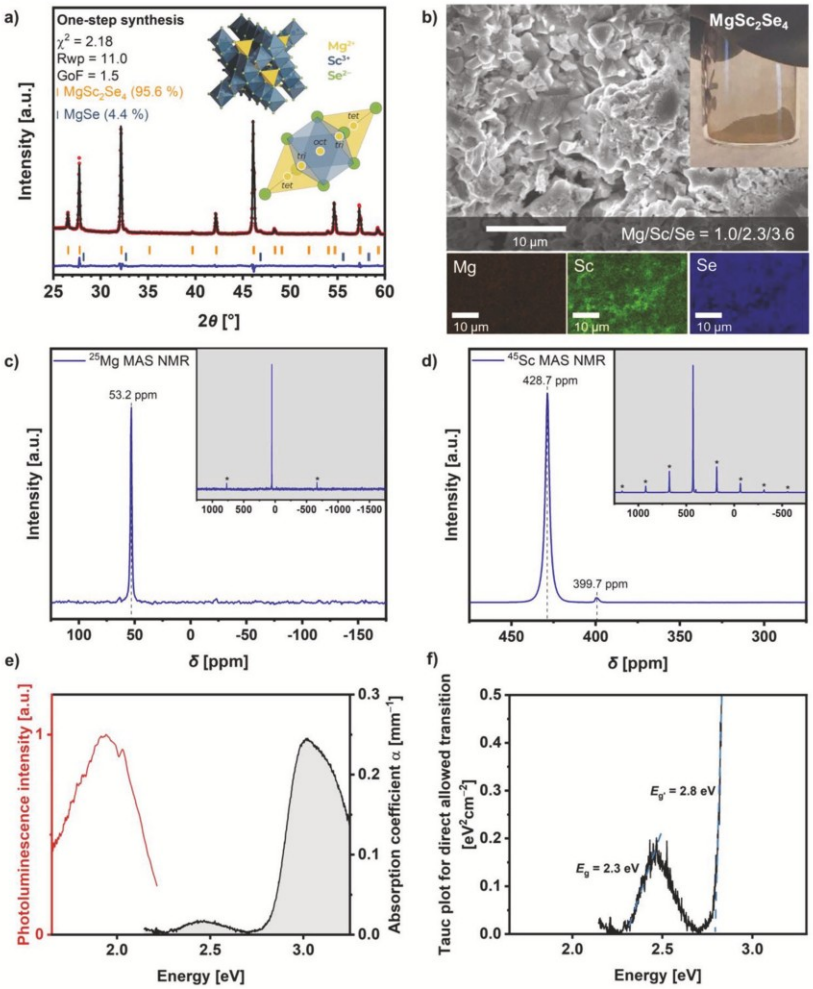

Figure 1. a) Rietveld refinement, based on the XRD pattern for one-step synthesized $MgSc_2Se_4$. The observed and calculated curves are shown in red and black in the top, and the difference curve is shown in blue. The inset in the right upper corner shows the crystal structure of $MgSc_2Se_4$ and the diffusion path for Mg^{2+}, as described by Guittard et al.;[27] b) SEM image of $MgSc_2Se_4$, photographic image of the $MgSc_2Se_4$ powder and EDS mapping of the elements Mg, Sc and Se; characterization of Mg and Sc positions in the spinel structure via c) ^{25}Mg solid-state NMR and d) ^{45}Sc solid-state NMR. Spinning sidebands are marked with an asterisk; e) absorption (black line) and photoluminescence (red line) of $MgSc_2Se_4$ and f) Tauc plot.

electrode should be inert and not form an alloy with magnesium. This is not as simple as for Li-ion and Na-ion conductors, where several working examples exist.[29] Nevertheless, the partial electronic conductivity σ_{el} can be calculated from the intercept of the Nyquist plot with the real axis at low frequency, i.e., from the electronic resistance R_{el}, in the impedance spectrum of an Au|$MgSc_2Se_4$|Au pouch cell (Figure 2a) by using the following equation (Equation 1):

$$\sigma_i = \frac{d}{A\,R_i} \quad (i = \text{el, ion, tot}) \tag{1}$$

A is the contact area of a deposited Au electrode (0.503 cm^2), d is the thickness of the pellet (0.130 cm), and R_i is the electronic (el), ionic (ion), or total (tot) resistance. Since the large overlap of the two transport contributions (ionic and electronic) makes it difficult to obtain a reliable analysis using equivalent circuits,[30] including those used in literature,[16,19] R_{el} was extracted from the last data point at low frequency. As a result, σ_{el} was calculated to be 3.4×10^{-8} S cm^{-1} at room temperature, which can also be confirmed by the dc polarization measurement ($\sigma_{el} = 2.1 \times 10^{-8}$ S cm^{-1}), shown in Figure 2b, in accordance with the results from the groups of Ceder and Fichtner.[16,19] The electronic conductivity, which is even around twice as high at an elevated temperature

ADVANCED SCIENCE NEWS
www.advancedsciencenews.com

ADVANCED ENERGY MATERIALS
www.advenergymat.de

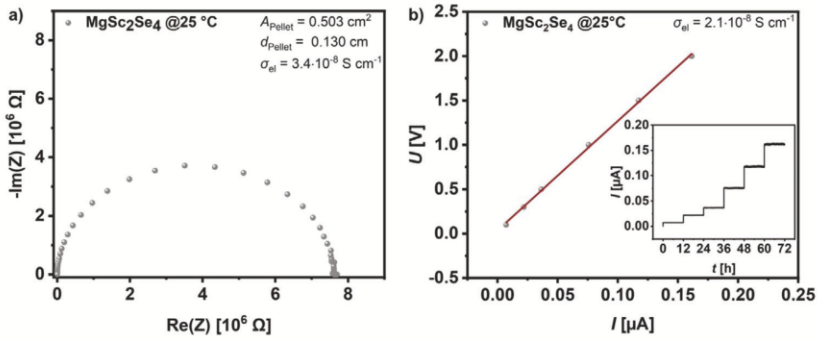

Figure 2. a) Nyquist plot of an Au|$MgSc_2Se_4$|Au pouch cell in the frequency range of 7 MHz to 100 mHz at 25 °C and b) DC polarization data obtained at different voltages (0.1, 0.3, 0.5, 1.0, 1.5 and 2.0 V, held for 12 h, shown in the inset) with linear fit (red) of the equilibrium values to determine the electronic DC resistance at 25 °C.

of 60 °C in comparison to room temperature (Figure S5a, Supporting Information), needs to be reduced to negligible values for the application of $MgSc_2Se_4$ as Mg-ion conducting SE. In addition, the zoomed-in view of the high frequency region (0.7–7 MHz) of the Nyquist plot (Figure S5b, Supporting Information) shows no offset of the semicircle, meaning that the ionic conductivity cannot be calculated according to the Jamnik and Maier model done in earlier reports.[16,17,19]

2.3. Verification of Ionic Conductivity

As we explained above, we consider previously reported ionic conductivity data not as reliable due to the insufficient analysis of the impedance data. To provide unequivocal evidence for Mg-ion conduction in $MgSc_2Se_4$, we assembled a Mg|$MgSc_2Se_4$|Au cell with the aim to plate Mg onto the Au electrode at room temperature (current density –428 µAh cm^{-2}). Mg precipitation can only occur if the SE shows Mg-ion conductivity. After the electrochemical experiment, the cell was disassembled, and the Au electrode surface was examined by SEM/EDS. **Figure 3** shows one of the Mg deposits on the backside of the Au electrode, grown from the SE|Au interface through the thin Au layer (300 nm). Magnesium is localized in the deposited particle, while gold and selenium are distributed within the remaining areas (see also Figure S6c,d, Supporting Information). Clearly, the particle is not a contamination from the $MgSc_2Se_4$ pellet. To exclude the possibility of a cross-contamination from Mg particles in the counter electrode, we also checked the morphology of the Mg slurry made from commercial Mg particles, mixed with conductive carbon black (super P) and polyvinylidene fluoride (PVdF) binder. As shown in Figure S7a,b (Supporting Information), the commercial Mg particles inside the mixture are covered with a carbon layer. More importantly, they have a distinctly different morphology (Figure S7c, Supporting Information) compared with the deposited particles, confirming that the Mg particle on the Au surface has been formed by electrochemical plating. This confirms the Mg-ion conductivity of $MgSc_2Se_4$ unequivocally, and to the best of our knowledge, this is the first experimental proof of Mg plating from a Mg-ion SE using an evaporated Au electrode. The thin gas phase deposited electrode has the advantage that the Mg can grow through it, so that a detaching of the electrode to obtain the Mg plating is not necessary. Instead, when using electrode foils, the Mg plating may only be visible at the SE|electrode interface, where contamination of the electrode interface by the SE electrolyte cannot be ruled out, making it difficult to determine the origin of the observed Mg by EDS.[31,32]

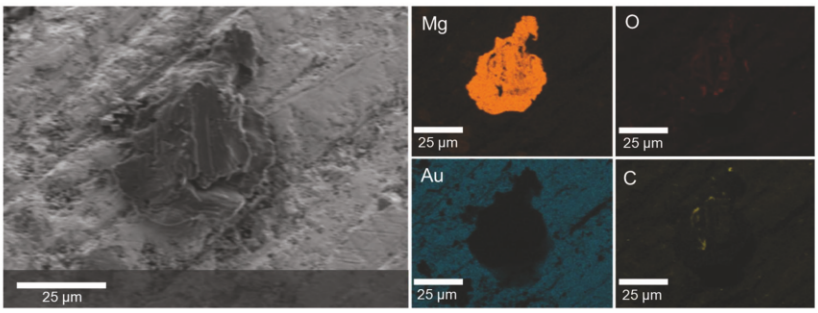

Figure 3. SEM image (left) and elemental EDS maps (right) of deposited Mg on the Au electrode backside, that was grown from the SE|Au interface through the Au layer, after Mg plating in a Mg|$MgSc_2Se_4$|Au cell at 25 °C.

ADVANCED SCIENCE NEWS
www.advancedsciencenews.com

ADVANCED ENERGY MATERIALS
www.advenergymat.de

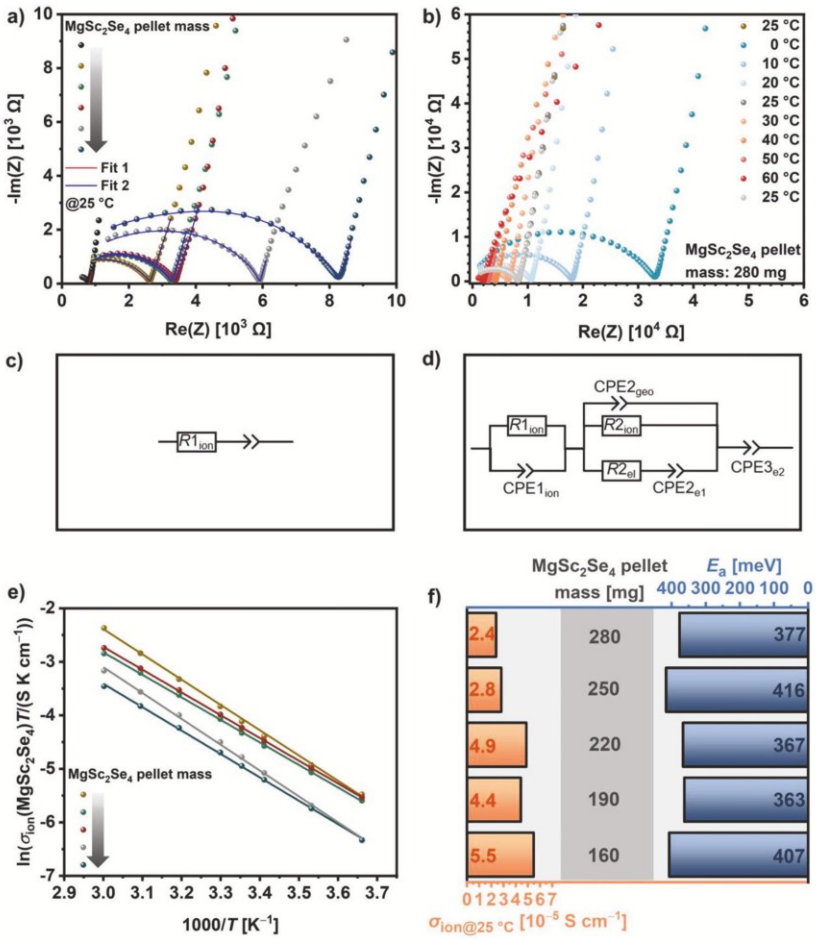

Figure 4. a) Nyquist plots of SS|UiO66-MgIL|$MgSc_2Se_4$|UiO66-MgIL|SS cells at 25 °C with varied spinel pellet mass/thickness (0 mg/0 mm, 160 mg/0.80 mm, 190 mg/0.88 mm, 220 mg/1.10 mm, 250 mg/1.14 mm and 280 mg/1.40 mm) and fits in red and blue; b) Nyquist plots at different temperatures ranging from 0 to 60 °C when a 280 mg spinel pellet is sandwiched; c) and d) equivalent circuits used to fit Nyquist plots for SS|UiO66-MgIL|SS (Fit 1 in a)) and SS|UiO66-MgIL|$MgSc_2Se_4$|UiO66-MgIL|SS cells (Fit 2 in a)); e) Arrhenius plots of the conductivity of $MgSc_2Se_4$ examined from different spinel pellet thicknesses and f) overview of the room temperature ionic conductivity and Mg^{2+} migration barrier calculated by variation of the spinel pellet thickness.

2.4. Ionic Conductivity and Mg^{2+} Migration Barrier

For the measurement of the partial ionic conductivity and the Mg^{2+} migration barrier of $MgSc_2Se_4$, we designed a sandwich-type cell configuration in the before-mentioned press cell and carried out temperature dependent impedance measurements. In detail, Mg-ion conducting interlayers, which block electrons and also improve the electrode/electrolyte contact, are inserted between the cold-pressed $MgSc_2Se_4$ pellet and the stainless-steel ion-blocking electrode (SS|UiO66-MgIL|$MgSc_2Se_4$|UiO66-MgIL|SS). In this case, the Mg-ion conducting ($\sigma_{ion} = 9.5 \times 10^{-5}$ S cm^{-1}) but almost electronically insulating ($\sigma_{el} = 1.7 \times 10^{-10}$ S cm^{-1}, see Figure S8, Supporting Information) UiO66-MgIL electrolyte, based on the Metal-Organic Framework (MOF) structure UiO-66 impregnated with an 1 M $Mg(TFSI)_2$-[EMIM][TFSI] ionic liquid, was used as interlayer.[33] To test the reliability of the chosen method, the $MgSc_2Se_4$ pellet thickness was systematically increased, which should lead to a corresponding proportional increase in the impedance of the cell. The record of the impedance spectra was performed when the impedance in the Nyquist plots at the Re(Z) axis intercept at 25 °C was almost identical, before and after the temperature variation between 0 and 60 °C, meaning the sandwiched system reached equilibrium. Thermal equilibration of the cells took ≈90 min after a temperature step. **Figure 4**a shows the impedance spectra taken at 25 °C for different $MgSc_2Se_4$ pellet thicknesses. The temperature dependent Nyquist plot for the cell with the thickest $MgSc_2Se_4$ pellet (280 mg, 1.40 mm) is exemplified in

ADVANCED SCIENCE NEWS
www.advancedsciencenews.com

ADVANCED ENERGY MATERIALS
www.advenergymat.de

Figure 4b, while the ones of the remaining cells (0, 160, 190, 220 and 250 mg) can be found in Figure S9 (Supporting Information). As expected, the resistance of the semicircle R_{ion}(SEs), representing the total resistance of the two UiO66-MgIL layers and the $MgSc_2Se_4$ pellet, increases with increasing spinel pellet thickness (see Figure 4a). The equivalent circuit shown in Figure 4c was used to describe the impedance of the SS|UiO66-MgIL|SS cell (black plot in Figure 4a), while the semicircle could not be fitted by a constant phase element (CPE) in parallel to the resistance $R1_{ion}$ due to less data points. For $R1_{ion}$ a resistance of 806 Ω, identical with the manually determined resistance of UiO66-MgIL (denoted as R_{ion}(UiO66-MgIL)) from the lowest data point at the intercept of the Re(Z) axis, was obtained. In order to describe the sandwich-type cells, including the $MgSc_2Se_4$ pellet, the physically meaningful equivalent circuit in Figure 4d was applied. The first partial circuit elements, $R1_{ion}$ and $CPE1_{ion}$ belong to the UiO66-MgIL. The following two resistances in parallel, $R2_{ion}$ and $R2_{el}$, represent the two conducting pathways for ions and electrons in the mixed conducting $MgSc_2Se_4$. $CPE2_{geo}$ is a geometric capacitance and the selectively electron-blocking UiO66-MgIL layer is represented by an interface capacitance $CPE2_{el}$ in the conducting pathways. Finally, $CPE3_{e2}$ describes the ion-blocking stainless-steel electrode. Since the total UiO66-MgIL layer thickness in the cells can deviate from those used in the SS|UiO66-MgIL|SS reference cell (0.60 mm), especially in case of the cell with 220 mg spinel pellet as shown in Table S3 (Supporting Information), R_{ion}(UiO66-MgIL) or $R1_{ion}$, respectively, was adapted to the layer thickness actually used (see Equation S1, Supporting Information). Table S5 (Supporting Information) presents the results of R_{ion}(UiO66-MgIL) and $R1_{ion}$ for each sandwich-type cell. Assuming that the contribution of R_{ion}(UiO66-MgIL) does not cause changes in R_{ion}(SEs) due to constant UiO66-MgIL layer thickness, the impedance of the $MgSc_2Se_4$ can be manually calculated from the difference of both, denoted as $R_{ion}(MgSc_2Se_4)$. Equally, if $R1_{ion}$ is assumed to be constant, $R2_{ion}$, the ionic resistances of $MgSc_2Se_4$ from the fitting, is obtained. Table S5 demonstrates that the results for both, $R_{ion}(MgSc_2Se_4)$ and $R2_{ion}$, are almost identical ($\leq$ 3% derivation $\triangleq \leq 2 \times 10^{-6}$ S cm^{-1}), meaning that fitting of the impedance data in this case is not absolutely necessary. For this reason, $R_{ion}(MgSc_2Se_4)$ was used for all following calculations. Applying Equation 1 to $R_{ion}(MgSc_2Se_4)$, quite close values of the room temperature ionic conductivities for $MgSc_2Se_4$ in the range of $\sigma_{ion}(MgSc_2Se_4) = 2.4–5.5 \times 10^{-5}$ S cm^{-1} (Figure 4f) were found for all cells independent from the interlayer thickness, meaning that the chosen method provides reliable results. At an elevated temperature of 60 °C, an increase of $\sigma_{ion}(MgSc_2Se_4)$ to $9.5 \times 10^{-5} – 2.8 \times 10^{-4}$ S cm^{-1} was observed. From the Arrhenius plots in Figure 4e, the Mg^{2+} migration barrier E_a of $MgSc_2Se_4$ was evaluated from the Arrhenius equation (Equation 2):

$$\sigma_{ion} = \frac{\sigma_0}{T} \exp\left(-\frac{E_a}{k_B T}\right) \quad (2)$$

with σ_0 representing the conductivity prefactor. E_A ranges from 363 to 416 meV for the different cells, being lower than the previously published values for Mg-ion SEs (see Table S6, Supporting Information) and close to the predicted value of 375 meV[16]. All cells operated stably and were reproducible independent from the

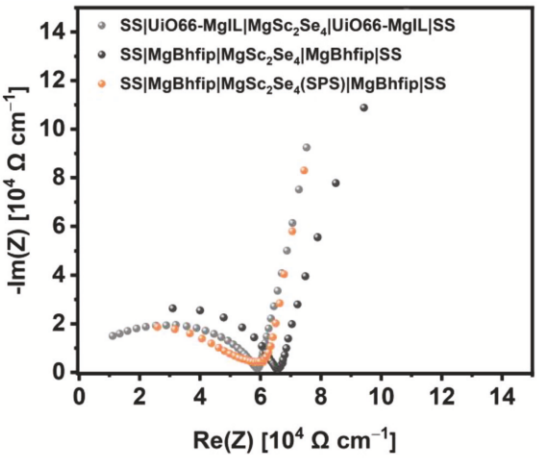

Figure 5. Normalized Nyquist plots of SS|MgBhfip|$MgSc_2Se_4$|MgBhfip|SS cells with sandwiched $MgSc_2Se_4$ pellets (cold-pressed/SPS sintered) showing similar Re(Z) axis intercept resistances compared to a SS|UiO66-MgIL|$MgSc_2Se_4$|UiO66-MgIL|SS cell (with 280 mg $MgSc_2Se_4$ as an example) at 25 °C.

$MgSc_2Se_4$ pellet thickness, confirming the reliability of our cell design with an UiO66-MgIL interlayer.

To check whether the IL from the UiO66-MgIL penetrated the sandwiched spinel pellet, which would influence the resistance of the $MgSc_2Se_4$ pellet, EDS measurements of the pellet cross section were carried out after cell disassembly. Figure S10a (Supporting Information) displays the cross-sectional view of one UiO66-MgIL layer in contact with the sandwiched $MgSc_2Se_4$ with the lowest pellet thickness (0.80 mm) used in this experiment. The element distribution and the spectra of the red labeled areas at the UiO66-MgIL and $MgSc_2Se_4$ layer (Figure S10b,c, Supporting Information) prove that the F, S, and N signals from the IL and $Mg(TFSI)_2$ included in the MOF pores are seen in the corresponding UiO66-MgIL layer but not in the spinel phase. This means that the different layers are chemically well separated and that the results of the EIS measurements are not influenced by diffusion of the IL into pores of the spinel. Furthermore, the unchanged XRD pattern of $MgSc_2Se_4$ powder after soaking it into the IL for one week (Figure S11, Supporting Information) confirms the spinel is chemically stable in contact with the IL.

Apart from the UiO66-MgIL, a 0.1 M $Mg[B(hfip)_4]_2$ liquid electrolyte (hfip = $CH(CF_3)_2$, solvent = 1,2-dimethoxyethane) denoted as MgBhfip[34] was also tested as interlayer. We used the same cell configuration to measure the impedance. Additionally, we also used $MgSc_2Se_4$ pellets prepared by spark plasma sintering (SPS) to increase the pellet density that should prevent penetration of liquid electrolyte (LE). As shown in the corresponding Nyquist plots (Figure S12a,b, Supporting Information), the impedance increased after storage caused by the evaporation of the LE solvent due to insufficiently tight cell housing. However, normalizing the impedance of the very first measurement after cell assembly by the $MgSc_2Se_4$ pellet thickness, quite similar resistances at the Re(Z) axis intercept were obtained (**Figure 5**). The resulting ionic conductivities of 1.9×10^{-5} S cm^{-1} (cold-pressed

ADVANCED SCIENCE NEWS
www.advancedsciencenews.com

ADVANCED ENERGY MATERIALS
www.advenergymat.de

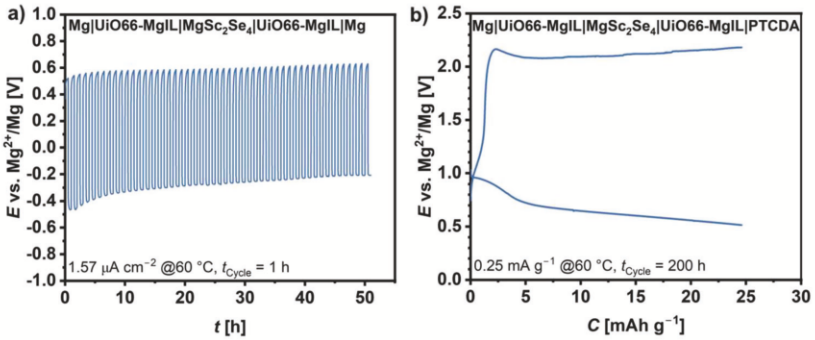

Figure 6. a) 50 cycles of plating/stripping of a Mg|UiO66-MgIL|$MgSc_2Se_4$|UiO66-MgIL|Mg cell at 60 °C by applying a current density of ±1.57 µA cm^{-2} and b) discharge/charge voltage profiles of a Mg|UiO66-MgIL|$MgSc_2Se_4$|UiO66-MgIL|PTCDA full cell at 60 °C by applying current rate of ±0.25 mA g^{-1}.

pellet) and 2.3×10^{-5} S cm^{-1} (SPS pellet), respectively, are slightly smaller than those measured with the UiO66-MgIL interlayer, justified by the fact that the resistances (intercepts) were not reduced by the unknown resistance of the LE-glass fiber layer. Another possibility might be that solvent from the interlayer vaporized already before the measurement. In any case, the quite similar results for the ionic conductivity confirm that the interlayer method can also work with different Mg-ion conducting media and with sintered $MgSc_2Se_4$ pellets instead of cold-pressed powder pellets as well.

Afterwards, symmetrical Mg|UiO66-MgIL|$MgSc_2Se_4$|UiO66-MgIL|Mg cells with Mg foil electrodes were assembled to validate repetitive plating/stripping behavior. Therefore, as shown in **Figure 6**a, 50 cycles at 60 °C were recorded using a current density of 1.57 µA cm^{-2} ($I = 1$ µA). In the initial cycles the symmetrical cell exhibits an overpotential of ≈0.5 V, similar to reported for our Mg|UiO66-MgIL|Mg cell[33]. Upon cycling, the overpotential span decreases and stabilizes, which could be related to the formation of a stable electrode|SE interface. The simultaneous asymmetric overpotential shift in positive direction appears to be due to slightly different surface textures of the both Mg foils caused by manual surface polishing with a knife. However, in general the Mg plating/stripping behavior underlines once more that the spinel indeed shows Mg-ion transport. In the subsequent impedance measurement shown in Figure S13a (Supporting Information), R_{ion}(SEs), the total impedance of the $MgSc_2Se_4$ ($m = 120$ mg, $d = 0.57$ mm) and the UiO66-MgIL ($m = 120$ mg, $d = 0.90$ mm), was received from the Re(Z) axis intercept in the Nyquist plot. According to the previous procedure, $R_{ion}(MgSc_2Se_4)$ was obtained from the difference of R_{ion}(SEs) and R_{ion}(UiO66-MgIL) (adapted to the actually used layer thickness), and used to calculate the ionic conductivity. The result of 8.9×10^{-5} S cm^{-1} matches well with the previous ones determined with stainless-steel electrodes at 60 °C. This fact demonstrates again the reproducibility of the interlayer method, even when different electrodes (ion-blocking or conducting) are used, since the electrode|SE interface resistance only appears at lower frequencies away from the SEs resistance at higher frequencies.

To demonstrate that $MgSc_2Se_4$ can indeed be used as an electrolyte, a Mg|UiO66-MgIL|$MgSc_2Se_4$|UiO66-MgIL|PTCDA full cell was assembled, including a perylene tetracarboxylic dianhydride (PTCDA) composite cathode, as reported in our earlier work[33]. The galvanostatic discharge and charge profile were recorded at 60 °C in the voltage range between 0.3 and 2.5 V (vs Mg^{2+}/Mg) with a current rate of 0.25 mA g^{-1}. As shown in Figure 6b, the profile exhibits a long plateau in both the discharge and the charge curve, describing the reversible enolization process of the C=O groups in the PTCDA molecule during Mg insertion/extraction. Moreover, a capacity of ≈25 mAh g^{-1} was reached during 100 h of discharge/charge in the first cycle, which is expected to show a strong decay in the following two cycles as reported for the Mg|UiO66-MgIL|PTCDA full cell.[33] However, the results indicate a working battery with $MgSc_2Se_4$ as an electrolyte, and the relative high conductivity of the spinel can be considered as reliably proven.

3. Conclusions

We present unequivocal evidence for Mg-ion transport in the $MgSc_2Se_4$ spinel through a Mg plating experiment. To the best of our knowledge, this is the first report of Mg plating onto a deposited metal electrode from an inorganic Mg-ion SE. In addition, we introduce a straightforward and reliable strategy to determine the partial ionic conductivity ($2.4–5.5 \times 10^{-5}$ S cm^{-1} at room temperature) and the Mg-ion migration barrier of (386 ± 24) meV of the mixed conducting spinel using an electron-blocking UiO66-MgIL interlayer which improves the electrode/electrolyte contact in the press cells and allows high-quality EIS measurements. The migration barrier obtained in the temperature range from 0 to 60 °C agrees well with the one predicted by theory and is lower than the ones published previously for solid-state Mg-ion conductors. Future work will aim to develop a way to reduce the electronic conductivity, which is 0.06–0.14% of the ionic conductivity, or to find less expensive materials as interlayer or coating in order to suppress the undesired electron transport.

4. Experimental Section

Synthesis: Initially, Mg powder (Sigma Aldrich, ≥99%), Sc powder (Chempur, 99.9% REO), and Se powder (Alfa Aesar, 99.999%) were weighted in a molar ratio of 1:2:4 and hand-milled with a mortar for 15 min

ADVANCED SCIENCE NEWS
www.advancedsciencenews.com

ADVANCED ENERGY MATERIALS
www.advenergymat.de

for the one-step synthesis of $MgSc_2Se_4$. The resulting powder was isostatically pressed into 0.5 g pellets (Ø = 10 mm) under a pressure of 3000 bar for 30 min. Then, the pellets were wrapped into a platinum foil (Chempur, 99.9%, 125 µm) and placed in separate quartz glass ampules, that were prior heated at 800 °C under dynamic vacuum to remove moisture. After vacuum sealing of the ampules, the solid-state reaction was carried out in a furnace (Nabertherm with controller P 300) at 950 °C for 20 h (180 °C h^{-1} heating rate). Finally, the furnace cooled down to room temperature. After breaking the ampules, the collected pellets were ground to a brownish powder.

Additionally, the synthesis was carried out in a two-step procedure, whereby first MgSe and Sc_2Se_3 were prepared from stoichiometric amounts of the elemental powders according to the previous one-step synthesis at 750 °C for 24 h (180 °C h^{-1} heating rate) and 800 °C for 30 h (60 °C h^{-1} heating rate), respectively. In the next step, the binary compounds were converted to $MgSc_2Se_4$ in a molar ratio of 1:1 at same conditions as described in the first procedure.

All preparations and sample treatments were carried out under an inert gas atmosphere (Ar or vacuum).

X-Ray diffraction (XRD): The binary and ternary selenides were structurally characterized by means of X-ray diffraction using an Empyrean powder diffractometer (Malvern PANalytical Ltd) with Cu K_α radiation. The samples were placed on silicon zero background holders and sealed with Kapton polyimide film inside a glove box to avoid contact with air and humidity. Measurements were carried out in a 2θ range from 10° to 90° with a step size of 0.026° and a counting time per step of 200 s. References were taken from: MgSe (ICSD 53 946), Sc_2Se_3 (ICSD 651 804), and $MgSc_2Se_4$ (ICSD 642 814).

Rietveld Analysis: Rietveld refinements were performed using the software FullProf Suite Version January 2021. The peak profile shape was described by Thompson-Cox-Hasting pseudo-Voigt functions. Start models for the Rietveld refinement were taken from: MgSe (ICSD 53 946) and $MgSc_2Se_4$ (ICSD 642 814).

Scanning Electron Microscopy (SEM) and Energy-Dispersive X-Ray Spectroscopy (EDS): SEM images of the prepared SE powder and pellets were obtained by a Merlin high-resolution scanning electron microscope (Carl Zeiss AG, Germany) at an acceleration voltage of 3 kV. The working distance was between 4 and 5 mm and a secondary electron detector was used. EDS mapping was carried out in 6 mm to 8 mm working distance using an X-Max-50 detector (Oxford Instruments, UK) at an acceleration voltage of 10 kV. Especially, for detection of the Mg deposition on the electrode surface a voltage of 5 kV was used and for the proof of Sc content in the $MgSc_2Se_4$ powder a higher voltage of 15 kV was necessary. For the cross-sectional view, the pellets were manually broken in halves and afterwards attached to the sample holder. The samples were transferred from the glove box with a Leica EM VCT500 shuttle to avoid air contamination.

Transmission Electron Microscopy (TEM): TEM images were obtained by Themis 300 (Thermo Fisher Scientific), which operates at an accelerating voltage of 300 kV. The powder sample was dispersed on the Mo TEM grid for TEM observation. Selected area electron diffraction (SAED) patterns were obtained to identify the crystal structure of the material.

Nuclear Magnetic Resonance (MAS NMR) Spectroscopy: ^{25}Mg and ^{45}Sc magic-angle spinning (MAS) NMR spectroscopy was performed at a magnetic field of 11.7 T corresponding to resonance frequencies of 30.6 and 121.5 MHz, respectively. ^{25}Mg NMR was performed in 1.3 mm rotors at a spinning speed of 22 kHz with a rotor-synchronized Hahn-echo sequence, a $\pi/2$ pulse duration of 3.7 µs, and a recycle delay of 15 s. ^{45}Sc NMR was performed in 2.5 mm rotors at 30 kHz with a Hahn-echo sequence, a $\pi/2$ pulse duration of 2.6 µs, and a recycle delay of 30 s. Spectra were referenced to aqueous solutions of 5 M $MgCl_2$ for ^{25}Mg and 1 M $ScCl_3$ for ^{45}Sc.

Absorption and Photoluminescence Spectroscopy: The $MgSc_2Se_4$ powder was suspended in oil and filled in a fused silica cuvette with a 1 mm optical path length. For µ-reflectance measurements, unpolarized light emitted from a tungsten lamp was utilized and focused onto the sample using a CaF_2 lens. The transmitted light was collected by a 20× objective with a numerical aperture of 0.45, resulting in a 160 µm spot size, and directed into the spectrometer. To obtain absorption spectra, the background intensity (T_{bg}) was subtracted from the sample transmission intensity (T_{sample}) and normalized using the transmission intensity through an identical fused silica cuvette filled with the same oil (T_{ref}). The absorption was calculated as

$$A = 1 - \frac{T_{sample} - T_{bg}}{T_{ref} - T_{bg}} \quad (3)$$

For µ-photoluminescence measurements, the samples were excited using a 532 nm (2.33 eV) laser. The beam was focused by a 20× objective with a numerical aperture of 0.45 into a 3 µm spot size, and the excitation power density was set at 930 W cm^{-2}. The photoluminescence was collected by the same objective and directed into the spectrometer. All optical measurements were carried out at room temperature of 295 K.

Cell Assembly and Electrochemical Measurements: All electrochemical measurements were performed with a VMP300 electrochemical workstation and recorded with the corresponding software EC-Lab from Bio-Logic Science Instruments SAS. Fitting of the experimental EIS data was performed using the RelaxIS 3 software (RHD Instruments, Darmstadt, Germany).

To determine the electronic conductivity, different cell configurations were tested. On the one hand, homemade battery cell casing were used already reported in a previous work[28]. $MgSc_2Se_4$ powder was filled in the PEEK housing with a diameter of 10 mm and pressed between two stainless-steel punches (SS) at 3 t for 3 min to create a pellet inside the housing. When using Ta or Au ion-blocking electrodes, the metal foils (Ø = 9 mm) were subsequently placed between the cold-pressed $MgSc_2Se_4$ pellet and the stainless-steel punches, and the cell was pressed under the same conditions as before. Then, a constant pressure was applied by the means of the screw of aluminum framework around the homemade cell casing with 10 Nm torque, like every time using this cell type. On the other hand, to prepare pouch cells, $MgSc_2Se_4$ powder (300 mg) was pressed into a pellet (Ø = 10 mm) under isostatic pressure of 3000 bar for 30 min. Next, the pellet was vacuum sealed in a quartz glass ampule and sintered at 950 °C for 6 h (180 °C h^{-1} heating rate). After the furnace was cooled down, the pellet was polished down to grit 4000 with SiC sandpaper and Au electrodes of 300 nm thickness (Ø = 8 mm) were vapor-deposited (Sputter Coater, tectra GmbH) on both sides of the $MgSc_2Se_4$ pellet using a 0.15–0.2 nm s^{-1} evaporation rate and a pressure < 10^{-6} mbar. The pellet was again vacuum sintered at 500 °C for 6 h and then sealed under argon into pouch cells using Ni current collectors to contact the Au electrodes. EIS and CA measurements of the symmetrical Me|$MgSc_2Se_4$|Me (Me = stainless-steel, Ta, Au) cells were performed in climate chambers (Weisstechnik) under strict temperature control to prevent errors due to temperature effects. The EIS data were collected from 7 MHz to 100 mHz with an alternating current (AC) amplitude of 10 mV and the CA was carried out in six steps from 0.1 to 2.0 V with 12 h resting time per step. Temperature was varied between −40 and 60 °C.

For the Mg plating experiment with Mg|$MgSc_2Se_4$|Au cells, 500 mg $MgSc_2Se_4$ powder was filled in a graphite pressing tool (Ø = 10 mm) and sintered by the means of spark plasma sintering (SPS) at 3.9 kN and 800 °C for 10 min to a dense pellet (rel. density: 85–91%). Next, the pellet was polished down to grit 4000 with SiC sandpaper and an Au electrode of 300 nm thickness (Ø = 8 mm) was vapor-deposited on one side. After vacuum sintering at 500 °C for 6 h, the other side of the pellet was polished again and coated with a Mg electrode slurry containing Mg powder (Sigma Aldrich, ≥99%), super P (MSE Supplies) and polyvinylidene fluoride (HSV900 PVDF binder, ≥99.5%) binder in a mass ratio of 8:1:1 in *N*-methylpyrrolidone (Sigma Aldrich, 99.5%) which was 77 wt.% of Mg. The coating was then dried at 120 °C for ≈10 min. After storing in Ar-filled glovebox overnight, a pouch cell with Ni current collectors was assembled and chronopotentiometry (CP) with a current of −1 µA for 215 h was used to plate theoretically 97 µg/1.1 µm Mg onto the gold electrode at room temperature.

In order to determine the ionic conductivity and the Mg-ion migration barrier, different amounts of $MgSc_2Se_4$ powder (160, 190, 220, 250, and 280 mg) were pressed in homemade battery cell casing (same procedure as for electronic conductivity). Then, 40 mg of an interlayer was added at both sides of the pellet to prevent electron transport. The interlayer

ADVANCED SCIENCE NEWS
www.advancedsciencenews.com

ADVANCED ENERGY MATERIALS
www.advenergymat.de

consisted out of a Mg-ion conducting Metal-Organic Framework (MOF) structure UiO-66 impregnated with 1 M $Mg(TFSI)_2$-[EMIM][TFSI] ionic liquid (magnesium bis (trifluoromethanesulfonyl) imide (TCI, >97%) dissolved in 1-ethyl-3-methylimidazolium bis (trifluoromethanesulfonyl) imide (TCI, >98%)) in a mass ratio of 1:1.25, called UiO66-MgIL as described in the previous report,[33] and was pressed under same conditions as before on the top and bottom side of the $MgSc_2Se_4$ pellet. After applying a pressure by the surrounding aluminum framework with a 10 Nm torque, with all SS|UiO66-MgIL|$MgSc_2Se_4$|UiO66-MgIL|SS cells temperature dependent EIS measurements between 0 and 60 °C were carried out from 3 MHz to 100 mHz with an AC amplitude of 10 mV.

Additionally, instead of the UiO66-MgIL, a LE interlayer was used to sandwich the cold-pressed $MgSc_2Se_4$ pellet (Ø = 10 mm, d = 2.14 mm, 500 mg) or SPS sintered $MgSc_2Se_4$ pellet (Ø = 9.78 mm, d = 1.58 mm, 392 mg), respectively. Therefore, glass fiber separators (Whatman GF/A) with Ø = 10 mm were moistened with one droplet (5 µL) of the $Mg[B(hfip)_4]_2$ LE[34] (0.1 M in 1,2-dimethoxyethane, Sigma Aldrich, 99.5%) and pressed in place of the UiO66-MgIL on both sides of the spinel layer.

Plating/stripping experiments were performed with symmetrical Mg|UiO66-MgIL|$MgSc_2Se_4$|UiO66-MgIL|Mg cells, prepared in an analog procedure mentioned before (see determination of ionic conductivity) with 120 mg $MgSc_2Se_4$ powder and 60 mg UiO66-MgIL per layer. Additionally, polished Mg foils (Sigma Aldrich, 99.9%, 100 µm) with a diameter of 9 mm were placed between the UiO66-MgIL layers and the SS punches. After pressing the cell at 3 t for 3 min, CP was carried out over 50 cycles with alternating plating/stripping times of 30 min for each step and a current of ±1 µA at 60 °C followed by an EIS measurement. The theoretical amount of magnesium plated/stripped on each side is estimated to 11 µg, which corresponds to a homogenous Mg layer of 102 nm.

The cycling experiment was performed with a Mg|UiO66-MgIL|$MgSc_2Se_4$|UiO66-MgIL|PTCDA full cell, prepared similar to the plating/stripping cell, while one of the Mg foils was replaced by a PTCDA composite cathode. The composite was prepared by mixing perylene tetracarboxylic dianhydride powder (PTCDA, Sigma Aldrich, 97%) with UiO66-MgIL and carbon nanofibers (Sigma Aldrich, >98% carbon basis) in a weight ratio of 6:5:1. After cell assembly, galvanostatic cycling was performed at 60 °C in the potential range of 0.3 to 2.5 V with a current of ±0.25 mA g^{-1} and 100 h per discharge/charge step.

Supporting Information

Supporting Information is available from the Wiley Online Library or from the author.

Acknowledgements

This work contributes to the research performed at CELEST (Center for Electrochemical Energy Storage Ulm-Karlsruhe) and was funded by the German Research Foundation (DFG) under Project ID 390874152 (POLiS Cluster of Excellence). The authors would like to thank Ruben Maile (Justus Liebig University) for providing the UiO-66 MOF material, Yushu Tang (KIT) for the TEM measurements and Elisa Monte (Justus Liebig University) for designing the graphical abstract.

Open access funding enabled and organized by Projekt DEAL.

Conflict of Interest

The authors declare no conflict of interest.

Data Availability Statement

The data that support the findings of this study are openly available in Zenodo at https://doi.org/10.5281/zenodo.8209991, reference number 8209991.

Keywords

ceramics, magnesium batteries, $MgSc_2Se_4$, mixed conductors, solid-state electrolytes

Received: June 23, 2023
Revised: August 26, 2023
Published online: September 8, 2023

[1] a) J. Janek, W. G. Zeier, *Nat. Energy* **2016**, *1*, 16141; b) J. T. Frith, M. J. Lacey, U. Ulissi, *Nat. Commun.* **2023**, *14*, 420; c) F. Schipper, D. Aurbach, *Russ. J. Electrochem.* **2016**, *52*, 1095.
[2] F. Liu, T. Wang, X. Liu, L.-Z. Fan, *Adv. Energy Mater.* **2021**, *11*, 2000787.
[3] Y. Liang, H. Dong, D. Aurbach, Y. Yao, *Nat. Energy* **2020**, *5*, 646.
[4] a) L. F. O'Donnell, S. G. Greenbaum, *Batteries* **2021**, *7*, 3; b) M. York, K. Larson, K. C. Harris, E. Carmona, P. Albertus, R. Sharma, M. Noked, E. Strauss, H. Ragones, D. Golodnitsky, *J. Solid State Electrochem.* **2022**, *26*, 1851.
[5] a) H. S. Hirsh, Y. Li, D. H. S. Tan, M. Zhang, E. Zhao, Y. S. Meng, *Adv. Energy Mater.* **2020**, *10*, 2001274; b) N. Yabuuchi, K. Kubota, M. Dahbi, S. Komaba, *Chem. Rev.* **2014**, *114*, 11636.
[6] L. Mei, J. Xu, Z. Wei, H. Liu, Y. Li, J. Ma, S. Dou, *Small* **2017**, *13*, 1701441.
[7] R. Deivanayagam, B. J. Ingram, R. Shahbazian-Yassar, *Energy Storage Mater.* **2019**, *21*, 136.
[8] J. Muldoon, C. B. Bucur, A. G. Oliver, T. Sugimoto, M. Matsui, H. S. Kim, G. D. Allred, J. Zajicek, Y. Kotani, *Energy Environ. Sci.* **2012**, *5*, 5941.
[9] Z. Lu, A. Schechter, M. Moshkovich, D. Aurbach, *J. Electroanal. Chem.* **1999**, *466*, 203.
[10] Y. Zhan, W. Zhang, B. Lei, H. Liu, W. Li, *Front. Chem.* **2020**, *8*, 125.
[11] S. Ikeda, M. Takahashi, J. Ishikawa, K. Ito, *Solid State Ion.* **1987**, *23*, 125.
[12] a) P. W. Jaschin, Y. Gao, Y. Li, S.-H. Bo, *J. Mater. Chem. A* **2020**, *8*, 2875; b) Z. A. Halim, S. Adnan, F. M. Salleh, N. S. Mohamed, *J. Magnes. Alloys* **2017**, *5*, 439.
[13] L. N. Skov, J. B. Grinderslev, A. Rosenkranz, Y.-S. Lee, T. R. Jensen, *Batter. Supercaps* **2022**, *5*, e20220016.
[14] T. Yamanaka, A. Hayashi, A. Yamauchi, M. Tatsumisago, *Solid State Ion.* **2014**, *262*, 601.
[15] a) C. Dietrich, D. A. Weber, S. J. Sedlmaier, S. Indris, S. P. Culver, D. Walter, J. Janek, W. G. Zeier, *J. Mater. Chem. A* **2017**, *5*, 18111; b) M. R. Busche, D. A. Weber, Y. Schneider, C. Dietrich, S. Wenzel, T. Leichtweiss, D. Schröder, W. Zhang, H. Weigand, D. Walter, S. J. Sedlmaier, D. Houtarde, L. F. Nazar, J. Janek, *Chem. Mater.* **2016**, *28*, 6152; c) M. Ghidiu, J. Ruhl, S. P. Culver, W. G. Zeier, *J. Mater. Chem. A* **2019**, *7*, 17735.
[16] P. Canepa, S.-H. Bo, G. Sai Gautam, B. Key, W. D. Richards, T. Shi, Y. Tian, Y. Wang, J. Li, G. Ceder, *Nat. Commun.* **2017**, *8*, 1759.
[17] J. Jamnik, J. Maier, *J. Electrochem. Soc.* **1999**, *146*, 4183.
[18] M. Dillenz, M. Sotoudeh, C. Glaser, J. Janek, A. Groß, H. Euchner, *Batter. Supercaps* **2022**, *5*, e202200164.
[19] L.-P. Wang, Z. Zhao-Karger, F. Klein, J. Chable, T. Braun, A. R. Schür, C.-R. Wang, Y.-G. Guo, M. Fichtner, *ChemSusChem* **2019**, *12*, 2286.
[20] a) S. Kundu, N. Solomatin, Y. Kauffmann, A. Kraytsberg, Y. Ein-Eli, *Appl. Mater. Today* **2021**, *23*, 100998; b) S. Kundu, N. Solomatin, A. Kraytsberg, Y. Ein-Eli, *Energy Tech.* **2022**, *10*, 2200896.
[21] H. Rickert, in *Inorganic Chemistry Concepts*, (Eds.: C. K. Jørgensen, M. F. Lappert, S. J. Lippard, J. L. Margrave, K. Niedenzu, H. Nöth, R. W.

Parry, H. Yamatera, H. Rickert), Springer, Berlin, Heidelberg, **1982**, pp. 79–117.
[22] A. Senocrate, I. Moudrakovski, G. Y. Kim, T.-Y. Yang, G. Gregori, M. Grätzel, J. Maier, *Angew. Chem.* **2017**, *129*, 7863.
[23] a) I. Riess, *Solid State Ionics* **1991**, *44*, 207; b) W. Weppner, R. A. Huggins, *Annu. Rev. Mater. Sci.* **1978**, *8*, 269.
[24] P. Canepa, G. Sai Gautam, D. Broberg, S.-H. Bo, G. Ceder, *Chem. Mater.* **2017**, *29*, 9657.
[25] a) K. D. Pham, M. Batouche, D. S. Mohammed, T. Seddik, T. V. Vu, D. D. Vo, N. N. Hieu, O. Y. Khyzhun, *J. Solid State Chem.* **2021**, *293*, 121763; b) W. Tahir, G. M. Mustafa, N. A. Noor, S. M. Alay-e-Abbas, Q. Mahmood, A. Laref, *Ceramics Int.* **2020**, *46*, 26637.
[26] W. M. Yim, A. K. Fan, E. J. Stofko, *J. Electrochem. Soc.* **1973**, *120*, 441.
[27] M. Guittard, C. Souleau, H. Farsam, *C. R. Hebd. Acad. Sci.* **1964**, *259*, 2847.
[28] W. Zhang, D. A. Weber, H. Weigand, T. Arlt, I. Manke, D. Schröder, R. Koerver, T. Leichtweiss, P. Hartmann, W. G. Zeier, J. Janek, *ACS Applied Mater. Interfaces* **2017**, *9*, 17835.
[29] Y. Gao, T. P. Mishra, S.-H. Bo, G. Sai Gautam, P. Canepa, *Annu. Rev. Mater. Res.* **2022**, *52*, 129.
[30] J. Zahnow, T. Bernges, A. Wagner, N. Bohn, J. R. Binder, W. G. Zeier, M. T. Elm, J. Janek, *ACS Appl. Energy Mater.* **2021**, *4*, 1335.
[31] E. Roedern, R.-S. Kühnel, A. Remhof, C. Battaglia, *Sci. Rep.* **2017**, *7*, 46189.
[32] K. Kisu, S. Kim, M. Inukai, H. Oguchi, S. Takagi, S. Orimo, *ACS Appl. Energy Mater.* **2020**, *3*, 3174.
[33] Z. Wei, R. Maile, L. M. Riegger, M. Rohnke, K. Müller-Buschbaum, J. Janek, *Batter. Supercaps* **2022**, *5*, e202200318.
[34] Z. Zhao-Karger, R. Liu, W. Dai, Z. Li, T. Diemant, B. P. Vinayan, C. Bonatto Minella, X. Yu, A. Manthiram, R. J. Behm, M. Ruben, M. Fichtner, *ACS Energy Lett.* **2018**, *3*, 2005.

3.2 Publication 2: "MgB_2Se_4 Spinels (B = Sc, Y, Er, Tm) as Potential Mg-Ion Solid Electrolytes – Partial Ionic Conductivity and the Ion Migration Barrier"

In the second publication of this dissertation, the influence of the MgB_2X_4 (B = Sc, Y, Ln; X = S, Se) spinel composition on the Mg-ion conductivity and migration barrier was studied. For this purpose, a selection of magnesium chalcogenide spinels was systematically investigated from both an experimental and a computational point of view.

The basis for the experimental study was laid by the successful solid-state synthesis of three new selenide spinels (B = Y, Er, Tm). As their DC polarization tests demonstrated a mixed-conducting nature analogous to $MgSc_2Se_4$, EIS measurements with electron-blocking interlayers (introduced in publication 1) proved to be suitable and reliable way for determining their ionic transport properties. By applying this specific method, it was found that the novel spinel compounds with larger B^{3+}-ions than Sc^{3+} (MgY_2Se_4 excepted) exhibit slightly higher ionic conductivities and lower migration barriers compared to $MgSc_2Se_4$. To validate these findings, DFT calculations on the expanded MgB_2X_4 system revealed that larger B^{3+}-ions widen the bottleneck of the migration path, thereby generally facilitating Mg-ion migration. However, it was also identified that the B^{3+}-ion radius influences the trigonal distortion of the octahedra and thus the volume ratio between octahedra and tetrahedra in the structure. Since both polyhedra are involved in the Mg^{2+} migration path, their volume ratio in turn affects the kinetic and static contributions to the migration barrier.

Conclusively, this comprehensive publication demonstrates that, dependent on the B^{3+}-ion in the MgB_2X_4 sulfide/selenide spinels, the right interplay between lattice expansion and trigonal distortion is important to achieve low Mg^{2+} migration barriers. Considering these guidelines will surely help to find good spinel-type Mg-ion conductors.

The experiments were designed and planned by the first author under supervision of Prof. M. Rohnke and Prof. J. Janek. The MgB_2Se_4 SEs were synthesized by C. Glaser and the UiO66-MgIL ionogel electrolyte was prepared by R. Maile under supervision of Prof. K. Müller-Buschbaum. C. Glaser performed all electrochemical experiments, the SEM, EDS and X-ray diffraction measurements, and the Rietveld refinements. The first author was supported by Dr. Z. Wei in the interpretation of the electrochemical data. Dr. S. Indris conducted and interpreted the NMR measurements. The DFT calculations were carried out and described in the publication by Dr. M. Dillenz, Dr. K. Sarkar and PD Dr. M. Sotoudeh under supervision of Prof. A. Groß. All other parts of the manuscript were written by the first author and revised by ten co-authors.

This study was part of the research within POLiS – Post Lithium Storage Cluster of Excellence.

RESEARCH ARTICLE

ADVANCED ENERGY MATERIALS
www.advenergymat.de

MgB_2Se_4 Spinels (B = Sc, Y, Er, Tm) as Potential Mg-Ion Solid Electrolytes – Partial Ionic Conductivity and the Ion Migration Barrier

*Clarissa Glaser, Manuel Dillenz, Kanchan Sarkar, Mohsen Sotoudeh, Zhixuan Wei, Sylvio Indris, Ruben Maile, Marcus Rohnke, Klaus Müller-Buschbaum, Axel Groß, and Jürgen Janek**

The magnesium chalcogenide spinel $MgSc_2Se_4$ with high Mg-ion room-temperature conductivity has recently attracted interest as solid electrolyte for magnesium ion batteries. Its ionic/electronic mixed-conducting nature and the influence of the spinel composition on the conductivity and Mg^{2+} migration barrier are yet not well understood. Here, results from a combined experimental and computational study on four MgB_2Se_4 spinels (B = Sc, Y, Er, Tm) are presented. The room-temperature ionic conductivities ($\sigma_{ion} = 2 \times 10^{-5}$–$7 \times 10^{-5}$ S cm^{-1}) of the spinels are accurately measured, as electron transport is effectively suppressed by purely Mg-ion conducting electrode interlayers. Using the same approach, reversible Mg plating/stripping as well as good electrochemical stability are achieved. Driven by the good accordance of the computationally and experimentally obtained Mg^{2+} migration barriers E_a(th) and E_a, respectively, further periodic density functional calculations are performed on the MgB_2Se_4 spinel system, revealing the role of trigonal distortion on the migration path geometry and E_a(th). These findings provide deeper understanding how to reach small Mg^{2+} migration barriers E_a in the MgB_2Se_4 spinels.

1. Introduction

With the growing demand on portable and resource-saving energy storage systems, multivalent-ion-based batteries with potentially higher energy densities and lower cost than the present-day lithium-ion batteries have attracted significant interest.[1,2] Among these alternative next-generation batteries, rechargeable magnesium batteries (RMB) stand out due to the excellent characteristics of the Mg anode. Magnesium has a much lower standard reduction potential (−2.37 V vs SHE) than Zn and Al metals (−0.76 and −1.66 V) and a volumetric capacity of 3833 mAh cm^{-3} which is almost twice that of Ca and Li and three times as much as Na. Furthermore, magnesium is highly abundant in the earth's crust (with 2.1% ≈10^4 times more often than lithium) and suspected to be less prone to dendrite formation as anode, compared to lithium.[3]

To circumvent the drawbacks of liquid-based cell systems such as the passivation and corrosion of the Mg electrode, and ensure a lower susceptibility to dendrite formation as well as higher levels of safety, solid-state battery concepts are pursued.[1,4,5] Here, one of the main challenges is to develop a solid electrolyte (SE) that has a sufficient Mg-ion room-temperature conductivity

C. Glaser, Z. Wei, M. Rohnke, J. Janek
Institute of Physical Chemistry
Justus Liebig University Giessen
Heinrich-Buff-Ring 17, D-35392 Giessen, Germany
E-mail: juergen.janek@phys.chemie.uni-giessen.de

The ORCID identification number(s) for the author(s) of this article can be found under https://doi.org/10.1002/aenm.202402269

DOI: 10.1002/aenm.202402269

C. Glaser, Z. Wei, M. Rohnke, J. Janek
Center for Materials Research (ZfM)
Justus Liebig University Giessen
Heinrich-Buff-Ring 16, D-35392 Giessen, Germany

M. Dillenz, K. Sarkar, M. Sotoudeh, A. Groß
Institute of Theoretical Chemistry
Ulm University
Albert-Einstein-Allee 11, D-89081 Ulm, Germany

S. Indris
Institute for Applied Materials-Energy Storage Systems (IAM-ESS)
Karlsruhe Institute of Technology (KIT)
Hermann-von-Helmholtz-Platz 1, D-76344 Eggenstein-Leopoldshafen, Germany

S. Indris
Applied Chemistry and Engineering Research Centre of Excellence (ACER CoE)
Université Mohammed VI Polytechnique (UM6P)
Lot 660, Hay Moulay Rachid, Ben Guerir 43150, Morocco

ADVANCED SCIENCE NEWS
www.advancedsciencenews.com

ADVANCED ENERGY MATERIALS
www.advenergymat.de

(σ_{ion} > 4–5 mS cm^{-1}).[6] The high charge density of Mg^{2+}, compared to the Li^+/Na^+ alkali counterparts, results in a much stronger Coulomb interaction in the solid host-framework, leading to typically sluggish Mg-ion mobility.[1] For this reason, the design of the crystal structure is fundamental as several structural factors can mitigate the strong Coulomb interactions experienced by the Mg^{2+} ion.[2,7] In general, materials owning interconnected 3D pathways, such as NASICON and spinel compounds, provide better platforms to support long-range ion diffusion, while 2D and 1D pathways are more easily blocked by intrinsic anti-site or extrinsic point defects. Compared to NASICON-structured compounds and other crystal structures, the spinel structure MgB_2X_4 (B = trivalent cation, X = chalcogenide) offers – apart from the 3D paths – a relatively large distance between the mobile Mg-cation in its transition state and the neighboring B-cations. This results in inherently weaker cation-cation repulsion in the activated state, possibly crucial to enabling multivalent-ion conduction even at ambient temperature.[2] In parallel, previous studies have shown that fast ion motion can be achieved when the energetically stable site of the mobile ion is less favored, in terms of coordination, than the activated site.[8] In the normal spinel structure, the Mg-ions, which typically strongly prefer the octahedral coordination environment, reside in tetrahedral sites (*tet*). During migration, the Mg-ions hop across an empty octahedral activated site (*oct*) to reach the next tetrahedral site which is expected to lead to a flattening of the energy profile along the *tet-oct-tet* migration path according to the Brønsted-Evans-Polanyi principle.[9–11]

Motivated by the features of the spinel structure, Canepa et al. studied a series of d^0-metal-based MgB_2X_4 spinels (B = Sc, Y, and In, X = S, Se, Te) by first principles-based nudged elastic band (NEB) calculations and predicted low migration barriers of E_a(th) = 0.36–0.42 eV[9] in agreement with our own corresponding computational studies.[11–13] Canepa et al. successfully synthesized $MgSc_2Se_4$ and determined a Mg^{2+} migration barrier of E_a(NMR) = 0.37 ± 0.09 eV by means of ^{25}Mg static variable-temperature spin-lattice relaxation nuclear magnetic resonance (SLR NMR) measurements, consistent with their computed data. As a first approach to determine the ionic conductivity of $MgSc_2Se_4$, they performed electrochemical impedance spectroscopy (EIS) with ion-blocking electrodes and interpreted the spectra according to the conventional model for mixed ionic-electronic conductors (MIECs) described by Jamnik and Maier.[9,14] Later on, in our previous work, we critically discussed the shortcomings of this approach in case of $MgSc_2Se_4$ and presented an alternative way, allowing accurate and unequivocal characterization of the ionic conductivity.[15] Specifically, a new kind of symmetrical transference cell is used, containing a pure Mg-ion conducting interlayer between the ion-blocking electrodes and the spinel pellet, to effectively suppress the electron transport. As a result, the partial ionic conductivity (σ_{ion} = 2.4–5.5 × 10^{-5} S cm^{-1} at room-temperature) was well determined from high-quality impedance spectra using a modified equivalent circuit, describing the impedance of a MIEC between charge carrier specific blocking electrodes and interlayers (adapted from previous works).[16–18] Furthermore, this approach, including electron-blocking interlayers, may also be an option to prevent self-discharge of a charged full cell due to the reported electronic conductivity (σ_{el} = ≈10^{-8} S cm^{-1} at room-temperature)[9,15,19] of the $MgSc_2Se_4$ SE. This self-discharge is proposed to arise from increased carrier concentration caused by point defects, and/or the presence of electron conducting secondary phases.[20,21] The latter seems to contribute to the electronic conductivity in any case, as Kundu et al. demonstrated that electronic transport occurs via a Berthelot-type mechanism of metal-type inclusions (e.g., Sc/ScSe), while Wang et al.'s attempts of compositional tuning to avoid point defects were rather unsuccessful.[19,21,22]

Recently, Koettgen et al. used density functional theory to calculate the Mg^{2+} migration barriers and the stability of several MgB_2X_4 (B = lanthanide, X = S, Se) spinels.[23] In their work, they demonstrated that the balance between a low E_a(th) and a stable spinel phase (with respect to competing AB_2X_4-type phases) is primarily given for the selenide spinels with the ionic radius r(Ln) of the lanthanides from Lu to Er [r(Lu–Er) = 0.861–0.890 Å; E_a(th,Lu–Er) = 0.369–0.358 eV]. These predicted stabilities agree well with experimental results (except for Ho).[24,25] Thus, this group of lanthanide-based selenide spinels emerges as attractive candidate for Mg-ion solid electrolytes, not least due to the predicted slightly lower migration barriers compared to the prototype $MgSc_2Se_4$. We assumed that the electrochemical and theoretical study of this series of spinels will provide a deeper understanding of their transport properties. To this end, we report here the successful synthesis of four MgB_2Se_4 spinels (B = Sc, Er, Tm, Y) together with their structural characterization by X-ray diffraction (XRD) and ^{25}Mg magic-angle spinning nuclear magnetic resonance (MAS NMR) spectroscopy. Furthermore, the partial conductivities as well as the Mg^{2+} migration barriers of the spinels with mixed ionic/electronic nature are evaluated from EIS and polarization measurements using charge carrier specific blocking electrodes and interlayers. Due to the good agreement of our experimental and computational predicted migration barriers, we extended our theoretical study based on periodic density functional theory (DFT) calculations to provide a deeper understanding on the structural details defining the migration barrier. These results are followed by further electrochemical investigations, demonstrating the good electrochemical stability and a reversible Mg plating/stripping cycling performance of the spinels. To the best of our knowledge, this is the most comprehensive report on Mg-ion conducting selenide spinels.

2. Results and Discussion

2.1. Structure Information of MgB_2Se_4 Spinels

The MgB_2Se_4 spinels (B = Er, Tm, Y) were initially prepared according to our reported one-step synthesis of $MgSc_2Se_4$[15] by reacting stoichiometric amounts of the elemental powders at 950 °C for 20 h. However, although high-purity $MgSc_2Se_4$ was obtained with this procedure, Rietveld refinement results based on the XRD patterns of the other three spinels (Figures S1 and S2, Supporting Information) reveal a significant fraction of

R. Maile, K. Müller-Buschbaum
Institute of Inorganic and Analytical Chemistry
Justus Liebig University Giessen
Heinrich-Buff-Ring 17, D-35392 Giessen, Germany

ADVANCED SCIENCE NEWS
www.advancedsciencenews.com

ADVANCED ENERGY MATERIALS
www.advenergymat.de

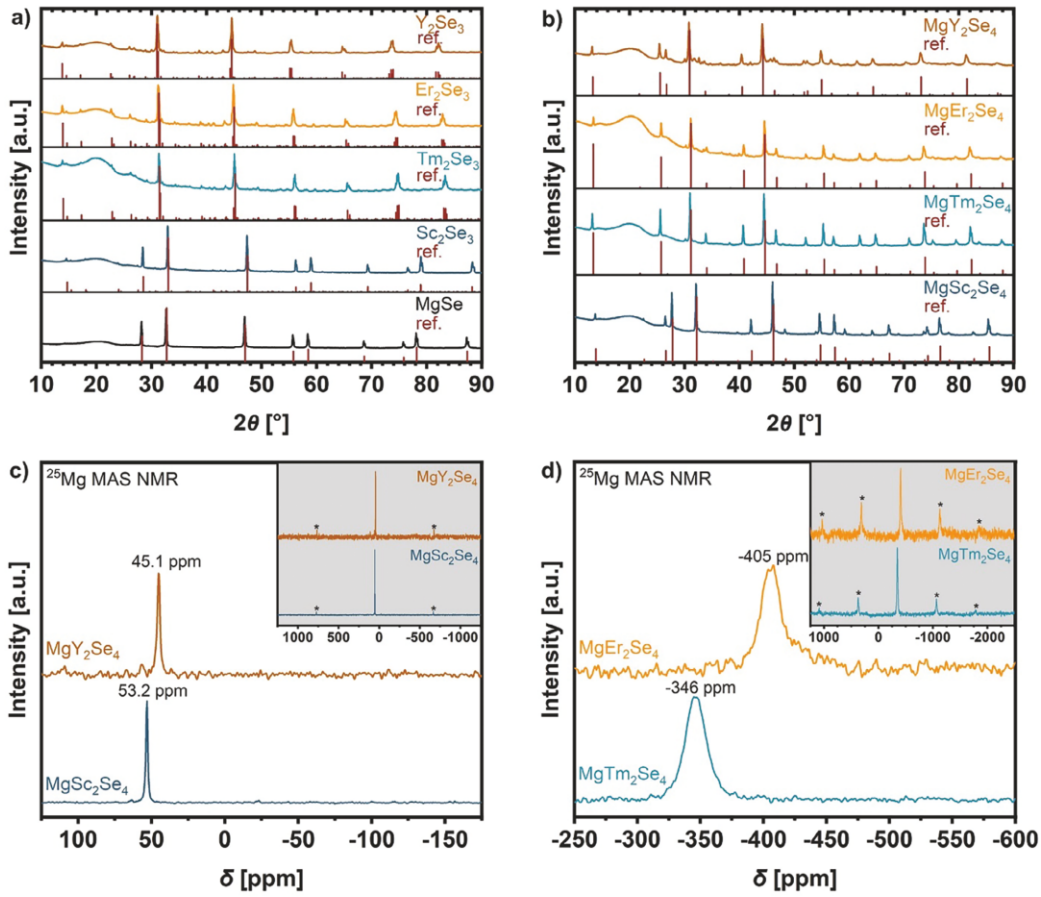

Figure 1. XRD patterns shown for a) synthesized binary selenides MgSe, Sc_2Se_3, Tm_2Se_3, Er_2Se_3 and Y_2Se_3, and b) synthesized spinels $MgSc_2Se_4$, $MgTm_2Se_4$, $MgEr_2Se_4$ and MgY_2Se_4 via the two-step route. ^{25}Mg solid-state NMR is performed for the characterization of Mg positions in c) $MgSc_2Se_4$ (one-step synthesis) and MgY_2Se_4, and d) $MgTm_2Se_4$ and $MgEr_2Se_4$. The spinning sidebands are marked with an asterisk. Data for $MgSc_2Se_4$ reproduced with permission.[15] Copyright 2023, Wiley-VCH.

impurities. The samples contained undesired B_2O_2Se between 6.2 wt% and 12.8 wt% and partially unreacted binary phases with up to 59.0 wt%, making them unusable for further analysis. As the experimental conditions for the spinel syntheses were identical, the higher content of oxide species compared to the Sc-based spinel might possibly be explained by a higher purity of the Sc powder, even if metal precursors with the same purity were purchased. To still obtain the new spinels in high purity, nevertheless, we carried out a two-step synthesis, using metal chips with less surface area and therefore probably less oxide impurity than the corresponding metal powder precursors. The XRD patterns of the first step of the synthesis (**Figure 1**a), the formation of the binary selenides, indicate B_2Se_3 compounds with a comparable high purity to Sc_2Se_3 and MgSe prepared from precursor powders. Thus, the binary selenides were found to be suitable reactants for synthesizing the corresponding spinels in a subsequent reaction step. As shown in Figure 1b, clearly fewer intensive peaks of impurities could be found in the XRD patterns of the final products using this two-step procedure, although the formation energy is much lower for the spinels built from the binaries.[9] The performed Rietveld refinements (Figure S3, Supporting Information) confirm the reduced fraction of B_2O_2Se and unreacted binaries in $MgTm_2Se_4$ (4.3 wt% and 0 wt%), $MgEr_2Se_4$ (3.0 wt% and 0.6 wt%), and MgY_2Se_4 (2.0 wt% and 8.9 wt%), as well as the spinel-type structure with Fd-3m space group (additional crystallographic data in Tables S1–S8, Supporting Information). The spinel structure consists of a cubic dense packing of Se-anions, where the B-ions reside in 16d sites (octahedra) and the Mg-ions occupying the 8a sites (tetrahedra).

To further investigate the position of the Mg-ions,^{25}Mg MAS NMR spectroscopy was carried out. The ^{25}Mg nucleus has a nuclear spin $I = 5/2$ and a large nuclear quadrupolar moment $Q = 201$ mb[26] and thus is very sensitive to asymmetric local environments. The ^{25}Mg MAS NMR spectra (Figure 1c,d)

ADVANCED SCIENCE NEWS
www.advancedsciencenews.com

ADVANCED ENERGY MATERIALS
www.advenergymat.de

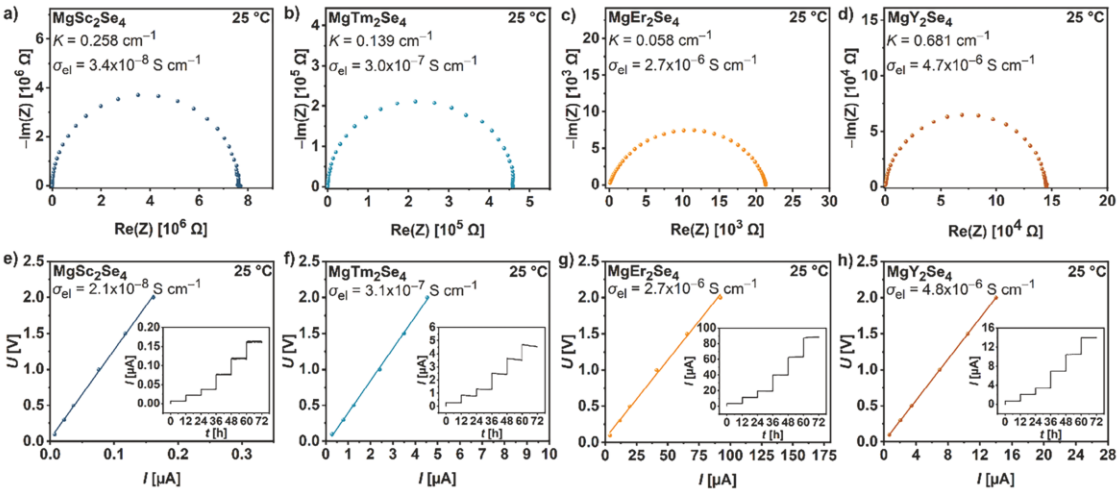

Figure 2. Nyquist plots of Au|MgB_2Se_4|Au pouch cells with a) $MgSc_2Se_4$, b) $MgTm_2Se_4$, c) $MgEr_2Se_4$ and d) MgY_2Se_4 in the frequency range from 7 MHz to 100 mHz at 25 °C; and e–h) corresponding DC polarization data obtained at different voltages (0.1 V, 0.3 V, 0.5 V, 1.0 V, 1.5 V, and 2.0 V, held for 12 h, shown in the inset) with linear fit of the ohmic electronic behavior at 25 °C. *K* represents the cell constant, as described in Equation (2). Data for $MgSc_2Se_4$ reproduced with permission.[15] Copyright 2023, Wiley-VCH.

show only a single isotropic peak for all spinels, indicating that Mg occupies exclusively the tetrahedral site. In case of the Sc- and Y-based spinels, representing diamagnetic compounds, the isotropic peak is very narrow (width of 1.5 ppm and 2.5 ppm, respectively) and the spinning sideband patterns are very weak. These characteristics reveal that the local environment, i.e., the surrounding Se tetrahedron, is highly symmetric. Instead, for the lanthanide-based spinels, consistent with their reported paramagnetism,[24] much broader isotropic peaks with large negative shifts and broader spinning sideband patterns were observed. Furthermore, energy disperse X-ray spectroscopy (EDS) images superimposed to scanning electron micrographs (SEM) display the uniform distribution of the elements Mg, Sc/Tm/Er/Y and Se in the samples. The spinel stoichiometry, which is ideally 1:2:4, is confirmed by the observed atomic ratios (Figure S4, Supporting Information), including small deficits especially in the Se fraction (0–17.5%), probably due to Se evaporation from the sample during the high-temperature synthesis. To gain more precise information about the inclusion of impurities in the nano-scale range, high-angle annular dark-field scanning transmission electron microscopy (HAADF-STEM) imaging including EDS mapping was performed (Figures S5–S8, Supporting Information). The recorded maps show a homogeneous distribution of the elements Mg, Sc/Tm/Er/Y and Se in the bulk of the particles, while some inhomogeneity can be observed at the edges, clearly visible in the layered EDS maps of the selected $MgSc_2Se_4$ and $MgEr_2Se_4$ particles but certainly also the case for $MgTm_2Se_4$ and MgY_2Se_4. This observed deviation from the spinel stoichiometry at the particle edges suggests that other phases must necessarily be present, presumably from associated elements or binary selenides. Apart from that, the collected TEM images demonstrate a typical particle size in the low micrometer range for all spinel powders ($MgSc_2Se_4$: 1–3 µm, $MgTm_2Se_4$: 0.5–1.5 µm, $MgEr_2Se_4$: 0.5–3 µm, MgY_2Se_4: 1–10 µm) (Figures S9–S12, Supporting Information), while the recorded selected area electron diffraction (SAED) patterns during the TEM measurements confirm the spinel structure as well.

2.2. Electronic Conductivity σ_{el}

To determine the room-temperature partial electronic conductivity of the MgB_2Se_4 spinels, EIS and chronoamperometry (CA) measurements were performed. Following the investigation of $MgSc_2Se_4$ in our earlier work,[15] we assembled symmetrical Au|MgB_2Se_4|Au pouch cells, containing a spinel pellet with vapor-deposited Au layers as ion-blocking electrodes. In the Nyquist plots (**Figure 2**a–d), produced from the EIS measurements, depressed semicircles with missing low-frequency tail were observed for all samples, as already obtained for $MgSc_2Se_4$.[9,15,19] These similarities to $MgSc_2Se_4$ indicate that the three new spinels seem to be MIECs as well, which have an electronic current path in parallel with the ionic current path. As there is no blockage of the electron transport due to the Au electrodes, there is no interface capacitance, explaining the lack of the capacitive tail at very low frequencies.[16] Besides that, the electronic current is much larger than the blocked ionic current, possibly even at high frequencies where the interfacial capacitance of the ions is short-circuited. Thus, the observed semicircle is only due to the combination of the electronic resistance and the geometrical capacitance, without any relation to the ionic resistance or the interfacial capacitance. For this reason, R_{el}, denoted as electronic resistance, can be determined based on the total resistance of the semicircle and then used to calculate the electronic conductivity σ_{el} by applying Equation (2) (Experimental Section). In comparison to $MgSc_2Se_4$ ($\sigma_{el} = 3.4 \times 10^{-8}$ S cm^{-1}), up to two orders of magnitude higher electronic conductivity for the new MgB_2Se_4 spinels [$\sigma_{el}(MgTm_2Se_4) = 3.0 \times 10^{-7}$ S cm^{-1},

ADVANCED SCIENCE NEWS
www.advancedsciencenews.com

ADVANCED ENERGY MATERIALS
www.advenergymat.de

$\sigma_{el}(MgEr_2Se_4)$ = 2.7 × 10^{-6} S cm^{-1}, $\sigma_{el}(MgY_2Se_4)$ = 4.7 × 10^{-6} S cm^{-1}] were calculated, although a smaller direct bandgap is predicted for $MgSc_2Se_4$ (E_B = 1.727 eV)[27] than for MgY_2Se_4 (E_B = 2.020 eV).[28] As these electronic conductivities evaluated from AC impedance data agree well with the values obtained by additional dc polarization measurements shown in Figure 2e–h, the impedance analysis is validated.

Interestingly, considering the phase composition obtained by the Rietveld refinements (Figure S3, Supporting Information), a clear trend of increasing electronic conductivity with the amount of binary impurity phases (B_2Se_3, BSe_3, etc.) emerges. While $MgSc_2Se_4$ and $MgTm_2Se_4$ contain mainly impurities of MgSe (wide-bandgap semiconductor)[29] and Tm_2O_2Se, respectively, which are probably less electron-conducting phases, the other spinels are contaminated with considerable amounts of electronically conducting Er_2Se_3 (σ_{el} = 1.3 × 10^{-1} S cm^{-1})[30] or Y_2Se_3/YSe (σ_{el} = 2.0 × 10^{-1} S cm^{-1}/3.3 × 10^{-1} S cm^{-1}).[30] This demonstrates that these impurities may have a large influence on the electronic conductivity of the investigated materials, possibly even more than point defects in the spinel phase itself, since small traces of electronically conductive impurities cannot be ruled out for all four spinels. Kundu et al.[21] suggest that these impurities may occur as nano-scaled free-electron containing inclusions around the particle surface, inducing electron transport between each other by jumping/tunneling through the low-electron conducting spinel matrix, described as a Berthelot-type conductivity.[31] This hypothesis is consistent with the inhomogeneous element distribution at the edges of the particles found in the present work, which could be attributed to electron-conducting impurity phases. Nevertheless, to make the spinels applicable, their contribution to self-discharge in electrochemical cells must be reduced either by minimizing the electronic conductivity due to optimization of the synthesis and the purity of precursors or by using electron-blocking interlayers.

2.3. Ionic Conductivity σ_{ion} and Mg^{2+} Migration Barrier E_a

For the measurements of the partial ionic conductivities and the Mg^{2+} migration barriers of the MgB_2Se_4 spinels, a sandwich-type cell configuration was used, already described for the investigation of $MgSc_2Se_4$ in our previous work.[15] Inside the cells, Mg-ion conducting and at the same time electron-blocking interlayers were inserted between the cold-pressed spinel pellet and the stainless-steel ion-blocking electrodes (SS). Hence, the interlayer does not only enable a proven better physical contact between the stiff electrodes and the rough spinel pellet,[15] but also suppresses the undesired electron transport which would otherwise make the evaluation much more difficult. As interlayer, the Mg-ion ionogel electrolyte UiO66-MgIL (σ_{el} = 1.7 × 10^{-10} S cm^{-1})[15] was used, consisting of the metal-organic framework (MOF) structure UiO-66 impregnated with an 1 M $Mg(TFSI)_2$-[EMIM][TFSI] ionic liquid (IL). **Figure 3a** shows the exemplary Nyquist plots based on room-temperature EIS measurements of the SS|UiO66-MgIL|MgB_2Se_4|UiO66-MgIL|SS cells with MgY_2Se_4 and without spinel pellet (reference cell). The Nyquist plot of the SS|UiO66-MgIL|SS reference cell exhibits only a tail, relating to an imperfect capacitor, as the expected semicircle at higher frequencies cannot be resolved due to the upper limit of the frequency range (1 MHz) of the used equipment. For this reason, a simplified equivalent circuit without constant phase element (CPE) in parallel to the resistance was chosen (see Figure 3b) to determine the ionic resistance $R1_{ion}$ of the UiO66-MgIL. Applying Equation (2), for the UiO66-MgIL-2 batch, used in this work, a room-temperature ionic conductivity σ_{ion}(UiO66-MgIL-2) = 2.8 × 10^{-4} S cm^{-1} is evaluated, slightly higher than for the UiO66-MgIL-1 batch (σ_{ion} = 9.5 × 10^{-5} S cm^{-1}) taken for the investigation of $MgSc_2Se_4$.[15] This small difference can probably be attributed to small, hardly avoidable differences in the MOF pore size or conductive salt ($Mg[TFSI]_2$) concentration. Figure 3c shows the equivalent circuit used for fitting the impedance spectra of all sandwich-type cells, where three contributions are connected in parallel: the overall (bulk and grain boundary) ionic charge transport in the spinel $R2_{ion}$, the electronic charge transport in the spinel $R2_{el}$ including the electron blockage $CPE2_{e1}$ at the UiO66-MgIL interlayer, and the geometrical capacitance $CPE2_{geo}$. This part of the model is a modification of the typical circuit used for describing the impedance of a MIEC between ion-blocking electrodes.[16–18,32] The previous circuit elements in parallel, $R1_{ion}$ and $CPE1_{ion}$, represent the UiO66-MgIL interlayers, while $CPE3_{e2}$ represents the ion-blocking stainless-steel electrodes. For the fitting, the value of $R1_{ion}$ was adjusted with Equation S1 (Supporting Information) to the thickness of the UiO66-MgIL interlayer used in each individual cell and set as a fixed resistance. A detailed overview of the accurate layer thicknesses in each cell and the obtained room-temperature resistances are listed in the Tables S9–S11 (Supporting Information). Applying Equation (2) to the fitted $R2_{ion}$, a room-temperature overall ionic conductivity of $\sigma_{ion}(MgY_2Se_4)$ = 1.4–2.6 × 10^{-5} S cm^{-1} for all three MgY_2Se_4-containg cells (shown in Figure 3a) was calculated. Since the conductivity results are almost constant for differently chosen spinel layer thicknesses [$d(MgY_2Se_4)$ = 0.72 mm, 0.86 mm, or 1.26 mm], $R2_{ion}$ is indeed primarily related to the ionic resistance of the spinel. Note that this resistance is obviously not influenced by the IL of the UiO66-MgIL interlayer, as EDS mapping of the UiO66-MgIL|$MgSc_2Se_4$|UiO66-MgIL pellet cross section after temperature dependent EIS measurements demonstrated that the IL does not penetrate into the spinel pellet.[15] As exemplary shown for the MgY_2Se_4 pellet (Figure S15, Supporting Information) in this work, this is also the case for all other used spinels pellets, which have a higher relative density ρ (see Table S10, Supporting Information) than the previous investigated $MgSc_2Se_4$ pellet (m = 160 mg, ρ = 78.6%).

Figure 3d shows exemplarily the Nyquist plots of the room-temperature EIS measurements for all spinel compounds with a pellet mass of 160 mg in the sandwich-type cells. An overview of all Nyquist plots obtained over the complete temperature range from 0 °C to 60 °C for at least three different layer thicknesses/masses per spinel are depicted in Figures S16–S19 (Supporting Information). Based on the fitted Nyquist plots the average conductivity per spinel at room-temperature and 60 °C was determined. As shown in Figure 3e, the newly examined MgB_2Se_4 spinels have a similarly high ionic conductivity as $MgSc_2Se_4$ [$\sigma_{ion}(MgSc_2Se_4)$ = 4.0 × 10^{-5} S cm^{-1}, $\sigma_{ion}(MgTm_2Se_4)$ = 6.5 × 10^{-5} S cm^{-1}, $\sigma_{ion}(MgEr_2Se_4)$ = 4.1 × 10^{-5} S cm^{-1}, $\sigma_{ion}(MgY_2Se_4)$ = 2.0 × 10^{-5} S cm^{-1} at 25 °C]. This was more or less expected due to the small differences in their predicted migration

ADVANCED SCIENCE NEWS
www.advancedsciencenews.com

ADVANCED ENERGY MATERIALS
www.advenergymat.de

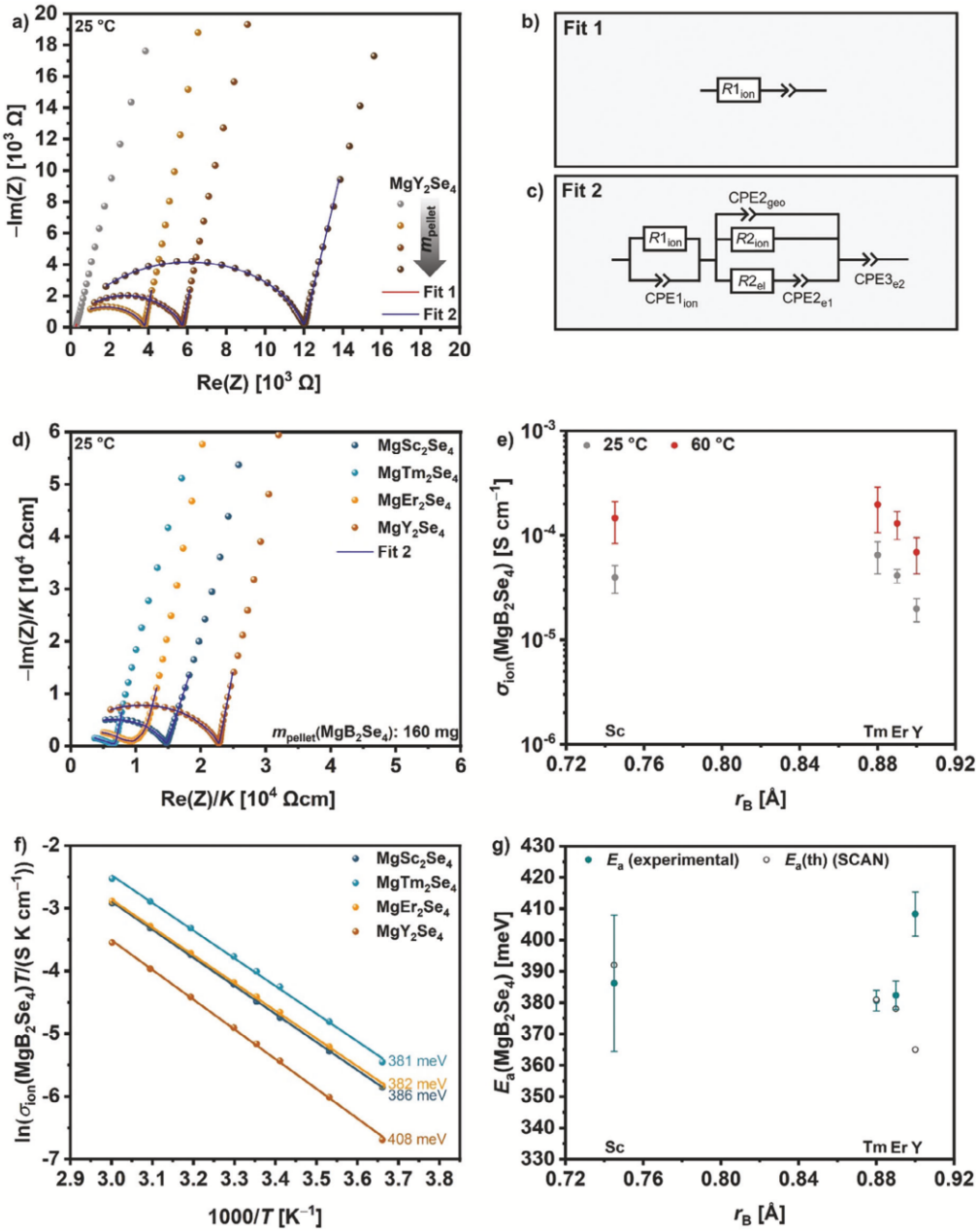

Figure 3. a) Nyquist plots of SS|UiO66-MgIL|MgB_2Se_4|UiO66-MgIL|SS cells at 25 °C exemplarily shown for MgY_2Se_4 with varied spinel pellet mass/thickness (0 mg/0 mm, 160 mg/0.72 mm, 220 mg/0.86 mm and 280 mg/1.26 mm) and used fits Fit 1 and Fit 2; applied equivalent circuit to fit the Nyquist plots for b) SS|UiO66-MgIL|SS cells (denoted as Fit 1) and c) SS|UiO66-MgIL|MgB_2Se_4|UiO66-MgIL|SS cells (denoted as Fit 2); d) comparison of Nyquist plots for SS|UiO66-MgIL|MgB_2Se_4|UiO66-MgIL|SS cells with different spinels at 25 °C exemplarily shown for a spinel pellet mass of 160 mg; e) overview of determined average ionic conductivities of the MgB_2Se_4 spinels at 25 °C and 60 °C; f) Arrhenius plots of the average ionic conductivities calculated for temperatures ranging from 0 °C to 60 °C and g) overview of determined Mg^{2+} migration barriers E_a of the MgB_2Se_4 spinels in comparison to theoretically predicted values E_a(th) by the SCAN method. Experimental data for $MgSc_2Se_4$ reproduced with permission.[15] Copyright 2023, Wiley-VCH.

ADVANCED SCIENCE NEWS
www.advancedsciencenews.com

ADVANCED ENERGY MATERIALS
www.advenergymat.de

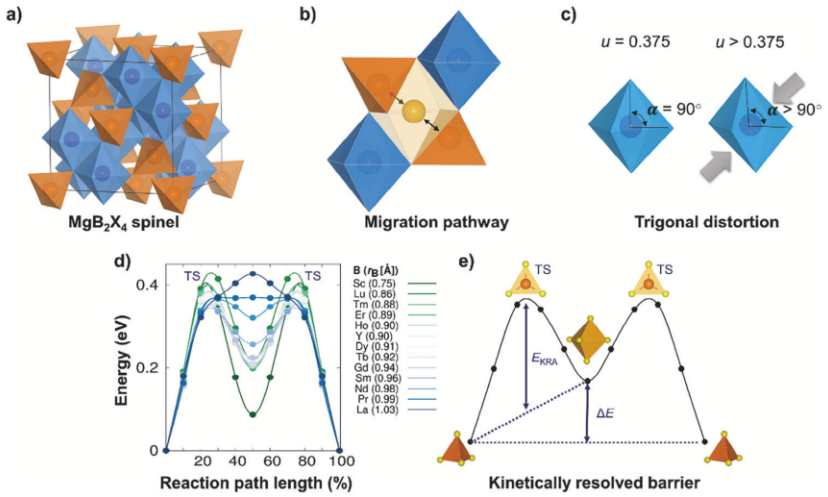

Figure 4. a) The MgB_2X_4 spinel crystal structure is shown on the left with the B-cation shown in blue and the Mg-cation in orange. b) The Mg^{2+} migration follows an interstitial mechanism. Mg^{2+} is tetrahedrally coordinated at the initial and final sites (orange) and migrates through empty octahedral (light orange) sites following a *tet-oct-tet* migration path. The transition state (TS) of the migration process is the triangular face shared by initial tetrahedral and intermediate octahedral sites. c) The trigonal distortion of octahedron specified by anion parameter u and the angle α. d) The energy along the migration path for MgB_2Se_4 spinel compounds determined by NEB. e) Schematic of the energy profile of the Mg^{2+} migration. The kinetically resolved barrier E_{KRA} and the difference in energy between tetrahedral and octahedral sites referred as site preference energy ΔE are indicated by arrows.

barriers [E_a(th) = 375–358 meV].[9,23] Note that impurities with fractions >5 wt%, in particular found in MgY_2Se_4, or the interfacial resistances that are probably material-dependent (not considered in our fittings) could have reduced the calculated conductivities. Moreover, it is worth to mention that in case of $MgEr_2Se_4$, the fitted ionic resistance of the spinel $R2_{ion}$ and the fitted total ionic resistance ($R1_{ion}$+$R2_{ion}$) are comparably higher than their corresponding estimates $R_{ion}(MgEr_2Se_4)$ and R_{ion}(SEs), directly calculated from the raw data (see Table S11, Supporting Information). In this simplified calculation, both, the total ionic resistance of the reference cell R_{ion}(UiO66-MgIL) and the sandwich-type cell R_{ion}(SEs) were directly calculated from the lowest data point at the intercept of the Re(Z) axis. From the difference of R_{ion}(SEs) and R_{ion}(UiO66-MgIL) the ionic resistance of the spinel $R_{ion}(MgEr_2Se_4)$ is given. The discrepancy between the fitted and directly calculated values results from the flattend shape of the Nyquist plots at the Re(Z) axes intercept, possibly induced due to an additional contribution from an interface or impurity. As this contribution is more integrated in the fitted values, the resistance determined directly from the raw data is lower, resulting in a slightly higher ionic conductivtiy (for example: 4.8×10^{-5} S cm^{-5} at 25 °C) for $MgEr_2Se_4$. Figure 3f shows the Arrhenius plots of the ionic conductivities for the temperature range from 0 °C to 60 °C. Applying the Arrhenius equation (Equation (3), Experimental Section), the Mg-ion migration barriers can be calculated to be $E_a(MgSc_2Se_4)$ = 386 ± 24 meV, $E_a(MgTm_2Se_4)$ = 381 ± 4 meV, $E_a(MgEr_2Se_4)$ = 382 ± 6 meV (raw data: 373 ± 5 meV), and $E_a(MgY_2Se_4)$ = 406 ± 9 meV. These values are lower than published ones for other classes of Mg-ion SEs[15] and close to our computationally derived migration barriers (E_a(th)) obtained from DFT calculations based on the strongly constrained and appropriately normed (SCAN) exchange-correlation functional (Figure 3g). In addition, our computational results exhibit a decreasing trend of the Mg^{2+} migration barrier with increasing B-ion radius r_B, in accordance to previous predictions.[9,23] This trend is not observed in the electrochemical results for the compounds synthesized here, since the experimental error exceeds the minor changes (<0.03 eV) of the migration barriers for the narrow range of the ionic radii r_B. However, to gain a deeper understanding of the calculated trend, we conducted a detailed computational study on the underlying contributions to the Mg^{2+} migration barrier, as described below.

2.4. Computational Study of Underlying Contributions to the Migration Barrier E_a(th)

Migration of Mg-ions within the spinel structure (**Figure 4a**) typically occurs via an interstitial mechanism, transitioning from initial tetrahedral sites through an empty octahedron to final tetrahedral sites (*tet-oct-tet*),[33] as illustrated in Figure 4b. The energy difference between tetrahedral and octahedral sites, known as site preference energy, influences the migration barriers, with lower barriers expected when site preference energy is minimized. However, Mg lanthanide spinels defy this trend, exhibiting lower barriers when site preference energy is maximized.[23] This phenomenon is attributed to the stabilization of the triangular transition state with increasing ionic radius r_B of the metal B. Despite its importance, the transition state energy is not usually explicitly considered in the design rule for identifying good Mg-ion conductors.

We expand upon the exploration of chemical patterns in the Mg ion transport in d^0-metal spinel chalcogenides by examining the influence of trigonal distortion (Figure 4c) on migration path

ADVANCED SCIENCE NEWS
www.advancedsciencenews.com

ADVANCED ENERGY MATERIALS
www.advenergymat.de

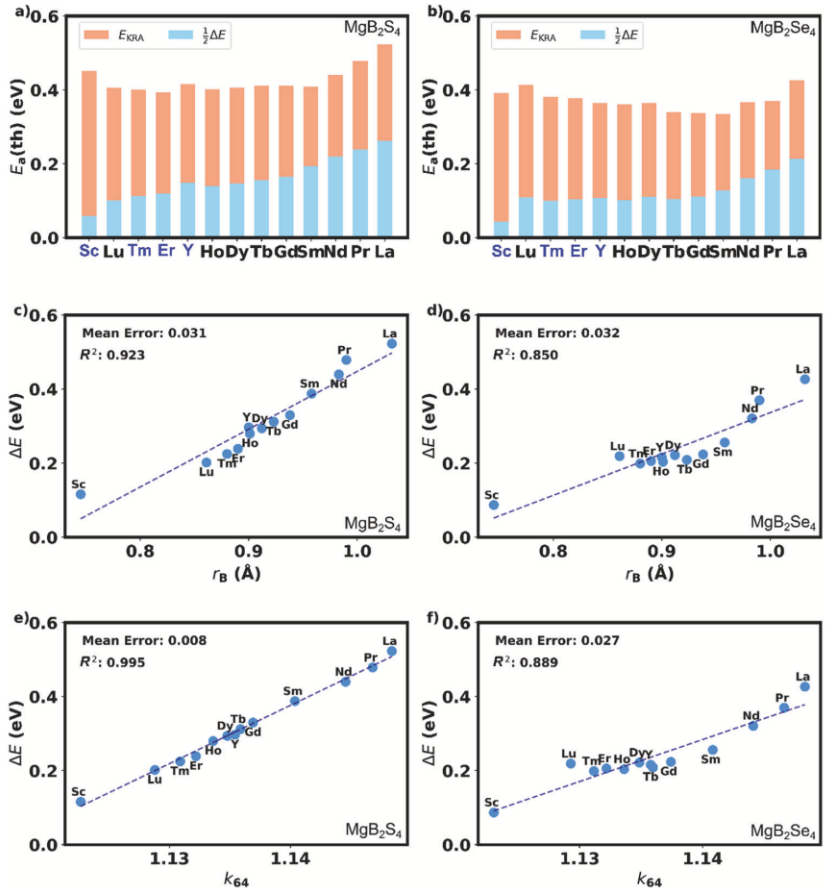

Figure 5. Migration barrier E_a(th) as the sum of half the site preference energy ΔE (blue) and the kinetically resolved barrier E_{KRA} (orange) for Mg-ion jumps in a) the MgB_2S_4 sulfide spinels and b) the MgB_2Se_4 selenide spinels. The linear regressions for ΔE as function of the ionic radius r_B of the B metal are shown with dashed lines for c) the sulfide spinels and d) the selenide spinels including the mean error and R^2 values. The linear regressions for ΔE as function of the ratio of the distance k_{64} including the mean error and R^2 values are shown for e) the sulfide spinels and f) the selenide spinels.

geometry, which corresponds to the changes in the ionic radius r_B of the metal B. Using DFT calculations combined with the NEB method, we assess migration barriers for various d^0-metal and lanthanide spinel chalcogenides (B = Sc, Y, Lu, Tm, Er, Ho, Dy, Tb, Gd, Sm, Nd, Pr, and La; X = S, Se). The calculated energy profiles along migration paths (*tet-oct-tet*) are illustrated in Figure 4d and Figure S20 (Supporting Information). We differentiate between transition state energy and site preference energy (ΔE) to determine directionally independent kinetically resolved barriers (E_{KRA}) using Equation (4) (Experimental Section), as shown in Figure 4e. While Mg-ion mobility is primarily governed by the theoretically predicted activation energy (E_a(th)), its relationship with individual contributions is complex and nonlinear. Hence, investigating the dependence of ΔE and E_{KRA} on trigonal distortion is the essence of migration barrier analysis.

The **Figure 5** provides a comprehensive analysis of the components of the migration barrier E_a(th), namely ΔE and E_{KRA}, and the correlations between ΔE and the ionic radius r_B of the transition metal B in MgB_2S_4 sulfide and MgB_2Se_4 selenide spinels. It is observed that for larger ionic radii, the site preference energy (ΔE) significantly contributes to the overall migration barrier, while for the smaller ionic radii the contribution of E_{KRA} grows and the site preference energy ΔE diminishes, as shown in Figure 5a,b. This trend is attributed to trigonal distortion resulting from the size difference between A-metal (e.g., Mg) in tetrahedral 8a sites and B-metal in octahedral 16d sites within the spinel structure. This mismatch causes a noticeable tilt in 16c and 16d octahedrons leading to an increased area in all faces of the tetrahedral site. While all faces of the tetrahedral site increase due to the distortion, only the octahedron faces shared with the tetrahedron are increasing, while others are decreasing in area. As a result, the volume of the tetrahedral 8a sites increases relative to the empty 16c sites, affecting their volume ratio as shown in Figure S21 (Supporting Information). Note that if only the

ADVANCED SCIENCE NEWS
www.advancedsciencenews.com

ADVANCED ENERGY MATERIALS
www.advenergymat.de

B-metal is varied, the trigonal distortion is simply a function of r_B, explaining the linear dependence of ΔE on the ionic radius (r_B) as shown in Figure 5c,d.

Figure 5e,f illustrates the dependence of ΔE on the ratio of the bond distances k_{64} between the central cation and the Se anions in the octahedron ($d(cn_6)$) and tetrahedron ($d(cn_4)$) that was proposed to determine the site preference energy.[13] In terms of site preference energy linearity, k_{64} outperforms significantly when compared to the ionic radii (r_B), as evidenced by its superior R^2 and mean squared error. To the best of our knowledge such a relation of the ionic radius and the anion dilation parameter u was so far not derived for sulfide and selenide spinels, so that we resort to calculated bond lengths $d(cn_6)$ and $d(cn_4)$ based on DFT calculations.

A distortion free crystal is expected for $k_{64} = 1.15$ ($u = 0.375$), a value close to that of $MgLa_2Se_4$. Additionally, the trigonal distortion of d^0-metal spinels increases as r_B decreases. Consequently, the site preference energy ΔE is most significant for $MgLa_2Se_4$ and diminishes with decreasing k_{64}, as the trigonal distortion stabilizes the octahedral site compared to the tetrahedral site. This stabilization occurs through the reduction of both bond length and volume of the octahedral relative to the tetrahedral site, thereby influencing the interplay between bond length and coordination.

The continuous stabilization of the transition state with increasing r_B is rationalized by the linear dependence of E_{KRA} on the area of the triangular faces shared by tetrahedra and octahedra shown in Figure S22 (Supporting Information). This triangular face represents the bottleneck of the migration path and the transition state is found to be stabilized with increasing area of the face. Note that – since the area of the transition state is directly affected by the trigonal distortion – also a linear correlation of E_{KRA} with the ratio of distances k_{64} is observed as shown in Figure S23 (Supporting Information).

To probe the determinants of site preference energy ΔE, we examined several parameters, including the ratio of distances (k_{64}), the ionic radii of metal B (r_B) and the anion (r_X), as well as the electronegativity of B-cation (χ_B) and the anion (χ_X). Pairwise correlations are shown in a heatmap (Figure S24, Supporting Information), that reveals significant associations. Noteworthy relationships emerged between ΔE and k_{64}, as well as between ΔE and both r_B and χ_B. Additionally, correlations are apparent between k_{64} and both r_B and χ_B. These robust linear correlations hint at potential multicollinearity among parameters, which introduces complexity in estimating individual contributions to ΔE, although it aligns with chemical principles. Before proceeding further, we prioritize the evaluation of crucial parameters associated with ΔE through a comprehensive array of feature importance techniques. These methods include fitting a Random Forest model using Recursive Feature Clustering and Gini Importance,[34] as well as employing ANOVA F-value,[35] Mutual Information,[36] Permutation Importance,[37] and LASSO.[38] Consistently across these techniques, factors such as k_{64} and r_B emerge as noteworthy contributors, as highlighted by the LASSO feature importance analysis illustrated in Figure S24 (Supporting Information). Given the pairwise correlations between parameters (Figure S24, Supporting Information) and their importance in terms of feature relevance (Figure S25, Supporting Information), we directed our attention to addressing multicollinearity to streamline parameter selection for feature engineering. To this end, we evaluated multicollinearity between k_{64} and r_B using different approaches such as variance inflation factor, tolerance values, and variance proportions with a linear regression model.[39] Indeed, strong correlation between k_{64} and r_B is found suggesting the existence of a simple relation between r_B and the anion parameter u (correlating with k_{64}).

We advocate for the exploration of alternative parameters in feature engineering to predict ΔE, given the observed high correlation between k_{64} and r_B. In Figure S26 (Supporting Information), we present an optimized parameter combination for predicting ΔE, where the pairing of k_{64} and r_X proves suffice. This choice is substantiated by their non-correlated or minimally correlated nature within the current range of d^0-metal- and lanthanide-based Mg chalcogenide spinels. Additionally, k_{64} and r_X demonstrate opposite correlations with ΔE, as depicted in Figure S24 (Supporting Information). Consequently, we adopt a simple linear regression model, described by Equation (1):

$$\Delta E = -13.7164\ \text{eV} + 13.2965\ \text{eV}\ k_{64} + \left(-0.5912\ \frac{\text{eV}}{\text{Å}} r_X\right) \quad (1)$$

This model attains an optimized R^2 score of 0.95 and a mean squared error of 0.0004. Although a quadratic polynomial model could potentially enhance the R^2 score to 0.967, we prioritize the simplicity of the linear regression model. The Supporting Information includes additional graphical representations of feature importance techniques, different regression models, and advanced algorithms.

The accuracy of the simple linear relation in Figure S27 (Supporting Information) illustrates that, indeed, the site preference energy in d^0-metal- and lanthanide-based Mg chalcogenide spinels seems to predominantly depend on the influence of the trigonal distortion on the competition between bond length and coordination and thus is independent of the lattice constants. While the trigonal distortion is mostly related to the metal B and thus the ratio of distances k_{64}, also the anion affects the inherent competition between sites as evident by the contribution of the anionic radius r_X in Figure S27 (Supporting Information). In addition, the triangular transition state is affected by the increase in trigonal distortion as illustrated in Figure 4c. Here, the trigonal distortion increases the area of the transition state and thus reduces the migration barriers. Nevertheless, the here presented data set does not allow to unambiguously attribute the influence on E_{KRA} solely on the trigonal distortion independent of the lattice constants. While the site preference energy ΔE seems to predominantly dependent on the trigonal distortion and the competition between bond length and coordination, further studies on an increased chemical space that allows to decouple the effects of cell volume and trigonal distortion are required to clarify the chemical trends underlying E_{KRA}.

2.5. Electrochemical Stability and Cycling Performance

The electrochemical stability of the UiO66-MgIL ionogel electrolyte and the sandwich-type layered UiO66-MgIL|MgB_2Se_4|UiO66-MgIL pellets against Mg metal was measured via linear sweep voltammetry (LSV). For this purpose,

ADVANCED SCIENCE NEWS
www.advancedsciencenews.com

ADVANCED ENERGY MATERIALS
www.advenergymat.de

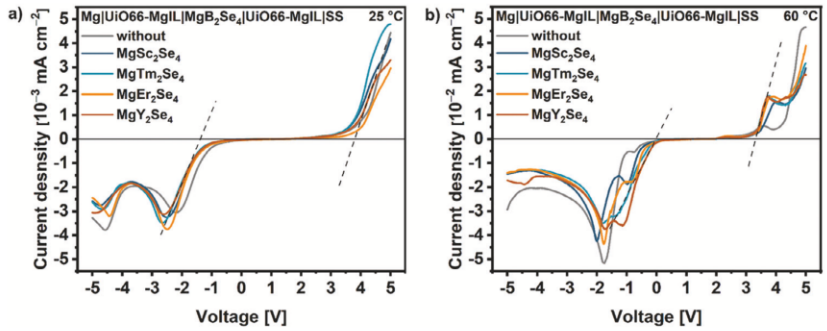

Figure 6. LSV curves of Mg|UiO66-MgIL|SS cell and Mg|UiO66-MgIL|MgB_2Se_4|UiO66-MgIL|SS two-electrode cells recorded at a scan rate of 0.1 mV s^{-1} and –0.1 mV s^{-1} at a) room-temperature and b) 60 °C with regression lines exemplarily shown for MgY_2Se_4.

asymmetric two-electrode cells were assembled using one Mg foil as both counter and reference electrode, and stainless-steel current collectors as working electrode. Note that under current load, the cell voltage does not represent the potential of the working electrode due to the overvoltage of the counter electrode. Then, starting from the open circuit voltage (OCV) the oxidation/reduction current was recorded to 5 V/−5 V (vs Mg^{2+}/Mg) with a scan rate of 0.1 mVs^{-1}/−0.1 mVs^{-1}. As shown in **Figure 6**a, at room-temperature, the oxidation current starts to grow in the range of 3.7 V to 3.9 V, while the reduction current increases significantly starting from −1.1 V to −1.3 V for all cells. Since the current profiles of the sandwich-type cells and the reference cell without spinel layer are quite identical, the UiO66-MgIL appears to limit the stability window, meaning the spinels themselves have possibly a larger range of electrochemical stability. Interestingly, all reduction current profiles show two peaks, which may be attributed to a two-step reduction of UiO66-MgIL electrolyte. A possible deposition of Mg during reduction cannot be confirmed as no Mg spots are observable on the stainless-steel electrode which is covered with adherent UiO66-MgIL (Figure S28, Supporting Information). At a temperature of 60 °C (Figure 6b), the reduction peaks merge with each other and the stability windows shrink (start oxidation: ≈3.3 V, start reduction: −0.1 V to −0.5 V), which may be correlated to a stronger decomposition of the IL or the UiO66 components, such as linkers, in the ionogel electrolyte. Apart from that, inspired by the mixed conductivity, we tested one of the spinels, $MgSc_2Se_4$, as cathode active material. However, the room-temperature galvanostatic discharge/charge voltage profiles (Figure S29, Supporting Information) recorded over ten cycles between 0.5 V and 2.7 V at 10 mA g^{-1} showed a negligibly low specific capacity. This can probably be explained by the results of the LSV at room-temperature which confirm that the spinels are not redox active between at least −1.1 V and 3.7 V and perhaps even beyond, in contrast to the report by Wang et al.[19]

In addition, we found that all MgB_2Se_4 spinels studied in this work enable reversible Mg plating and stripping at 60 °C in a symmetric Mg|UiO66-MgIL|MgB_2Se_4|UiO66-MgIL|Mg cell. As shown in **Figure 7**, the cells were initially activated by 50 cycles of alternating plating and stripping with a current density of ±1.57 µA cm^{-2} and a dwell time of 30 min per step (plated charge amount of 0.785 µAh cm^{-2}, corresponding to 2 nm of Mg per cycle assuming homogeneous plating/stripping). Afterward, the step time was increased to 10 h and further 20 cycles were recorded (15.7 µAh cm^{-2}, corresponding to 41 nm of Mg). During the cycling process stable Mg plating and stripping with a symmetrical overpotential of ≈±0.4 V was demonstrated for the cells containing the spinels with a phase purity ≥95% ($MgSc_2Se_4$, $MgTm_2Se_4$, $MgEr_2Se_4$). The performance is better and more symmetrical than for the reference cell itself (±0.5 V), possibly due to the separation of the ionogel layer in the cell by a homogenous solid-state spinel pellet. Nevertheless, note that the overpotential generally exceeds the estimated *IR* drops of 0.62 mV to 2.58 mV across the spinels, calculated from their ionic conductivities at 60 °C, indicating interface-dominating resistances inside the symmetrical cells.

Finally, to provide evidence that Mg-ion transport takes place in such sandwich-type cells, Mg plating experiments were performed in Mg|UiO66-MgIL|MgB_2Se_4|UiO66-MgIL|Cu cells using a current of –5 µA for 35 h and a temperature of 60 °C. Afterward, the surface of the Cu foil was analyzed for Mg deposits by SEM-EDS, where indeed several spots could be found. Figure S30 (Supporting Information) shows exemplarily an overview of Mg deposits with 10 µm to 30 µm in size observed for the $MgSc_2Se_4$-based cell. This Mg deposit formation confirms once again, supplementary to our first plating experiment using a Mg|MgB_2Se_4|Au cell,[15] that the here investigated Mg spinels can conduct Mg-ions.

However, although the spinels show Mg-ion conduction, reversible Mg plating/stripping cycling and an electrochemical stability till 3.7 V to be suitable in combination with the most transition metal chalcogenide cathodes,[40] their room-temperature ionic conductivity (**Figure 8**) still does not reach the order of mS cm^{-1}. In this context, it should be noted that during impedance fitting of the SS|UiO66-MgIL|MgB_2Se_4|UiO66-MgIL|SS cells, the contribution of impurities and interfacial resistances could not be extracted from the ionic resistances of the spinels. Accordingly, the actual ionic conductivity could be higher. Moreover, the spinel's potential is far from being exhausted, as some other solid electrolytes, such as Li-argyrodites, have shown that the ionic conductivity can be increased by compositional tuning.[41–45] In principle there are two main strategies: One strategy involves aliovalent substitution, which can change the concentration of the mobile ion in the compound, potentially

ADVANCED SCIENCE NEWS
www.advancedsciencenews.com

ADVANCED ENERGY MATERIALS
www.advenergymat.de

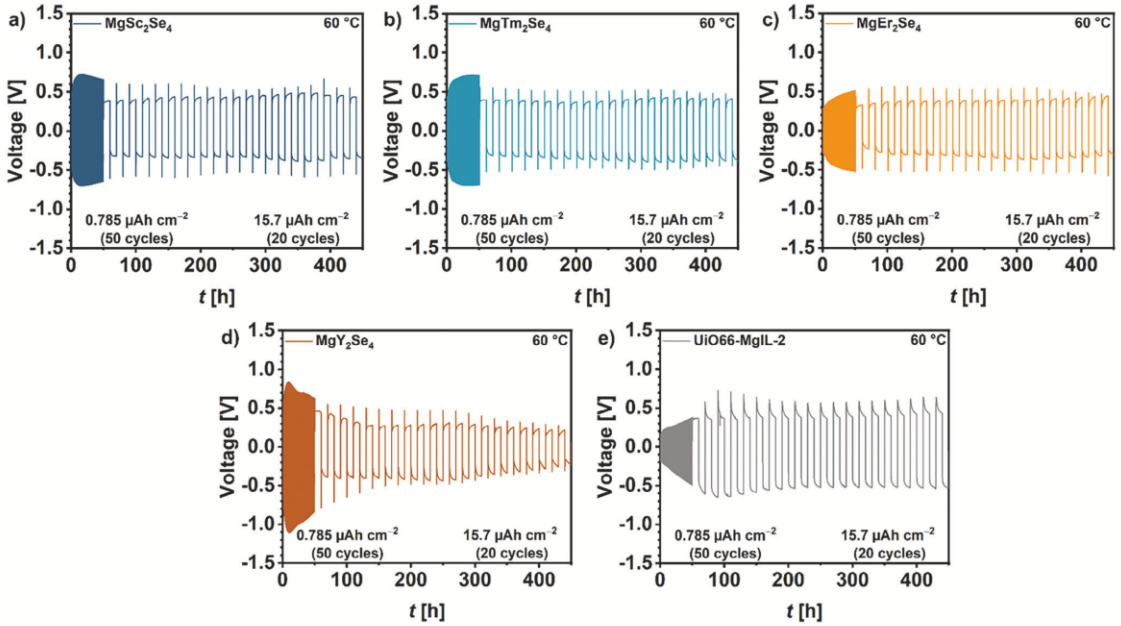

Figure 7. Long-term cycling performance during Mg plating/stripping at 60 °C for 70 cycles (50 cycles with t_{cycle} = 1 h and 20 cycles with t_{cycle} = 20 h) of Mg|UiO66-MgIL|MgB_2Se_4|UiO66-MgIL|Mg cells with a) $MgSc_2Se_4$, b) $MgTm_2Se_4$, c) $MgEr_2Se_4$, d) MgY_2Se_4, and e) without spinel pellet by applying a current density of ±1.57 µA cm^{-2}, which corresponds to a plated charge amount of 0.785 µAh cm^{-2} and 1.57 µAh cm^{-2}, respectively.

resulting in a higher ionic conductivity.[44,45] The second one is based on a high-entropy multicationic or polyanionic substitution, which increases the compositional disorder (configurational entropy) and thus the ionic conductivity.[42,43,46] Both strategies seem to be applicable for the MgB_2Se_4 spinels and should be considered in the future.

Another criterion for the application of the spinels as a SE remains their electronic conductivity. The electron transference numbers [$t_{el}(MgSc_2Se_4) = 8{\times}10^{-2}$%, $t_{el}(MgTm_2Se_4) = 5 \times 10^{-1}$%, $t_{el}(MgEr_2Se_4)$ = 6%, $t_{el}(MgY_2Se_4)$ = 19%] are more than two orders of magnitude higher than the 10^{-6}–10^{-4}% of typical SEs,[5] that increases the risk of self-discharge of a battery.[11] Here, impurities of binary compounds, such as BSe and B_2Se_3 (B = Sc, Y, Er, Tm), may play a role for the electronic transport in these materials, as we found that the electronic conductivity increases with the binary phases in the investigated spinels. Thus, there is still the potential to make the spinels applicable by minimizing the electronic conductivity due to optimization of the synthesis and the purity of precursors. Additionally, compositional tuning or the development of electron-blocking interlayers and coatings may be further options.

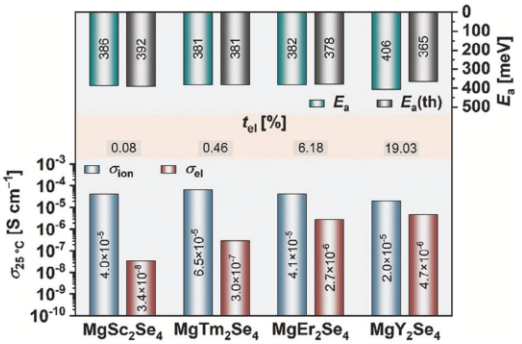

Figure 8. Overview about the room-temperature ionic conductivity σ_{ion}, the room-temperature electronic conductivity σ_{el} (from EIS), the electronic transference numbers $t_{el} = \sigma_{el}/(\sigma_{ion} + \sigma_{el})$, and the Mg^{2+} migration barrier E_a (experimental) and E_a(th) (SCAN).

3. Conclusion

In the present work, we report the successful synthesis of three MgB_2Se_4 spinels (B = Er, Tm, Y) with Fd-3m space group, showing a mixed conduction nature [$t_{el}(MgB_2Se_4) = 5 \times 10^{-1}$%–19%] like their prototype $MgSc_2Se_4$ [$t_{el}(MgSc_2Se_4) = 8 \times 10^{-2}$%]. Comparing the phase compositions obtained from Rietveld analysis with the measured electronic conductivities [$\sigma_{el}(MgSc_2Se_4) = 3.4 \times 10^{-8}$ S cm^{-1}, $\sigma_{el}(MgTm_2Se_4) = 3.0 \times 10^{-7}$ S cm^{-1}, $\sigma_{el}(MgEr_2Se_4) = 2.7 \times 10^{-6}$ S cm^{-1}, $\sigma_{el}(MgY_2Se_4) = 4.7 \times 10^{-6}$ S cm^{-1}], we suggest that impurities of binary compounds, such as BSe and B_2Se_3 (B = Sc, Y, Er, Tm), may play a role for the electronic transport in these materials. To enable an accurate determination of the ionic conductivity from impedance measurements, the electron transport was effectively blocked by introducing purely Mg-ion conducting interlayers

ADVANCED SCIENCE NEWS
www.advancedsciencenews.com

ADVANCED ENERGY MATERIALS
www.advenergymat.de

in the electrochemical cells. As a result, room-temperature ionic conductivities of $\sigma_{ion}(MgTm_2Se_4) = 6.5 \times 10^{-5}$ S cm^{-1}, $\sigma_{ion}(MgEr_2Se_4) = 4.1 \times 10^{-5}$ S cm^{-1} and $\sigma_{ion}(MgY_2Se_4) = 2.0 \times 10^{-5}$ S cm^{-1} were found, partially higher than in case of $MgSc_2Se_4$ ($\sigma_{ion} = 4.0 \times 10^{-5}$ S cm^{-1}) in our previous study.[15] In addition, our further electrochemical studies demonstrate that all four spinels are electrochemically stable between −1.1 V and 3.7 V (vs Mg^{2+}/Mg), enabling reversible Mg plating/stripping and exhibiting lower Mg-ion migration barriers [$E_a(MgSc_2Se_4) = 386 \pm 24$ meV, $E_a(MgTm_2Se_4) = 381 \pm 4$ meV, $E_a(MgEr_2Se_4) = 382 \pm 6$ meV (raw data: 373 ± 5 meV) and $E_a(MgY_2Se_4) = 406 \pm 9$ meV] than other types of Mg-ion SEs. These experimentally determined Mg-ion migration barriers are in an excellent agreement with our DFT derived migration barriers E_a(th) based on the SCAN exchange-correlation functional. Moreover, the distinct influence of the trigonal distortion on the migration path geometry, and thus, the migration barrier was demonstrated. This reveals the linear correlation of the geometric descriptor based on the ratio of the bond distances in octahedral and tetrahedral sites (k_{64}) to the kinetic (E_{KRA}) and static (ΔE) contributions of the overall migration barrier E_a(th). Our results contribute to a better understanding of the transport properties in MgB_2Se_4 spinels and show their potential as SEs once an effective way to reduce the electronic conductivity is found.

4. Experimental Section

Materials: Magnesium powder (Sigma Aldrich, ≥99%), scandium powder (chemPUR, 99.9% REO), thulium powder (abcr, 99.9% REO), erbium powder (abcr, 99.9% REO), yttrium powder (abcr, 99.9% REO), thulium chips (chemPUR, 99.9% REO), erbium chips (chemPUR, 99.9% REO), yttrium chips (abcr, 99.9% REO), selenium powder (Alfa Aesar, 99.999%), gold granules (chemPUR, 99.99%), metal-organic framework ($Zr_6O_4(OH)_4(BDC)_6$, BDC = 1,4-dicarboxylate, denoted as UiO66 and prepared as),[47] magnesium bis(trifluoromethanesulfonyl)imide ($Mg(TFSI)_2$, TCI, >97%), 1-ethyl-3-methylimidazolium bis(trifluoromethanesulfonyl)imide ([EMIM][TFSI], TCI, >98%), Mg foil (chemPUR 99.98%), super P (MSE Supplies), polyvinylidene fluoride binder (HSV900 PVDF binder, ≥99.5%), glass fiber separator (GF/D, Whatman), magnesium tetrakis(hexafluoroisopropyloxy)borate ($Mg[B(hfip)_4]_2$, prepared as),[48] 1,2-dimethoxyethane (Sigma Aldrich, 99.5%), magnesium foil (Sigma Aldrich, 100 µm, 99.9%), copper foil (MSE, 9 µm, ≥99.9%).

Synthesis of MgB_2Se_4 Spinels: In the one-step synthesis, magnesium powder, scandium/thulium/erbium/yttrium powder and selenium powder were hand-milled in a molar ratio of 1:2:4 for 15 min. Then, 0.5 g of each powder mixture was pressed into a pellet (Ø = 10 mm) under a pressure of 300 MPa for 30 min. After pressing, each pellet was wrapped into a platinum foil and vacuum sealed in a separate quartz glass ampule, prior backed out at 800 °C under dynamic vacuum to remove moisture. To perform the solid-state reaction, the ampules were heated at 950 °C for 20 h (180 °C h^{-1} heating rate) in a furnace (Nabertherm with controller P 300). When the samples reached room-temperature again, the pellets were collected by breaking the ampules and afterward ground to powders.

In the two-step synthesis, first the binary selenides were prepared. MgSe and Sc_2Se_3 were synthesized from stoichiometric amounts of the elemental powders according to the previous one-step synthesis at 750 °C for 24 h (180 °C h^{-1} heating rate) and 800 °C for 30 h (60 °C h^{-1} heating rate), respectively. Instead, the Tm_2Se_3, Er_2Se_3 and Y_2Se_3 syntheses were carried out with stoichiometric amounts of selenium powder and thulium, erbium or yttrium metal chips, respectively, which were less prone against oxidation than powders. The selenium powder was placed on the bottom of a graphite crucible and then covered with the metal chips. After sealing the crucible in an evacuated quartz glass ampule, heating at 800 °C for 48 h (60 °C h^{-1} heating rate) was performed. In the second synthesis step, MgSe was mixed and pelletized in a 1:1 ratio with either Sc_2Se_3, Tm_2Se_3, Er_2Se_3 or Y_2Se_3 to obtain the corresponding MgB_2Se_4 spinel by thermal conversion. For the $MgSc_2Se_4$ synthesis the same conditions as described in the one-step synthesis were applied, while a longer heating time of 30 h was used for the other spinels. All preparations and sample treatments were performed under argon atmosphere or in vacuum.

X-Ray Diffraction (XRD): The powder XRD) patterns of the binary and ternary selenides were collected by the means of an Empyrean powder diffractometer (Malvern PANalytical Ltd) with Cu K_α radiation. To avoid contact with air and humidity, the samples placed on top of silicon zero background holders were sealed with Kapton polyimide film inside a glove box. Data were recorded in the 2θ range from 10° to 90° with a step size of 0.026° and a counting time per step of 200 s. References were taken from ICSD Inorganic Crystal Structure Database: MgSe (ICSD 53 946), Sc_2Se_3 (ICSD 651 804), $MgSc_2Se_4$ (ICSD 642 814), Tm_2Se_3 (ICSD 652 078), $MgTm_2Se_4$ (ICSD 76 051), Er_2Se_3 (ICSD 79 227), Er_2O_2Se (ICSD 25 810), $MgEr_2Se_4$ (ICSD 630 754), Y_2Se_3 (ICSD 652 183), YSe (ICSD 183 015), and MgY_2Se_4 (ICSD 76 052). Reference data retrieved from the Materials Project from database version *v2022.10.28*:[49] Tm_2O_2Se, (mp-753920) and Y_2O_2Se (mp-752658).

Rietveld Analysis: Rietveld refinements based on the powder XRD patterns were performed using the software FullProf Suite version January 2021. Start models for the Rietveld refinement were taken from references listed in Experimental Section under X-ray diffraction.

Scanning Electron Microscopy (SEM) and Energy-Dispersive X-Ray Spectroscopy (EDS): SEM images and EDS maps of the samples were obtained with a Gemini SEM 560 high-resolution scanning electron microscope (Carl Zeiss AG, Germany) at an acceleration voltage of 10 kV (pellet cross section, Cu and SS electrode) or 15 kV (SE powders). A working distance between 8 mm and 9 mm and an aperture size of 60 µm and 120 µm were chosen. All images were collected with the in-lens detector and the mapping was carried out by using an X-Max50 detector (Oxford Instruments, UK). To avoid air contamination, the samples were transferred from the glove box with a Leica EM VCT500 (Leica Microsystems Germany) shuttle.

Transmission Electron Microscopy (TEM): TEM images and EDS maps were taken by Themis 300 (Thermo Fisher Scientific) using an accelerating voltage of 300 kV. The spinel powders were dispersed on the Mo TEM grid for TEM observation. SAED patterns were collected to identify the crystal structure of the synthesized materials.

Nuclear Magnetic Resonance (NMR) Spectroscopy: ^{25}Mg MAS NMR spectroscopy was performed at a magnetic field of 11.7 T corresponding to a resonance frequency of 30.6 MHz. The measurements were carried out in 1.3 mm rotors at a spinning speed of 22 kHz with a rotor-synchronized Hahn-echo pulse sequence and a $\pi/2$ pulse duration of 3.7 µs. The recycle delay was 15 s for $MgSc_2Se_4$/MgY_2Se_4 and 1 s for $MgEr_2Se_4$/$MgTm_2Se_4$. The spectra were referenced to an aqueous solution of 5 M $MgCl_2$.

Cell Assembly and Electrochemical Measurements: The electrochemical measurements were performed with a VMP300 electrochemical workstation from Bio-Logic Science Instruments SAS and recorded with the corresponding software EC-Lab, unless specified otherwise. RelaxIS 3 software (RHD Instruments, Darmstadt, Germany) was used for fitting of the experimental EIS data.

The electronic conductivity of the MgB_2Se_4 powders was measured using pouch cells. Pellets of 6 mm to 10 mm diameter were pressed from 150 mg to 300 mg MgB_2Se_4 powder under isostatic pressure of 3000 bar for 30 min. Afterward, each pellet was separately sealed in a quartz glass ampule and sintered at 950 °C for 6 h (180 °C h^{-1} heating rate). Then, the sintered pellets were polished down to grit 4000 using SiC sandpaper. Au electrodes (Ø = 5.5–9 mm) with a thickness of 300 nm were vapor-deposited on both sides of the pellet by the mean of a sputter coater (tectra GmbH, Germany). The Au deposition rate was set to 0.15–0.2 nm s^{-1} at a pressure <10^{-6} mbar. After a second sintering step at 500 °C for 6 h, the pellets were sealed under argon into pouch cells, connected with the Au electrodes to Ni current collectors. EIS and CA measurements of the symmetrical Au|MgB_2Se_4|Au cells were performed in climate chambers

ADVANCED SCIENCE NEWS
www.advancedsciencenews.com

ADVANCED ENERGY MATERIALS
www.advenergymat.de

(Weisstechnik, Germany) at 25 °C. The impedance data were collected from 7 MHz to 100 mHz with an alternating current (AC) amplitude of 10 mV. The dc polarization was carried out in six steps from 0.1 V to 2.0 V with 12 h resting time per step. From the obtained resistances R, the electronic conductivities σ_{el} were calculated based on the following equation:

$$\sigma = \frac{d}{A}\frac{1}{R} = \frac{K}{R} \tag{2}$$

d and A represent the thickness and the contact area of the electrolyte pellet, respectively, and are summarized in the cell constant K.

To measure the ionic conductivity, a home-made battery cell casing was used, as introduced in an earlier work.[50] Different amounts (160 mg, 220 mg and 280 mg) of MgB_2Se_4 powder were filled in the PEEK housing of the cell with a diameter of 10 mm. Then, the powders were pressed between two stainless-steel stamps (SS) at 3 t for 3 min to create a pellet inside the housing. Two purely Mg-ion conducting interlayer were added by pressing 40 mg of an ionogel SE, denoted as UiO66-MgIL, on both sides of the MgB_2Se_4 pellet under previous conditions. The ionogel SE consisted out of a Mg-ion conducting metal-organic framework (MOF) structure UiO-66 impregnated in a mass ratio of 1:1.25 with a 1 M $Mg(TFSI)_2$ ionic liquid based on [EMIM][TFSI], as described in an earlier report.[15] A constant pressure was applied by the means of the screw of aluminum framework around the homemade cell casing with 10 Nm torque. The impedance spectra of the SS|UiO66-MgIL|MgB_2Se_4|UiO66-MgIL|SS cells were recorded between 0 °C and 60 °C in a frequency range from 3 MHz to 100 mHz with an AC amplitude of 10 mV. After evaluation of the ionic resistances of the MgB_2Se_4 spinels, the ionic conductivities were calculated according to Equation (2). Then, the Mg-ion migration barriers (E_a) were obtained by rearrangement of the Arrhenius equation (Equation (3)):

$$\sigma_{ion} = \frac{\sigma_0}{T}\exp\left(-\frac{E_a}{k_B T}\right) \tag{3}$$

with σ_0 representing the conductivity prefactor.

The LSV measurements were performed with Mg|UiO66-MgIL|MgB_2Se_4|UiO66-MgIL|SS cells, which were initially assembled analogous to the cells used to determine the ionic conductivity using 220 mg MgB_2Se_4 powder (or 0 mg for reference cell) and 40 mg UiO66-MgIL per layer. Then, a polished Mg foil (Ø = 9 mm) was placed between one UiO66-MgIL layer and the SS stamp. After pressing the cell at 3 t for 1 min, LSV from open circuit voltage (OCV) to 5 V or –5 V, respectively, was carried out with a scan rate of 0.1 mV s^{-1}/–0.1 mV s^{-1} at 25 °C and 60 °C.

For the Mg plating/stripping measurements, symmetrical Mg|UiO66-MgIL|MgB_2Se_4|UiO66-MgIL|Mg cells with two Mg electrodes were prepared according to the previous procedure. Then, CP was performed over 70 cycles (50 cycles with t_{cycle} = 1 h and 20 cycles with t_{cycle} = 20 h) at 60 °C by applying a current density of 1.57 µA cm^{-2}. In case of the Mg plating experiments, Mg|UiO66-MgIL|MgB_2Se_4|UiO66-MgIL|Cu cells were assembled by using a Mg foil and a Cu foil electrode. After that CP measurements with a current of –5 µA for 35 h were carried out at 60 °C, whereby 79 µg Mg should be theoretically deposited on the Cu electrode.

To investigate $MgSc_2Se_4$ as a cathode active material, two-electrode Swagelok cells were assembled. The cathode electrode was prepared by casting 70 wt% $MgSc_2Se_4$, 20 wt% super P, and 10 wt% PVDF binder onto an Al foil, resulting in a loading mass of 1 mg cm^{-2} to 1.5 mg cm^{-2} active material. The anode, consisting of a polished Mg foil (Ø = 9 mm), was separated from the cathode by a glass fiber separator and 100 µL of a $Mg[B(hfip)_4]_2$ liquid electrolyte (0.4 M in 1,2-dimethoxyethane) was used. Galvanostatic discharge/charge voltage profiles were recorded with a Maccor Series 4000 (Maccor, USA) at room-temperature over ten cycles between 0.5 V and 2.7 V (vs Mg^{2+}/Mg) at a current density of 10 mA g^{-1}.

Computational Details: The influence of the trigonal distortion on the Mg^{2+} migration barriers was studied by periodic first-principles calculations based on DFT.[51] The projector augmented-wave method (PAW)[52] and the SCAN[53] exchange and correlation functional was used as implemented in Vienna Ab initio Simulation Package (VASP).[54] The conventional unit cell containing eight formula units with 56 atoms was chosen assuring a minimal distance of 10 Å between mobile defects. The supercell was relaxed without any restrictions until all forces on the atoms converged below 0.01 eV $Å^{-1}$. The cutoff energy was set to 520 eV and a 2 × 2 × 2 k-point mesh was used in conjunction with a convergence criterion for the total energies of 1×10^{-5} eV per supercell. The Mg-ion migration barriers were determined by the climbing image nudged elastic band (CI-NEB) method[55] using four distinct images between the initial tetrahedral and intermediate octahedral site, and the complete energy profile was obtained by mirroring at the intermediate of the migration event. The force convergence criterion for the NEB calculations was set to 0.05 eV $Å^{-1}$. All migration barriers were determined in the low-vacancy limit and upon fixing the volume to the one of the pristine structures.

In addition, possible influence of the structural distortions due to the presence of the vacancy and due to the charge compensation were checked for all experimentally synthesized compounds and are shown in Table S12 (Supporting Information).

To obtain further insight into the chemical trends for the migration barrier E_a(th), it was beneficial to separate contributions from the transition state energy E_{TS} and the site preference energy ΔE to the overall barrier E_a(th). This could be achieved by constructing directionally independent kinetically resolved activation barriers E_{KRA} (Equation (4)):

$$E_{KRA} = E_{TS} - \frac{1}{2}(E_{oct} - E_{tet}) \tag{4}$$

Note that this construction was only valid if the transition state was at 50% migration path length and breaks down if the intermediate octahedral site was the transition state of the Mg-ion migration.

Supporting Information

Supporting Information is available from the Wiley Online Library or from the author.

Acknowledgements

This work contributes to the research performed at CELEST (Center for Electrochemical Energy Storage Ulm-Karlsruhe) and was funded by the German Research Foundation (DFG) under Project ID 390874152 (POLiS Cluster of Excellence). The authors would like to thank Zhirong Zhao-Karger (KIT/Helmholtz Institute Ulm) for providing the $Mg[B(hfip)_4]_2$ salt, Yushu Tang (KIT) for the TEM measurements and Anika Siebert (JLU) for helping with the plating experiment.

Conflict of Interest

The authors declare no conflict of interest.

Data Availability Statement

The data that support the findings of this study are openly available in Zenodo at https://doi.org/10.5281/zenodo.12732117, reference number 12732117. All electronic structure calculations used in this work are made available under the Creative Commons Attribution license (CC BY 4.0) on the NOMAD repository (https://nomad-lab.eu) under the following link: https://doi.org/10.17172/NOMAD/2021.11.18-1.

Keywords

density functional theory, magnesium batteries, magnesium chalcogenide spinels, magnesium electrolytes, solid electrolytes

ADVANCED SCIENCE NEWS
www.advancedsciencenews.com

ADVANCED ENERGY MATERIALS
www.advenergymat.de

Received: May 26, 2024
Revised: August 5, 2024
Published online: August 20, 2024

[1] Y. Zhan, W. Zhang, B. Lei, H. Liu, W. Li, *Front. Chem.* **2020**, *8*, 125.
[2] Z. W. B. Iton, K. A. See, *Chem. Mater.* **2022**, *34*, 881.
[3] a) M. Guo, C. Yuan, T. Zhang, X. Yu, *Small* **2022**, *18*, 2106981; b) Y. Liang, H. Dong, D. Aurbach, Y. Yao, *Nat. Energy* **2020**, *5*, 646.
[4] P. W. Jaschin, Y. Gao, Y. Li, S.-H. Bo, *J. Mater. Chem. A* **2020**, *8*, 2875.
[5] Y. Gao, T. P. Mishra, S.-H. Bo, G. Sai Gautam, P. Canepa, *Annu. Rev. Mater. Res.* **2022**, *52*, 129.
[6] J. Janek, W. G. Zeier, *Nat. Energy* **2023**, *8*, 230.
[7] M. Dillenz, M. Sotoudeh, H. Euchner, A. Groß, *Front. Energy Res.* **2020**, *8*, 584654.
[8] a) Z. Rong, R. Malik, P. Canepa, G. Sai Gautam, M. Liu, A. Jain, K. Persson, G. Ceder, *Chem. Mater.* **2015**, *27*, 6016; b) M. Liu, Z. Rong, R. Malik, P. Canepa, A. Jain, G. Ceder, K. A. Persson, *Energy Environ. Sci.* **2015**, *8*, 964.
[9] P. Canepa, S.-H. Bo, G. Sai Gautam, B. Key, W. D. Richards, T. Shi, Y. Tian, Y. Wang, J. Li, G. Ceder, *Nat. Commun.* **2017**, *8*, 1759.
[10] a) M. G. Evans, M. Polanyi, *Trans. Faraday Soc.* **1938**, *34*, 11; b) J. N. Bronsted, *Chem. Rev.* **1928**, *5*, 231.
[11] M. Dillenz, M. Sotoudeh, C. Glaser, J. Janek, A. Groß, H. Euchner, *Batteries Supercaps* **2022**, *5*, 202200164.
[12] a) M. Sotoudeh, A. Groß, *JACS Au* **2022**, *2*, 463; b) M. Sotoudeh, A. Groß, *J. Phys. Chem. Lett.* **2022**, *13*, 10092.
[13] M. Sotoudeh, M. Dillenz, A. Groß, *Adv. Energy and Sustainable Res.* **2021**, *2*, 2100113.
[14] a) J. Jamnik, J. Maier, *J. Electrochem. Soc.* **1999**, *146*, 4183; b) J. Jamnik, J. Maier, *Phys. Chem. Chem. Phys.* **2001**, *3*, 1668.
[15] C. Glaser, Z. Wei, S. Indris, P. Klement, S. Chatterjee, H. Ehrenberg, Z. Zhao-Karger, M. Rohnke, J. Janek, *Adv. Energy Mater.* **2023**, *13*, 2301980.
[16] R. A. Huggins, *Ionics* **2002**, *8*, 300.
[17] J. Zahnow, T. Bernges, A. Wagner, N. Bohn, J. R. Binder, W. G. Zeier, M. T. Elm, J. Janek, *ACS Appl. Energy Mater.* **2021**, *4*, 1335.
[18] S. Burkhardt, M. S. Friedrich, J. K. Eckhardt, A. C. Wagner, N. Bohn, J. R. Binder, L. Chen, M. T. Elm, J. Janek, P. J. Klar, *ACS Energy Lett.* **2019**, *4*, 2117.
[19] L.-P. Wang, Z. Zhao-Karger, F. Klein, J. Chable, T. Braun, A. R. Schür, C.-R. Wang, Y.-G. Guo, M. Fichtner, *ChemSusChem* **2019**, *12*, 2286.
[20] P. Canepa, G. Sai Gautam, D. Broberg, S.-H. Bo, G. Ceder, *Chem. Mater.* **2017**, *29*, 9657.
[21] S. Kundu, N. Solomatin, Y. Kauffmann, A. Kraytsberg, Y. Ein-Eli, *Appl. Mater. Today* **2021**, *23*, 100998.
[22] S. Kundu, N. Solomatin, A. Kraytsberg, Y. Ein-Eli, *Energy Technol.* **2022**, *10*, 2200896.
[23] J. Koettgen, C. J. Bartel, G. Ceder, *Chem. Commun.* **2020**, *56*, 1952.
[24] D. Reig-i-Plessis, A. Cote, S. van Geldern, R. D. Mayrhofer, A. A. Aczel, G. J. MacDougall, *Phys. Rev. Mater.* **2019**, *3*, 114408.
[25] a) D. Reig-i-Plessis, S. V. Geldern, A. A. Aczel, D. Kochkov, B. K. Clark, G. J. MacDougall, *Phys. Rev. B* **2019**, *99*, 134438; b) J. Flahaut, M. Guittard, M. Patrie, M. P. Pardo, S. M. Golabi, L. Domange, *Acta Crystallogr.* **1965**, *19*, 14; c) M. Guittard, C. Souleau, H. Farsam, *C. R. Hebd. Acad. Sci.* **1964**, *259*, 2847.
[26] P. Raghavan, *At. Data Nucl. Data Tables* **1989**, *42*, 189.
[27] W. Tahir, G. M. Mustafa, N. A. Noor, S. M. Alay-e-Abbas, Q. Mahmood, A. Laref, *Ceram. Int.* **2020**, *46*, 26637.
[28] M. Zanib, N. A. Noor, M. A. Iqbal, I. Mahmood, A. Mahmood, S. M. Ramay, N. Y. Al-Garadi, T. Uzzaman, *Curr. Appl. Phys.* **2020**, *20*, 1097.
[29] D. J. Chadi, *Phys. Rev. Lett.* **1994**, *72*, 534.
[30] H. Bergmann, H. Hein, P. Kuhn, U. Vetter, G. Czack, E. Koch, E. Warkentin, *Sc, Y, La-Lu Rare Earth Elements C 9*, Springer Berlin Heidelberg, Berlin Heidelberg **1985**.
[31] a) B. Fisher, K. Chashka, L. Patlagan, G. Reisner, *Phys. Rev. B* **2004**, *70*, 205109; b) C. M. Hurd, *J. Phys. C: Solid State Phys.* **1985**, *18*, 6487; c) I. Balberg, *J. Appl. Phys.* **2011**, *110*, 61301.
[32] J. Maier, *Z. Phys. Chem.* **1984**, *140*, 191.
[33] M. Sotoudeh, S. Baumgart, M. Dillenz, J. Döhn, K. Forster-Tonigold, K. Helmbrecht, D. Stottmeister, A. Groß, *Adv. Energy Mater.* **2024**, *14*, 2302550.
[34] a) L. Breiman, *Mach. Learn.* **2001**, *45*, 5; b) P. Geurts, D. Ernst, L. Wehenkel, *Mach. Learn.* **2006**, *63*, 3.
[35] I. Guyon, A. Elisseef, *J. Mach. Learn. Res.* **2003**, *3*, 1157.
[36] B. C. Ross, *PLoS One* **2014**, *9*, 87357.
[37] A. Fisher, C. Rudin, F. Dominici, *J. Mach. Learn. Res.* **2019**, *20*, 1.
[38] R. Tibshirani, *J. R. Stat. Soc. Ser. B Stat. Method.* **1996**, *58*, 267.
[39] D. A. Belsley, E. Kuh, R. E. Welsch, *Regression Diagnostics. Identifying Influential Data and Sources of Collinearity*, John Wiley & Sons Inc, Hoboken, New Jersey, **1980**.
[40] C. Pei, F. Xiong, Y. Yin, Z. Liu, H. Tang, R. Sun, Q. An, L. Mai, *Small* **2021**, *17*, 2004108.
[41] X. Bai, Y. Duan, W. Zhuang, R. Yang, J. Wang, *J. Mater. Chem. A* **2020**, *8*, 25663.
[42] J. Lin, G. Cherkashinin, M. Schäfer, G. Melinte, S. Indris, A. Kondrakov, J. Janek, T. Brezesinski, F. Strauss, *ACS Mater. Lett.* **2022**, *4*, 2187.
[43] F. Strauss, J. Lin, M. Duffiet, K. Wang, T. Zinkevich, A.-L. Hansen, S. Indris, T. Brezesinski, *ACS Mater. Lett.* **2022**, *4*, 418.
[44] P. Adeli, J. D. Bazak, A. Huq, G. R. Goward, L. F. Nazar, *Chem. Mater.* **2021**, *33*, 146.
[45] L. Zhou, N. Minafra, W. G. Zeier, L. F. Nazar, *Acc. Chem. Res.* **2021**, *54*, 2717.
[46] Y. Zeng, B. Ouyang, J. Liu, Y.-W. Byeon, Z. Cai, L. J. Miara, Y. Wang, G. Ceder, *Science* **2022**, *378*, 1320.
[47] Z. Wei, R. Maile, L. M. Riegger, M. Rohnke, K. Müller-Buschbaum, J. Janek, *Batteries Supercaps* **2022**, *5*, 202200318.
[48] Z. Zhao-Karger, R. Liu, W. Dai, Z. Li, T. Diemant, B. P. Vinayan, C. Bonatto Minella, X. Yu, A. Manthiram, R. J. Behm, M. Ruben, M. Fichtner, *ACS Energy Lett.* **2018**, *3*, 2005.
[49] A. Jain, S. P. Ong, G. Hautier, W. Chen, W. D. Richards, S. Dacek, S. Cholia, D. Gunter, D. Skinner, G. Ceder, K. A Persson, *APL Mater.* **2013**, *1*, 11002.
[50] W. Zhang, D. A. Weber, H. Weigand, T. Arlt, I. Manke, D. Schröder, R. Koerver, T. Leichtweiss, P. Hartmann, W. G. Zeier, J. Janek, *ACS Appl. Mater. Interfaces* **2017**, *9*, 17835.
[51] a) P. Hohenberg, W. Kohn, *Phys. Rev.* **1964**, *136*, B864; b) W. Kohn, L. J. Sham, *Phys. Rev.* **1965**, *140*, A1133.
[52] P. E. Blöchl, *Phys. Rev. B* **1994**, *50*, 17953.
[53] J. Sun, A. Ruzsinszky, J. P. Perdew, *Phys. Rev. Lett.* **2015**, *115*, 36402.
[54] a) G. Kresse, J. Furthmüller, *Phys. Rev. B* **1996**, *54*, 11169; b) G. Kresse, J. Hafner, *Phys. Rev. B* **1993**, *47*, 558; c) G. Kresse, D. Joubert, *Phys. Rev. B* **1999**, *59*, 1758.
[55] D. Sheppard, R. Terrell, G. Henkelman, *J. Chem. Phys.* **2008**, *128*, 134106.

3.3 Publication 3: "High Room-Temperature Magnesium Ion Conductivity in Spinel-Type $MgYb_2Se_4$ Solid Electrolyte"

The third publication of this dissertation aims to expand the family of the electrochemically investigated MgB_2Se_4 (B = Sc, Y, Er, Tm) spinels of the first two publications by $MgYb_2Se_4$ and the multicationic/multianionic compounds $MgSc_{0.4}Y_{0.4}Er_{0.4}Tm_{0.4}Yb_{0.4}Se_4$ and $Mg_{0.75}Sc_2Se_{3.5}Br_{0.5}$, whose transport properties have not yet been predicted in any computational study. For this reason, the three novel spinels were successfully prepared via solid-state synthesis and analyzed analogous to their mixed-conducting pioneers.

By performing EIS measurements of the new spinels, it was found that the conducted multielement substitution in the MgB_2Se_4 system does not lead to an improvement in the ionic transport properties. Instead, with respect to $MgYb_2Se_4$, the highest room-temperature ionic conductivity ($\sigma_{ion} > 10^{-4}$ S cm^{-1}) and the lowest Mg^{2+} migration barrier ($E_a = 364$ meV) were observed among all experimentally studied spinels. Since, according to the guidelines derived in publication 2, this was not expected for $MgYb_2Se_4$ with a comparatively small B^{3+}-ion radius (r_B: $Yb^{3+} < Tm^{3+} < Er^{3+} < Y^{3+}$), further DFT calculations were initiated on the MgB_2Se_4 system. In this context, an exceptional low magnesium insertion energy was revealed for $MgYb_2Se_4$, suggesting weak binding interactions between the Mg-ions and the host lattice, thus leading to the facilitated Mg^{2+} transport in the spinel. This property, combined with its rather low electronic conductivity ($\sigma_{el} < 10^{-9}$ S cm^{-1}) and good oxidative stability (3.9 V vs. Mg^{2+}/Mg) observed by DC polarization and linear sweep voltammetry (LSV) measurements, makes $MgYb_2Se_4$ a highly attractive material for Mg^{2+} SE applications.

Finally, this third publication not only extends the guidelines for finding good spinel-type Mg-ion conductors by including the magnesium insertion energy but also presents with $MgYb_2Se_4$ one of the best candidates as Mg-ion SE to date.

The experiments were designed and planned by the first author and assisted by Dr. Z. Wei. J. S. Bark synthesized the multicationic and the $MgYb_2Se_4$ spinel with the assistance of C. Glaser, who prepared the multianionic spinels supported by Dr. S. Singh. The first author performed all electrochemical experiments, the SEM, EDS and X-ray diffraction measurements, and the Rietveld refinement. Dr. S. Indris conducted and interpreted the NMR measurement. FAAS and TXRF were performed by R. Müller. The DFT calculations were carried out and described in the manuscript by PD Dr. M. Sotoudeh, Dr. M. Dillenz and Dr. K. Sarkar. The manuscript was written by C. Glaser and revised by twelve co-authors. The work was supervised by Prof. K. Leopold, Prof. L. F. Nazar, Prof. A. Groß, and Prof. J. Janek.

This study was part of the research within POLiS – Post Lithium Storage Cluster of Excellence.

CHEMISTRY OF MATERIALS

pubs.acs.org/cm

Article

High Room-Temperature Magnesium Ion Conductivity in Spinel-Type $MgYb_2Se_4$ Solid Electrolyte

Clarissa Glaser, Mohsen Sotoudeh, Manuel Dillenz, Kanchan Sarkar, Jasmin S. Bark, Shashwat Singh, Zhixuan Wei, Sylvio Indris, Riccarda Müller, Kerstin Leopold, Linda F. Nazar, Axel Groß, and Jürgen Janek*

Cite This: *Chem. Mater.* 2025, 37, 3353−3362

Read Online

ACCESS | Metrics & More | Article Recommendations | Supporting Information

ABSTRACT: We present three magnesium selenide spinels, $MgSc_{0.4}Y_{0.4}Er_{0.4}Tm_{0.4}Yb_{0.4}Se_4$, $Mg_{0.75}Sc_2Se_{3.5}Br_{0.5}$ and $MgYb_2Se_4$, as potential solid electrolytes (SE) for magnesium batteries. In particular, the latter spinel exhibits a room-temperature ionic conductivity exceeding 10^{-4} S cm^{-1} and a low Mg^{2+} migration barrier of 364 meV. The high ionic mobility is attributed to the low magnesium insertion energy revealed by density functional theory (DFT), which indicates a weak binding interaction between magnesium ions and the host lattice. Furthermore, like the two multicomponent spinels, $MgYb_2Se_4$ exhibits lower electronic conductivity compared to previously studied MgB_2Se_4 spinels (B = Sc, Y, Er, Tm) and a good electrochemical stability, making it a strong candidate for Mg^{2+} SE applications.

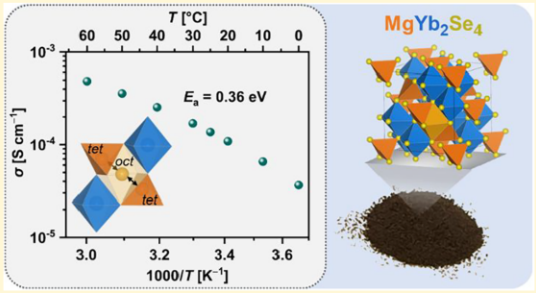

1. INTRODUCTION

Rechargeable magnesium batteries (RMBs) are considered as promising candidates for next-generation energy-storage solutions since they are expected to be more sustainable than today's widely used lithium-ion batteries. This is based on the high abundance of magnesium in the earth's crust (10^4 times more often than lithium) and its twice to five-times higher volumetric capacity of 3833 mAh cm^{-3} compared to Li metal (2066 mAh cm^{-3}) and LiC_6 (760 mAh cm^{-3}) negative electrodes, respectively, caused by the higher charge density of the Mg-ion.[1] In addition, magnesium has a low standard reduction potential (−2.37 V vs SHE) − and in contrast to Li − a low tendency for dendrite formation during plating.[1,2]

However, the development of room-temperature SEs for solid-state Mg batteries is challenging, as Mg^{2+} ions have a sluggish mobility in the solid state due to their high charge density.[3] Thus, most of the reported Mg SEs, such as oxides (NASICON-type $Mg_{0.5}Zr_2(PO_4)_3$ and modifications),[4−7] sulfides (MgS-P_2S_5−MgI_2 solid solutions)[8] and halides ($MgAl_2Cl_{8-y}Br_y$),[9] do not reach conductivities higher than 3 × 10^{-5} S cm^{-1} at ambient conditions.[10,11] The only reported Mg^{2+} SEs that have achieved a room-temperature Mg-ion conductivity σ_{ion} > 10^{-4} S cm^{-1} are the magnesium borohydride derivatives β-$Mg(BH_4)\cdot CH_3NH_2$ (σ_{ion} = 1.5 × 10^{-4} S cm^{-1}) and $Mg(BH_4)\cdot 1.5NH_3$-60 wt %TiO_2 (σ_{ion} = 3.0 × 10^{-4} S cm^{-1}).[12,13] Nevertheless, these compounds show a relatively low electrochemical stability (≤1.3 V vs Mg^{2+}/Mg), making it challenging for the pairing with suitable cathodes.

Instead, the recently studied MgB_2Se_4 (B = Sc, Y, Er, Tm) spinels show oxidation stabilities >3.7 V − sufficient for most transition metal chalcogenide cathodes − and roughly comparable ionic conductivities (σ_{ion} = 2 to 7 × 10^{-5} S cm^{-1} at 25 °C).[14] This class of SEs benefits from the spinel-type structure, which provides three-dimensional (3D) conduction pathways and a relatively large distance between the migrating Mg^{2+} in its transition state and the neighboring B-cations.[15] Along with this, the increased polarizability of the Se anions compared to their oxygen and sulfur counterparts weakens the bonding interactions with the Mg-ions, resulting in higher conductivities and lower Mg^{2+} migration barriers E_a.[16,17] The E_a values are predicted to be between 290 and 375 meV for several d^0-metal- and lanthanide-based MgB_2Se_4 (B = Sc, Lu, Tm, Er, Y, Ho, Dy, Tb, Sm, Pm, Nd, Pr, La) spinels calculated by density functional theory (DFT).[18,19] However, both computational and synthesis results suggest that only compounds with an ionic radius r_B of the B metal between those of Sc and Ho (r_{Sc-Ho} = 0.861−0.901 Å) favor the spinel structure in the ground state and possess sufficient stability.[18,20−22] Interestingly, the compound $MgYb_2Se_4$ (r_{Yb}

Received: January 17, 2025
Revised: April 24, 2025
Accepted: April 24, 2025
Published: May 3, 2025

https://doi.org/10.1021/acs.chemmater.5c00131
Chem. Mater. 2025, 37, 3353−3362

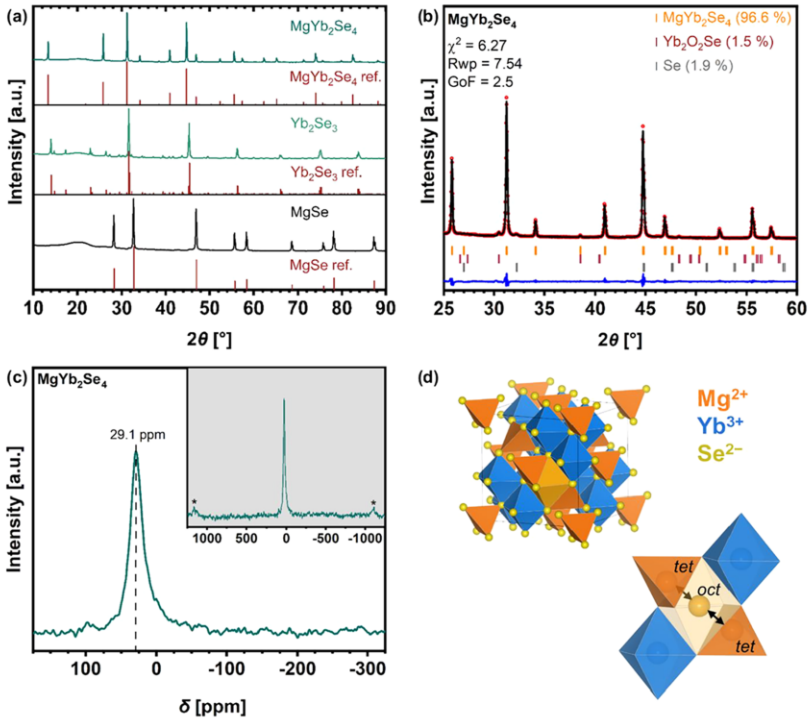

Figure 1. (a) XRD patterns of synthesized MgSe, Yb_2Se_3 and $MgYb_2Se_4$, and (b) Rietveld refinement against the XRD data for $MgYb_2Se_4$. Observed and calculated patterns are shown in red and black, and the difference curve is shown in blue. (c) The ^{25} Mg solid-state NMR spectrum, collected at a magnetic field of 11.7 T and a spinning speed of 35 kHz, confirms the Mg position on the tetrahedral site in $MgYb_2Se_4$. The spinning sidebands are marked with an asterisk. (d) Crystal structure of $MgYb_2Se_4$ spinel and the *tet-oct-tet* migration pathway for Mg^{2+}. Panel (d) adapted with permission from ref [14]. Copyright 2024, Glaser et al.[14]

= 0.868 Å) is included in this series of potentially stable spinels,[20,22] but has never been considered as Mg-ion SE in any computational or electrochemical study.

Also, multicomponent magnesium spinels with multielement substitution on a single crystallographic site (B-site or Se-site) have not yet been investigated. Multicomponent solid electrolytes with increased compositional or lattice site disorder over their ordered, single-component counterparts have recently demonstrated improved ion transport properties.[23−28] For instance, multicationic and multianionic lithium argyrodites such as $Li_{6.5}[P_{0.25}Si_{0.25}Ge_{0.25}Sb_{0.25}]S_5I$,[23] $Li_{6.6}P_{0.4}Ge_{0.6}S_5I$[24] and $Li_6PS_5[Cl_{0.33}Br_{0.33}I_{0.33}]$[25] showed lower activation energies (E_a = 0.19−0.29 eV) and higher room-temperature ionic conductivities (σ_{ion} = 10^{-3}−10^{-2} S cm^{-1}) compared to the anion-ordered Li_6PS_5I structure (E_a = 0.38 eV, σ_{ion} = ∼10^{-6} S cm^{-1}).[24] This success makes it promising to apply multielement substitution also to stable MgB_2Se_4 spinels in order to improve Mg transport properties, possibly realized with compounds such as $MgSc_{0.4}Y_{0.4}Er_{0.4}Tm_{0.4}Yb_{0.4}Se_4$ and $Mg_{1-0.5x}Sc_2Se_{4-x}Br_x$ ($0 < x \leq 1$).

For these reasons, in the present work we expand the family of experimentally investigated MgB_2Se_4 (B = Sc, Y, Er, Tm) spinels with $MgYb_2Se_4$ and the above-mentioned multicationic/multianionic compounds (meanly discussed in the Supporting Information) as potential Mg-ion SEs. Among them, $MgYb_2Se_4$ was found to exhibit the highest ionic conductivity and the lowest Mg-ion migration barrier, and also a lower electronic conductivity compared with the prior studied mixed-conducting spinels. The resulting lower electronic transference number as well as the evidence of high electrochemical stability make this spinel an attractive candidate for Mg-ion SEs. We hope that this work, along with its theoretical considerations, motivates further advancement in the development of room-temperature Mg-ion conductors for Mg batteries.

2. RESULTS AND DISCUSSION

2.1. Structural Information. The $MgYb_2Se_4$ spinel was synthesized under vacuum according to our reported two-step solid-state synthesis.[14] In the first step, the precursors MgSe and Yb_2Se_3 were prepared by reacting stoichiometric amounts of the corresponding elements at 750 and 800 °C, respectively. In the second step, the spinel was formed by a 1:1 reaction of the precursors at 950 °C. As a result, Figure 1a shows that the X-ray diffraction (XRD) pattern of the synthesized spinel and precursors are in excellent agreement with the corresponding Bragg reflections of the reference structures. In addition, Rietveld refinement based on the XRD data of the $MgYb_2Se_4$ sample (Figure 1b, crystallographic information in Table S1) confirms that the material adopts a cubic spinel structure with the $Fd\bar{3}m$ space group and was obtained in a high purity (96.6 wt %). The minor fraction of impurity was identified as unreacted selenium (1.9 wt %) and Yb_2O_2Se (1.5 wt %), whose formation must be due to an as yet unknown oxygen

https://doi.org/10.1021/acs.chemmater.5c00131
Chem. Mater. 2025, 37, 3353−3362

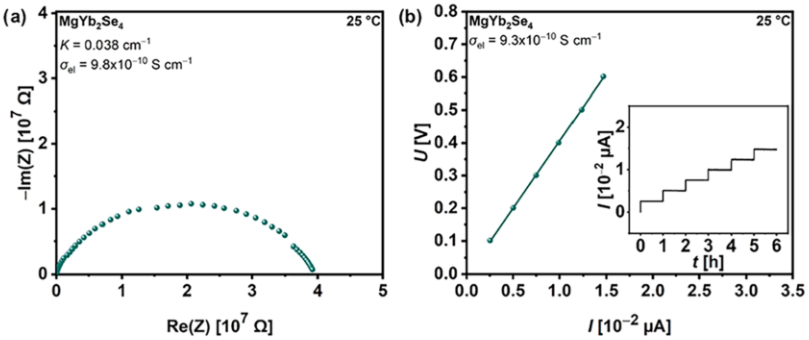

Figure 2. (a) Nyquist plot of the impedance data of a ClMgYb$_2$Se$_4$|C symmetric ion-blocking cell in the frequency range from 3 MHz to 100 mHz at 25 °C. *K* represents the cell constant, as described in eq 1. (b) DC polarization data at 25 °C obtained for a ClMgYb$_2$Se$_4$|C cell. During the measurement, different voltages (0.1, 0.2, 0.3, 0.4, 0.5, and 0.6 V) were held for 1 h each. The steady-state current at the end of each holding step (shown in the inset) was plotted against the corresponding voltage to calculate the electronic resistance R_{el} of MgYb$_2$Se$_4$ using a linear fit.

source, which could not be observed in the binary precursor materials (cf. Figure S1).

To gain deeper insight into the MgYb$_2$Se$_4$ structure, we employed ^{25}Mg magic-angle spinning nuclear magnetic resonance (MAS NMR) spectroscopy, a technique that characterizes the local environment and coordination of Mg ions within the material. The ^{25}MAS NMR spectrum (Figure 1c) of MgYb$_2$Se$_4$ shows only a single isotropic peak at 29 ppm, indicating a single coordination environment for Mg. Combined with the XRD refinement results, confirming a normal spinel structure, Mg therefore exclusively occupies the tetrahedral site. Consequently, the MgYb$_2$Se$_4$ spinel structure (illustrated in Figure 1d) has the Mg^{2+}-ions on the 8a sites (tetrahedral (*tet*)) and the Yb^{3+}-ions on the 16d sites (octahedral (*oct*)). This results in an ideal element stoichiometry of Mg/Yb/Se (1:2:4), which was also corroborated by energy dispersive X-ray spectroscopy (EDS) analysis of the powder with particles ranging from 1 to 100 μm in size (Figure S2).

2.2. Electronic Conductivity. The room-temperature partial electronic conductivity of MgYb$_2$Se$_4$ was evaluated using electrochemical impedance spectroscopy (EIS) in a Cl MgYb$_2$Se$_4$|C symmetric cell employing ion-blocking carbon (C) electrodes. Consistent with previous studies on MgB$_2$Se$_4$ spinels,[14,29] a depressed semicircle without a low-frequency tail appeared in the Nyquist plot (Figure 2a), indicating the presence of an electronic current path in parallel to the ionic one. In principle, this results in two semicircles, representing the parallel combination of the ionic resistance and the geometrical capacitance at high frequencies, and the parallel combination of the electronic resistance and the geometrical capacitance at lower frequencies.[30] If the ionic conductivity is much larger than the electronic conductivity ($\sigma_{ion} \gg \sigma_{el}$), the low-frequency semicircle is considerable larger than the high-frequency semicircle, whose resistance approaches to zero in the extreme cases. Thus, the observed semicircle is solely attributed to the electronic resistance and geometrical capacitance. The absence of an interface capacitance or a blocking tail at low frequencies confirms this behavior based on the lack of electron blockage.[14] Consequently, the total resistance of the semicircle corresponds to the electronic resistance, R_{el}, which is used to calculate the electronic conductivity, σ_{el}, by eq 1, applicable to both electronic and ionic conduction

$$\sigma_x = \frac{d}{A}\frac{1}{R_x} = \frac{K}{R_x} \quad x = \text{ion or el} \tag{1}$$

d and *A* represent the thickness and the contact area of the spinel pellet, respectively, and are summarized in the cell constant *K*.

A significant outcome of this study is the determination of the electronic conductivity of MgYb$_2$Se$_4$, evaluated by impedance measurements as $\sigma_{el} = 9.8 \times 10^{-10}$ S cm^{-1}, and further validated by additional DC polarization measurements (Figure 2b). Notably, this value is over an order of magnitude lower than those of the previously studied spinels, including MgSc$_2$Se$_4$, MgY$_2$Se$_4$, MgEr$_2$Se$_4$, and MgTm$_2$Se$_4$.[14,29] Therefore, at this point MgYb$_2$Se$_4$ seems to be a better potential SE, even if the present state of knowledge on the rarely studied MgB$_2$Se$_4$ spinels does not yet allow the identification of a certain cause for its lower σ_{el} value. According to prior studies on MgSc$_2$Se$_4$, there are only two hypotheses for the emergence of the electronic conductivity. Canepa et al. proposed in their study that the electronic conductivity arises either from the existence of intrinsic defects neutralized by electrons, or from the presence of electronic conducting secondary phases in the prepared material.[19,31] The latter hypothesis was also supported by Kundu et al., who further specified that electronic transport possibly occurs via electron jumping/tunneling between well-distributed electron-conducting inclusions (e.g., Sc/ScSe), through the low-conducting spinel matrix.[32,33] Following these two hypotheses, the electronic conductivity of the MgB$_2$Se$_4$ spinels is probably dependent on the interplay of various factors, including the extent of secondary phases/defects, the nature of secondary phases/defects (electron-conducting or not) and their distribution in the material. Since these factors partly depend on the specific elemental composition of the spinels and are still partly unknown, this makes it difficult to draw conclusions about the lower electronic conductivity of MgYb$_2$Se$_4$ in comparison to the other MgB$_2$Se$_4$ spinels investigated so far.

As with MgYb$_2$Se$_4$, two of the synthesized multicationic and multianionic spinels, MgSc$_{0.4}$Y$_{0.4}$Er$_{0.4}$Tm$_{0.4}$Yb$_{0.4}$Se$_4$ and Mg$_{0.75}$Sc$_2$Se$_{3.5}$Br$_{0.5}$, obtained in high phase purity (Figures S3–S5 and S7–S11), also demonstrate low σ_{el} values ($\sigma_{el} = 3.3 \times 10^{-9}$ and 3.6×10^{-13} S cm^{-1}, Figures S6 and S12). In particular, the latter exhibits an electronic conductivity that is almost five orders of magnitude lower than that of its Br-free,

https://doi.org/10.1021/acs.chemmater.5c00131
Chem. Mater. 2025, 37, 3353−3362

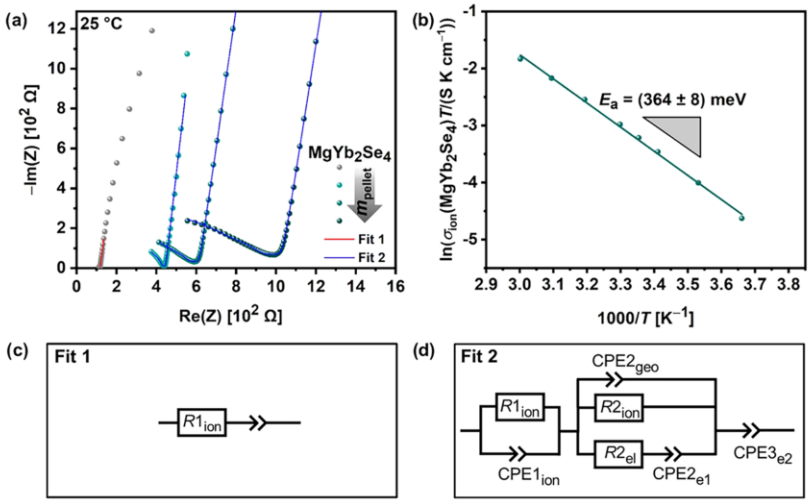

Figure 3. (a) Nyquist plots of SS|UiO66-MgIL|SS reference cell (gray) and SS|UiO66-MgIL|$MgYb_2Se_4$|UiO66-MgIL|SS cells with varied spinel pellet mass/thickness (160 mg/0.46 mm, 220 mg/0.54 mm and 280 mg/0.76 mm) at 25 °C fitted with the equivalent circuits Fit 1 and Fit 2; (b) Arrhenius plot of the average conductivities shown for temperatures from 0 to 60 °C; and (c−d) equivalent circuits Fit 1 and Fit 2 applied to fit the Nyquist plots.

pristine compound $MgSc_2Se_4$ (σ_{el} = 2.0 × 10^{-8} S cm^{-1}). This comparison suggests that the substitution of Se with Br counteracts the electronic transport, at least for the specific composition of $Mg_{0.75}Sc_2Se_{3.5}Br_{0.5}$. However, the manner in which this is happening can only be speculated at the current stage: On the one hand, this certain degree of aliovalent anion substitution might counteract the formation of the before mentioned intrinsic defects, which possibly induce electronic conductivity.[31] One the other hand, the aliovalent anion substitution could lead to changes in the electron−phonon interactions of the material.[34] If the interaction strength exceeds a specific threshold, polarons can form, in which the effective mass of the electrons is increased and thus lower electronic conductivity occurs. Nevertheless, whether either of these two cases is true will need to be investigated in the future.

2.3. Ionic Conductivity. The Mg-ion conductivity and the migration barrier along the *tet-oct-tet* migration pathway (Figure 1d) were determined from EIS measurements using symmetric SS|UiO66-MgIL|$MgYb_2Se_4$|UiO66-MgIL|SS cells. These cells contain two charge carrier specific blocking electrodes: ion-blocking stainless-steel (SS) outer electrodes, and electron-blocking interlayers consisting of the pure Mg-ion-conducting ionogel electrolyte UiO66-MgIL [σ_{el}(25 °C) = 1.7 × 10^{-10} S cm^{-1},[29] and σ_{ion}(25 °C) = 7.6 × 10^{-4} S cm^{-1}, Tables S2−S3]. The latter, the ionogel electrolyte, was prepared from a 1:1.25 (mass ratio) mixture of the metal−organic framework $Zr_6O_4(OH)_4(BDC)_6$ with BDC = 1,4-dicarboxylate (denoted as UiO66) and a 1 M $Mg(TFSI)_2$ ionic liquid based on [EMIM][TFSI] (denoted as MgIL) and appears as a dry and free-flowing powder since strong adhesive forces holding the viscous MgIL in the UiO66 framework.[29,35] By using UiO66-MgIL as an interlayer, this ensures better and sufficient physical contact between the rigid, hardly deformable electrodes (here: SS, but also Mg foils) and the rough spinel pellets, and also effectively suppresses the electron transport within the cell, so that the ionic conductivity can be accurately determined from the resulting impedance spectra.[29]

Figure 3a shows the Nyquist plots of room-temperature EIS measurements of cells with varied spinel pellet thicknesses (Table S2) and a reference SS|UiO66-MgIL|SS cell without a spinel pellet. As previously reported,[14,29] the ionic resistance $R1_{ion}$ of the UiO66-MgIL in the reference cell can be obtained by fitting the Nyquist plot with a simple equivalent circuit shown in Figure 3c. The $R1_{ion}$ was then adjusted to the UiO66-MgIL interlayer thickness used in the spinel-containing cells (Tables S2−S3 and eq S1), and set as a fixed parameter to determine the ionic resistance $R2_{ion}$ of $MgYb_2Se_4$ by applying the equivalent circuit in Figure 3d, which models the impedance of a mixed conductor between charge carrier specific blocking electrodes. By applying eq 1 with $R2_{ion}$, an average room-temperature Mg-ion conductivity of σ_{ion} = (1.4 ± 0.3) × 10^{-4} S cm^{-1} is evaluated. This value for $MgYb_2Se_4$ is considerably higher than that of the already investigated MgB_2Se_4 (B = Sc, Y, Er and Tm) spinels of the same material class (σ_{ion} = 2 × 10^{-5}−7 × 10^{-5} S cm^{-1})[14,29] and comparable to that of β-$Mg(BH_4)\cdot CH_3NH_2$ (σ_{ion} = 1.5 × 10^{-4} S cm^{-1})[12] and $Mg(BH_4)\cdot 1.5NH_3$-60 wt %TiO_2 (σ_{ion} = 3.0 × 10^{-4} S cm^{-1}).[13] To our knowledge, these borohydride compounds exhibit the highest room-temperature ionic conductivity among the Mg-ion SEs, even though the latter is not competitive due to its high electronic conductivity (σ_{el}/σ_{ion} = 0.6).[13]

Figure 3b shows the Arrhenius plot of the average ionic conductivities of $MgYb_2Se_4$, determined from EIS measurements in the temperature range between 0 and 60 °C (Figures S13−S14). Based on that, the activation energy E_a = 364 meV was calculated using the Arrhenius equation (eq 2)

$$\sigma_{ion} = \frac{\sigma_0}{T}\exp\left(-\frac{E_a}{k_B T}\right) \quad (2)$$

https://doi.org/10.1021/acs.chemmater.5c00131
Chem. Mater. 2025, 37, 3353−3362

where σ_0 is the conductivity pre-exponential factor. This E_a value is lower than those reported for the other experimentally studied magnesium spinels (381−406 meV)[14,29] An explanation for the lower E_a and the higher ionic conductivity of $MgYb_2Se_4$ compared to the other investigated spinels cannot be derived from the experimental data and is not immediately obvious. Thus, we will consider these results in the next section (Section 2.4) from a theoretical point of view.

An overview of the transport properties of the multicationic $MgSc_{0.4}Y_{0.4}Er_{0.4}Tm_{0.4}Yb_{0.4}Se_4$ spinel and multianionic $Mg_{1-0.5x}Sc_2Se_{4-x}Br_x$ (x = 0.25, 0.5, 0.75) compounds provides Figure 4. In comparison to the pristine $MgSc_2Se_4$, these SE compounds do not show any significant improvement in their migration barrier E_a and ionic conductivity σ_{ion}, as determined by EIS measurements of SS|MgIL|SE|MgIL|SS cells (Figures S15−S18 and Tables S4−S5). More specifically, the σ_{ion} values remain constant and comparable to that of the pristine $MgSc_2Se_4$ and even decrease for the multianionic compounds with $x \geq 0.75$, where partial decomposition of the spinel phase occurred (cf. Figure S7). Note that these σ_{ion} values are slightly overestimated because instead of UiO66-MgIL interlayers, glass fiber-MgIL interlayers were used, which wet the surface of the spinel pellets, resulting in higher conductivities. However, since σ_{ion} of $MgSc_2Se_4$ was determined with both, glass fiber-MgIL interlayer (σ_{ion} = 9.8 × 10^{-5} S cm^{-1}, this work) and UiO66-MgIL interlayer (σ_{ion} = 2.4−5.5 × 10^{-5} S cm^{-1}),[29] the true σ_{ion} values of the multicationic and multianionic (x < 0.75) spinels with similar ionic conductivities can also be assigned to the latter range. This demonstrates that the conducted multielement substitution in MgB_2Se_4 spinels does not lead to the desired result of improved ion transport properties.

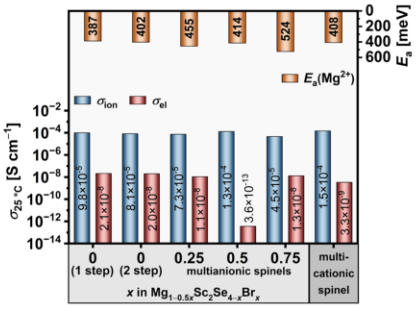

Figure 4. Overview of experimentally determined Mg-ion migration barriers E_a, ionic conductivities σ_{ion} and electronic conductivities σ_{el} of the prepared multicationic and multianionic compounds as well as of one- and two-step synthesized $MgSc_2Se_4$. Data for one-step synthesized $MgSc_2Se_4$ were used from ref 29.

2.4. Computational Investigation. The variation in the theoretically predicted migration barrier E_a(th) of MgB_2Se_4 spinels is related to the cationic radii, as the incorporation of larger lanthanides into the spinel structure increases the unit cell volume.[18,36] In particular, a 17% increase in the radius of the cations from 1.001 Å (Lu^{3+}) to 1.172 Å (La^{3+}) is associated with an approximate 17% expansion in the unit cell volume. A recent study introduced the distance ratio k_{64}, which is a bond length relationship between the migrating cation and selenium anions at octahedral (d(cn6)) and tetrahedral (d(cn4)) coordination sites, as a parameter to quantify the impact of trigonal distortion.[37] The k_{64} value has been demonstrated to be an optimal geometrical descriptor for both the static and kinetic components of E_a(th).[14] Figure 5a illustrates the theoretical migration energy barriers E_a(th) for Mg^{2+} ions in MgB_2Se_4 spinels as a function of k_{64}, which were obtained by DFT calculations alongside with the NEB method, assuming a vacancy diffusion mechanism in the dilute vacancy limit (one Mg vacancy per supercell). For all compounds considered, the calculated E_a(th) value is in the range of 306−366 meV. The larger ratio k_{64}, which is driven by the inclusion of larger cations, correlates with enhanced Mg^{2+} mobility, as evidenced by a reduction in calculated migration barriers from 343 meV in $MgLu_2Se_4$ to 306 meV in $MgPr_2Se_4$. The reduction in the Mg^{2+} migration barrier can be observed to follow an approximately linear trend with increasing cation radii, with the exception of $MgLa_2Se_4$, where a deviation can be seen to occur due to the destabilization of Mg^{2+} in the octahedral coordination.

These generally low E_a(th) values within the considered range of MgB_2Se_4 spinels indicate a high mobility for the Mg-ion in these compounds, but the dependence of the migration barrier on the individual contributing factors is complicated. Our DFT calculations show a linear relationship between the static (site preference energy ΔE) and kinetic (kinetically resolved activation energy E_{KRA})[38] components of the migration barrier and the k_{64} parameter as shown in Figure S19. To overcome the difficulties associated with the

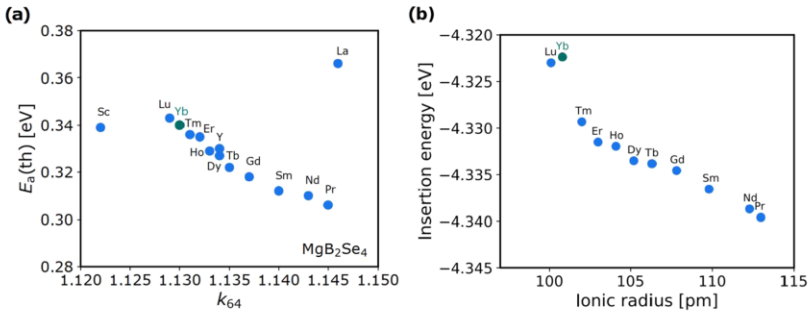

Figure 5. (a) Computationally predicted E_a(th) obtained using a PBE-DFT approach alongside with the NEB method. (b) Insertion energy, relative to a metallic magnesium anode, plotted as a function of ionic radius for MgB_2Se_4 compounds. Each compound is represented by a sphere, with the associated transition metal indicated above.

https://doi.org/10.1021/acs.chemmater.5c00131
Chem. Mater. 2025, 37, 3353−3362

directional dependence of E_a(th), we introduce a kinetically resolved activation energy (E_{KRA}), which involves calculating the average energy of the initial and final states of the hop and subtracting it from the activation energy. However, the insertion energy of magnesium within the spinel structure, relative to a metallic magnesium anode (eq 3), exhibits distinct behavior across the lanthanides, with ytterbium (Yb) demonstrating the smallest insertion energy, as illustrated in Figure 5b. The insertion energy, E_{insert}, is defined as

$$E_{insert}(Mg) = E(Mg_{x+y}B_2X_4) - E(Mg_yB_2X_4) - xE(Mg) \quad (3)$$

where $E(Mg_yB_2X_4)$ represents the total energy of the spinel with a magnesium concentration y in the unit cell, and E(Mg) is the cohesive energy of bulk magnesium in its metallic phase. In the present study, the variable y is determined by the magnesium content of the supercell. This is achieved by removing one Mg atom from a total of eight, thus yielding y = 0.875, while ensuring that $x + y = 1$ is maintained to preserve charge balance and spinel stoichiometry. The smallest insertion energy observed for Yb suggests that the interactions between magnesium ions and the host lattice are relatively weak in the $MgYb_2Se_4$ crystal structure. Consequently, the weaker binding corresponds to lower probability of "residence" of ions at specific sites within the lattice, thereby facilitating more efficient and rapid ionic transport through the material.[39]

A reduction in the activation barrier from 346 to 306 meV is equivalent to a change in E_a(th) of only 40 meV. At typical operating temperatures (e.g., 300 K), this modest change has a small impact on ionic conductivity, with a conductivity of about 1.7×10^{-6} for E_a(th) = 346 meV and 7.7×10^{-6} for E_a(th) = 306 meV considering the Boltzmann factor $\exp(-E_a/k_BT)$, which does not correspond to a full order of magnitude change in conductivity. Note that the calculated conductivity values are dependent on the assumed pre-exponential factor σ_0, and that variations in the pre-exponential term could lead to significant changes in the conductivity at 300 K, potentially influencing the observed effect of the 40 meV activation energy difference. σ_0 is associated with a number of factors, including the concentration of charge carriers, the attempt frequency of ionic jumps and the entropy of activation, i.e., the change in the local vibrations around the jumping ion. A reduction in binding energy facilitates a higher ion mobility by lowering the energy required to displace an ion from its equilibrium position, thereby increasing the attempt frequency and overall ionic conductivity. It can therefore be concluded that while alterations in the activation energy predominantly impact the exponential term, reductions in binding energy can result in a less rigid bond, increasing the attempt frequency.

Note that ytterbium also exists in the +2 oxidation state (Yb^{2+}), which is characterized by a filled 4f orbital configuration ([Xe] $4f^{14}$) with additional electronic stability, affecting its ionic radius and interactions with the lattice. We hypothesize that in the context of $MgYb_2Se_4$, the reduction of Yb^{3+} to Yb^{2+} may occur under certain conditions due to the chemical environment and the ability of magnesium to reduce the Yb^{3+} ions, as supported by previous reports of binary compounds such as YbSe forming in similar systems.[20] For this reason, the calculated low insertion energy in this spinel could be the result of a combination of factors such as the unique electronic structure of Yb, the possible formation of Yb^{2+} ions in the solid state and the associated defect chemistry. However, computational models may inadequately capture the interplay between Yb^{2+} and compensating defects or vacancies in the crystal structure. This can lead to an overestimation of the energy barrier for ion migration. These effects are different from those observed for Tm, Er, Y, and Sc which typically adopt the +3 oxidation state and have an unfilled shell, resulting in different bonding and migration properties.

2.5. Cycling Performance and Electrochemical Stability. To further investigate the $MgYb_2Se_4$ spinel as potential Mg-ion SE, the cycling performance and electrochemical stability of the sandwich-type UiO66-MgIL|$MgYb_2Se_4$|UiO66-MgIL pellets against Mg metal were evaluated. The Mg plating-stripping cycling was performed with a symmetric Mg|UiO66-MgIL|$MgYb_2Se_4$|UiO66-MgIL|Mg cell at 60 °C. As shown in Figure 6a, the cell was initially activated over 50 cycles at a current density of 1.57 μA cm^{-2} and a dwell time of 30 min for each plating or stripping step (plated charge amount of 0.785 μAh cm^{-2} ≙ ideally 2 nm of Mg). Afterward, the plated charge was increased by a factor of 20 (≙ 41 nm of Mg for each step of 10 h) for further 20 cycles. Reversible plating-stripping cycling at an increasing overpotential from 0.6 to 1.2 V was observed with this amount of charge. Since the overpotential increases and exceeds the estimated IR drop of 0.21 mV across the sandwiched pellet (spinel: IR = 0.18 mV, d = 54 mm, $\sigma_{ion} = 4.8 \times 10^{-4}$ S cm^{-1} and UiO66-MgIL: IR = 0.03 mV, d = 52 mm, $\sigma_{ion} = 2.5 \times 10^{-3}$ S cm^{-1}) this clearly indicates interface-dominating resistances inside the cell.

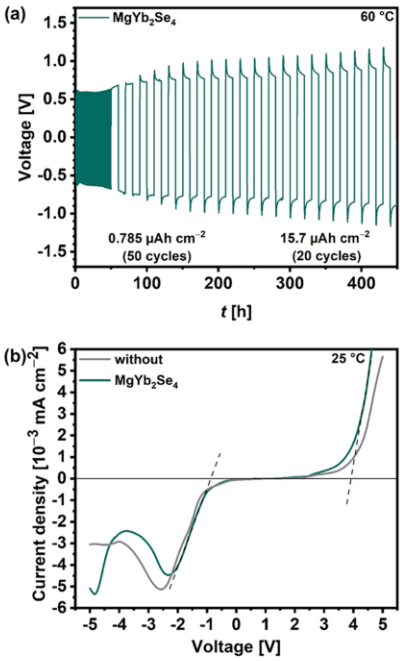

Figure 6. (a) Long-term cycling performance during Mg plating/stripping of a Mg|UiO66-MgIL|$MgYb_2Se_4$|UiO66-MgIL|Mg cell at 60 °C by applying a current density of ±1.57 μA cm^{-2}, and (b) LSV curves of Mg|UiO-66-MgIL|SS cells ("without") and Mg|UiO-66-MgIL|$MgYb_2Se_4$|UiO66-MgIL|SS cells recorded at a scan rate of −0.1/0.1 mV s^{-1} at room-temperature.

Linear sweep voltammetry (LSV) was carried out with asymmetric two-electrode cells, where one Mg foil served as

https://doi.org/10.1021/acs.chemmater.5c00131
Chem. Mater. 2025, 37, 3353−3362

both the counter and reference electrode, and a stainless-steel current collector acted as the working electrode. The oxidation/reduction onset potential was measured with a scan rate of −0.1 or 0.1 mV s^{-1} from open circuit voltage (OCV) to −5 or 5 V (vs Mg^{2+}/Mg). As shown in Figure 6b, the onset potentials for reduction and oxidation currents were observed at −0.9 and 3.9 V, respectively, consistent with those of the earlier reported spinels (Figure S20),[14] but also similar to the spinel-free reference cell. This indicates that the spinel's stability possibly exceeds these specified limits, as these are constrained by the decomposition of the UiO66-MgIL electrolyte. To determine the presumably larger range of the electrochemical stability window, it is therefore necessary to cycle the cells without UiO66-MgIL interlayers. Unfortunately, due to the poor physical contact between the stiff SS/Mg electrodes and the spinel pellet,[29] this is not feasible at the present until suitable electrodes have been developed that can adapt well to the solid electrolyte surface. Nevertheless, these first results already demonstrate that the preliminary oxidation stability of 3.9 V is in any case higher than that of the borohydride SEs (≲1.3 V vs Mg^{2+}/Mg^2),[12,13] which considerably broadens the selection of cathode materials for the spinels.

3. CONCLUSIONS

In summary, we present three spinel-type phases, $MgSc_{0.4}Y_{0.4}Er_{0.4}Tm_{0.4}Yb_{0.4}Se_4$, $Mg_{0.75}Sc_2Se_{3.5}Br_{0.5}$ and $MgYb_2Se_4$, with lower electronic conductivity (σ_{el} = 3.3 × 10^{-9}, 3.6 × 10^{-13}, and 9.8 × 10^{-10} S cm^{-1}) than previously reported for magnesium selenide spinels ($\sigma_{el} > 10^{-8}$ S cm^{-1}). Among them, $MgYb_2Se_4$ exhibits a relatively low Mg^{2+} migration barrier (364 meV) and a very high room-temperature ionic conductivity (σ_{ion} = 1.4 × 10^{-4} S cm^{-1}). The theoretical calculations offer no simple and straightforward explanation for the low activation barrier and relatively high ionic conductivity. The tendency of ytterbium to also form Yb^{2+} ions in the solid state and corresponding defects, though not proven in our case, may be one factor. According to our calculations, $MgYb_2Se_4$ shows an anomaly in the magnesium insertion energy, i.e., easier reduction by magnesium, that might be related to the tendency of Yb^{3+} ions to be reduced to Yb^{2+}. However, how this affects the magnesium mobility needs to considered with more advanced theoretical calculations. Future studies using first-principles molecular dynamics and defect thermodynamics calculations may provide a more complete understanding of the potential role of Yb oxidation states and defect interactions in facilitating magnesium ion transport in $MgYb_2Se_4$. Finally, the resulting low electronic transference number (7 × 10^{-6}) of $MgYb_2Se_4$ in contrast to $MgSc_2Se_4$, MgY_2Se_4, $MgEr_2Se_4$, and $MgTm_2Se_4$ (5 × 10^{-3} − 0.2) coupled with its high electrochemical stability window (−0.9 to 3.9 V vs Mg^{2+}/Mg) make this spinel a highly attractive candidate as a Mg-ion SE.

4. EXPERIMENTAL SECTION

4.1. Materials. magnesium powder (Sigma-Aldrich, ≥99%), ytterbium chips (chemPUR, 99.9% REO), selenium powder (Alfa Aesar, 99.999%), scandium bromide ($ScBr_3$, Fisher Scientific, ultra dry, 99.99%), scandium selenide (Sc_2Se_3, as-prepared[29]), thulium selenide (Tm_2Se_3, as-prepared[14]), erbium selenide (Er_2Se_3, as-prepared[14]) and yttrium selenide (Y_2Se_3, as-prepared[14]), magnesium scandium selenide ($MgSc_2Se_4$, as-prepared[29]), magnesium bis (trifluoromethanesulfonyl) imide ($Mg(TFSI)_2$, TCI, >97%), 1-ethyl-3-methylimidazolium bis (trifluoromethanesulfonyl) imide ([EMIM]-[TFSI], TCI, >98%), metal−organic framework ($Zr_6O_4(OH)_4(BDC)_6$ with BDC = 1,4-dicarboxylate, denoted as UiO66 and as-prepared[35]), Mg foil (chemPUR, 99.98%), super P (MSE Supplies, >99%), glass fiber separators (Whatmann GF/A).

4.2. Synthesis of $MgYb_2Se_4$ Spinel. First, the binary selenides MgSe and Yb_2Se_3 were prepared. To synthesize MgSe, a stoichiometric mixture of magnesium and selenium powder were hand-milled for 15 min, and 0.5 g of the powder mixture was pressed into a pellet (Ø = 10 mm) by applying an isostatic pressure of 300 MPa for 30 min. Then, the pellet was vacuum sealed in a quartz glass ampule (first baked out 800 °C for 2 h under dynamic vacuum) and heated at 750 °C for 24 h (180 °C h^{-1} heating rate) in a furnace (Nabertherm with controller P 300). The Yb_2Se_3 synthesis was carried out with stoichiometric amounts of selenium powder and ytterbium metal chips. The selenium powder was placed on the bottom of a graphite crucible and covered with the metal chips. After vacuum sealing the crucible in a quartz glass ampule, the reaction was performed at 800 °C for 48 h (60 °C h^{-1} heating rate). In the next step, a stoichiometric mixture of MgSe and Yb_2Se_3 was hand-milled and pressed to a 0.5 g pellet using the same conditions as described above. To finally obtain the $MgYb_2Se_4$ spinel, the pellet was vacuum sealed in an ampule and heated at 950 °C for 20 h (180 °C h^{-1} heating rate). All preparations and sample treatments were performed under dry argon atmosphere (glovebox) or in vacuum and all reactants were used as received.

4.3. Synthesis of $MgSc_{0.4}Y_{0.4}Er_{0.4}Tm_{0.4}Yb_{0.4}Se_4$ Spinel Solid Solution. A stoichiometric mixture (5:1:1:1:1:1) of MgSe, Sc_2Se_3, Y_2Se_3, Er_2Se_3, Tm_2Se_3 and Yb_2Se_3 was hand-milled and pressed to a 0.5 g pellet. Then, the pellet was vacuum sealed in an ampule and heated at 950 °C for 30 h (180 °C h^{-1} heating rate).

4.4. Synthesis of $Mg_{1-0.5x}Sc_2Se_{4-x}Br_x$ (x = 0.25, 0.5, 0.75, 1). Mixtures of (1−0.5x) MgSe, (1−1/6x) Sc_2Se_3 and (1/3x) $ScBr_3$ were hand-milled and pressed to 0.5 g pellets. Afterward, each pellet was vacuum sealed in an ampule and heated at 950 °C for 24 h (180 °C h^{-1} heating rate).

4.5. X-ray Diffraction (XRD). Powder XRD patterns of the samples were collected on an Empyrean powder diffractometer (Malvern PANalytical Ltd.). Each sample was placed on top of a silicon zero background holder and sealed with Kapton polyimide film under argon atmosphere to avoid contact with air and humidity. Using Cu Kα radiation the diffraction data was recorded in the 2θ range from 5 to 90° with a step size of 0.026° and a counting time per step of 200 s. References taken from ICSD Inorganic Crystal Structure Database: MgSe (ICSD 53946),[40] YbSe (ICSD 106048),[41] Yb_2Se_3 (ICSD 652191),[42] $MgYb_2Se_4$ (ICSD 76053),[43] Yb_2O_2Se (ICSD 25811),[44] Se (ICSD 164263),[45] Se (ICSD 23072),[46] Se (ICSD 40016),[47] Sc_2Se_3 (ICSD 651804),[42] $MgSc_2Se_4$ (ICSD 642814),[43] Tm_2Se_3 (ICSD 652078),[42] $MgTm_2Se_4$ (ICSD 76051),[43] Er_2Se_3 (ICSD 79227),[48] $MgEr_2Se_4$ (ICSD 630754),[43] Y_2Se_3 (ICSD 652183)[49] and MgY_2Se_4 (ICSD 76052).[43] Reference data for $ScBr_3$ (mp-1186984) were retrieved from the Materials Project from database version v2023.11.1.[50]

4.6. Rietveld Analysis. Rietveld refinement against the $MgYb_2Se_4$ XRD data was performed using the software FullProf Suite version January 2021. Starting models for the Rietveld refinement were taken from references listed in Section 4.5.

4.7. Flame Atomic Absorption Spectrometry (FAAS). Quantification of Mg was performed using the flame unit of an AA-7000 spectrometer (Shimadzu Corporation, Japan) equipped with a Mg hollow cathode lamp at 285.2 nm and ASC-7000 liquid auto sampler (Shimadzu Corporation, Japan). Synthetic air (15.0 L min^{-1}; MTI, Neu-Ulm, Germany) and acetylene (1.8 L min^{-1}; MTI, Neu-Ulm, Germany) were used as fuel gases. Quantification was achieved by means of external calibration in the range from 0.2 to 1.0mg L^{-1}.

4.8. Total Reflection X-ray Fluorescence Spectrometry (TXRF). For the measurements high-efficiency module S2 Picofox (Bruker Nano GmbH, Berlin, Germany) equipped with Mo X-ray tube was used. The measurement lifetime was set to 1000 s and excitation of the sample was carried out using a voltage of 50 kV and a

https://doi.org/10.1021/acs.chemmater.5c00131
Chem. Mater. 2025, 37, 3353−3362

current of 600 μA. For quantification Cr internal standard solution (1000 mg L^{-1}; Merck KGaA, Germany) was used. Spectra PicoFox (7.2.5.0, Bruker Nano GmbH) software was used to evaluate the obtained spectra and for deconvolution the profile Bayes normal fit was selected.

4.9. Scanning Electron Microscopy (SEM) and Energy-Dispersive X-ray Spectroscopy (EDS). SEM images and EDS maps of the samples were recorded with a Gemini SEM 560 high-resolution scanning electron microscope (Carl Zeiss AG, Germany). An acceleration voltage of 15 kV, a working distance of 8.8 mm and an aperture size of 60 μm were used. The SEM images were collected with the in-lens detector and a X-Max50 detector (Oxford Instruments, U.K.) was used for the EDS mapping. To avoid air contamination, the sample transfer was carried out with a Leica EM VCT500 (Leica Microsystems Germany) shuttle.

4.10. Nuclear Magnetic Resonance (NMR) Spectroscopy. ^{25}Mg magic-angle spinning (MAS) NMR spectroscopy was performed at a magnetic field of 11.7 T, corresponding to a resonance frequency of 30.6 MHz. The measurements were carried out in 1.3 mm rotors at a spinning speed of 35 kHz with a rotor-synchronized Hahn-echo pulse sequence and a $\pi/2$ pulse duration of 3.7 μs. The recycle delay was 1 s and the spectra were referenced to an aqueous solution of 5 M $MgCl_2$.

4.11. Cell Assembly and Electrochemical Measurements. All electrochemical measurements were carried out with a VMP300 electrochemical workstation from Bio-Logic Science Instruments SAS and recorded with the corresponding software EC-Lab. The RelaxIS 3 software (RHD Instruments, Darmstadt, Germany) was used to fit the obtained impedance data.

To measure the electronic conductivity σ_{el}, a homemade battery cell casing was used, as introduced in an earlier work.[51] For a typical measurement, 120−160 mg spinel powder was filled in the PEEK housing (Ø = 10 mm) of the cell. Then, a pellet was formed inside the housing by pressing the powder between two stainless-steel stamps (SS) using a hand press. Layers of 24 mg super P (vacuum-dried at 150 °C for 24 h), denoted with C, were inserted between the spinel pellet and the stainless-steel stamps, working as ion-blocking electrodes. For densification, the symmetric C|spinel|C cell was pressed at 3 t for 3 min and subsequently fixed in an aluminum framework with 10 N m torque by means of a screw. The electrochemical impedance spectroscopy (EIS) measurements were carried out in a frequency range from 3 MHz to 100 mHz with a current (AC) amplitude of 10 mV. For the chronoamperometry (CA) measurements the voltage was increased stepwise (0.1, 0.2, 0.3, 0.4, 0.5, and 0.6 V) with 1 h resting time per step. Then, the steady-state current at the end of each step was plotted against the corresponding voltage to calculate the electronic resistance R_{el} of the spinel pellet from a linear fit. From the obtained R_{el} value of the EIS and CA measurements, σ_{el} was calculated based on eq 1.

To determine the ionic conductivity σ_{ion} and the Mg-ion migration barrier of $MgYb_2Se_4$, different amounts (160, 220, and 280 mg) of spinel powder were pressed in the PEEK housing, analogous to the procedure mentioned above. Purely Mg-ion conducting interlayers made from 40 mg ionogel SE, denoted as UiO66-MgIL, were employed as electron-blocking electrodes. The UiO66-MgIL consisted out of the metal−organic framework (MOF) compound $Zr_6O_4(OH)_4(BDC)_6$ with BDC = 1,4-dicarboxylate (denoted as UiO66) impregnated in a mass ratio of 1:1.25 with a 1 M $Mg(TFSI)_2$ ionic liquid based on [EMIM][TFSI] (denoted as MgIL), as described in an earlier report.[29] Then, the symmetrical SS|UiO66-MgIL|$MgYb_2Se_4$|UiO66-MgIL|SS cells were densified as mentioned before. In case of the $MgSc_2Se_4$ and its multicationic/multianionic derivates, 160 mg spinel powder was pressed in the PEEK housing and MOF-free electron-blocking interlayers were employed as less expensive alternative. These interlayers consisted out of glass fiber separators (Ø = 10 mm) moistened with one droplet (5 μL) of MgIL. After fixing all cells in an aluminum framework, EIS measurements were recorded at different temperatures between 0 and 60 °C, with each temperature hold for 1.5 h before the measurement. A frequency range from 3 MHz to 100 mHz and an AC amplitude of 10 mV were chosen. From the obtained resistance from the fitting of the impedance data, the ionic conductivity was calculated according to eq 1.

For the LSV measurements, asymmetric Mg|UiO66-MgIL|$MgYb_2Se_4$|UiO66-MgIL|SS cells were assembled. First, symmetrical cells with 220 mg $MgYb_2Se_4$ powder (or 0 mg for the reference cell) and 40 mg UiO66-MgIL per layer were prepared, analogous to the determination of σ_{ion}. Then, a Mg foil (Ø = 9 mm) polished with a scalpel was placed between one UiO66-MgIL layer and the SS stamp. After applying a pressure of 3 t for 1 min to the cell, LSV from open circuit voltage (OCV) to 5 or −5 V, respectively, was carried out with a scan rate of 0.1/−0.1 mV s^{-1} at 25°C and 60 °C.

The Mg plating/stripping measurements were performed with symmetrical Mg|UiO66-MgIL|$MgYb_2Se_4$|UiO66-MgIL|Mg cells. Here, two Mg electrodes were included according to the previous procedure. Then, chronopotentiometric stripping/plating was carried out over 70 cycles (50 cycles with t_{cycle} = 1 h and 20 cycles with t_{cycle} = 20 h) at 60 °C with a current density of ±0.785 and 1.57μA cm^{-2} per step, respectively.

4.12. Computational Details. Periodic density functional theory (DFT)[52,53] calculations to determine the Mg^{2+} migration barriers in d^0-metal- and lanthanide-based MgB_2Se_4 spinels were performed. We employed the Perdew, Burke, and Ernzerhof (PBE)[54] exchange and correlation functional and the projector augmented wave method (PAW)[55] as implemented in the Vienna Ab initio Simulation Package (VASP).[56−58] The calculations were conducted for the conventional unit cell with 56 atoms and all forces on the atoms converged below 0.01 eV $Å^{-1}$. The atomic composition consists of 8 Mg, 16 Yb, and 32 Se atoms. This enlarged supercell allows a more accurate representation of defects, disorder, and electronic interactions in the material. The total energy was converged below 1×10^{-5} eV per supercell, using a $2 \times 2 \times 2$ k-point mesh and a cutoff energy of 520 eV.

We employed the Climbing Image Nudged Elastic Band (CI-NEB)[59] method with four images between tetrahedral and octahedral sites. The complete energy profile was obtained by mirroring at the octahedral site, representing an intermediate site of the migration event. The forces in the NEB calculations were converged to 0.05 eV $Å^{-1}$. All migration barriers were determined in the dilute vacancy limit (one vacancy per supercell), with the volume fixed to the one of the pristine structures.

■ ASSOCIATED CONTENT

Data Availability Statement

The data that support the findings of this study are openly available in Zenodo at https://doi.org/10.5281/zenodo.14610415, reference number 14610415. All electronic structure calculations used in this work are made available under the Creative Commons Attribution license (CC-BY 4.0) on the NOMAD respository (https://nomad-lab.eu) under the following link: https://doi.org/10.17172/NOMAD/2025.05.02-1.

Supporting Information

The Supporting Information is available free of charge at https://pubs.acs.org/doi/10.1021/acs.chemmater.5c00131.

Additional information on XRD patterns, crystallographic data, SEM images, EDS maps, electrochemical characterization, ionic and electronic conductivities, activation energies, LSV data, Mg plating/stripping data, FAAS data, and TXRF data (PDF)

■ AUTHOR INFORMATION

Corresponding Author

Jürgen Janek − *Institute of Physical Chemistry and Center for Materials Research (ZfM), Justus Liebig University Giessen,*

https://doi.org/10.1021/acs.chemmater.5c00131
Chem. Mater. 2025, 37, 3353−3362

Giessen 35392, Germany; orcid.org/0000-0002-9221-4756; Email: Juergen.Janek@phys.chemie.uni-giessen.de

Authors

Clarissa Glaser − *Institute of Physical Chemistry and Center for Materials Research (ZfM), Justus Liebig University Giessen, Giessen 35392, Germany;* orcid.org/0000-0003-4561-8982

Mohsen Sotoudeh − *Institute of Theoretical Chemistry, Ulm University, Ulm 89081, Germany;* orcid.org/0000-0002-0970-5336

Manuel Dillenz − *Institute of Theoretical Chemistry, Ulm University, Ulm 89081, Germany;* orcid.org/0000-0002-4901-154X

Kanchan Sarkar − *Institute of Theoretical Chemistry, Ulm University, Ulm 89081, Germany*

Jasmin S. Bark − *Institute of Physical Chemistry and Center for Materials Research (ZfM), Justus Liebig University Giessen, Giessen 35392, Germany*

Shashwat Singh − *Department of Chemistry and the Waterloo Institute for Nanotechnology, University of Waterloo, Waterloo N2L 3G1 Ontario, Canada*

Zhixuan Wei − *Institute of Physical Chemistry and Center for Materials Research (ZfM), Justus Liebig University Giessen, Giessen 35392, Germany;* orcid.org/0009-0007-1824-3640

Sylvio Indris − *Institute for Applied Materials-Energy Storage Systems (IAM-ESS), Karlsruhe Institute of Technology (KIT), Eggenstein-Leopoldshafen 76344, Germany;* orcid.org/0000-0002-5100-113X

Riccarda Müller − *Institute of Analytical and Bioanalytical Chemistry, Ulm University, Ulm 89081, Germany*

Kerstin Leopold − *Institute of Analytical and Bioanalytical Chemistry, Ulm University, Ulm 89081, Germany;* orcid.org/0000-0003-0586-7239

Linda F. Nazar − *Department of Chemistry and the Waterloo Institute for Nanotechnology, University of Waterloo, Waterloo N2L 3G1 Ontario, Canada;* orcid.org/0000-0002-3314-8197

Axel Groß − *Institute of Theoretical Chemistry, Ulm University, Ulm 89081, Germany;* orcid.org/0000-0003-4037-7331

Complete contact information is available at: https://pubs.acs.org/10.1021/acs.chemmater.5c00131

Author Contributions

The manuscript was written through contributions of all authors. All authors have given approval to the final version of the manuscript.

Notes

The authors declare no competing financial interest.

■ ACKNOWLEDGMENTS

This work contributes to the research performed at CELEST (Center for Electrochemical Energy Storage Ulm-Karlsruhe) and was funded by the German Research Foundation (DFG) under Project ID 390874152 (POLiS Cluster of Excellence). Further financial support by the Dr. Barbara Mez-Starck Foundation is gratefully acknowledged. L.F.N. thanks NSERC for financial support to S.S. (University of Waterloo). The authors would like to thank Ruben Maile (Justus Liebig University) for providing the UiO66 MOF material and Zhou Yu (University of Waterloo) for collecting the SEM images of the $Mg_{1-0.5x}Sc_2Se_{4-x}Br_x$ compounds. Computer time provided by the state of Baden-Württemberg through bwHPC and the German Research Foundation (DFG) under grant no INST 40/575-1 FUGG (JUSTUS 2 cluster) are gratefully acknowledged.

■ REFERENCES

(1) Liu, F.; Wang, T.; Liu, X.; Fan, L.-Z. Challenges and Recent Progress on Key Materials for Rechargeable Magnesium Batteries. *Adv. Energy Mater.* **2021**, *11*, No. 2000787.

(2) Liang, Y.; Dong, H.; Aurbach, D.; Yao, Y. Current Status and Future Directions of Multivalent Metal-Ion Batteries. *Nat. Energy* **2020**, *5*, 646−656.

(3) Zhan, Y.; Zhang, W.; Lei, B.; Liu, H.; Li, W. Recent Development of Mg Ion Solid Electrolyte. *Front. Chem.* **2020**, *8*, No. 125.

(4) Ikeda, S.; Takahashi, M.; Ishikawa, J.; Ito, K. Solid Electrolytes with Multivalent Cation Conduction. 1. Conducting Species in Mg-Zr-PO4 System. *Solid State Ionics* **1987**, *23*, 125−129.

(5) Adamu, M.; Kale, G. M. Novel Sol−Gel Synthesis of MgZr4P6O24 Composite Solid Electrolyte and Newer Insight into the Mg2+ -Ion Conducting Properties Using Impedance Spectroscopy. *J. Phys. Chem. C* **2016**, *120*, 17909−17915.

(6) Kawamura, J.; Morota, K.; Kuwata, N.; Nakamura, Y.; Maekawa, H.; Hattori, T.; Imanaka, N.; Okazaki, Y.; Adachi, G. High Temperature 31P NMR Study on Mg2+ Ion Conductors. *Solid State Commun.* **2001**, *120*, 295−298.

(7) Takeda, H.; Nakano, K.; Tanibata, N.; Nakayama, M. Novel Mg-Ion Conductive Oxide of μ-Cordierite Mg0.6Al1.2Si1.8O6. *Sci. Technol. Adv. Mater.* **2020**, *21*, 131−138.

(8) Yamanaka, T.; Hayashi, A.; Yamauchi, A.; Tatsumisago, M. Preparation of Magnesium Ion Conducting MgS−P2S5−MgI2 Glasses by a Mechanochemical Technique. *Solid State Ionics* **2014**, *262*, 601−603.

(9) Tomita, Y.; Saito, R.; Morishita, M.; Yamane, Y.; Kohno, Y. Synthesis, Crystal Structure and Ionic Conductivity of MgAl2X8 (X = Cl, Br). *Solid State Ionics* **2021**, *361*, No. 115566.

(10) Halim, Z. A.; Adnan, S.; Salleh, F. M.; Mohamed, N. S. Effects of Mg2+ Interstitial Ion on the Properties of Mg0.5+x/2Si2-xAlx(PO4)3 Ceramic Electrolytes. *J. Magn. Alloys* **2017**, *5*, 439−447.

(11) Jaschin, P. W.; Gao, Y.; Li, Y.; Bo, S.-H. A Materials Perspective on Magnesium-Ion-Based Solid-State Electrolytes. *J. Mater. Chem. A* **2020**, *8*, 2875−2897.

(12) Amdisen, M. B.; Grinderslev, J. B.; Skov, L. N.; Jensen, T. R. Methylamine Magnesium Borohydrides as Electrolytes for All-Solid-State Magnesium Batteries. *Chem. Mater.* **2023**, *35*, 1440−1448.

(13) Wang, Q.; Li, H.; Zhang, R.; Liu, Z.; Deng, H.; Cen, W.; Yan, Y.; Chen, Y. Oxygen Vacancies Boosted Fast Mg2+ Migration in Solids at Room Temperature. *Energy Storage Mater.* **2022**, *51*, 630−637.

(14) Glaser, C.; Dillenz, M.; Sarkar, K.; Sotoudeh, M.; Wei, Z.; Indris, S.; Maile, R.; Rohnke, M.; Müller-Buschbaum, K.; Groß, A.; Janek, J. MgB2Se4 Spinels (B = Sc, Y, Er, Tm) as Potential Mg-Ion Solid Electrolytes − Partial Ionic Conductivity and the Ion Migration Barrier. *Adv. Energy Mater.* **2024**, *14*, No. 2402269.

(15) Iton, Z. W. B.; See, K. A. Multivalent Ion Conduction in Inorganic Solids. *Chem. Mater.* **2022**, *34*, 881−898.

(16) Sotoudeh, M.; Groß, A. Descriptor and Scaling Relations for Ion Mobility in Crystalline Solids. *JACS Au* **2022**, *2*, 463−471.

(17) Sotoudeh, M.; Baumgart, S.; Dillenz, M.; Döhn, J.; Forster-Tonigold, K.; Helmbrecht, K.; Stottmeister, D.; Groß, A. Ion Mobility in Crystalline Battery Materials. *Adv. Energy Mater.* **2024**, *14*, No. 2302550.

(18) Koettgen, J.; Bartel, C. J.; Ceder, G. Computational Investigation of Chalcogenide Spinel Conductors for All-Solid-State Mg Batteries. *Chem. Commun.* **2020**, *56*, 1952−1955.

(19) Canepa, P.; Bo, S.-H.; Sai Gautam, G.; Key, B.; Richards, W. D.; Shi, T.; Tian, Y.; Wang, Y.; Li, J.; Ceder, G. High Magnesium Mobility in Ternary Spinel Chalcogenides. *Nat. Commun.* **2017**, *8*, No. 1759.
(20) Reig-i-Plessis, D.; Cote, A.; van Geldern, S.; Mayrhofer, R. D.; Aczel, A. A.; MacDougall, G. J. Neutron Scattering Measurement of Crystalline-Electric Fields in Magnesium Rare-Earth Selenide Spinels. *Phys. Rev. Mater.* **2019**, *3*, No. 114408.
(21) Reig-i-Plessis, D.; Geldern, S. V.; Aczel, A. A.; Kochkov, D.; Clark, B. K.; MacDougall, G. J. Deviation from the Dipole-Ice Model in the Spinel Spin-Ice Candidate MgEr2Se4. *Phys. Rev. B* **2019**, *99*, No. 134438.
(22) Flahaut, J.; Guittard, M.; Patrie, M.; Pardo, M. P.; Golabi, S. M.; Domange, L. Phase cubiques type Th3P4 dans les sulfures, les séléniures et les tellurures L2X3 et L3X4 des terres rares, et dans leurs combinaisons ML2X4 avec les sulfures et séléniures MX de calcium, strontium et baryum. Formation et propriétés cristallines. *Acta Crystallogr.* **1965**, *19*, 14−19.
(23) Lin, J.; Cherkashinin, G.; Schäfer, M.; Melinte, G.; Indris, S.; Kondrakov, A.; Janek, J.; Brezesinski, T.; Strauss, F. A High-Entropy Multicationic Substituted Lithium Argyrodite Superionic Solid Electrolyte. *ACS Mater. Lett.* **2022**, *4*, 2187−2194.
(24) Kraft, M. A.; Ohno, S.; Zinkevich, T.; Koerver, R.; Culver, S. P.; Fuchs, T.; Senyshyn, A.; Indris, S.; Morgan, B. J.; Zeier, W. G. Inducing High Ionic Conductivity in the Lithium Superionic Argyrodites Li6+xP1-xGeS5I for All-Solid-State Batteries. *J. Am. Chem. Soc.* **2018**, *140*, 16330−16339.
(25) Strauss, F.; Lin, J.; Duffiet, M.; Wang, K.; Zinkevich, T.; Hansen, A.-L.; Indris, S.; Brezesinski, T. High-Entropy Polyanionic Lithium Superionic Conductors. *ACS Mater. Lett.* **2022**, *4*, 418−423.
(26) Minafra, N.; Kraft, M. A.; Bernges, T.; Li, C.; Schlem, R.; Morgan, B. J.; Zeier, W. G. Local Charge Inhomogeneity and Lithium Distribution in the Superionic Argyrodites Li6PS5X (X = Cl, Br, I). *Inorg. Chem.* **2020**, *59*, 11009−11019.
(27) Zeng, Y.; Ouyang, B.; Liu, J.; Byeon, Y.-W.; Cai, Z.; Miara, L. J.; Wang, Y.; Ceder, G. High-entropy mechanism to boost ionic conductivity. *Science* **2022**, *378*, 1320−1324.
(28) Bérardan, D.; Franger, S.; Meena, A. K.; Dragoe, N. Room temperature lithium superionic conductivity in high entropy oxides. *J. Mater. Chem. A* **2016**, *4*, 9536−9541.
(29) Glaser, C.; Wei, Z.; Indris, S.; Klement, P.; Chatterjee, S.; Ehrenberg, H.; Zhao-Karger, Z.; Rohnke, M.; Janek, J. To Be or Not to Be − Is MgSc2Se4 a Mg-Ion Solid Electrolyte? *Adv. Energy Mater.* **2023**, *13*, No. 2301980.
(30) Huggins, R. A. Simple Method to Determine Electronic and Ionic Components of the Conductivity in Mixed Conductors a Review. *Ionics* **2002**, *8*, 300−313.
(31) Canepa, P.; Gautam, G. S.; Broberg, D.; Bo, S.-H.; Ceder, G. Role of Point Defects in Spinel Mg Chalcogenide Conductors. *Chem. Mater.* **2017**, *29*, 9657−9667.
(32) Kundu, S.; Solomatin, N.; Kauffmann, Y.; Kraytsberg, A.; Ein-Eli, Y. Revealing and Excluding the Root Cause of the Electronic Conductivity in Mg-ion MgSc2Se4 Solid Electrolyte. *Appl. Mater. Today* **2021**, *23*, No. 100998.
(33) Kundu, S.; Solomatin, N.; Kraytsberg, A.; Ein-Eli, Y. MgSc2Se4 Solid Electrolyte for Rechargeable Mg Batteries: An Electric Field-Assisted All-Solid-State Synthesis. *Energy Technol.* **2022**, *10*, No. 2200896.
(34) Yamada, Y.; Kanemitsu, Y. Electron-Phonon Interactions in Halide Perovskites. *NPG Asia Mater.* **2022**, *14*, No. 48.
(35) Wei, Z.; Maile, R.; Riegger, L. M.; Rohnke, M.; Müller-Buschbaum, K.; Janek, J. Ionic Liquid-Incorporated Metal-Organic Framework with High Magnesium Ion Conductivity for Quasi-Solid-State Magnesium Batteries. *Batteries Supercaps* **2022**, *5*, No. e202200318.
(36) Sotoudeh, M.; Groß, A. Stability of Magnesium Binary and Ternary Compounds for Batteries Determined from First Principles. *J. Phys. Chem. Lett.* **2022**, *13*, 10092−10100.
(37) Sotoudeh, M.; Dillenz, M.; Groß, A. Mechanism of Magnesium Transport in Spinel Chalcogenides. *Adv. Energy Sustainable Res.* **2021**, *2*, No. 2100113.
(38) van der Ven, A.; Ceder, G.; Asta, M.; Tepesch, P. D. First-principles theory of ionic diffusion with nondilute carriers. *Phys. Rev. B* **2001**, *64*, No. 184307.
(39) Sotoudeh, M.; Groß, A. Computational screening and descriptors for the ion mobility in energy storage materials. *Curr. Opin. Electrochem.* **2024**, *46*, No. 101494.
(40) Goldschmidt, V. M. Geochemische Verteilungsgesetze VIII. Bau und Eigenschaften von Krystallen. *Z. Phys. Chem.* **1927**, *127*, 446−454.
(41) Patrie, M.; Pardo, M. P.; Guittard, M.; Domange, L.; Flahaut, J. Nouveaux resultats relatifs a l'etude cristallographique des sulfures, seleniures et tellurures L2X3 des elements des terres rares, de l'yttrium et du scandium. *Colloq. Int. C. N. R. S.* **1967**, *157*, 397−405.
(42) Guittard, M.; Pardo, M. P.; Laruelle, P.; Flahaut, J. Les sulfures, seleniures et tellurures L2X3 de terres rares, d'yttrium et de scandium orthorhombiques du type Sc2S3. *Inorg. Chem.* **1965**, *4*, 970−973.
(43) Guittard, M.; Souleau, C.; Farsam, H. Sur Une Nouvelle Serie De Spinelles Selenies Des Terres Rares De l'yttrium Et Du Scandium. *C. R. Hebd. Acad. Sci.* **1964**, *259*, 2847−2849.
(44) Eick, H. A. The crystal structure and lattice parameters of some rare earth mono-seleno oxides. *Acta Crystallogr.* **1960**, *13*, 161.
(45) McCann, D. R.; Cartz, L. Bond distances and chain angle of hexagonal selenium at high pressure. *J. Appl. Phys.* **1972**, *43*, 4473−4477.
(46) Keller, R.; Holzapfel, W. B.; Schulz, H. Effect of pressure on the atom positions in Se and Te. *Phys. Rev. B* **1977**, *16*, No. 4404.
(47) Avilov, A. S.; Imanov, R. M. Structure of Selenium. *Sov. Phys. Crystallogr.* **1969**, *14*, 259−260.
(48) Fang, C. M.; Meetsma, A.; Wiegers, G. A. Crystal structure of erbium sesquiselenide, Er2Se3. *J. Alloys Compd.* **1995**, *218*, 224−227.
(49) Slovyanskikh, V. K.; Kuznetsov, N. T.; Gracheva, N. V. Lanthanide selenides Ln Se1.4+-x of the yttrium subgroup. *Russ. J. Inorg. Chem.* **1982**, *27*, 745−746.
(50) Jain, A.; Ong, S. P.; Hautier, G.; Chen, W.; Richards, W. D.; Dacek, S.; Cholia, S.; Gunter, D.; Skinner, D.; Ceder, G.; Persson, K. A. Commentary: The Materials Project: A Materials Genome Approach to Accelerating Materials Innovation. *APL Mater.* **2013**, *1*, No. 011002.
(51) Zhang, W.; Weber, D. A.; Weigand, H.; Arlt, T.; Manke, I.; Schröder, D.; Koerver, R.; Leichtweiss, T.; Hartmann, P.; Zeier, W. G.; Janek, J. Interfacial Processes and Influence of Composite Cathode Microstructure Controlling the Performance of All-Solid-State Lithium Batteries. *ACS Appl. Mater. Interfaces* **2017**, *9*, 17835−17845.
(52) Hohenberg, P.; Kohn, W. Inhomogeneous Electron Gas. *Phys. Rev.* **1964**, *136*, No. B864.
(53) Kohn, W.; Sham, L. J. Self-Consistent Equations Including Exchange and Correlation Effects. *Phys. Rev.* **1965**, *140*, No. A1133.
(54) Perdew, J. P.; Burke, K.; Ernzerhof, M. Generalized Gradient Approximation Made Simple. *Phys. Rev. Lett.* **1996**, *77*, No. 3865.
(55) Blöchl, P. E. Projector Augmented-Wave Method. *Phys. Rev. B* **1994**, *50*, No. 17953.
(56) Kresse, G.; Furthmüller, J. Efficient Iterative Schemes for Ab Initio Total-Energy Calculations Using a Plane-Wave Basis Set. *Phys. Rev. B* **1996**, *54*, No. 11169.
(57) Kresse, G.; Hafner, J. Ab Initio Molecular Dynamics for Liquid Metals. *Phys. Rev. B* **1993**, *47*, No. 558.
(58) Kresse, G.; Joubert, D. From Ultrasoft Pseudopotentials to the Projector Augmented-Wave Method. *Phys. Rev. B* **1999**, *59*, No. 1758.
(59) Henkelman, G.; Uberuaga, B. P.; Jónsson, H. A Climbing Image Nudged Elastic Band Method for Finding Saddle Points and Minimum Energy Paths. *J. Chem. Phys.* **2000**, *113*, 9901−9904.

https://doi.org/10.1021/acs.chemmater.5c00131
Chem. Mater. 2025, 37, 3353−3362

4 Conclusions

In this doctoral thesis, the Mg-ion transport properties of several ternary magnesium-based selenide spinels with the formula MgB_2Se_4 (B = Sc, Y, Ln) has been systematically studied from both an experimental and a computational point of view. Therefore, solid-state reaction routes for the synthesis of the spinels and reliable cell concepts for their electrochemical investigation as Mg-ion SEs were developed, as well as detailed DFT calculations were performed on the MgB_2Se_4 system.

In the first both publication of this dissertation, four spinels ($MgSc_2Se_4$, MgY_2Se_4, $MgEr_2Se_4$, and $MgTm_2Se_4$) were synthesized and studied as potential Mg-ion SEs. Among them, $MgSc_2Se_4$ was obtained in high purity (>95 wt%) from its elemental precursor powders by a facile one-step solid-state synthesis, while due to incomplete conversions and the formation of oxide impurities (6-13 wt%), a two-step solid-state route was developed in case of the other spinels. By replacing the Y, Er, and Tm powders with corresponding, less oxidation-prone metal chips and incorporating an additional reaction step via the binary selenides, the two-step procedure proved to be an effective way to reduce the oxide impurities (2-4 wt%) and increase the yield in these compounds.

After the successful syntheses, electrochemical characterization using EIS and DC polarization measurements revealed a moderate electronic conductivity ($\sigma_{el} = 3 \cdot 10^{-8}$-$5 \cdot 10^{-6}$ S cm) in the spinels. The electron transport may possibly arise from electron-conducting secondary phases, as suggest due to inhomogeneous Mg:B:Se element distributions at the surface of the spinel particles observed by TEM-EDS mapping, whereas also the contribution of electrons generated by point defects cannot be ruled out. However, regardless of the origin, electronic conduction in a SE can lead to battery self-discharge and dendrite formation, thereby representing a still open challenge for the application of these spinels.

Another challenge, addressed in this work, laid in the reliable proof of the long-range Mg^{2+}-ion transport capability of the MgB_2Se_4 spinels, which was not achieved by the few existing studies on $MgSc_2Se_4$. Using the same spinel as a pioneer material, the implementation of two independent methods, namely electrochemical deposition of Mg metal and reversible Mg plating/stripping cycling, demonstrated that in each case Mg-ions were transferred through the spinel layer from one to the other electrode. This unequivocally confirmed Mg-ion transport beyond short-range in the class of MgB_2Se_4 spinels for the first time. To tackle the difficulty of extracting the partial ionic conductivity of the mixed-conducting spinels, a symmetrical cell with pure Mg^{2+}-ion conducting interlayers between the spinel and the outer stainless-steel electrodes was developed. This straightforward concept turned out to effectively suppress the electron transport within the cell, thus allowing a precise determination of the spinels' high Mg-ion conductivities (σ_{ion} = 2-7$\cdot 10^{-5}$ S cm at 25 °C) and low Mg^{2+} migration barriers (E_a = 381-406 meV) by EIS measurements.

Driven by the good accordance between the obtained experimental and computational Mg^{2+} migration barriers of the four spinels, the execution of systematic DFT calculations on the

MgB_2Se_4 system revealed that as radius of the B^{3+}-ion increases, the spinel structure and hence the trigonal bottleneck of the migration path expands. This lowers the migration barrier and thus generally facilitates Mg-ion migration. However, it was also found that the B^{3+}-ion radius affects the degree of trigonal distortion of the octahedra, thereby changing the ratio of the volumes and of the Mg-Se distances (k_{64}) between octahedra and tetrahedra along the migration path. This in turn influences the kinetic (E_{KRA}) and static (ΔE) contributions of the overall migration barrier, which were identified to be linearly correlated to k_{64}. Consequently, dependent on the B^{3+}-ion, the right interplay between lattice expansion and trigonal distortion is important to achieve low Mg^{2+} migration barriers in the MgB_2Se_4 spinels.

In the final publication of this dissertation, the family of the electrochemically investigated Mg-based spinels was expanded by three further compounds, $MgYb_2Se_4$, $Mg_{0.75}Sc_2Se_{3.5}Br_{0.5}$, and $MgSc_{0.4}Y_{0.4}Er_{0.4}Tm_{0.4}Yb_{0.4}Se_4$, which were successfully synthesized via the two-step procedure. While with respect to the multianionic/multicationic compounds it was shown that the conducted multielement substitution in the MgB_2Se_4 system did not improve the ionic transport properties, $MgYb_2Se_4$ demonstrated the lowest Mg^{2+} migration barrier (E_a = 364 meV) and the highest room-temperature ionic conductivity ($\sigma_{ion} > 10^{-4}$ S cm^{-1}) among all studied spinels. This outstanding high magnesium ion mobility of $MgYb_2Se_4$ is proposed to be related to its exceptional low magnesium insertion energy, revealed by DFT calculations. Based on this, it is expected that the interactions between the magnesium ions and the host lattice are relatively weak, thereby facilitating the ionic transport through the $MgYb_2Se_4$ spinel. Therefore, this highlights that the magnesium insertion energy should also be considered when searching for MgB_2Se_4 spinels with high Mg-ion conductivity.

In addition to its outstanding ionic transport properties, $MgYb_2Se_4$ was found to exhibit a more than one order of magnitude lower electronic conductivity ($\sigma_{el} \approx 1 \cdot 10^{-9}$ S cm^{-1}) than its pioneers. Given by the identified high ionic conductivity, this results in an electronic transference number of $t_{el} = 7 \cdot 10^{-6}$, close to that of current alkali SEs [$t_{el}(\sigma_{el} << \sigma_{ion}) \approx \sigma_{el}/\sigma_{ion} = 10^{-8}$-$10^{-6}$].[18] Thus, the combination of its transport properties with the generally good oxidative stability (≥3.7 V vs. Mg^{2+}/Mg), observed for all investigated spinels, makes $MgYb_2Se_4$ one of the best candidates as Mg-ion SE to date.

In summary, this doctoral thesis represents the most comprehensive study on ternary magnesium-based selenide spinels as potential Mg-ion SEs so far. For the first time, long-range Mg^{2+}-ion conduction in this class of materials has been unequivocally proven and precisely determined by implementing straightforward and universal strategies. These allowed to reveal the excellent transport properties of $MgYb_2Se_4$ and pave the way for research into other mixed magnesium ion conductors. Moreover, the detailed computational studies expand the understanding of the Mg^{2+} migration in MgB_2Se_4 system and provide general guidelines for finding good spinel-type Mg-ion conductors.

5 Outlook

The findings presented in this doctoral thesis will surely open up several avenues for further research. This chapter briefly outlines the most relevant follow-up studies to further deepen the understanding of the transport properties of MgB_2Se_4 spinels.

i) Study on the Origin and Prevention of Electronic Conductivity

At present, the high electronic conductivity of the spinels investigated within this doctoral thesis is of concern, as it is $\geq 8 \cdot 10^{-4}$ times (except for $MgYb_2Se_4$ with $7 \cdot 10^{-6}$ times) the determined ionic conductivity and hence significantly higher than for currently used alkali SEs [$t_{el}(\sigma_{el} << \sigma_{ion}) \approx \sigma_{el}/\sigma_{ion} = 10^{-8}$-$10^{-6}$].[18] This may drastically reduce the performance of a battery by self-discharge and dendrite formation.[35,51] Therefore, it is crucial to uncover the origin of the electron conduction in this materials and to develop strategies for its prevention.

Previous studies on $MgSc_2Se_4$ propose that the electronic conductivity arises from the formation of point defects neutralized by electrons or from the presence of electron-conducting secondary phases.[36] Based on the results of this doctoral thesis, the latter in particular might be related to the inhomogeneous element distribution at the surface of the spinel particles as well as to the observed impurities of B_2Se_3 compounds, which become strong electronic conductors even at small stoichiometric deviations.[164] Similar findings were also reported for $MgSc_2Se_4$ by Kundu et al., who subsequently synthesized the spinel using an electric field-assisted method to reduce the evaporation of volatile Mg and Se from the surface of the particles and thus the formation of electronically conductive phases such as Sc and ScSe.[39] Applying this method lowered the electronic transference number to $t_{el} = 5 \cdot 10^{-6}$, but still not to the range of current SEs. Therefore, more effort is required to reach this range, for example, through a design-of-experiment study to optimize synthesis parameters, including the precursor mixing procedure and densification, heating/cooling rates, reaction atmosphere, etc. This will demonstrate whether the electronic transference number can be reduced further by minimizing the impurities, thereby revealing them to be the cause of the electronic conductivity.

If a higher purity of the spinels does not correlate with a reduced electronic transference number, the electronic conductivity is likely due to point defects, which may be difficult to address. Thus, to prevent electron conduction within an electrochemical cell, as demonstrated in this doctoral thesis, electron-blocking interlayers or also coatings can be a solution. However, these should be less expensive than the currently used metal-organic framework-based interlayers, which opens up another field of research.

ii) Investigations on Mg-Ion Diffusion

To gain further insights into the ionic transport properties of ternary Mg-based spinels, it is also essential to investigate their Mg-ion diffusion. For this purpose, ^{25}Mg NMR spin-lattice relaxation time measurements could be performed on the three ^{25}Mg-enriched, diamagnetic spinels ($^{25}MgSc_2S_4$, $^{25}MgSc_2Se_4$, and $^{25}MgY_2Se_4$), which have already been synthesized within the scope

of this doctoral thesis (see section A.4). These measurements enable, based on the observed relation times T_1, the calculation of the jump frequencies and thus in turn the determination of the Mg-ion diffusion coefficients of the spinels.[165] Moreover, the temperature and field dependence of T_1 might provide further information about the short-range migration barriers, the dimensionality of the diffusion, and correlation effects in the motion of the Mg-ions.[166] Considering these properties in dependence on the B-ion (Sc or Y) and the anion (Se or S) will surely deepen the understanding of how the spinel composition affects the Mg-ion transport.

Supplementary to the NMR spectroscopy, time-of-flight secondary ion mass spectrometry (ToF-SIMS) offers an additional technique for investigating the Mg-ion diffusion by tracer diffusion analysis. To this end, a possible approach would be to coat pellets of the pristine spinels $MgSc_2S_4$, $MgSc_2Se_4$, and MgY_2Se_4 with a thin layer of their ^{25}Mg-enriched analogues and a marker. By tracking the ^{25}Mg isotope diffusion from the coating/marker into the pellets with natural Mg composition (79% ^{24}Mg, 10% ^{25}Mg and 11% ^{26}Mg)[167], this might allow to estimate the Mg-ion diffusion coefficients of the spinels, also dependent on the temperature or on an electric field exposition.

iii) Advanced Theoretical Studies on the Ionic Transport Properties

According to the DFT calculations of this dissertation, it is proposed that the exceptionally high ionic conductivity and low Mg-ion migration barrier of $MgYb_2Se_4$ result from its anomalously low magnesium insertion energy, i.e., an easier reduction by magnesium, which might be related to the tendency of Yb^{3+} to be reduced to the more stable Yb^{2+} (filled 4f orbitals: $[Xe]4f^{14}$). However, how this affects the magnesium ion mobility in the spinel requires more advanced calculations. Thus, performing first-principles molecular dynamics and defect thermodynamic calculations in future studies may provide a more complete understanding of the potential reduction of Yb^{3+} and the compensating defects whose interaction might facilitate the magnesium ion transport in $MgYb_2Se_4$.

References

(1) United Nations Framework Convention on Climate Change. *Paris Agreement. Article 2(A)* **2015**.

(2) International Energy Agency. *World Energy Outlook 2023,* IEA, Paris **2023**. https://www.iea.org/reports/world-energy-outlook-2023 (accessed 07.11.2024).

(3) Gutsch, M.; Leker, J. Global Warming Potential of Lithium-Ion Battery Energy Storage Systems: A Review. *J. Energy Storage* **2022**, *52*, No. 105030. DOI: 10.1016/j.est.2022.105030.

(4) Crippa, M.; Guizzardi, D.; Pagani, F.; Schiavina, M.; Melchiorri, M.; Pisoni, E.; Graziosi, F.; Muntean, M.; Maes, J.; Dijkstra, L.; van Damme, M.; Clarisse, L.; Coheur, P. Insights into the Spatial Distribution of Global, National, and Subnational Greenhouse Gas Emissions in the Emissions Database for Global Atmospheric Research (EDGAR v8.0). *Earth Syst. Sci. Data* **2024**, *16*, 2811–2830. DOI: 10.5194/essd-16-2811-2024.

(5) Moriarty, P.; Wang, S. J. Can Electric Vehicles Deliver Energy and Carbon Reductions? *Energy Procedia* **2017**, *105*, 2983–2988. DOI: 10.1016/j.egypro.2017.03.713.

(6) Zhang, H.; Wang, L.; Li, H.; He, X. Criterion for Identifying Anodes for Practically Accessible High-Energy-Density Lithium-Ion Batteries. *ACS Energy Lett.* **2021**, *6*, 3719–3724. DOI: 10.1021/acsenergylett.1c01713.

(7) Deivanayagam, R.; Ingram, B. J.; Shahbazian-Yassar, R. Progress in Development of Electrolytes for Magnesium Batteries. *Energy Storage Mater.* **2019**, *21*, 136–153. DOI: 10.1016/j.ensm.2019.05.028.

(8) Corrigan, D. A. Electric Vehicle Batteries: Past, Present, and Future. *Electrochem. Soc. Interface* **2022**, *31*, 63–68. DOI: 10.1149/2.F09223IF.

(9) van Noorden, R. The Rechargeable Revolution: A Better Battery. *Nature* **2014**, *507*, 26–28. DOI: 10.1038/507026a.

(10) Fichtner, M. *Magnesium Batteries*; Royal Society of Chemistry: Cambridge **2019.** DOI: 10.1039/9781788016407.

(11) Muldoon, J.; Bucur, C. B.; Gregory, T. Quest for Nonaqueous Multivalent Secondary Batteries: Magnesium and Beyond. *Chem. Rev.* **2014**, *114*, 11683–11720. DOI: 10.1021/cr500049y.

(12) Canepa, P.; Sai Gautam, G.; Hannah, D. C.; Malik, R.; Liu, M.; Gallagher, K. G.; Persson, K. A.; Ceder, G. Odyssey of Multivalent Cathode Materials: Open Questions and Future Challenges. *Chem. Rev.* **2017**, *117*, 4287–4341. DOI: 10.1021/acs.chemrev.6b00614.

(13) Liu, F.; Wang, T.; Liu, X.; Fan, L.-Z. Challenges and Recent Progress on Key Materials for Rechargeable Magnesium Batteries. *Adv. Energy Mater.* **2021**, *11*, No. 2000787. DOI: 10.1002/aenm.202000787.

(14) Liang, Y.; Dong, H.; Aurbach, D.; Yao, Y. Current Status and Future Directions of Multivalent Metal-Ion Batteries. *Nat. Energy* **2020**, *5*, 646–656. DOI: 10.1038/s41560-020-0655-0.

(15) Aurbach, D.; Weissman, I.; Gofer, Y.; Levi, E. Nonaqueous Magnesium Electrochemistry and its Application in Secondary Batteries. *Chem. Rec.* **2003**, *3*, 61–73. DOI: 10.1002/tcr.10051.

(16) Lipson, A. L.; Han, S.-D.; Pan, B.; See, K. A.; Gewirth, A. A.; Liao, C.; Vaughey, J. T.; Ingram, B. J. Practical Stability Limits of Magnesium Electrolytes. *J. Electrochem. Soc.* **2016**, *163*, A2253-A2257. DOI: 10.1149/2.0451610jes.

(17) Lu, Z.; Schechter, A.; Moshkovich, M.; Aurbach, D. On the Electrochemical Behavior of Magnesium Electrodes in Polar Aprotic Electrolyte Solutions. *J. Electroanal. Chem.* **1999**, *466*, 203–217. DOI: 10.1016/S0022-0728(99)00146-1.

(18) Zhan, Y.; Zhang, W.; Lei, B.; Liu, H.; Li, W. Recent Development of Mg Ion Solid Electrolyte. *Front. Chem.* **2020**, *8*, No. 125. DOI: 10.3389/fchem.2020.00125.

(19) Zhao-Karger, Z.; Gil Bardaji, M. E.; Fuhr, O.; Fichtner, M. A New Class of Non-Corrosive, Highly Efficient Electrolytes for Rechargeable Magnesium Batteries. *J. Mater. Chem. A* **2017**, *5*, 10815–10820. DOI: 10.1039/c7ta02237a.

(20) Jaschin, P. W.; Gao, Y.; Li, Y.; Bo, S.-H. A Materials Perspective on Magnesium-Ion-Based Solid-State Electrolytes. *J. Mater. Chem. A* **2020**, *8*, 2875–2897. DOI: 10.1039/c9ta11729f.

(21) Sun, Q.; Luo, S.; Huang, R.; Liu, Q.; Yan, S.; Lin, X. Insights on Solid Electrolytes for Solid-State Magnesium Batteries: Progress and Prospects. *Energy Storage Mater.* **2024**, *70*, No. 103508. DOI: 10.1016/j.ensm.2024.103508.

(22) Ikeda, S.; Takahashi, M.; Ishikawa, J.; Ito, K. Solid Electrolytes with Multivalent Cation Conduction. 1. Conducting Species in Mg-Zr-PO_4 System. *Solid State Ion.* **1987**, *23*, 125–129. DOI: 10.1016/0167-2738(87)90091-9.

(23) Adamu, M.; Kale, G. M. Novel Sol–Gel Synthesis of $MgZr_4P_6O_{24}$ Composite Solid Electrolyte and Newer Insight into the Mg^{2+}-Ion Conducting Properties Using Impedance Spectroscopy. *J. Phys. Chem. C* **2016**, *120*, 17909–17915. DOI: 10.1021/acs.jpcc.6b05036.

(24) Kawamura, J.; Morota, K.; Kuwata, N.; Nakamura, Y.; Maekawa, H.; Hattori, T.; Imanaka, N.; Okazaki, Y.; Adachi, G. High Temperature ^{31}P NMR Study on Mg^{2+} Ion Conductors. *Solid State Commun.* **2001**, *120*, 295–298. DOI: 10.1016/S0038-1098(01)00386-6.

(25) Takeda, H.; Nakano, K.; Tanibata, N.; Nakayama, M. Novel Mg-Ion Conductive Oxide of μ-Cordierite $Mg_{0.6}Al_{1.2}Si_{1.8}O_6$. *Sci. Technol. Adv. Mater.* **2020**, *21*, 131–138. DOI: 10.1080/14686996.2020.1730237.

(26) Halim, Z. A.; Adnan, S.; Salleh, F. M.; Mohamed, N. S. Effects of Mg^{2+} Interstitial Ion on the Properties of $Mg_{0.5+x/2}Si_{2-x}Al_x(PO_4)_3$ Ceramic Electrolytes. *J. Magnes. Alloys* **2017**, *5*, 439–447. DOI: 10.1016/j.jma.2017.09.005.

(27) Yamanaka, T.; Hayashi, A.; Yamauchi, A.; Tatsumisago, M. Preparation of Magnesium Ion Conducting $MgS–P_2S_5–MgI_2$ Glasses by a Mechanochemical Technique. *Solid State Ion.* **2014**, *262*, 601–603. DOI: 10.1016/j.ssi.2013.10.037.

(28) Tomita, Y.; Saito, R.; Morishita, M.; Yamane, Y.; Kohno, Y. Synthesis, Crystal Structure and Ionic Conductivity of $MgAl_2X_8$ (X = Cl, Br). *Solid State Ion.* **2021**, *361*, No. 115566. DOI: 10.1016/j.ssi.2021.115566.

(29) Amdisen, M. B.; Grinderslev, J. B.; Skov, L. N.; Jensen, T. R. Methylamine Magnesium Borohydrides as Electrolytes for All-Solid-State Magnesium Batteries. *Chem. Mater.* **2023**, *35*, 1440–1448. DOI: 10.1021/acs.chemmater.2c03641.

(30) Wang, Q.; Li, H.; Zhang, R.; Liu, Z.; Deng, H.; Cen, W.; Yan, Y.; Chen, Y. Oxygen Vacancies Boosted Fast Mg^{2+} Migration in Solids at Room Temperature. *Energy Storage Mater.* **2022**, *51*, 630–637. DOI: 10.1016/j.ensm.2022.07.012.

(31) Pei, C.; Xiong, F.; Yin, Y.; Liu, Z.; Tang, H.; Sun, R.; An, Q.; Mai, L. Recent Progress and Challenges in the Optimization of Electrode Materials for Rechargeable Magnesium Batteries. *Small* **2021**, *17*, No. 2004108. DOI: 10.1002/smll.202004108.

(32) Canepa, P.; Bo, S.-H.; Sai Gautam, G.; Key, B.; Richards, W. D.; Shi, T.; Tian, Y.; Wang, Y.; Li, J.; Ceder, G. High Magnesium Mobility in Ternary Spinel Chalcogenides. *Nat. Commun.* **2017**, *8*, No. 1759. DOI: 10.1038/s41467-017-01772-1.

(33) Jamnik, J.; Maier, J. Treatment of the Impedance of Mixed Conductors Equivalent Circuit Model and Explicit Approximate Solutions. *J. Electrochem. Soc.* **1999**, *146*, 4183–4188. DOI: 10.1149/1.1392611.

(34) Jamnik, J.; Maier, J. Generalised Equivalent Circuits for Mass and Charge Transport: Chemical Capacitance and its Implications. *Phys. Chem. Chem. Phys.* **2001**, *3*, 1668–1678. DOI: 10.1039/b100180i.

(35) Dillenz, M.; Sotoudeh, M.; Glaser, C.; Janek, J.; Groß, A.; Euchner, H. Unravelling Charge Carrier Mobility in d_0-Metal-Based Spinels. *Batter. Supercaps* **2022**, *5*, No. e202200164. DOI: 10.1002/batt.202200164.

(36) Canepa, P.; Sai Gautam, G.; Broberg, D.; Bo, S.-H.; Ceder, G. Role of Point Defects in Spinel Mg Chalcogenide Conductors. *Chem. Mater.* **2017**, *29*, 9657–9667. DOI: 10.1021/acs.chemmater.7b02909.

(37) Wang, L.-P.; Zhao-Karger, Z.; Klein, F.; Chable, J.; Braun, T.; Schür, A. R.; Wang, C.-R.; Guo, Y.-G.; Fichtner, M. $MgSc_2Se_4$—A Magnesium Solid Ionic Conductor for All-Solid-State Mg Batteries? *ChemSusChem* **2019**, *12*, 2286–2293. DOI: 10.1002/cssc.201900225.

(38) Kundu, S.; Solomatin, N.; Kauffmann, Y.; Kraytsberg, A.; Ein-Eli, Y. Revealing and Excluding the Root Cause of the Electronic Conductivity in Mg-ion $MgSc_2Se_4$ Solid Electrolyte. *Appl. Mater. Today* **2021**, *23*, No. 100998. DOI: 10.1016/j.apmt.2021.100998.

(39) Kundu, S.; Solomatin, N.; Kraytsberg, A.; Ein-Eli, Y. $MgSc_2Se_4$ Solid Electrolyte for Rechargeable Mg Batteries: An Electric Field-Assisted All-Solid-State Synthesis. *Energy Tech.* **2022**, *10*, No. 2200896. DOI: 10.1002/ente.202200896.

(40) Dillenz, M.; Sotoudeh, M.; Euchner, H.; Groß, A. Screening of Charge Carrier Migration in the $MgSc_2Se_4$ Spinel Structure. *Front. Energy Res.* **2020**, *8*, No. 584654. DOI: 10.3389/fenrg.2020.584654.

(41) Sotoudeh, M.; Groß, A. Stability of Magnesium Binary and Ternary Compounds for Batteries Determined from First Principles. *J. Phys. Chem. Lett.* **2022**, *13*, 10092–10100. DOI: 10.1021/acs.jpclett.2c02316.

(42) Koettgen, J.; Bartel, C. J.; Ceder, G. Computational Investigation of Chalcogenide Spinel Conductors for All-Solid-State Mg Batteries. *Chem. Commun.* **2020**, *56*, 1952–1955. DOI: 10.1039/c9cc09510a.

(43) Glaser, C.; Wei, Z.; Indris, S.; Klement, P.; Chatterjee, S.; Ehrenberg, H.; Zhao-Karger, Z.; Rohnke, M.; Janek, J. To Be or Not to Be – Is $MgSc_2Se_4$ a Mg-Ion Solid Electrolyte? *Adv. Energy Mater.* **2023**, *13*, No. 2301980. DOI: 10.1002/aenm.202301980.

(44) Glaser, C.; Dillenz, M.; Sarkar, K.; Sotoudeh, M.; Wei, Z.; Indris, S.; Maile, R.; Rohnke, M.; Müller-Buschbaum, K.; Groß, A.; Janek, J. MgB_2Se_4 Spinels (B = Sc, Y, Er, Tm) as Potential Mg-Ion Solid Electrolytes – Partial Ionic Conductivity and the Ion Migration Barrier. *Adv. Energy Mater.* **2024**, *14*, No. 2402269. DOI: 10.1002/aenm.202402269.

(45) Glaser, C.; Sotoudeh, M.; Dillenz, M.; Sarkar, K.; Bark, J. S.; Singh, S.; Wei, Z.; Indris, S.; Müller, R.; Leopold, K.; Nazar, L. F.; Groß, A.; Janek, J. High Room-Temperature Magnesium Ion Conductivity in Spinel-Type $MgYb_2Se_4$ Solid Electrolyte. *Chem. Mater.* **2025**, *37*, 3353–3362. DOI: 10.1021/acs.chemmater.5c00131.

(46) York, M.; Larson, K.; Harris, K. C.; Carmona, E.; Albertus, P.; Sharma, R.; Noked, M.; Strauss, E.; Ragones, H.; Golodnitsky, D. Recent Advances in Solid-State Beyond Lithium Batteries. *J. Solid State Electrochem.* **2022**, *26*, 1851–1869. DOI: 10.1007/s10008-022-05223-w.

(47) Aurbach, D.; Schechter, A.; Moshkovich, M.; Cohen, Y. On the Mechanisms of Reversible Magnesium Deposition Processes. *J. Electrochem. Soc.* **2001**, *148*, A1004–A1014. DOI: 10.1149/1.1387980.

(48) Matsui, M. Study on Electrochemically Deposited Mg Metal. *J. Power Sources* **2011**, *196*, 7048–7055. DOI: 10.1016/j.jpowsour.2010.11.141.

(49) Wu, Y. A.; Yin, Z.; Farmand, M.; Yu, Y.-S.; Shapiro, D. A.; Liao, H.-G.; Liang, W.-I.; Chu, Y.-H.; Zheng, H. *In-situ* Multimodal Imaging and Spectroscopy of Mg Electrodeposition at Electrode-Electrolyte Interfaces. *Sci. Rep.* **2017**, *7*, No. 42527. DOI: 10.1038/srep42527.

(50) Davidson, R.; Verma, A.; Santos, D.; Hao, F.; Fincher, C.; Xiang, S.; van Buskirk, J.; Xie, K.; Pharr, M.; Mukherjee, P. P.; Banerjee, S. Formation of Magnesium Dendrites during Electrodeposition. *ACS Energy Lett.* **2019**, *4*, 375–376. DOI: 10.1021/acsenergylett.8b02470.

(51) Han, F.; Westover, A. S.; Yue, J.; Fan, X.; Wang, F.; Chi, M.; Leonard, D. N.; Dudney, N. J.; Wang, H.; Wang, C. High Electronic Conductivity as the Origin of Lithium Dendrite Formation within Solid Electrolytes. *Nat. Energy* **2019**, *4*, 187–196. DOI: 10.1038/s41560-018-0312-z.

(52) Shinde, S. S.; Wagh, N. K.; Kim, S.-H.; Lee, J.-H. Li, Na, K, Mg, Zn, Al, and Ca Anode Interface Chemistries Developed by Solid-State Electrolytes. *Adv. Sci.* **2023**, *10*, No. e2304235. DOI: 10.1002/advs.202304235.

(53) Palacin, M. R.; Johansson, P.; Dominko, R.; Dlugatch, B.; Aurbach, D.; Li, Z.; Fichtner, M.; Lužanin, O.; Bitenc, J.; Wei, Z.; Glaser, C.; Janek, J.; Fernández-Barquín, A.; Mainar, A. R.; Leonet, O.; Urdampilleta, I.; Blázquez, J. A.; Tchitchekova, D. S.; Ponrouch, A.; Canepa, P.; Gautam, G. S.; Casilda, R. S. R. G.; Martinez-Cisneros, C. S.; Torres, N. U.; Varez, A.; Sanchez, J.-Y.; Kravchyk, K. V.; Kovalenko, M. V.; Teck, A. A.; Shiel, H.; Stephens, I. E. L.; Ryan, M. P.; Zemlyanushin, E.; Dsoke, S.; Grieco, R.; Patil, N.; Marcilla, R.; Gao, X.; Carmalt, C. J.; He, G.; Titirici, M.-M. Roadmap on Multivalent Batteries. *J. Phys. Energy* **2024**, *6*, No. 031501. DOI: 10.1088/2515-7655/ad34fc.

(54) Samsonov, G. V. Mechanical Properties of the Elements. In *Handbook of the Physicochemical Properties of the Elements,* 1st ed.; Samsonov, G. V., Ed.; Springer US: Boston, MA **1968**; pp 387–446. DOI: 10.1007/978-1-4684-6066-7_7.

(55) Wen, T.; Deng, Y.; Qu, B.; Huang, G.; Song, J.; Xu, C.; Du, A.; Xie, Q.; Wang, J.; Cui, G.; Peng, D.-L.; Zhou, X.; Pan, F. Re-envisioning the Key Factors of Magnesium Metal Anodes for Rechargeable Magnesium Batteries. *ACS Energy Lett.* **2023**, *8*, 4848–4861. DOI: 10.1021/acsenergylett.3c01959.

(56) Huang, Y.; Zheng, S.; Liao, H.; Qiao, S.; Han, G.; Wang, G.; Huang, Z.; Li, J.; Lu, X.; Zhou, X. Synergistic Modulation of the Thermoelectric Performance of Melt-Spun p-Type Mg_2Sn via Na_2S and Si Alloying. *J. Mater. Chem. A* **2022**, *10*, 5452–5459. DOI: 10.1039/D1TA10582E.

(57) Tsukeda, T.; Nakagawa, T.; Moriwaki, M.; Kikura, K.; Sakurae, R.; Aida, T.; Tabata, H.; Kurihara, H.; Suzuki, M. Effect of Fabrication Parameter on Microstructure of Mg–5.3 mass%Al–3 mass%Ca for Development of Mg Rechargeable Batteries. *Mater. Trans.* **2022**, *63*, 408–414. DOI: 10.2320/matertrans.MT-MA2022008.

(58) Zhao, H. L.; Guan, S.; Zhang, C. X.; Zheng, F. Y.; Wang, L. G.; Li, Q. K. Rapidly Solidified AZ31 Magnesium Alloy Ribbons Used in Rechargeable Batteries. *MSF* **2005**, *488-489*, 291–294. DOI: 10.4028/www.scientific.net/MSF.488-489.291.

(59) Wenzel, S.; Leichtweiss, T.; Krüger, D.; Sann, J.; Janek, J. Interphase Formation on Lithium Solid Electrolytes – An In Situ Approach to Study Interfacial Reactions by Photoelectron Spectroscopy. *Solid State Ion.* **2015**, *278*, 98–105. DOI: 10.1016/j.ssi.2015.06.001.

(60) Wang, Q.; Li, H.; Xu, T.; Chen, Y.; Yan, Y. Understanding Mg-Ion Deposition Behavior on MgBi Alloy in Solid-State Form. *Energy Mater.* **2025**, *5*, No. 500022. DOI: 10.20517/energymater.2024.102.

(61) Chen, K.-J.; Hung, F.-Y.; He, Y.-T. Charge-Discharge Properties of Sputtered Mg Anode in Flexible All-Solid-State Mg-Ion Batteries. *ACS omega* **2022**, *7*, 43161–43168. DOI: 10.1021/acsomega.2c05843.

(62) Wei, Z.; Singh, D. K.; Helmbrecht, K.; Sann, J.; Yusim, Y.; Kieser, J. A.; Glaser, C.; Rohnke, M.; Groß, A.; Janek, J. In Situ Observation of Room-Temperature Magnesium Metal Deposition on a NASICON/IL Hybrid Solid Electrolyte. *Adv. Energy Mater.* **2023**, *13*, No. 2302525. DOI: 10.1002/aenm.202302525.

(63) Ortmann, T.; Justus Liebig University Giessen. The Sodium Metal Electrode and its Interface with Inorganic Solid Electrolytes for Solid-State Batteries, Justus-Liebig-Universität Gießen **2024**.

(64) Yim, T.; Woo, S.-G.; Lim, S.-H.; Yoo, J.-Y.; Cho, W.; Park, M.-S.; Han, Y.-K.; Kim, Y.-J.; Yu, J. Magnesium Anode Pretreatment Using a Titanium Complex for Magnesium Battery. *ACS Sustainable Chem. Eng.* **2017**, *5*, 5733–5739. DOI: 10.1021/acssuschemeng.7b00306.

(65) Liang, Y.; Feng, R.; Yang, S.; Ma, H.; Liang, J.; Chen, J. Rechargeable Mg Batteries with Graphene-like MoS_2 Cathode and Ultrasmall Mg Nanoparticle Anode. *Adv. Mater.* **2011**, *23*, 640–643. DOI: 10.1002/adma.201003560.

(66) You, C.; Wu, X.; Yuan, X.; Chen, Y.; Liu, L.; Zhu, Y.; Fu, L.; Wu, Y.; Guo, Y.-G.; van Ree, T. Advances in Rechargeable Mg Batteries. *J. Mater. Chem. A* **2020**, *8*, 25601–25625. DOI: 10.1039/D0TA09330K.

(67) Li, B.; Masse, R.; Liu, C.; Hu, Y.; Li, W.; Zhang, G.; Cao, G. Kinetic Surface Control for Improved Magnesium-Electrolyte Interfaces for Magnesium Ion Batteries. *Energy Storage Mater.* **2019**, *22*, 96–104. DOI: 10.1016/j.ensm.2019.06.035.

(68) Son, S.-B.; Gao, T.; Harvey, S. P.; Steirer, K. X.; Stokes, A.; Norman, A.; Wang, C.; Cresce, A.; Xu, K.; Ban, C. An Artificial Interphase Enables Reversible Magnesium Chemistry in Carbonate Electrolytes. *Nat. Chem.* **2018**, *10*, 532–539. DOI: 10.1038/s41557-018-0019-6.

(69) Wu, N.; Yin, Y.-X.; Guo, Y.-G. Size-Dependent Electrochemical Magnesium Storage Performance of Spinel Lithium Titanate. *Chem. Asian J.* **2014**, *9*, 2099–2102. DOI: 10.1002/asia.201402286.

(70) Luo, L.; Zhen, Y.; Lu, Y.; Zhou, K.; Huang, J.; Huang, Z.; Mathur, S.; Hong, Z. Structural Evolution from Layered $Na_2Ti_3O_7$ to $Na_2Ti_6O_{13}$ Nanowires Enabling a Highly Reversible Anode for Mg-Ion Batteries. *Nanoscale* **2020**, *12*, 230–238. DOI: 10.1039/C9NR08003A.

(71) Zeng, J.; Yang, Y.; Li, C.; Li, J.; Huang, J.; Wang, J.; Zhao, J. Li_3VO_4: An Insertion Anode Material for Magnesium Ion Batteries with High Specific Capacity. *Electrochim. Acta* **2017**, *247*, 265–270. DOI: 10.1016/j.electacta.2017.06.143.

(72) Shao, Y.; Gu, M.; Li, X.; Nie, Z.; Zuo, P.; Li, G.; Liu, T.; Xiao, J.; Cheng, Y.; Wang, C.; Zhang, J.-G.; Liu, J. Highly Reversible Mg Insertion in Nanostructured Bi for Mg Ion Batteries. *Nano Lett.* **2014**, *14*, 255–260. DOI: 10.1021/nl403874y.

(73) Yaghoobnejad Asl, H.; Fu, J.; Kumar, H.; Welborn, S. S.; Shenoy, V. B.; Detsi, E. In Situ Dealloying of Bulk Mg_2Sn in Mg-Ion Half Cell as an Effective Route to Nanostructured Sn for High Performance Mg-Ion Battery Anodes. *Chem. Mater.* **2018**, *30*, 1815–1824. DOI: 10.1021/acs.chemmater.7b04124.

(74) Pandeeswari, J.; Jenisha, G.; Walle, K. Z.; Kotobuki, M. Recent Research Progress on All-Solid-State Mg Batteries. *Batteries* **2023**, *9*, No. 570. DOI: 10.3390/batteries9120570.

(75) Pereira-Ramos, J. P.; Messina, R.; Perichon, J. Electrochemical Formation of a Magnesium Vanadium Bronze $Mg_xV_2O_5$ in Sulfone-Based Electrolytes at 150°C. *J. Electroanal. Chem. Interfacial Electrochem.* **1987**, *218*, 241–249. DOI: 10.1016/0022-0728(87)87019-5.

(76) Verrelli, R.; Black, A. P.; Pattanathummasid, C.; Tchitchekova, D. S.; Ponrouch, A.; Oró-Solé, J.; Frontera, C.; Bardé, F.; Rozier, P.; Palacín, M. R. On the Strange Case of Divalent Ions Intercalation in V_2O_5. *J. Power Sources* **2018**, *407*, 162–172. DOI: 10.1016/j.jpowsour.2018.08.024.

(77) Gershinsky, G.; Yoo, H. D.; Gofer, Y.; Aurbach, D. Electrochemical and Spectroscopic Analysis of Mg^{2+} Intercalation into Thin Film Electrodes of Layered Oxides: V_2O_5 and MoO_3. *Langmuir* **2013**, *29*, 10964–10972. DOI: 10.1021/la402391f.

(78) Spahr, M. E.; Novák, P.; Haas, O.; Nesper, R. Electrochemical Insertion of Lithium, Sodium, and Magnesium in Molybdenum(VI) Oxide. *J. Power Sources* **1995**, *54*, 346–351. DOI: 10.1016/0378-7753(94)02099-O.

(79) Sian, T. S.; Reddy, G. B.; Shivaprasad, S. M. Effect of Microstructure and Stoichiometry on Absorption in Mg Intercalated MoO_3 Thin Films. *Electrochem. Solid-State Lett.* **2006**, *9*, A120–A122. DOI: 10.1149/1.2163427.

(80) Icaza, J. C.; Haasch, R. T.; Guduru, R. K. Effect of Ion Size and Charge Density on the Electrochemical Characteristics of α-MoO_3 Using Aqueous Be^{2+} and Mg^{2+} Sulfate Electrolytes. *J. Alloys Compd.* **2018**, *740*, 88–95. DOI: 10.1016/j.jallcom.2017.12.377.

(81) Ling, C.; Zhang, R.; Arthur, T. S.; Mizuno, F. How General is the Conversion Reaction in Mg Battery Cathode: A Case Study of the Magnesiation of α-MnO_2. *Chem. Mater.* **2015**, *27*, 5799–5807. DOI: 10.1021/acs.chemmater.5b02488.

(82) Tian, Y.; Zeng, G.; Rutt, A.; Shi, T.; Kim, H.; Wang, J.; Koettgen, J.; Sun, Y.; Ouyang, B.; Chen, T.; Lun, Z.; Rong, Z.; Persson, K.; Ceder, G. Promises and Challenges of Next-Generation "Beyond Li-Ion" Batteries for Electric Vehicles and Grid Decarbonization. *Chem. Rev.* **2021**, *121*, 1623–1669. DOI: 10.1021/acs.chemrev.0c00767.

(83) Aurbach, D.; Lu, Z.; Schechter, A.; Gofer, Y.; Gizbar, H.; Turgeman, R.; Cohen, Y.; Moshkovich, M.; Levi, E. Prototype Systems for Rechargeable Magnesium Batteries. *Nature* **2000**, *407*, 724–727. DOI: 10.1038/35037553.

(84) Aurbach, D.; Suresh, G. S.; Levi, E.; Mitelman, A.; Mizrahi, O.; Chusid, O.; Brunelli, M. Progress in Rechargeable Magnesium Battery Technology. *Adv. Mater.* **2007**, *19*, 4260–4267. DOI: 10.1002/adma.200701495.

(85) Levi, E.; Lancry, E.; Mitelman, A.; Aurbach, D.; Ceder, G.; Morgan, D.; Isnard, O. Phase Diagram of Mg Insertion into Chevrel Phases, $Mg_xMo_6T_8$ (T = S, Se). 1. Crystal Structure of the Sulfides. *Chem. Mater.* **2006**, *18*, 5492–5503. DOI: 10.1021/cm061656f.

(86) Levi, E.; Lancry, E.; Mitelman, A.; Aurbach, D.; Isnard, O.; Djurado, D. Phase Diagram of Mg Insertion into Chevrel Phases, $Mg_xMo_6T_8$ (T = S, Se). 2. The Crystal Structure of Triclinic $MgMo_6Se_8$. *Chem. Mater.* **2006**, *18*, 3705–3714. DOI: 10.1021/cm060715m.

(87) Sun, X.; Bonnick, P.; Duffort, V.; Liu, M.; Rong, Z.; Persson, K. A.; Ceder, G.; Nazar, L. F. A High Capacity Thiospinel Cathode for Mg Batteries. *Energy Environ. Sci.* **2016**, *9*, 2273–2277. DOI: 10.1039/c6ee00724d.

(88) Gu, Y.; Katsura, Y.; Yoshino, T.; Takagi, H.; Taniguchi, K. Rechargeable Magnesium-Ion Battery Based on a $TiSe_2$-Cathode with d-p Orbital Hybridized Electronic Structure. *Sci. Rep.* **2015**, *5*, No. 12486. DOI: 10.1038/srep12486.

(89) Sun, X.; Bonnick, P.; Nazar, L. F. Layered TiS_2 Positive Electrode for Mg Batteries. *ACS Energy Lett.* **2016**, *1*, 297–301. DOI: 10.1021/acsenergylett.6b00145.

(90) Pei, C.; Yin, Y.; Sun, R.; Xiong, F.; Liao, X.; Tang, H.; Tan, S.; Zhao, Y.; An, Q.; Mai, L. Interchain-Expanded Vanadium Tetrasulfide with Fast Kinetics for Rechargeable Magnesium Batteries. *ACS Appl. Mater. Interfaces* **2019**, *11*, 31954–31961. DOI: 10.1021/acsami.9b09592.

(91) Shen, Y.; Wang, Y.; Miao, Y.; Yang, M.; Zhao, X.; Shen, X. High-Energy Interlayer-Expanded Copper Sulfide Cathode Material in Non-Corrosive Electrolyte for Rechargeable Magnesium Batteries. *Adv. Mater.* **2020**, *32*, No. e1905524. DOI: 10.1002/adma.201905524.

(92) Liu, B.; Luo, T.; Mu, G.; Wang, X.; Di Chen; Shen, G. Rechargeable Mg-Ion Batteries Based on WSe_2 Nanowire Cathodes. *ACS nano* **2013**, *7*, 8051–8058. DOI: 10.1021/nn4032454.

(93) Makino, K.; Katayama, Y.; Miura, T.; Kishi, T. Electrochemical Insertion of Magnesium to $Mg_{0.5}Ti_2(PO_4)_3$. *J. Power Sources* **2001**, *99*, 66–69. DOI: 10.1016/S0378-7753(01)00480-3.

(94) Zeng, J.; Yang, Y.; Lai, S.; Huang, J.; Zhang, Y.; Wang, J.; Zhao, J. A Promising High-Voltage Cathode Material Based on Mesoporous $Na_3V_2(PO_4)_3$/C for Rechargeable Magnesium Batteries. *Chem. Eur. J.* **2017**, *23*, 16898–16905. DOI: 10.1002/chem.201704303.

(95) Lipson, A. L.; Han, S.-D.; Kim, S.; Pan, B.; Sa, N.; Liao, C.; Fister, T. T.; Burrell, A. K.; Vaughey, J. T.; Ingram, B. J. Nickel Hexacyanoferrate, a Versatile Intercalation Host for Divalent Ions from Nonaqueous Electrolytes. *J. Power Sources* **2016**, *325*, 646–652. DOI: 10.1016/j.jpowsour.2016.06.019.

(96) Kim, D.-M.; Kim, Y.; Arumugam, D.; Woo, S. W.; Jo, Y. N.; Park, M.-S.; Kim, Y.-J.; Choi, N.-S.; Lee, K. T. Co-Intercalation of Mg^{2+} and Na^+ in $Na_{0.69}Fe_2(CN)_6$ as a High-Voltage Cathode for Magnesium Batteries. *ACS Appl. Mater. Interfaces* **2016**, *8*, 8554–8560. DOI: 10.1021/acsami.6b01352.

(97) Chae, M. S.; Hyoung, J.; Jang, M.; Lee, H.; Hong, S.-T. Potassium Nickel Hexacyanoferrate as a High-Voltage Cathode Material for Nonaqueous Magnesium-Ion Batteries. *J. Power Sources* **2017**, *363*, 269–276. DOI: 10.1016/j.jpowsour.2017.07.094.

(98) Pan, B.; Zhou, D.; Huang, J.; Zhang, L.; Burrell, A. K.; Vaughey, J. T.; Zhang, Z.; Liao, C. 2,5-Dimethoxy-1,4-Benzoquinone (DMBQ) as Organic Cathode for Rechargeable Magnesium-Ion Batteries. *J. Electrochem. Soc.* **2016**, *163*, A580-A583. DOI: 10.1149/2.0021605jes.

(99) Janek, J.; Zeier, W. G. Challenges in Speeding up Solid-State Battery Development. *Nat. Energy* **2023**, *8*, 230–240. DOI: 10.1038/s41560-023-01208-9.

(100) Higashi, S.; Miwa, K.; Aoki, M.; Takechi, K. A Novel Inorganic Solid State Ion Conductor for Rechargeable Mg Batteries. *Chem. Commun.* **2014**, *50*, 1320–1322. DOI: 10.1039/c3cc47097k.

(101) FIZ Karlsruhe. *Inorganic Crystal Structure Database (ICSD)*. https://icsd.fiz-karlsruhe.de / (accessed 07.11.2024).

(102) Anuar, N. K.; Adnan, S. B. R. S.; Jaafar, M. H.; Mohamed, N. S. Studies on Structural and Electrical Properties of $Mg_{0.5+y}(Zr_{2-y}Fe_y)_2(PO_4)_3$ Ceramic Electrolytes. *Ionics* **2016**, *22*, 1125–1133. DOI: 10.1007/s11581-015-1623-8.

(103) Anuar, N. K.; Mohamed, N. S. Structural and Electrical Properties of Novel $Mg_{0.9+0.5y}Zn_{0.4}Al_yZr_{1.6-y}(PO_4)_3$ Ceramic Electrolytes Synthesized via Nitrate Sol–Gel Method. *J. Sol-Gel. Sci. Technol.* **2016**, *80*, 249–258. DOI: 10.1007/s10971-016-4091-3.

(104) Kajihara, K.; Nagano, H.; Tsujita, T.; Munakata, H.; Kanamura, K. High-Temperature Conductivity Measurements of Magnesium-Ion-Conducting Solid Oxide $Mg_{0.5-x}(Zr_{1-x}Nb_x)_2(PO_4)_3$ (x = 0.15) Using Mg Metal Electrodes. *J. Electrochem. Soc.* **2017**, *164*, A2183–A2185. DOI: 10.1149/2.1691709jes.

(105) Matsuo, M.; Oguchi, H.; Sato, T.; Takamura, H.; Tsuchida, E.; Ikeshoji, T.; Orimo, S. Sodium and Magnesium Ionic Conduction in Complex Hydrides. *J. Alloys Compd.* **2013**, *580*, S98-S101. DOI: 10.1016/j.jallcom.2013.01.058.

(106) Unemoto, A.; Matsuo, M.; Orimo, S. Complex Hydrides for Electrochemical Energy Storage. *Adv. Funct. Mater.* **2014**, *24*, 2267–2279. DOI: 10.1002/adfm.201303147.

(107) Skov, L. N.; Grinderslev, J. B.; Rosenkranz, A.; Lee, Y.-S.; Jensen, T. R. Towards Solid-State Magnesium Batteries: Ligand-Assisted Superionic Conductivity. *Batter. Supercaps* **2022**, *5*, No. e202200163. DOI: 10.1002/batt.202200163.

(108) Yan, Y.; Grinderslev, J. B.; Jørgensen, M.; Skov, L. N.; Skibsted, J.; Jensen, T. R. Ammine Magnesium Borohydride Nanocomposites for All-Solid-State Magnesium Batteries. *ACS Appl. Energy Mater.* **2020**, *3*, 9264–9270. DOI: 10.1021/acsaem.0c01599.

(109) Roedern, E.; Kühnel, R.-S.; Remhof, A.; Battaglia, C. Magnesium Ethylenediamine Borohydride as Solid-State Electrolyte for Magnesium Batteries. *Sci. Rep.* **2017**, *7*, No. 46189. DOI: 10.1038/srep46189.

(110) Le Ruyet, R.; Fleutot, B.; Berthelot, R.; Benabed, Y.; Hautier, G.; Filinchuk, Y.; Janot, R. $Mg_3(BH_4)_4(NH_2)_2$ as Inorganic Solid Electrolyte with High Mg^{2+} Ionic Conductivity. *ACS Appl. Energy Mater.* **2020**, *3*, 6093–6097. DOI: 10.1021/acsaem.0c00980.

(111) Nguyen, H.; Banerjee, A.; Wang, X.; Tan, D.; Wu, E. A.; Doux, J.-M.; Stephens, R.; Verbist, G.; Meng, Y. S. Single-Step Synthesis of Highly Conductive Na_3PS_4 Solid Electrolyte for Sodium All Solid-State Batteries. *J. Power Sources* **2019**, *435*, No. 126623. DOI: 10.1016/j.jpowsour.2019.05.031.

(112) Kondo, S.; Takada, K.; Yamamura, Y. New Lithium Ion Conductors Based on Li_2S-SiS_2 System. *Solid State Ion.* **1992**, *53-56*, 1183–1186. DOI: 10.1016/0167-2738(92)90310-L.

(113) Kennedy, J.; Sahami, S.; Shea, S.; Zhang, Z. Preparation and Conductivity Measurements of SiS_2-Li_2S Glasses Doped with LiBr and LiCl. *Solid State Ion.* **1986**, *18-19*, 368–371. DOI: 10.1016/0167-2738(86)90142-6.

(114) Deiseroth, H.-J.; Kong, S.-T.; Eckert, H.; Vannahme, J.; Reiner, C.; Zaiß, T.; Schlosser, M. Li_6PS_5X: A Class of Crystalline Li-Rich Solids with an Unusually High Li^+ Mobility. *Angew. Chem.* **2008**, *120*, 767–770. DOI: 10.1002/ange.200703900.

(115) Schlem, R.; Ghidiu, M.; Culver, S. P.; Hansen, A.-L.; Zeier, W. G. Changing the Static and Dynamic Lattice Effects for the Improvement of the Ionic Transport Properties within the Argyrodite $Li_6PS_{5-x}Se_xI$. *ACS Appl. Energy Mater.* **2020**, *3*, 9–18. DOI: 10.1021/acsaem.9b01794.

(116) Liu, Z.; Tang, Y.; Wang, Y.; Huang, F. High Performance Li_2S–P_2S_5 Solid Electrolyte Induced by Selenide. *J. Power Sources* **2014**, *260*, 264–267. DOI: 10.1016/j.jpowsour.2014.03.036.

(117) Ujiie, S.; Hayashi, A.; Tatsumisago, M. Structure, Ionic Conductivity and Electrochemical Stability of Li_2S–P_2S_5–LiI Glass and Glass–Ceramic Electrolytes. *Solid State Ion.* **2012**, *211*, 42–45. DOI: 10.1016/j.ssi.2012.01.017.

(118) Yang, X.; Gupta, S.; Chen, Y.; Sari, D.; Hau, H.-M.; Cai, Z.; Dun, C.; Qi, M.; Ma, L.; Liu, Y.; Urban, J. J.; Ceder, G. Fast Room-Temperature Mg-Ion Conduction in Clay-Like Halide Glassy Electrolytes. *Adv. Energy Mater.* **2024**, *14*, No. 2400163. DOI: 10.1002/aenm.202400163.

(119) Famprikis, T.; Canepa, P.; Dawson, J. A.; Islam, M. S.; Masquelier, C. Fundamentals of Inorganic Solid-State Electrolytes for Batteries. *Nat. Mater.* **2019**, *18*, 1278–1291. DOI: 10.1038/s41563-019-0431-3.

(120) Song, T.; Lin, Y.; Da Wang; Chen, Q.; Ling, C.; Shi, S. Renewing Fundamental Understanding of Ionic Transport in Inorganic Crystalline Solid-State Electrolytes from the Perspective of Lattice Dynamics. *Adv. Energy Mater.* **2024**, *14*, No. 2302440. DOI: 10.1002/aenm.202302440.

(121) Iton, Z. W. B.; See, K. A. Multivalent Ion Conduction in Inorganic Solids. *Chem. Mater.* **2022**, *34*, 881–898. DOI: 10.1021/acs.chemmater.1c04178.

(122) Ohno, S.; Banik, A.; Dewald, G. F.; Kraft, M. A.; Krauskopf, T.; Minafra, N.; Till, P.; Weiss, M.; Zeier, W. G. Materials Design of Ionic Conductors for Solid State Batteries. *Prog. Energy* **2020**, *2*, No. 022001. DOI: 10.1088/2516-1083/ab73dd.

(123) Culver, S. P.; Koerver, R.; Krauskopf, T.; Zeier, W. G. Designing Ionic Conductors: The Interplay between Structural Phenomena and Interfaces in Thiophosphate-Based Solid-State Batteries. *Chem. Mater.* **2018**, *30*, 4179–4192. DOI: 10.1021/acs.chemmater.8b01293.

(124) Sai Gautam, G.; Canepa, P.; Urban, A.; Bo, S.-H.; Ceder, G. Influence of Inversion on Mg Mobility and Electrochemistry in Spinels. *Chem. Mater.* **2017**, *29*, 7918–7930. DOI: 10.1021/acs.chemmater.7b02820.

(125) Bachman, J. C.; Muy, S.; Grimaud, A.; Chang, H.-H.; Pour, N.; Lux, S. F.; Paschos, O.; Maglia, F.; Lupart, S.; Lamp, P.; Giordano, L.; Shao-Horn, Y. Inorganic Solid-State

Electrolytes for Lithium Batteries: Mechanisms and Properties Governing Ion Conduction. *Chem. Rev.* **2016**, *116*, 140–162. DOI: 10.1021/acs.chemrev.5b00563.

(126) Malik, R.; Burch, D.; Bazant, M.; Ceder, G. Particle Size Dependence of the Ionic Diffusivity. *Nano Lett.* **2010**, *10*, 4123–4127. DOI: 10.1021/nl1023595.

(127) Li, Z.; Liu, P.; Zhu, K.; Zhang, Z.; Si, Y.; Wang, Y.; Jiao, L. Solid-State Electrolytes for Sodium Metal Batteries. *Energy Fuels* **2021**, *35*, 9063–9079. DOI: 10.1021/acs.energyfuels.1c00347.

(128) Levi, E.; Levi, M. D.; Chasid, O.; Aurbach, D. A Review on the Problems of the Solid State Ions Diffusion in Cathodes for Rechargeable Mg Batteries. *J. Electroceram.* **2009**, *22*, 13–19. DOI: 10.1007/s10832-007-9370-5.

(129) Jain, A.; Ong, S. P.; Hautier, G.; Chen, W.; Richards, W. D.; Dacek, S.; Cholia, S.; Gunter, D.; Skinner, D.; Ceder, G.; Persson, K. A. Commentary: The Materials Project: A Materials Genome Approach to Accelerating Materials Innovation. *APL Mater.* **2013**, *1*, No. 011002. DOI: 10.1063/1.4812323.

(130) Rong, Z.; Malik, R.; Canepa, P.; Sai Gautam, G.; Liu, M.; Jain, A.; Persson, K.; Ceder, G. Materials Design Rules for Multivalent Ion Mobility in Intercalation Structures. *Chem. Mater.* **2015**, *27*, 6016–6021. DOI: 10.1021/acs.chemmater.5b02342.

(131) Evans, M. G.; Polanyi, M. Inertia and Driving Force of Chemical Reactions. *Trans. Faraday Soc.* **1938**, *34*, 11–24. DOI: 10.1039/tf9383400011.

(132) van der Ven, A.; Ceder, G.; Asta, M.; Tepesch, P. D. First-Principles Theory of Ionic Diffusion with Nondilute Carriers. *Phys. Rev. B* **2001**, *64*, No. 184307. DOI: 10.1103/PhysRevB.64.184307.

(133) Guo, M.; Yuan, C.; Zhang, T.; Yu, X. Solid-State Electrolytes for Rechargeable Magnesium-Ion Batteries: From Structure to Mechanism. *Small* **2022**, *18*, No. e2106981. DOI: 10.1002/smll.202106981.

(134) Wang, C.; Xu, B. B.; Zhang, X.; Sun, W.; Chen, J.; Pan, H.; Yan, M.; Jiang, Y. Ion Hopping: Design Principles for Strategies to Improve Ionic Conductivity for Inorganic Solid Electrolytes. *Small* **2022**, *18*, No. e2107064. DOI: 10.1002/smll.202107064.

(135) Shannon, R. D. Revised Effective Ionic Radii and Systematic Studies of Interatomic Distances in Halides and Chalcogenides. *Acta Crystallogr., Sect. A: Fond. Crystallogr.* **1976**, *32*, 751–767. DOI: 10.1107/S0567739476001551.

(136) Kraft, M. A.; Culver, S. P.; Calderon, M.; Böcher, F.; Krauskopf, T.; Senyshyn, A.; Dietrich, C.; Zevalkink, A.; Janek, J.; Zeier, W. G. Influence of Lattice Polarizability on the Ionic Conductivity in the Lithium Superionic Argyrodites Li_6PS_5X (X = Cl, Br, I). *J. Am. Chem. Soc.* **2017**, *139*, 10909–10918. DOI: 10.1021/jacs.7b06327.

(137) Tamura, S.; Yamane, M.; Hoshino, Y.; Imanaka, N. Highly Conducting Divalent Mg^{2+} Cation Solid Electrolytes with Well-Ordered Three-Dimensional Network Structure. *J. Solid State Chem.* **2016**, *235*, 7–11. DOI: 10.1016/j.jssc.2015.12.008.

(138) Jansen, M. Volume Effect or Paddle-Wheel Mechanism—Fast Alkali-Metal Ionic Conduction in Solids with Rotationally Disordered Complex Anions. *Angew. Chem. Int. Ed. Engl.* **1991**, *30*, 1547–1558. DOI: 10.1002/anie.199115471.

(139) Wilmer, D.; Funke, K.; Witschas, M.; Banhatti, R. D.; Jansen, M.; Korus, G.; Fitter, J.; Lechner, R. E. Anion Reorientation in an Ion Conducting Plastic Crystal – Coherent Quasielastic Neutron Scattering from Sodium Ortho-Phosphate. *Phys. B: Condens. Matter* **1999**, *266*, 60–68. DOI: 10.1016/S0921-4526(98)01494-X.

(140) Karlsson, L. Mechanisms of Ionic Conduction in Li_2SO_4 and $LiNaSO_4$: Paddle Wheel or Percolation? *Solid State Ion.* **1995**, *76*, 301–308. DOI: 10.1016/0167-2738(94)00278-Z.

(141) Martinolich, A. J.; Lee, C.-W.; Lu, I.-T.; Bevilacqua, S. C.; Preefer, M. B.; Bernardi, M.; Schleife, A.; See, K. A. Solid-State Divalent Ion Conduction in $ZnPS_3$. *Chem. Mater.* **2019**, *31*, 3652–3661. DOI: 10.1021/acs.chemmater.9b00207.

(142) Smith, J. G.; Siegel, D. J. Low-Temperature Paddlewheel Effect in Glassy Solid Electrolytes. *Nat. Commun.* **2020**, *11*, No. 1483. DOI: 10.1038/s41467-020-15245-5.

(143) Zhang, Z.; Li, H.; Kaup, K.; Zhou, L.; Roy, P.-N.; Nazar, L. F. Targeting Superionic Conductivity by Turning on Anion Rotation at Room Temperature in Fast Ion Conductors. *Matter* **2020**, *2*, 1667–1684. DOI: 10.1016/j.matt.2020.04.027.

(144) Zhou, L.; Assoud, A.; Shyamsunder, A.; Huq, A.; Zhang, Q.; Hartmann, P.; Kulisch, J.; Nazar, L. F. An Entropically Stabilized Fast-Ion Conductor: $Li_{3.25}[Si_{0.25}P_{0.75}]S_4$. *Chem. Mater.* **2019**, *31*, 7801–7811. DOI: 10.1021/acs.chemmater.9b00657.

(145) Rickert, H. Mobility, Diffusion and Partial Conductivity of Ions and Electrons. In *Electrochemistry of Solids*; Jørgensen, C. K., Lappert, M. F., Lippard, S. J., Margrave, J. L., Niedenzu, K., Nöth, H., Parry, R. W., Yamatera, H., Rickert, H., Eds.; Inorganic Chemistry Concepts; Springer Berlin Heidelberg: Berlin, Heidelberg **1982**; pp 79–117. DOI: 10.1007/978-3-642-68312-1_6.

(146) Tubandt, C. Über einseitige Ionen-und gemischte Stromleitung in Kristallen. *Z. Elektrochem. Angew. Phys. Chem.* **1920**, *26*, 358–363. DOI: 10.1002/bbpc.19200261703.

(147) Tubandt, C. Über Elektrizitätsleitung in festen kristallisierten Verbindungen. Zweite Mitteilung. Überführung und Wanderung der Ionen in einheitlichen festen Elektrolyten. *Z. Anorg. Allg. Chem.* **1921**, *115*, 105–126. DOI: 10.1002/zaac.19211150106.

(148) Takahashi, T.; Ikeda, S.; Yamamoto, O. Solid-State Ionics—Solids with High Ionic Conductivity in the Systems Silver Iodide-Silver Oxyacid Salts. *J. Electrochem. Soc.* **1972**, *119*, 477–482. DOI: 10.1149/1.2404235.

(149) Huggins, R. A. Simple Method to Determine Electronic and Ionic Components of the Conductivity in Mixed Conductors a Review. *Ionics* **2002**, *8*, 300–313. DOI: 10.1007/BF02376083.

(150) Neiman, A. Y.; Pestereva, N. N.; Zhou, Y.; Nechaev, D. O.; Koteneva, E. A.; Vanec, K.; Higgins, B.; Volkova, N. A.; Korchuganova, I. G. The Nature and the Mechanism of Ion Transfer in Tungstates $Me^{2+}\{WO_4\}$ (Ca, Sr, Ba) and $Me_2^{3+}\{WO_4\}_3$ (Al, Sc, In) According to the Data Acquired by the Tubandt Method. *Russ. J. Electrochem.* **2013**, *49*, 895–907. DOI: 10.1134/S1023193512120075.

(151) Bottelberghs, P. H.; Everts, E. Charge Carriers and DC Polarization Phenomena in Solid Na_2WO_4. *J. Solid State Chem.* **1975**, *14*, 342–348. DOI: 10.1016/0022-4596(75)90053-5.

(152) Pestereva, N. N.; Vyatkin, I. A.; Lopatin, D. A.; Guseva, A. F. Nature of Ionic Conductivity of Lanthanide Tungstates with Imperfect Scheelite Structure. *Russ. J. Electrochem.* **2016**, *52*, 1082–1089. DOI: 10.1134/S1023193516110094.

(153) Mizzoni, M. S. Correlation of Dielectric Dispersions with Electronic and Ionic Conduction Mechanisms in Glass. *J. Electrochem. Soc.* **1973**, *120*, 1592–1595. DOI: 10.1149/1.2403310.

(154) Sokolov, I. A.; Murin, I. V.; Wiemhöfer, H.-D.; Pronkin, A. A. The Nature of Current Carriers and Electric Conductivity in the $PbCl_2$-2PbO • SiO_2 Glasses. *Glass Phys. Chem.* **2000**, *26*, 148–157. DOI: 10.1007/BF02735960.

(155) Riess, I. Review of the Limitation of the Hebb-Wagner Polarization Method for Measuring Partial Conductivities in Mixed Ionic Electronic Conductors. *Solid State Ion.* **1996**, *91*, 221–232. DOI: 10.1016/S0167-2738(96)83022-0.

(156) Wang, S.; Yan, M.; Li, Y.; Vinado, C.; Yang, J. Separating Electronic and Ionic Conductivity in Mix-Conducting Layered Lithium Transition-Metal Oxides. *J. Power Sources* **2018**, *393*, 75–82. DOI: 10.1016/j.jpowsour.2018.05.005.

(157) Shao, B.; Huang, Y.; Han, F. Electronic Conductivity of Lithium Solid Electrolytes. *Adv. Energy Mater.* **2023**, *13*, No. 2204098. DOI: 10.1002/aenm.202204098.

(158) Hebb, M. H. Electrical Conductivity of Silver Sulfide. *J. Chem. Phys.* **1952**, *20*, 185–190. DOI: 10.1063/1.1700165.

(159) Lee, K.-R.; Lee, J.-H.; Yoo, H.-I. Reassessment of Conventional Polarization Technique to Measure Partial Electronic Conductivity of Electrolytes. *Solid State Ion.* **2010**, *181*, 724–729. DOI: 10.1016/j.ssi.2010.03.015.

(160) Huggins, R. A. General Equivalent Circuit of Batteries and Fuel Cells. *Ionics* **1999**, *5*, 269–274. DOI: 10.1007/BF02375850.

(161) Cherkashinin, G.; Hausbrand, R.; Jaegermann, W. Performance of Li-Ion Batteries: Contribution of Electronic Factors to the Battery Voltage. *J. Electrochem. Soc.* **2019**, *166*, A5308-A5312. DOI: 10.1149/2.0441903jes.

(162) Thangadurai, V.; Weppner, W. Determination of the Sodium Ion Transference Number of the Dion−Jacobson-Type Layered Perovskite $NaCa_2Nb_3O_{10}$ Using AC Impedance and DC Methods. *Chem. Mater.* **2002**, *14*, 1136–1143. DOI: 10.1021/cm011189w.

(163) Bumberger, A. E.; Nenning, A.; Fleig, J. Transmission Line Revisited – The Impedance of Mixed Ionic and Electronic Conductors. *Phys. Chem. Chem. Phys.* **2024**, *26*, 15068–15089. DOI: 10.1039/d4cp00975d.

(164) Bergmann, H.; Hein, H.; Kuhn, P.; Vetter, U.; Czack, G.; Koch, E.; Warkentin, E. *Sc, Y, La-Lu Rare Earth Elements C 9*; Springer Berlin Heidelberg: Berlin, Heidelberg **1985.** DOI: 10.1007/978-3-662-06345-3.

(165) Kaus, M.; Guin, M.; Yavuz, M.; Knapp, M.; Tietz, F.; Guillon, O.; Ehrenberg, H.; Indris, S. Fast Na^+ Ion Conduction in NASICON-Type $Na_{3.4}Sc_2(SiO_4)_{0.4}(PO_4)_{2.6}$ Observed by ^{23}Na NMR Relaxometry. *J. Phys. Chem. C* **2017**, *121*, 1449–1454. DOI: 10.1021/acs.jpcc.6b10523.

(166) Heitjans, P.; Indris, S. Diffusion and Ionic Conduction in Nanocrystalline Ceramics. *J. Phys.: Condens. Matter* **2003**, *15*, R1257-R1289. DOI: 10.1088/0953-8984/15/30/202.

(167) Audi, G.; Bersillon, O.; Blachot, J.; Wapstra, A. H. The Nubase Evaluation of Nuclear and Decay Properties. *Nucl. Phys. A* **2003**, *729*, 3–128. DOI: 10.1016/j.nuclphysa.2003.11.001.

(168) Werner, S.; Glaser, C.; Kasper, T.; Lê, T. N. N.; Gross, S.; Smarsly, B. M. H_2S Dosimetry by CuO: Towards Stable Sensors by Unravelling the Underlying Solid-State Chemistry. *Chem. Eur. J.* **2022**, *28*, No. e202103437. DOI: 10.1002/chem.202103437.

Appendix

A Supporting Information

A.1 Publication 1: "To be or not to be – Is $MgSc_2Se_4$ a Mg-Ion Solid Electrolyte?"

ADVANCED ENERGY MATERIALS

Supporting Information

for *Adv. Energy Mater.*, DOI 10.1002/aenm.202301980

To Be or Not to Be – Is $MgSc_2Se_4$ a Mg-Ion Solid Electrolyte?

*Clarissa Glaser, Zhixuan Wei, Sylvio Indris, Philip Klement, Sangam Chatterjee, Helmut Ehrenberg, Zhirong Zhao-Karger, Marcus Rohnke and Jürgen Janek**

WILEY-VCH

Supporting Information

To be or not to be – Is $MgSc_2Se_4$ a Mg-Ion Solid Electrolyte?

*Clarissa Glaser, Zhixuan Wei, Sylvio Indris, Philip Klement, Sangam Chatterjee, Helmut Ehrenberg, Zhirong Zhao-Karger, Marcus Rohnke and Jürgen Janek**

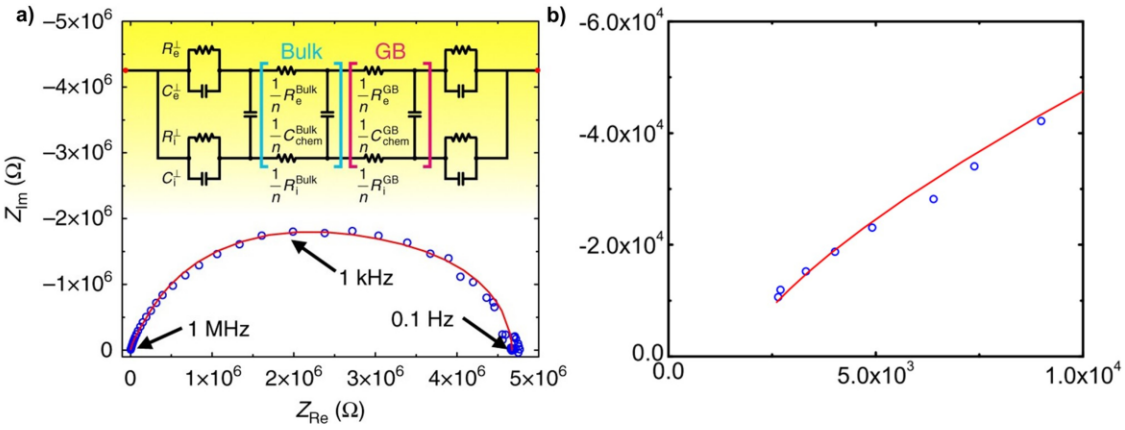

Figure S1. a) Impedance spectrum of a Ta|$MgSc_2Se_4$|Ta cell, and the equivalent circuit utilized by Canepa et al.[1] for fitting their impedance data. The observed data is shown in blue circles and the fit is displayed in red. The equivalent circuit utilizes two Jamnik-Maier elements,[2,3] which the authors tentatively attributed to contributions from bulk and grain boundary, respectively; b) shows the Nyquist plot in a) at low Re(Z) with a red fit when using only one Jamnik-Maier element in the equivalent circuit. Reproduced under terms of the CC-BY 4.0 license.[1] Copyright © 2017**,** P. Canepa et al., Nature Commun. 2017, published by Springer Nature.

Note: Canepa et al.[1] assumed that the intercept of the Re(Z) axis at high frequency represents the ionic and electronic resistance contributions in parallel and consequently calculated the ionic conductivity from the intercept. Independent from the utilized equivalent circuit (one or two Jamnik-Maier elements, **Figure S1**), there is a lack of data points at the high frequency range (> 1 MHz) which inevitably leads to a poor fit in this area. Since the impedance values become smaller at higher frequencies, this ends up in a large error of the intercept resistance, potentially larger than the intercept resistance itself. For this reason, we consider the evaluation of ionic conductivity in this way to be not reliable.

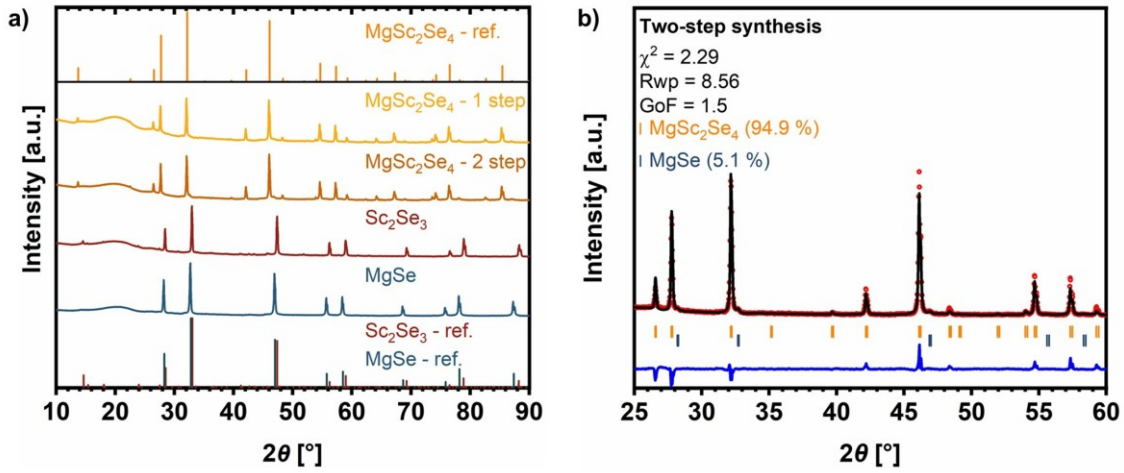

Figure S2. a) XRD patterns of synthesized MgSe, Sc_2Se_3 and $MgSc_2Se_4$ (via one- and two-step procedure) compared with simulated reference patterns; b) Rietveld refinement, based on the XRD pattern for via two-steps synthesized $MgSc_2Se_4$. The observed and calculated curves are shown in red and black in the top, and the difference curve is shown in blue.

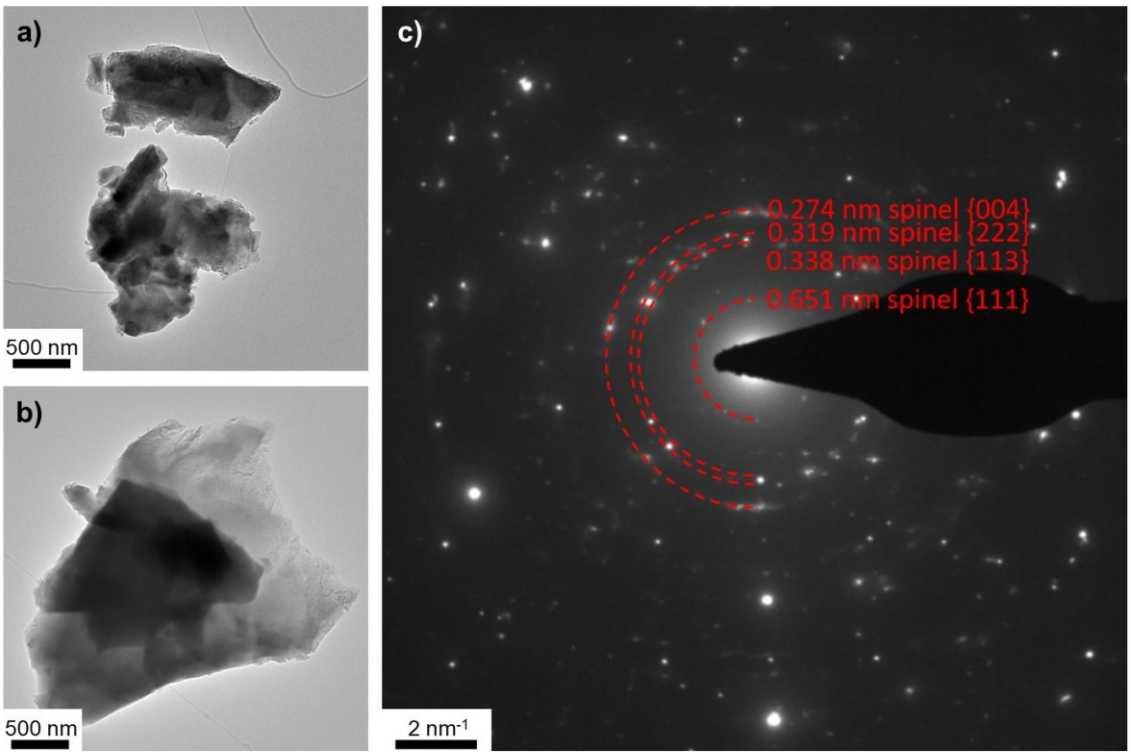

Figure S3. a-b) TEM images of via one-step synthesized $MgSc_2Se_4$ with particles size from 1-3 µm. c) The SAED pattern confirms the spinel phase.

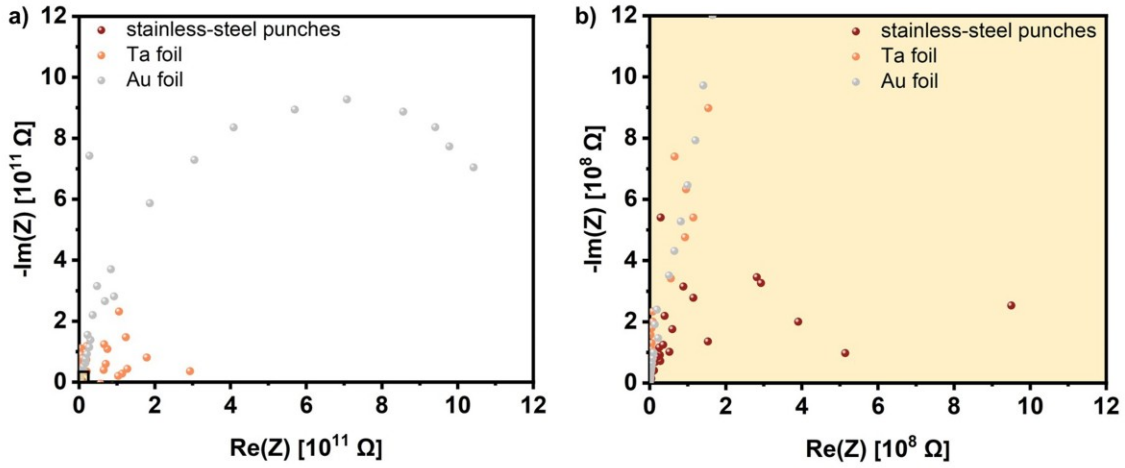

Figure S4. a) Nyquist plot of different Me|$MgSc_2Se_4$|Me press cells (Me = stainless-steel, Ta, Au) in the frequency range of 7 MHz to 100 mHz at 25 °C and b) zoomed-in view of the higher frequency range. The poor physical contact using ion-blocking foils or punches was probably caused by rough pellet and electrode surfaces.

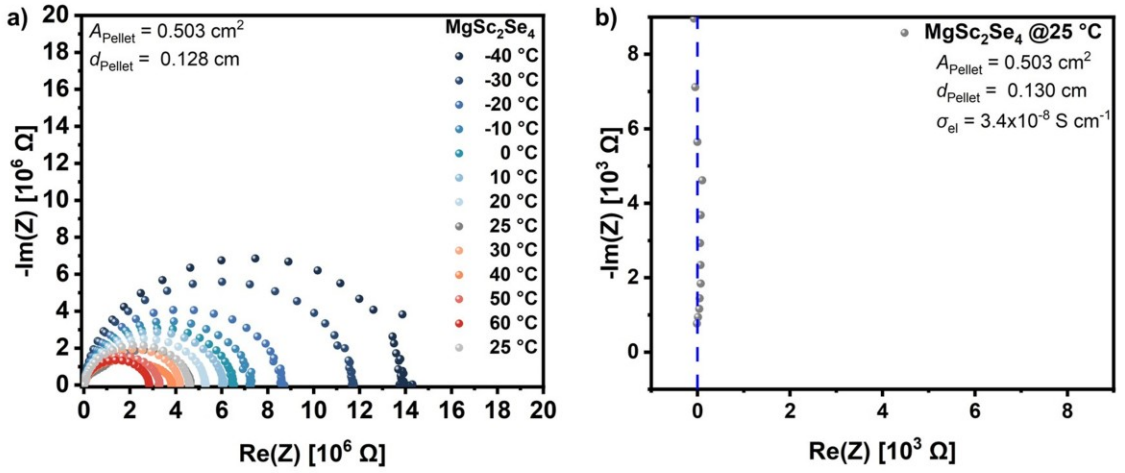

Figure S5. a) Nyquist plots at different temperatures ranging from –40 to 60 °C of an Au|$MgSc_2Se_4$|Au pouch cell in the frequency range of 7 MHz to 100 mHz; b) a zoomed-in view of Nyquist plot of **Figure 2a** shows no offset of the semicircle at high frequencies (0.7-7 MHz).

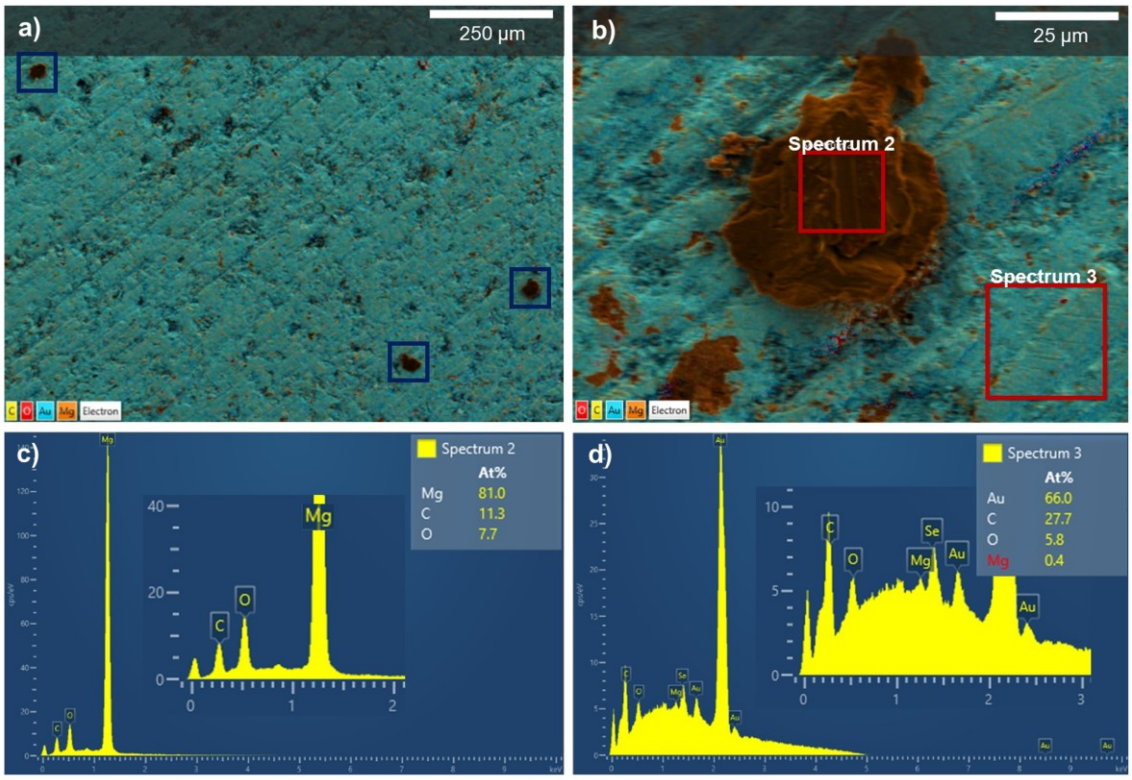

Figure S6. a) EDS map of Au electrode backside after Mg plating in a Mg|$MgSc_2Se_4$|Au cell shows three of the plated Mg spots labeled with blue boxes; b) EDS map of a deposited Mg particle and c-d) spectra of the red marked areas in b) confirming that the deposited particle is not a contamination from the $MgSc_2Se_4$ pellet.

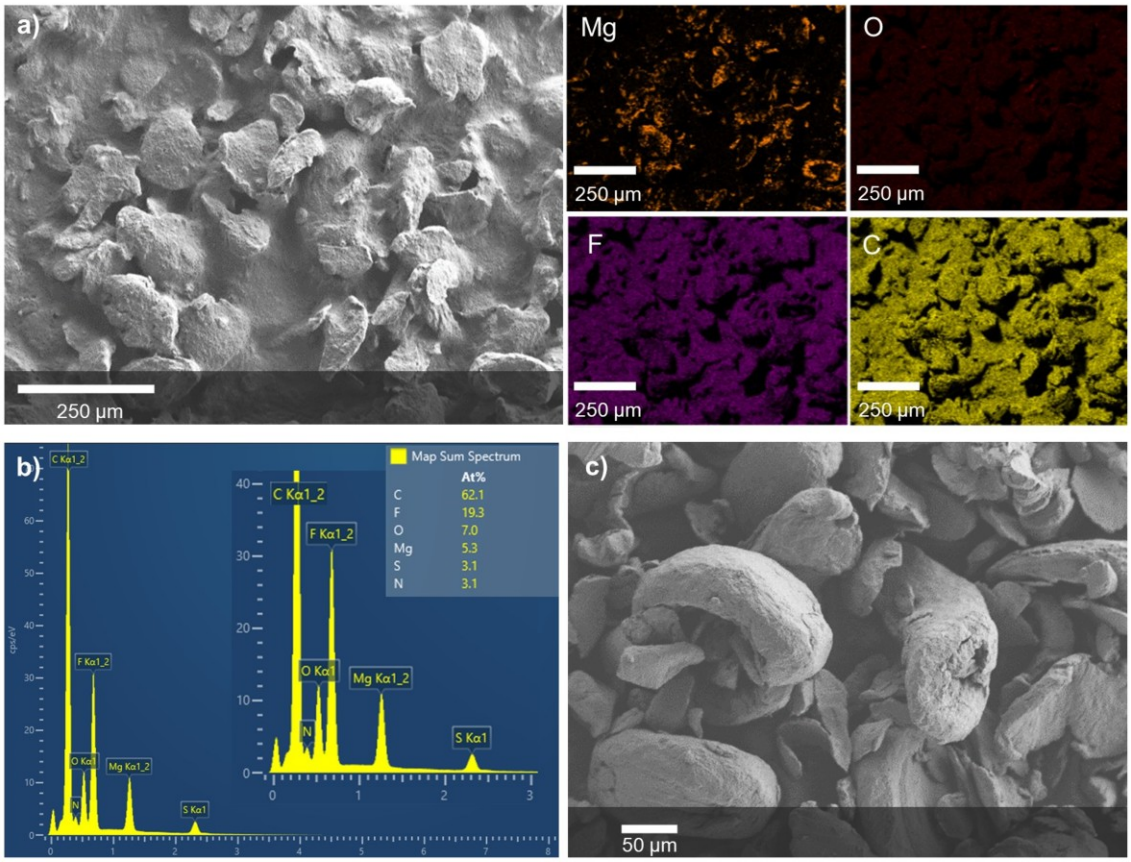

Figure S7. a) SEM image and elemental EDS maps of the Mg-slurry electrode of the Mg|$MgSc_2Se_4$|Au cell; b) observed elements from Mg-slurry electrode and c) SEM image of commercial Mg powder.

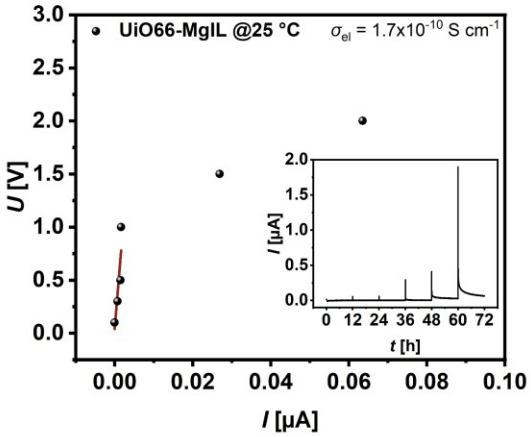

Figure S8. DC polarization data from a SS|UiO66-MgIL|SS cell obtained at different voltages (0.1, 0.3, 0.5, 1.0, 1.5 and 2.0 V, held for 12 h, shown in the inset) with linear fit (red) of the equilibrium values (with exclusion of the last two values) to determine the electronic DC resistance at 25 °C.

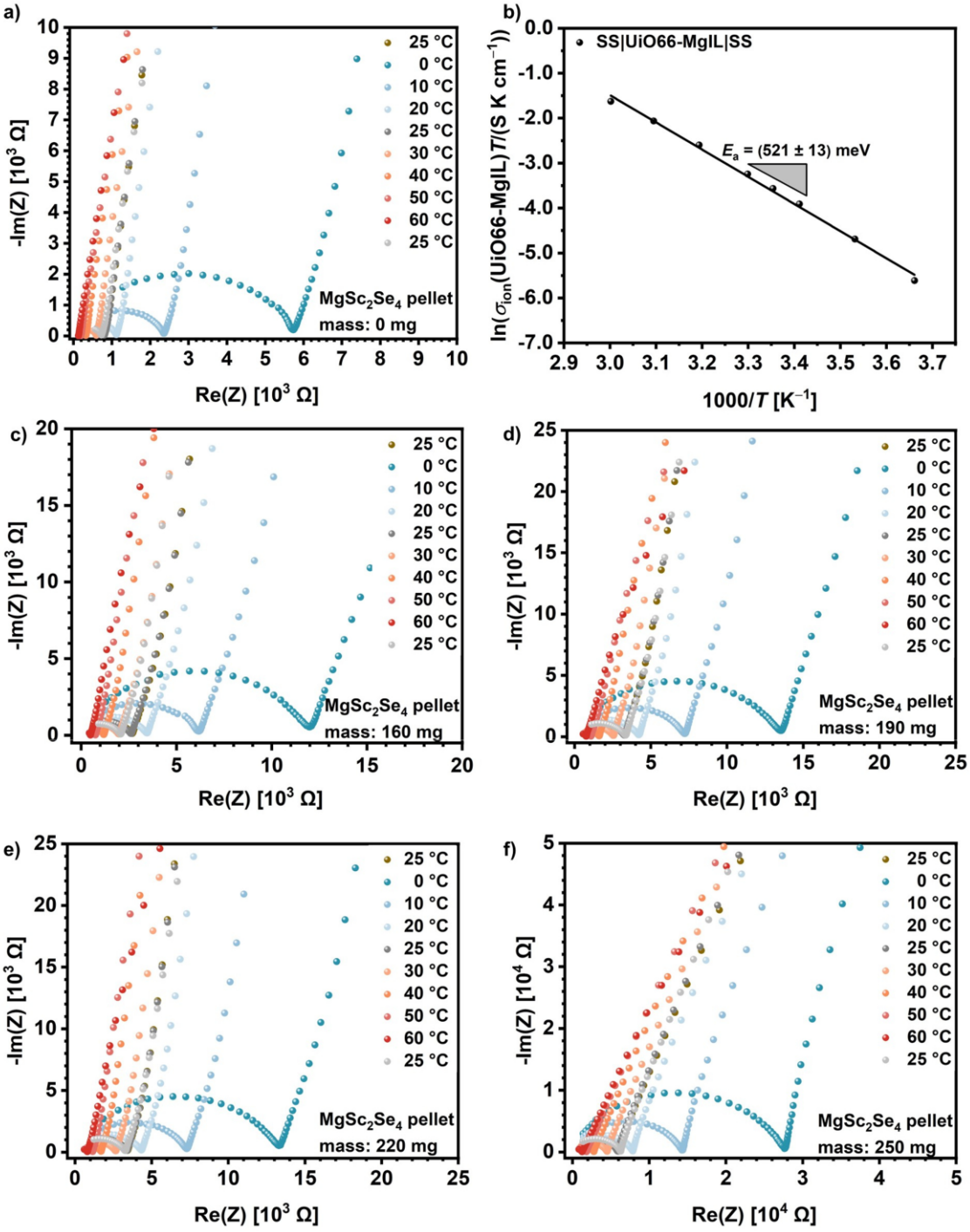

Figure S9. a) Nyquist plots of SS|UiO66-MgIL|SS cell at different temperatures ranging from 0 to 60 °C and b) corresponding Arrhenius plot; c-f) Nyquist plots of SS|UiO66-MgIL|$MgSc_2Se_4$|UiO66-MgIL|SS cells with different amount/pellet thickness of spinel at different temperatures ranging from 0 to 60 °C.

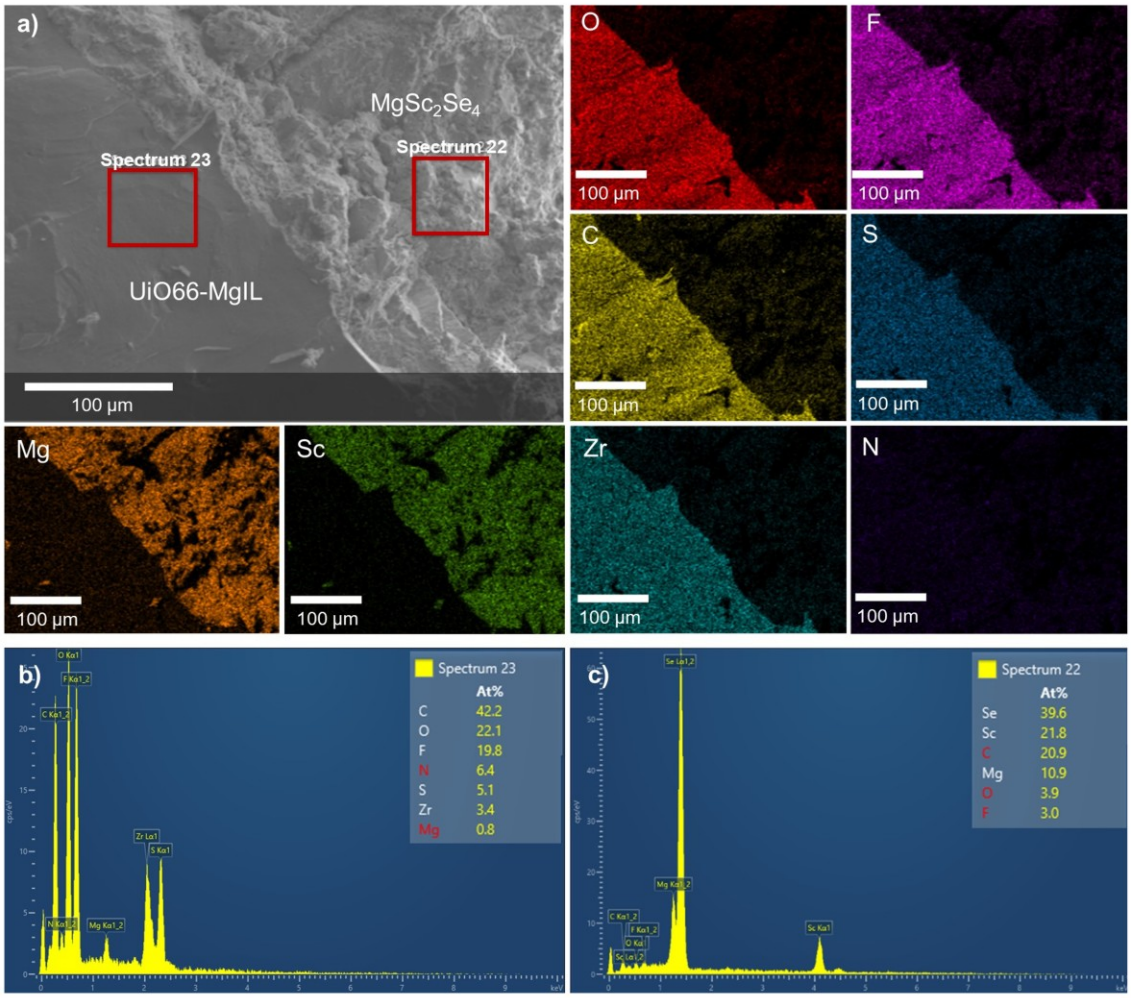

Figure S10. a) SEM image and elemental EDS maps of the UiO66-MgIL|$MgSc_2Se_4$|UiO66-MgIL pellet cross section showing one UiO66-MgIL layer (bottom left corner) pressed onto the 160 mg $MgSc_2Se_4$ pellet (upper right corner) after disassembling the cell; b) and c) show observed elements in spectrum 23 (UiO66-MgIL layer) and spectrum 22 ($MgSc_2Se_4$ pellet) confirming that the IL (containing F, N and S) does not penetrate the $MgSc_2Se_4$ pellet. Red labeled elements overlap with each other or have ≤ 3 at% which is below the detection limit.

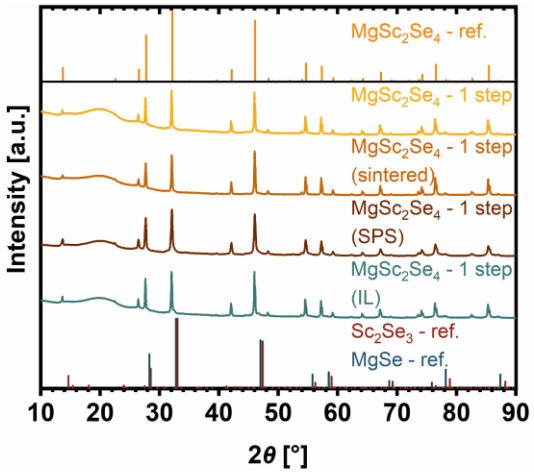

Figure S11. Comparison of XRD patterns of untreated, at 950 °C for 6 h vacuum sintered (sintered pellet), at 800 °C for 10 min spark plasma sintered (SPS pellet) and one week in IL soaked $MgSc_2Se_4$ powder. After the various treatments of the one-step synthesized $MgSc_2Se_4$, the spinel structure is retained and no new secondary phases appear.

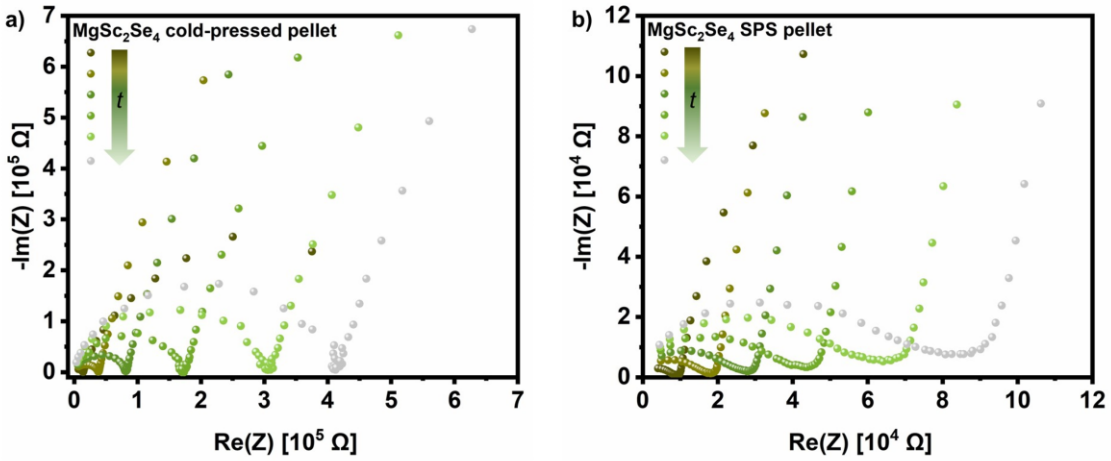

Figure S12. Nyquist plots at different times *t* (0, 2, 4, 6, 8 and 10 h) after assembling of a SS|MgBhfip|$MgSc_2Se_4$|MgBhfip|SS cell with a) $MgSc_2Se_4$ cold-pressed pellet (Ø = 10 mm, *d* = 2.14 mm) and b) $MgSc_2Se_4$ SPS pellet (Ø = 9.78 mm, *d* = 1.58 mm).

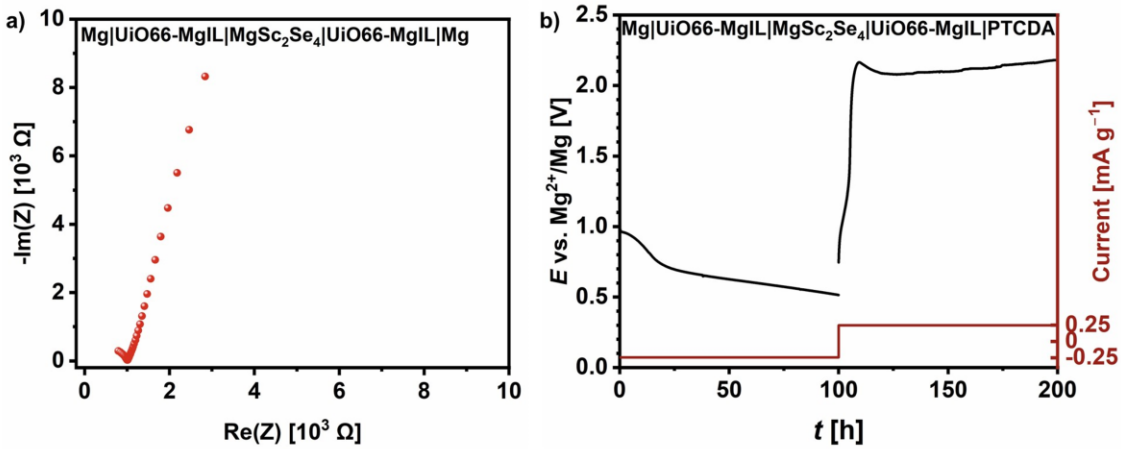

Figure S13. a) Nyquist plot of a Mg|UiO66-MgIL|$MgSc_2Se_4$|UiO66-MgIL|Mg cell after 50 cycles of plating/stripping at 60 °C and by applying ±1.57 µA cm^{-2}; b) voltage and current curves of a Mg|UiO66-MgIL|$MgSc_2Se_4$|UiO66-MgIL|PTCDA full cell at 60 °C.

Table S1. Crystallographic data for one-step synthesized $MgSc_2Se_4$ obtained from Rietveld refinement, based on the corresponding XRD pattern measured using Cu K_α radiation.

Crystallographic information	Result
Crystal system	Cubic
Space group	Fd-3m
Lattice parameters	a = b = c = 11.12781 Å
Cell volume	1377.936 $Å^3$
Density	4.146 g cm^{-3}
X^2	2.18
R_{wp}	11.0
R_{exp}	7.45
Bragg R-factor	5.00
RF-factor	3.74
GoF-index	1.5

Table S2. Crystallographic data for two-step synthesized $MgSc_2Se_4$ obtained from Rietveld refinement, based on the corresponding XRD pattern measured using Cu K_α radiation.

Crystallographic information	Result
Crystal system	Cubic
Space group	Fd-3m
Lattice parameters	$a = b = c$ = 11.12973 Å
Cell volume	1378.650 Å^3
Density	4.144 g cm^{-3}
X^2	2.29
R_{wp}	8.56
R_{exp}	5.66
Bragg R-factor	3.43
RF-factor	2.17
GoF-index	1.5

Table S3. Thickness d of $MgSc_2Se_4$ pellet and UiO66-MgIL layer (sum of layers) of the SS|UiO66-MgIL|SS reference cell and the SS|UiO66-MgIL|$MgSc_2Se_4$|UiO66-MgIL|SS cells with different amount of spinel powder.

#Cell	m($MgSc_2Se_4$) [mg]	d($MgSc_2Se_4$) [mm]	d(UiO66-MgIL) [mm]
1	0	0	0.60
2	160	0.80	0.56
3	190	0.88	0.56
4	220	1.10	0.38
5	250	1.14	0.56
6	280	1.40	0.59

Table S4. Fitted data of the resistances *R*, the constant phase elements CPE and the alpha values *a* for the CPEs from cell 1 (SS|UiO66-MgIL|SS) using the equivalent circuit in **Figure 2c**. Resistances of $R1_{ion}$ from the SS|UiO66-MgIL|$MgSc_2Se_4$|UiO66-MgIL|SS cells 2-6 were calculated by **Equation S1**, and the remaining values were obtained using the equivalent circuit in **Figure 2d**. Note: The equivalent circuit (**Figure 2d**) describes the two conducting pathways, ionic and electronic. Since the electronic resistance is expected to be much higher (~10^4 times) than the ionic resistance, the preferred pathway in the equivalent circuit is via the latter. It is therefore not possible to determine reliable values for the electronic resistance ($R2_{el}$) by this equivalent circuit.

#Cell	$R1_{ion}$ [Ω]	$CPE1_{ion}$ [F]	a_{CPE1}	$R2_{ion}$ [Ω]	$CPE2_{e1}$ [F]	a_{CPE2} (e1)	$R2_{el}$ [Ω]	$CPE2_{geo}$ [F]	a_{CPE2} (geo)	$CPE3_{e2}$ [F]	a_{CPE3} (e2)
1	806	$1.6\cdot10^{-6}$	0.87	-	-	-	-	-	-	-	-
2	752	$3.5\cdot10^{-10}$	0.99	1870	$7.3\cdot10^{-10}$	0.85	12232	$1.2\cdot10^{-10}$	0.92	$1.7\cdot10^{-6}$	0.84
3	752	$2.4\cdot10^{-9}$	0.86	2532	$2.4\cdot10^{-10}$	0.85	45516	$1.4\cdot10^{-9}$	0,76	$1.9\cdot10^{-6}$	0.86
4	510	$9.3\cdot10^{-10}$	0.86	2974	$5.7\cdot10^{-9}$	1.00	$1.1\cdot10^{5}$	$2.7\cdot10^{-9}$	0.73	$1.2\cdot10^{-6}$	0.86
5	752	$2.4\cdot10^{-10}$	0.91	5169	$2.8\cdot10^{-12}$	1.00	$3.0\cdot10^{5}$	$1.2\cdot10^{-9}$	0,78	$3.9\cdot10^{-6}$	0.87
6	792	$2.3\cdot10^{-8}$	0.85	7464	$1.7\cdot10^{-10}$	0.85	8536	$1.7\cdot10^{-11}$	0.99	$2.3\cdot10^{-6}$	0.85

Table S5. Extracted resistance data from **Table S4** in comparison to the manually determined resistance values R_{ion}(SEs) (cell 1-6) and R_{ion}(UiO66-MgIL) (cell 1) taken from the lowest impedance data point at the intercept of the Re(Z) axis before the tail at lower frequencies appears. Resistances of R_{ion}(UiO66-MgIL) for the SS|UiO66-MgIL|$MgSc_2Se_4$|UiO66-MgIL|SS cells 2-6 were calculated by **Equation S1**. Then, $R_{ion}(MgSc_2Se_4)$ was calculated from the difference of R_{ion}(SEs) and R_{ion}(UiO66-MgIL). The associated resistances ($R1_{ion}$ and R_{ion}(UiO66-MgIL), $R2_{ion}$ and $R_{ion}(MgSc_2Se_4)$, $R1_{ion}+R2_{ion}$ and R_{ion}(SEs)) show almost identical values.

#Cell	$R1_{ion}$ [Ω]	R_{ion}(UiO66-MgIL) [Ω]	$R2_{ion}$ [Ω]	$R_{ion}(MgSc_2Se_4)$ [Ω]	$R1_{ion}+R2_{ion}$ [Ω]	R_{ion}(SEs) [Ω]
1	806	806	-	-	806	806
2	752	752	1870	1862	2622	2614
3	752	752	2532	2536	3284	3287
4	510	510	2974	2875	3484	3386
5	752	752	5169	5161	5921	5912
6	792	792	7564	7466	8356	8258

Since the total UiO66-MgIL layer thickness in the SS|UiO66-MgIL|$MgSc_2Se_4$|UiO66-MgIL|SS cells can deviate from those used in the SS|UiO66-MgIL|SS reference cell 1 (**Table S3**), the impedances of the UiO66-MgIL were adapted to the layer thickness actually used by the given **Equation S1**:

$$R_{\text{ion}}(i) = \frac{d(\text{UiO66-MgIL})}{d(\text{UiO66-MgIL-Cell 1})} R_{\text{ion}}(i\text{ -Cell 1}) \quad (i = \text{UiO66-MgIL}, R1_{\text{ion}}) \tag{S1}$$

Table S6. Ionic conductivity σ_{ion} and Mg^{2+} migration barrier E_a of $MgSc_2Se_4$ in comparison to other reported inorganic Mg-ion solid electrolytes.

Category	Material	*T* [°C]	σ_{ion} [S cm^{-1}]	*Ea* [eV]
Phosphate	$MgZr_4(PO_3)_6$[4]	400 800	$2.9\cdot10^{-5}$ $6.1\cdot10^{-3}$	0.82
	$MgZr_4(PO_3)_6$ (sol-gel)[5]	725	$7.23\cdot10^{-3}$	0.84
	$Mg_{1.1}(Zr_{0.85}Nb_{0.15})_4P_6O_{24}\cdot0.4Zr_2O(PO_4)_2$[6]	800	$9.5\cdot10^{-3}$	1.28
Oxide	$Mg_{0.6}Al_{1.2}Si_{1.8}O_6$[7]	500	$1.6\cdot10^{-6}$	1.32
Sulfide	$MgS–P_2S_5–MgI_2$[8]	200	$2.1\cdot10^{-7}$	-
Borohydride	$Mg(BH_4)_2$[9]	150	$1.0\cdot10^{-9}$	-
	$Mg(NH_2)(BH_4)$[9]	150	$1.0\cdot10^{-6}$	1.31
	$Mg_3(BH_4)_4(NH_2)_2$[10]	100	$4.1\cdot10^{-5}$	0.84
	$Mg(en)(BH_4)_2$[11]	30 70	$5.0\cdot10^{-8}$ $6.0\cdot10^{-5}$	1.6
	$Mg(BH_4)_2(CH_3NH_2)$[12]	25	$1.5\cdot10^{-4}$	0.6
	$Mg(BH_4)_2\cdot1.5THF$-MgO(75 wt%)[13]	70	$\sim10^{-4}$	1.4
	$Mg(BH_4)_2\cdot1.6NH_3$-MgO(75 wt%)[14]	30 70	$1.2\cdot10^{-5}$ $1.1\cdot10^{-3}$	1.12
Halide	$MgAl_2Cl_2Br_6$[15]	127	$1.3\cdot10^{-6}$	0.52
Selenide	$MgSc_2Se_4$ (This work)	25	$2.4\text{-}5.5\cdot10^{-5}$	0.36-0.42

References

[1] P. Canepa, S.-H. Bo, G. Sai Gautam, B. Key, W. D. Richards, T. Shi, Y. Tian, Y. Wang, J. Li, G. Ceder, *Nat. Commun.* **2017**, *8*, 1759.

[2] J. Jamnik, J. Maier, *J. Electrochem. Soc.* **1999**, *146*, 4183.

[3] J. Jamnik, J. Maier, *Phys. Chem. Chem. Phys.* **2001**, *3*, 1668.

[4] S. Ikeda, M. Takahashi, J. Ishikawa, K. Ito, *Solid State Ion.* **1987**, *23*, 125.

[5] M. Adamu, G. M. Kale, *J. Phys. Chem. C* **2016**, *120*, 17909.

[6] J. Kawamura, K. Morota, N. Kuwata, Y. Nakamura, H. Maekawa, T. Hattori, N. Imanaka, Y. Okazaki, G. Adachi, *Solid State Commun.* **2001**, *120*, 295.

[7] H. Takeda, K. Nakano, N. Tanibata, M. Nakayama, *Sci. Technol. Adv. Mater.* **2020**, *21*, 131.

[8] T. Yamanaka, A. Hayashi, A. Yamauchi, M. Tatsumisago, *Solid State Ion.* **2014**, *262*, 601.

[9] S. Higashi, K. Miwa, M. Aoki, K. Takechi, *Chem. Commun.* **2014**, *50*, 1320.

[10] R. Le Ruyet, B. Fleutot, R. Berthelot, Y. Benabed, G. Hautier, Y. Filinchuk, R. Janot, *ACS Appl. Energy Mater.* **2020**, *3*, 6093.

[11] E. Roedern, R.-S. Kühnel, A. Remhof, C. Battaglia, *Sci. Rep.* **2017**, *7*, 46189.

[12] M. B. Amdisen, J. B. Grinderslev, L. N. Skov, T. R. Jensen, *Chem. Mater.* **2023**, *35*, 1440.

[13] L. N. Skov, J. B. Grinderslev, A. Rosenkranz, Y.-S. Lee, T. R. Jensen, *Batter. Supercaps* **2022**, *5*, e20220016.

[14] Y. Yan, J. B. Grinderslev, M. Jørgensen, L. N. Skov, J. Skibsted, T. R. Jensen, *ACS Appl. Energy Mater.* **2020**, *3*, 9264.

[15] Y. Tomita, R. Saito, M. Morishita, Y. Yamane, Y. Kohno, *Solid State Ion.* **2021**, *361*, 115566.

A.2 Publication 2: "MgB_2Se_4 Spinels (B = Sc, Y, Er, Tm) as Potential Mg-Ion Solid Electrolytes – Partial Ionic Conductivity and the Ion Migration Barrier"

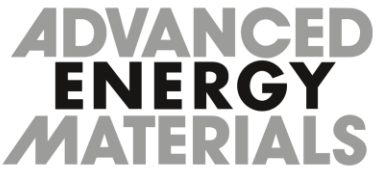

Supporting Information

for *Adv. Energy Mater.*, DOI 10.1002/aenm.202402269

MgB_2Se_4 Spinels (B = Sc, Y, Er, Tm) as Potential Mg-Ion Solid Electrolytes – Partial Ionic Conductivity and the Ion Migration Barrier

*Clarissa Glaser, Manuel Dillenz, Kanchan Sarkar, Mohsen Sotoudeh, Zhixuan Wei, Sylvio Indris, Ruben Maile, Marcus Rohnke, Klaus Müller-Buschbaum, Axel Groß and Jürgen Janek**

WILEY-VCH

Supporting Information

MgB_2Se_4 Spinels (B = Sc, Y, Er, Tm) as Potential Mg-Ion Solid Electrolytes – Partial Ionic Conductivity and the Ion Migration Barrier

*Clarissa Glaser, Manuel Dillenz, Kanchan Sarkar, Mohsen Sotoudeh, Zhixuan Wei, Sylvio Indris, Ruben Maile, Marcus Rohnke, Klaus Müller-Buschbaum, Axel Groß and Jürgen Janek**

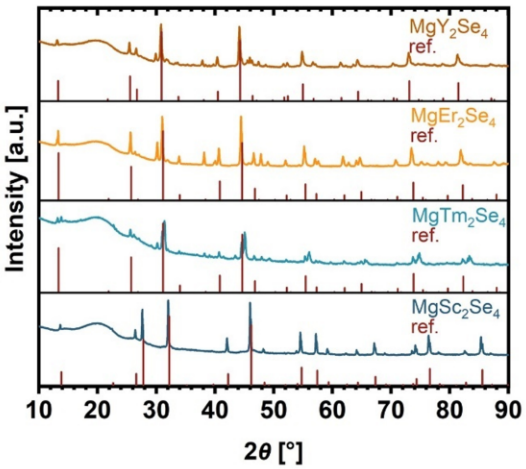

Figure S1. XRD patterns of spinels $MgSc_2Se_4$, $MgTm_2Se_4$, $MgEr_2Se_4$ and MgY_2Se_4 synthesized via one-step route. Data for $MgSc_2Se_4$ reproduced with permission.[1] Copyright 2023, Wiley-VCH.

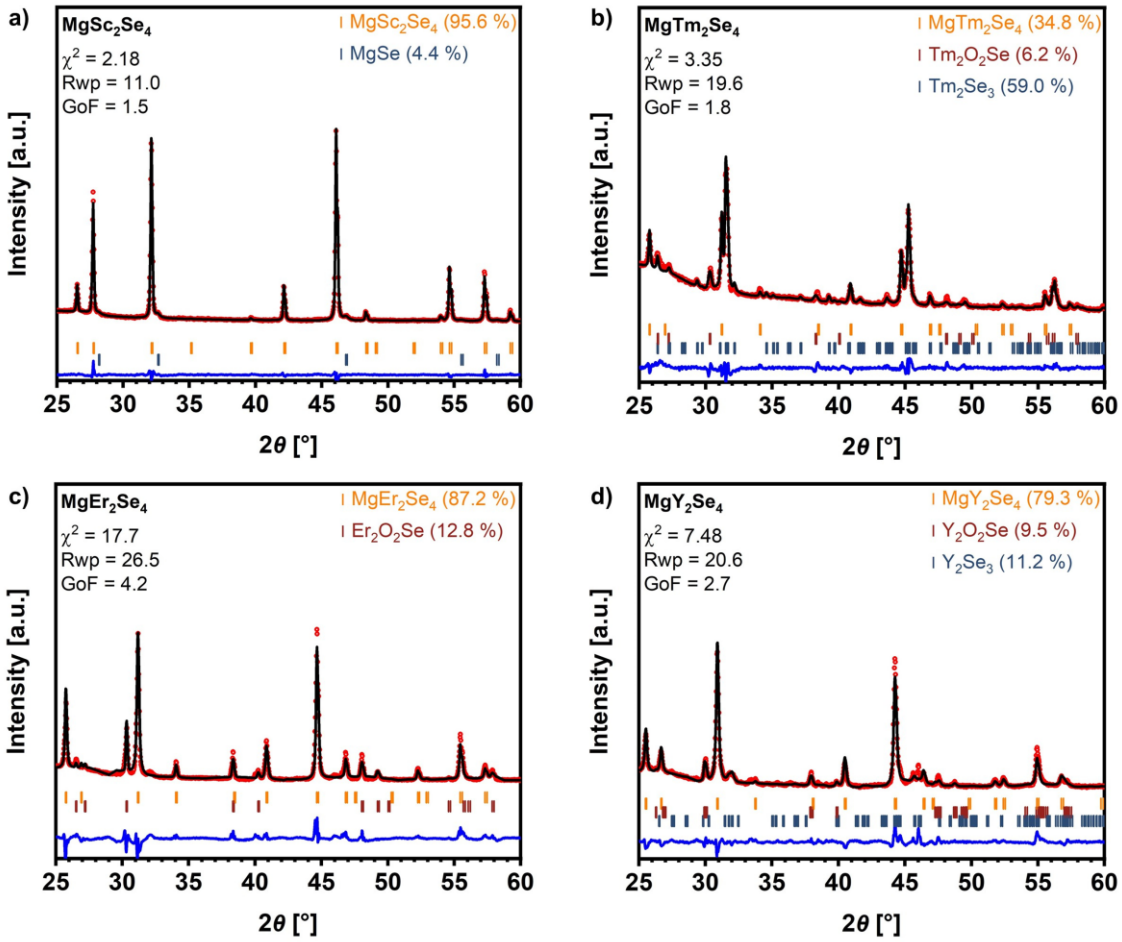

Figure S2. Rietveld refinement of one-step synthesized a) $MgSc_2Se_4$, b) $MgTm_2Se_4$, c) $MgEr_2Se_4$ and d) MgY_2Se_4, based on the XRD pattern from **Figure S1**. The observed and the calculated curves are shown in red and black, and the resulting difference curve is presented in blue. Data for $MgSc_2Se_4$ reproduced with permission.[1] Copyright 2023, Wiley-VCH.

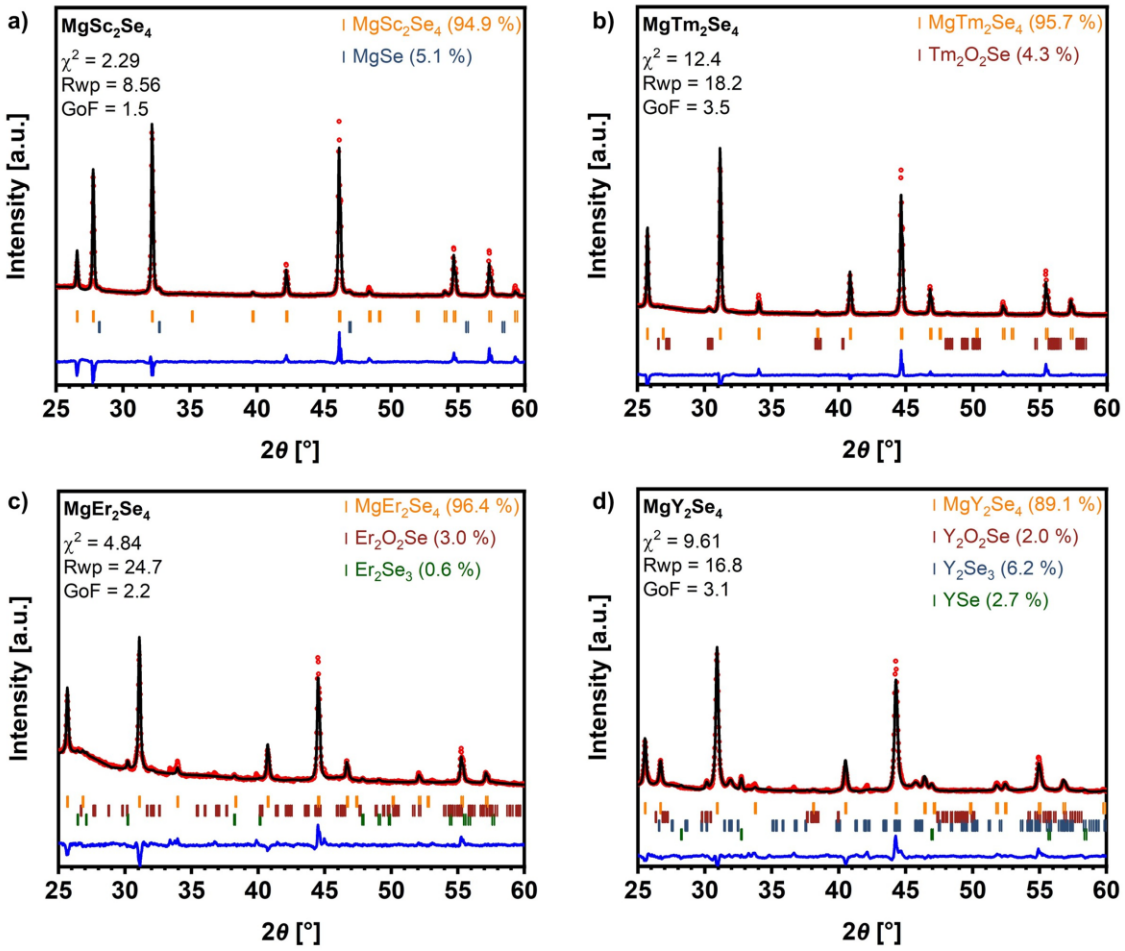

Figure S3. Rietveld refinement of two-step synthesized a) $MgSc_2Se_4$, b) $MgTm_2Se_4$, c) $MgEr_2Se_4$ and d) MgY_2Se_4, based on the XRD pattern from **Figure 1b**. The observed and the calculated curves are shown in red and black, and the resulting difference curve is presented in blue. Data for $MgSc_2Se_4$ reproduced with permission.[1] Copyright 2023, Wiley-VCH.

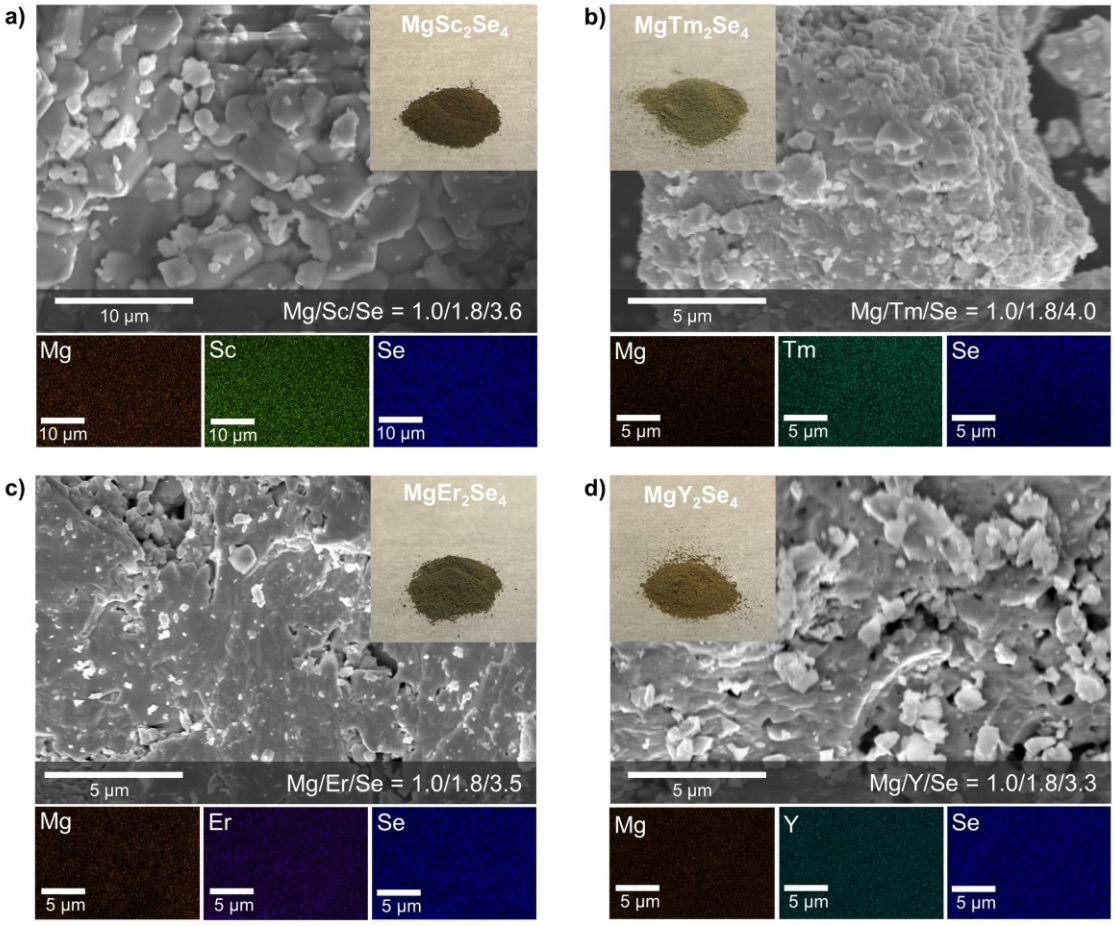

Figure S4. SEM images and light optical images of a) $MgSc_2Se_4$ powder, b) $MgTm_2Se_4$ powder, c) $MgEr_2Se_4$ powder and d) MgY_2Se_4 powder with EDS mapping of the corresponding elements Mg, Sc/Tm/Er/Y and Se.

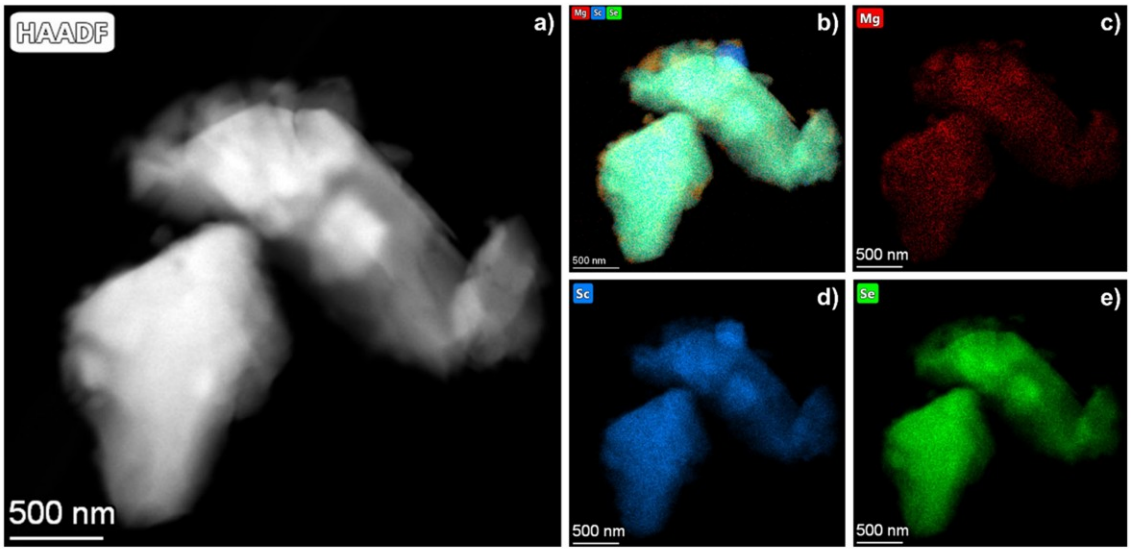

Figure S5. a) HAADF image of a $MgSc_2Se_4$ particle (one-step synthesis); b) layered EDS maps of the elemental distributions and c–e) single EDS maps of the elemental distributions of Mg, Sc and Se.

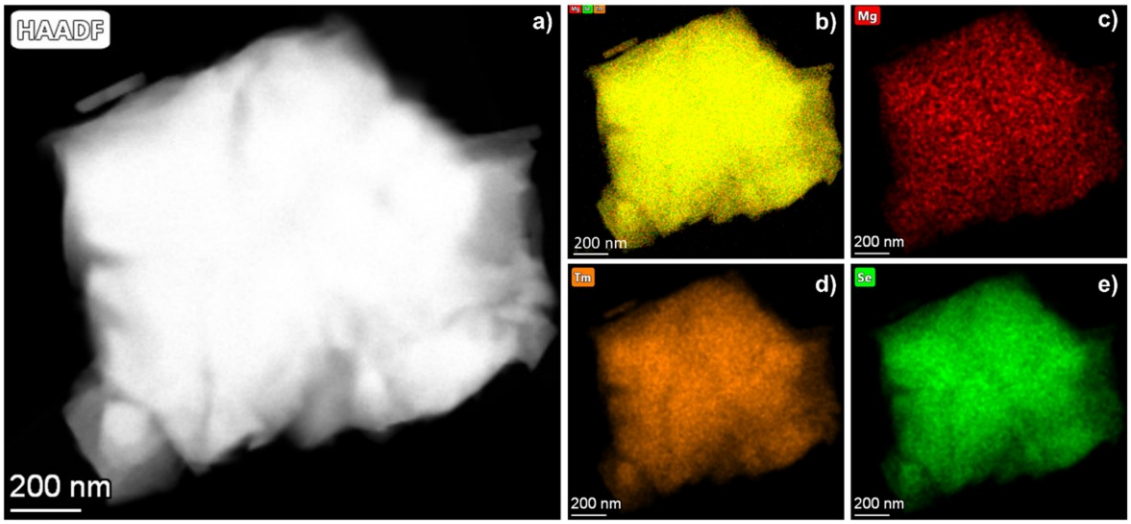

Figure S6. a) HAADF image of a $MgTm_2Se_4$ particle (two-step synthesis); b) layered EDS maps of the elemental distributions and c–e) single EDS maps of the elemental distributions of Mg, Tm and Se.

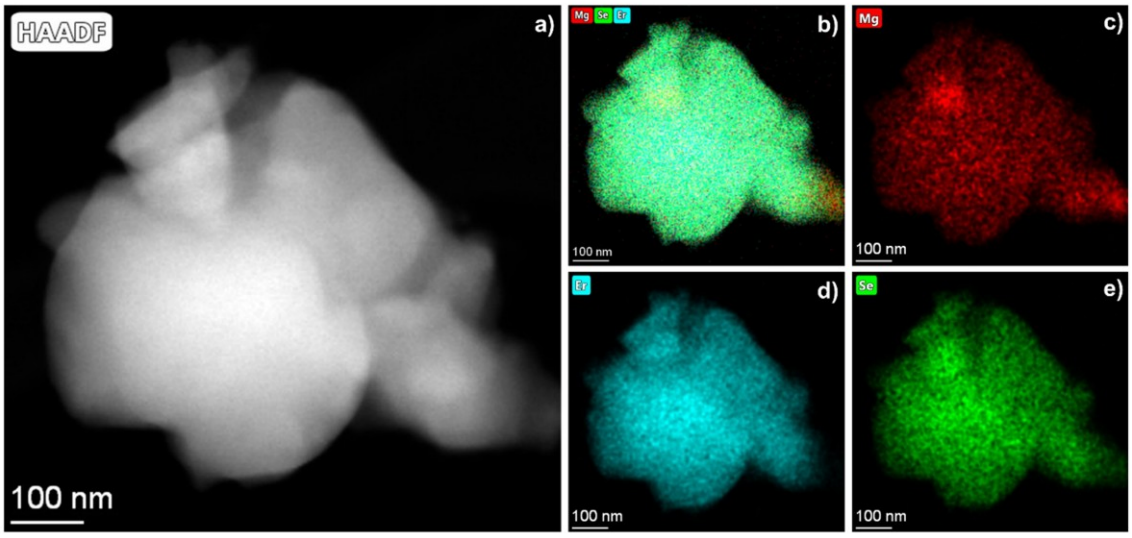

Figure S7. a) HAADF image of a $MgEr_2Se_4$ particle (two-step synthesis); b) layered EDS maps of the elemental distributions and c–e) single EDS maps of the elemental distributions of Mg, Er and Se.

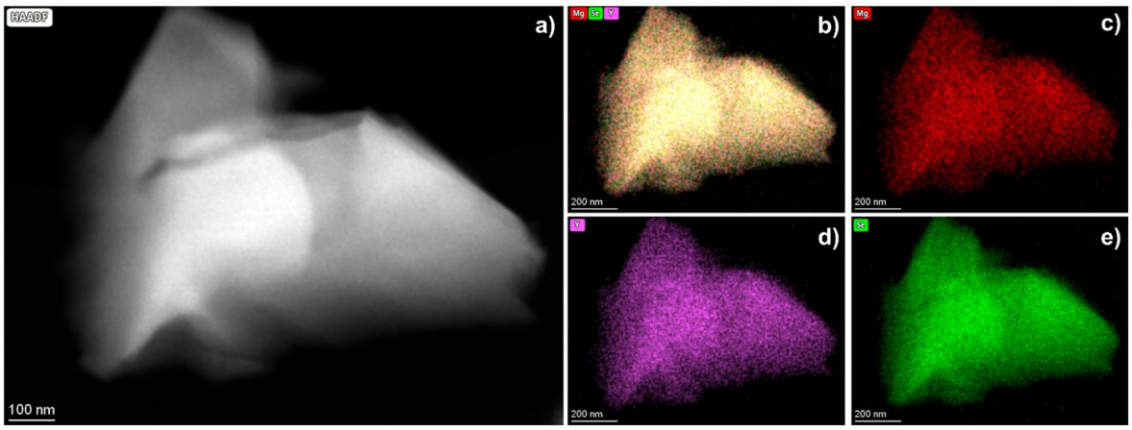

Figure S8. a) HAADF image of a MgY_2Se_4 particle (two-step synthesis); b) layered EDS maps of the elemental distributions and c–e) single EDS maps of the elemental distributions of Mg, Y and Se.

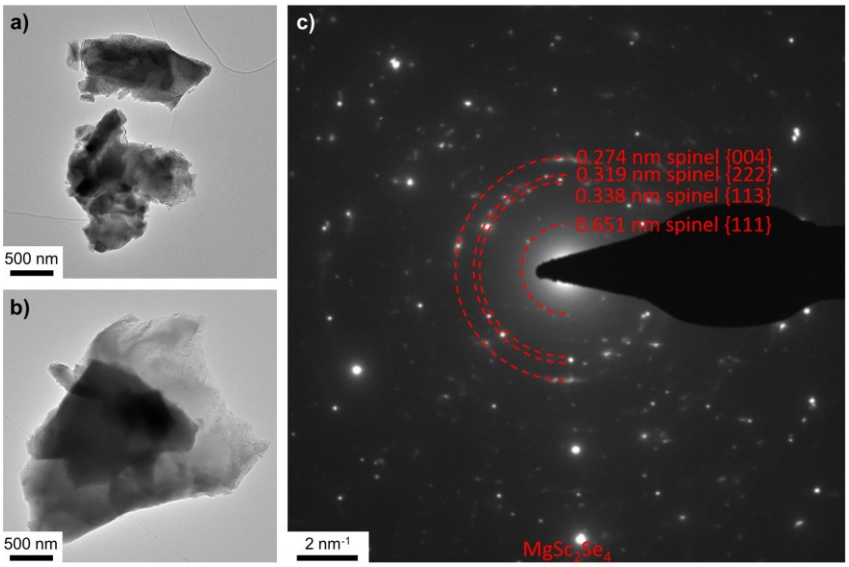

Figure S9. a–b) TEM images of $MgSc_2Se_4$ particles (one-step synthesis) with a size of 1 µm to 3 µm and c) SAED pattern confirming the synthesis of the $MgSc_2Se_4$ spinel phase. Data reproduced with permission.[1] Copyright 2023, Wiley-VCH.

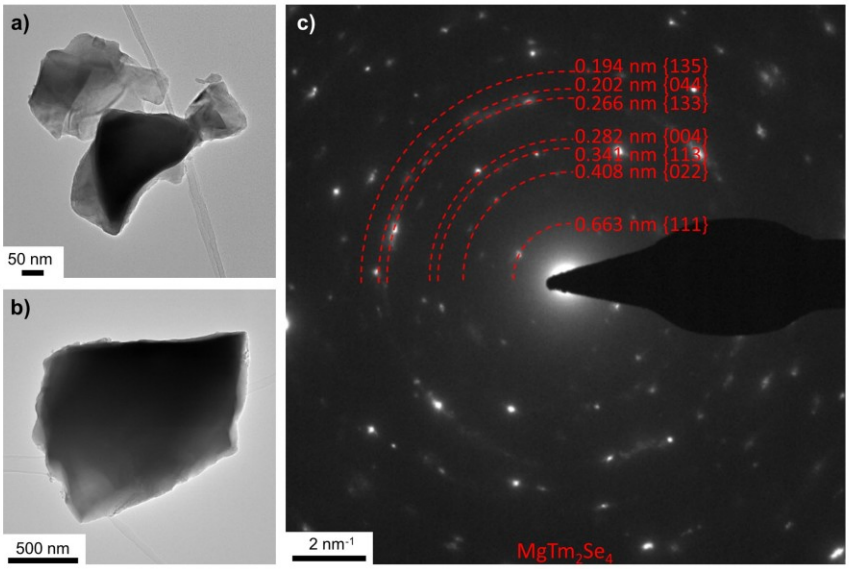

Figure S10. a–b) TEM images of $MgTm_2Se_4$ particles (two-step synthesis) with a size of 0.5 µm to 1.5 µm and c) SAED pattern confirming the synthesis of the $MgTm_2Se_4$ spinel phase.

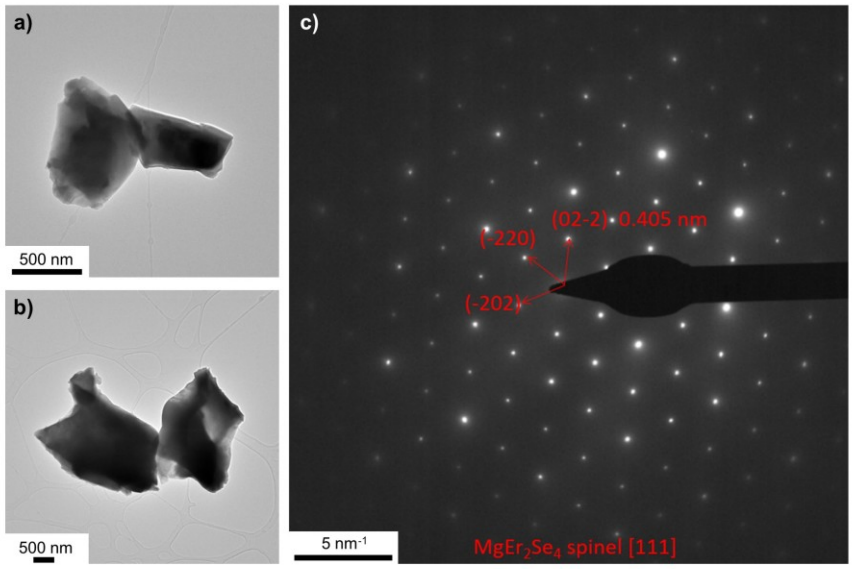

Figure S11. a–b) TEM images of $MgEr_2Se_4$ particles (two-step synthesis) with a size of 0.5 µm to 3 µm and c) SAED pattern confirming the synthesis of the $MgEr_2Se_4$ spinel phase.

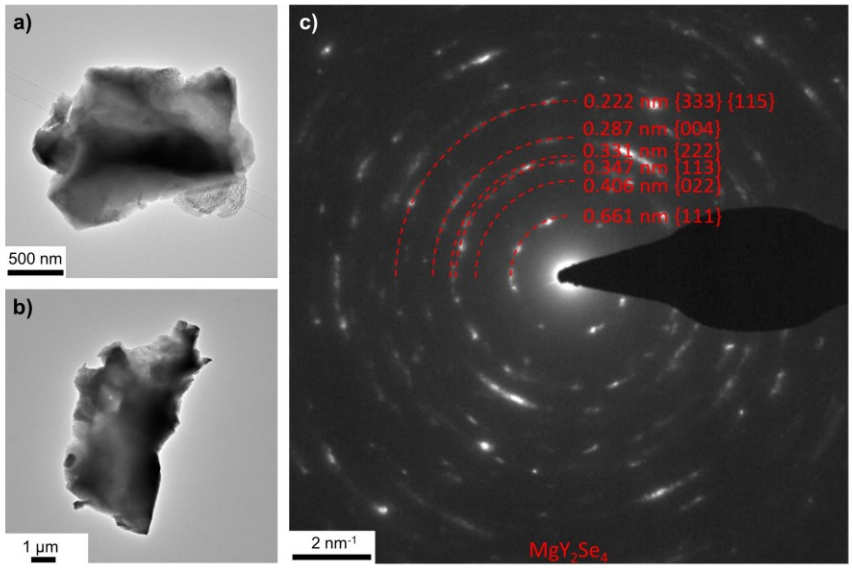

Figure S12. a–b) TEM images of MgY_2Se_4 particles (two-step synthesis) with a size of 1 µm to 10 µm and c) SAED pattern confirming the synthesis of the MgY_2Se_4 spinel phase.

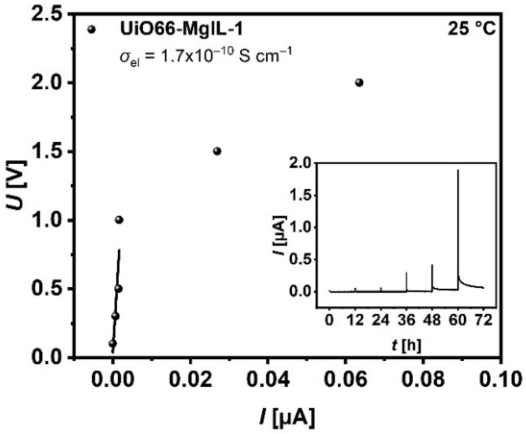

Figure S13. DC polarization data of a SS|UiO66-MgIL|SS cell obtained at different voltages (0.1 V, 0.3 V, 0.5 V, 1.0 V, 1.5 V and 2.0 V, held for 12 h, shown in the inset) with linear fit of the ohmic electronic behavior at 25 °C. Data reproduced with permission.[1] Copyright 2023, Wiley-VCH.

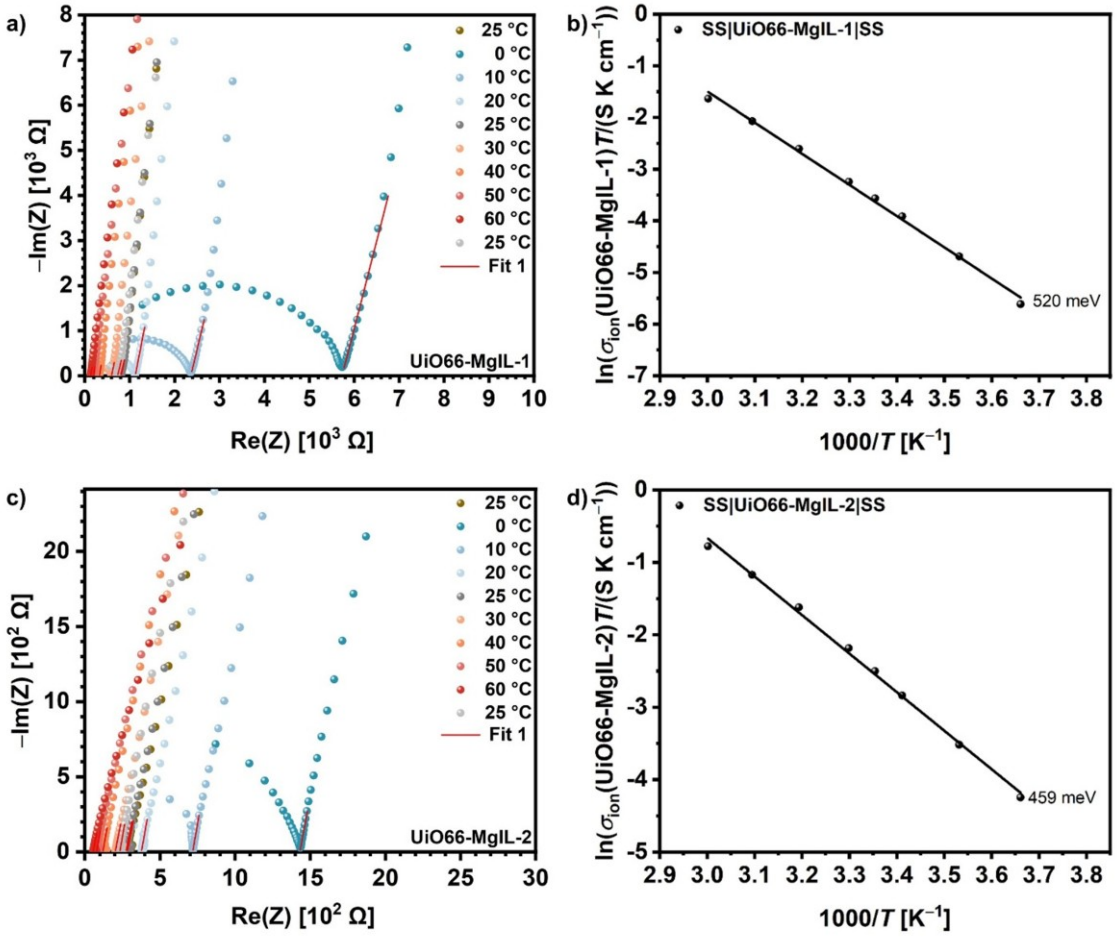

Figure S14. Fitted Nyquist plots of SS|UiO66-MgIL|SS cell at different temperatures ranging from 0 °C to 60 °C of a) batch UiO66-MgIL-1 and b) batch UiO66-MgIL-2 and corresponding Arrhenius plots in b) and d). Data for UiO66-MgIL-1 reproduced with permission.[1] Copyright 2023, Wiley-VCH.

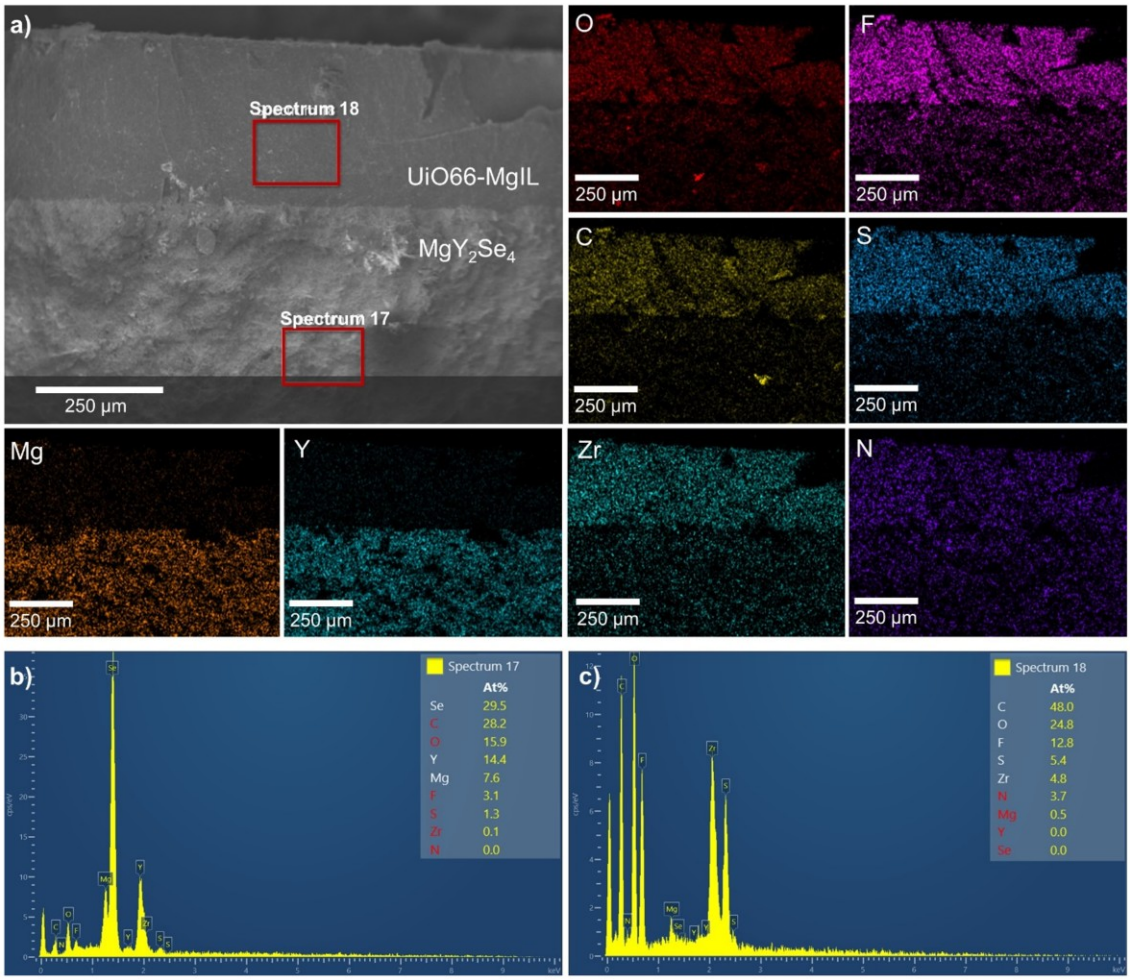

Figure S15. a) SEM image and elemental EDS maps of the UiO66-MgIL|MgY_2Se_4|UiO66-MgIL pellet cross section showing one UiO66-MgIL interlayer (top) pressed onto the 160 mg MgY_2Se_4 pellet (bottom) after disassembling the cell; b) and c) display the observed elements in spectrum 17 (MgY_2Se_4 pellet) and spectrum 18 (UiO66-MgIL interlayer) and confirm that the IL (containing F, N and S) does not penetrate the spinel pellet. The red labeled elements overlap with each other or have ≤3 at% which is below the detection limit. Note that for better visualization, an automatic brightness adjustment was set instead of a normalized brightness based on the element with the highest intensity, which means that even small amounts of elements below the detection limit become visible in the EDS maps.

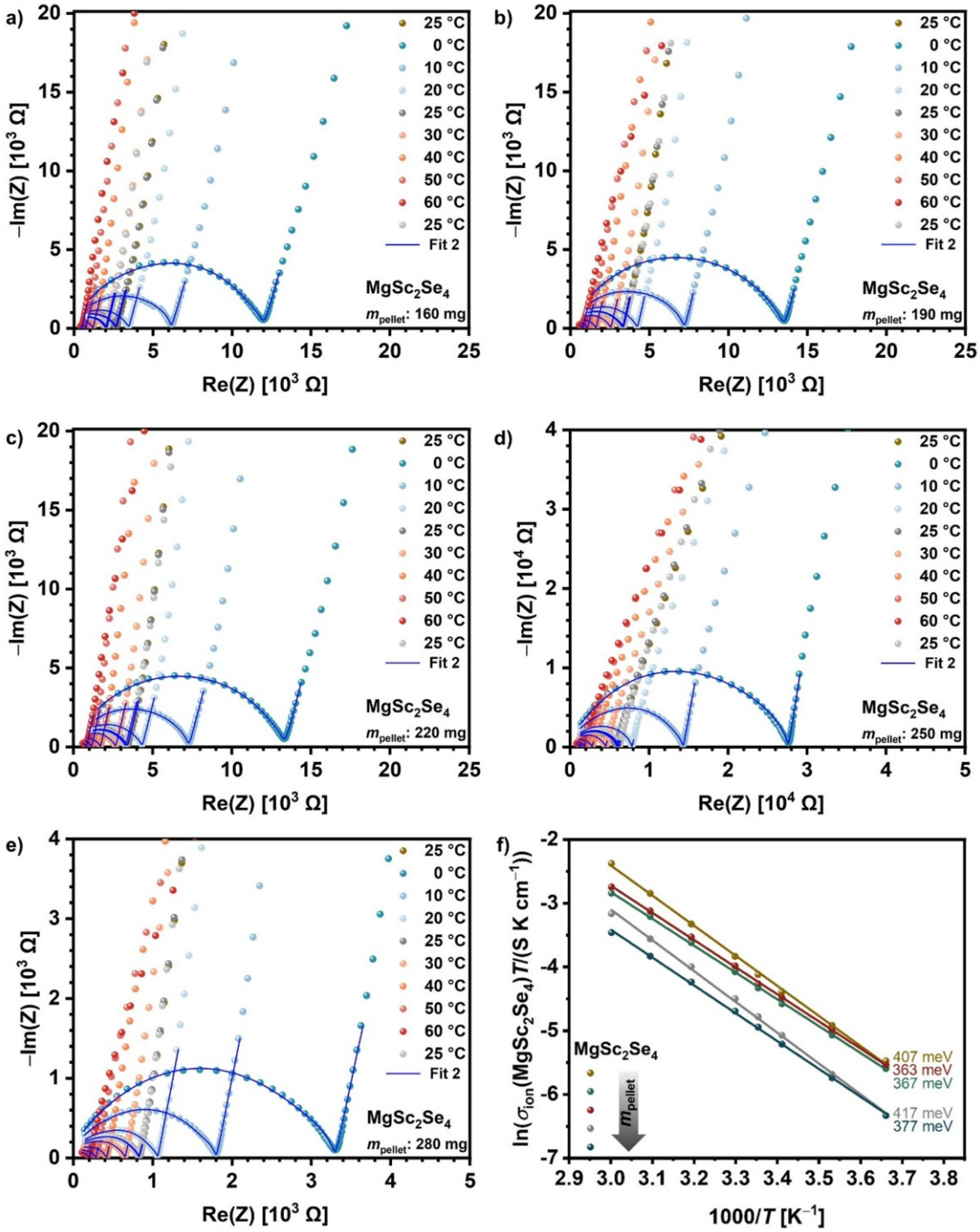

Figure S16. Fitted Nyquist plots of SS|UiO66-MgIL|$MgSc_2Se_4$|UiO66-MgIL|SS cells at different temperatures ranging from 0 °C to 60 °C using a spinel pellet mass/thickness of a) 160 mg/0.80 mm, b) 190 mg/0.88 mm, c) 220 mg/1.10 mm, d) 250 mg/1.14 mm and e) 280 mg/1.40 mm; and f) Arrhenius plots of the ionic conductivity of $MgSc_2Se_4$ for each cell. Data reproduced with permission.[1] Copyright 2023, Wiley-VCH.

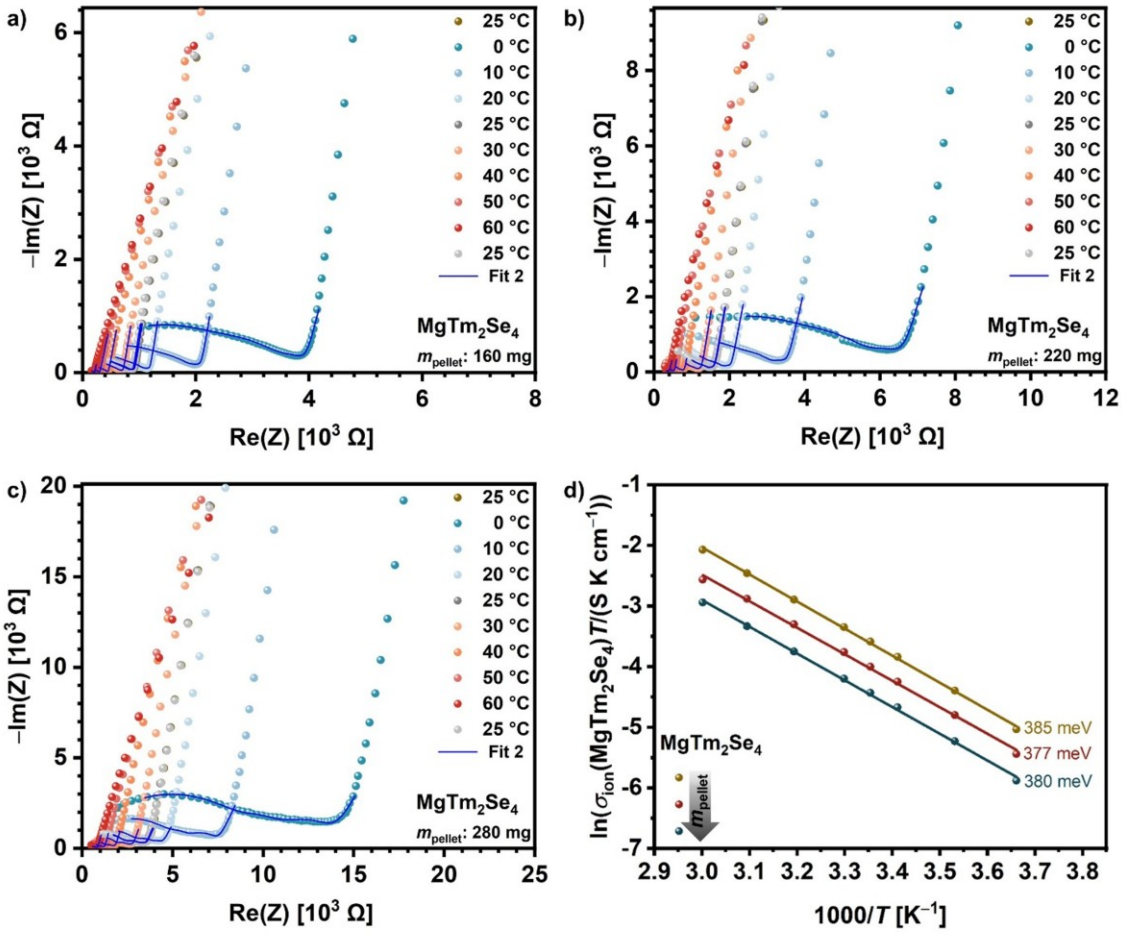

Figure S17. Fitted Nyquist plots of SS|UiO66-MgIL|$MgTm_2Se_4$|UiO66-MgIL|SS cells at different temperatures ranging from 0 °C to 60 °C using a spinel pellet mass/thickness of a) 160 mg/0.46 mm, b) 220 mg/0.62 mm, and c) 280 mg/1.00 mm; and f) Arrhenius plots of the ionic conductivity of $MgTm_2Se_4$ for each cell.

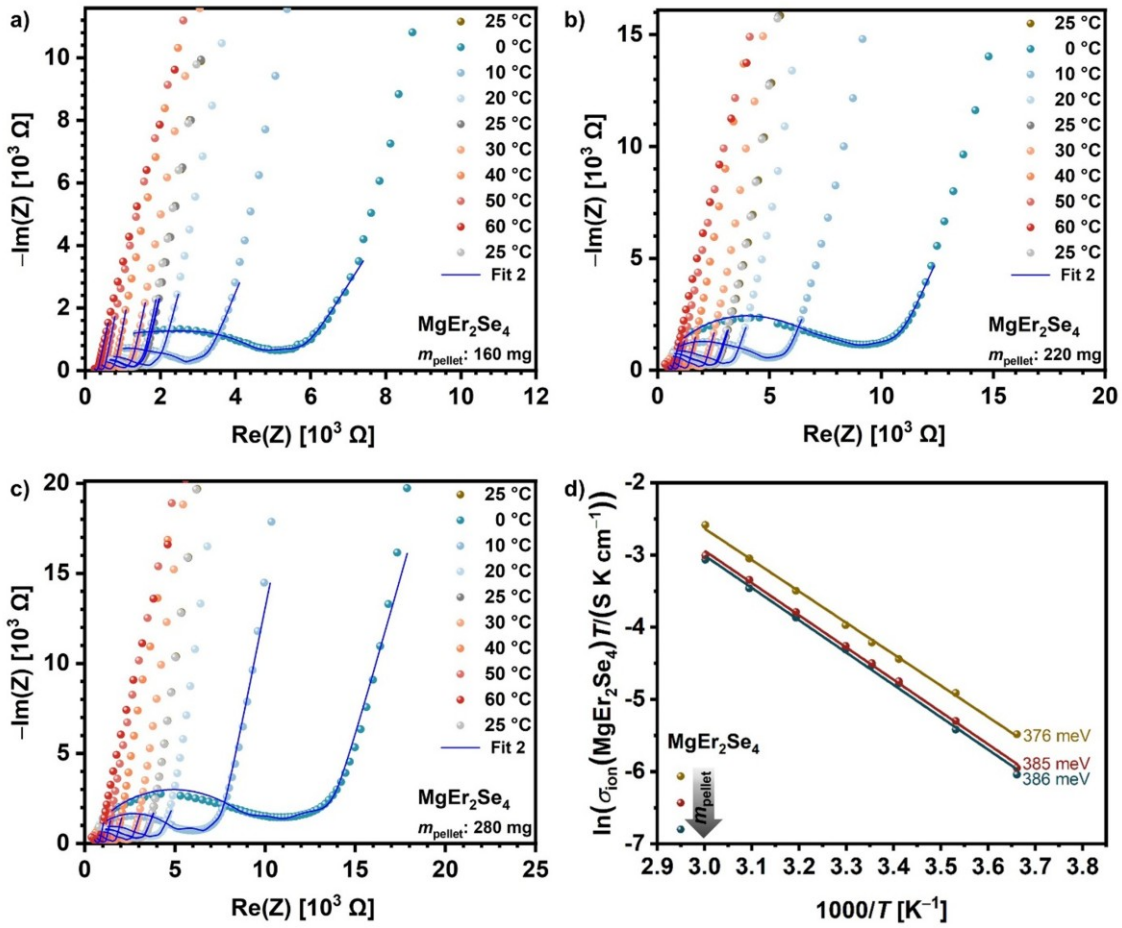

Figure S18. Fitted Nyquist plots of SS|UiO66-MgIL|$MgEr_2Se_4$|UiO66-MgIL|SS cells at different temperatures ranging from 0 °C to 60 °C using a spinel pellet mass/thickness of a) 160 mg/0.50 mm, b) 220 mg/0.68 mm, and c) 280 mg/0.82 mm; and f) Arrhenius plots of the ionic conductivity of $MgEr_2Se_4$ for each cell.

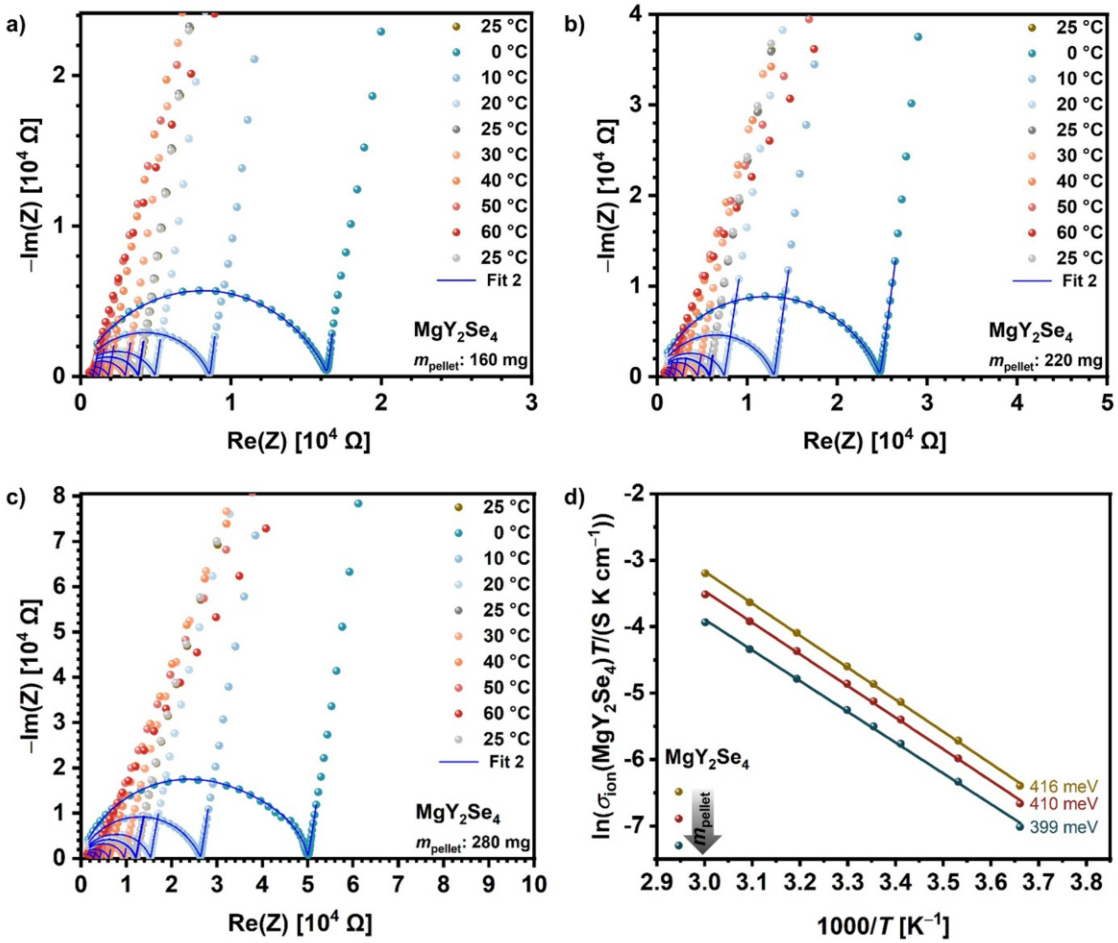

Figure S19. Fitted Nyquist plots of SS|UiO66-MgIL|MgY_2Se_4|UiO66-MgIL|SS cells at different temperatures ranging from 0 °C to 60 °C using a spinel pellet mass/thickness of a) 160 mg/0.72 mm, b) 220 mg/0.86 mm, and c) 280 mg/1.26 mm; and f) Arrhenius plots of the ionic conductivity of MgY_2Se_4 for each cell.

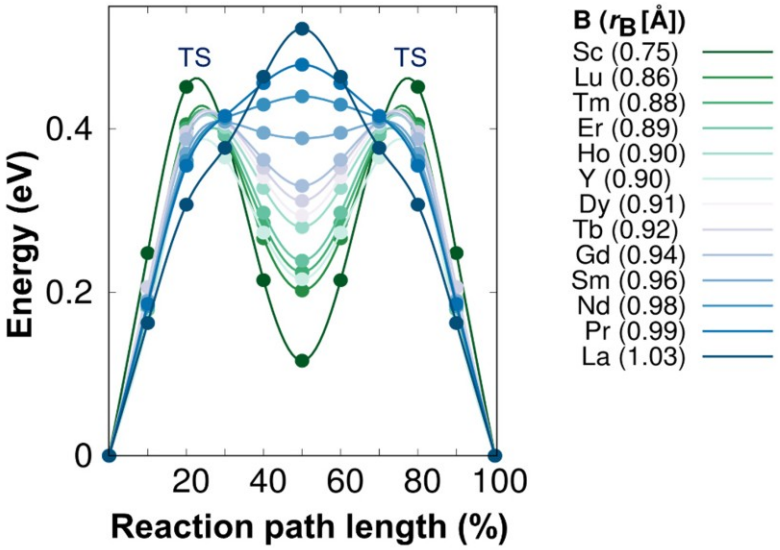

Figure S20. The energy along the migration path for MgB_2S_4 spinel compounds calculated by the NEB method.

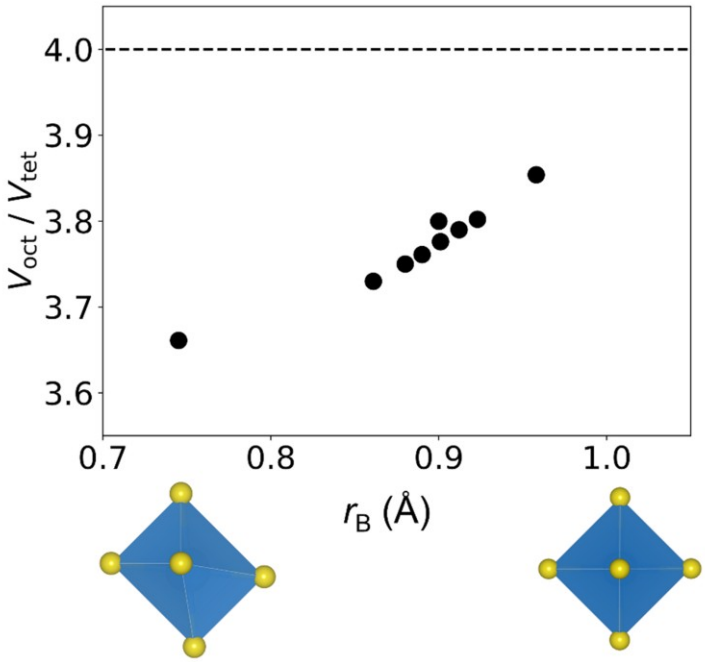

Figure S21. The dependence of the ratio of the volume of the octahedral site and the volume of the tetrahedral site on the ionic radius r_B of the metal B. In the regular (distortion free) system the volume of the octahedron is four times larger than the volume of the tetrahedron. As a consequence of trigonal distortion this ratio is decreasing with decreasing r_B.

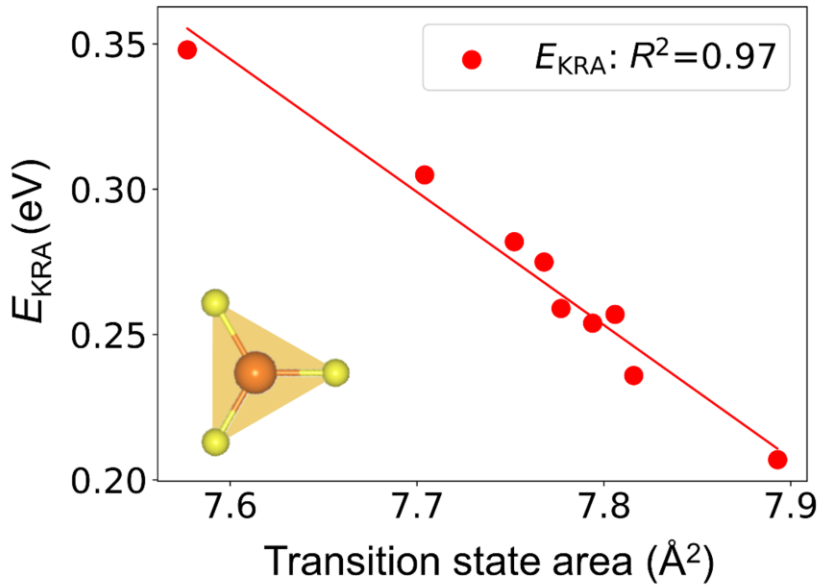

Figure S22. Kinetically resolved barrier E_{KRA} as function of the transition state area. Increasing the area leads to a stabilization of the transition state and decreases E_{KRA}.

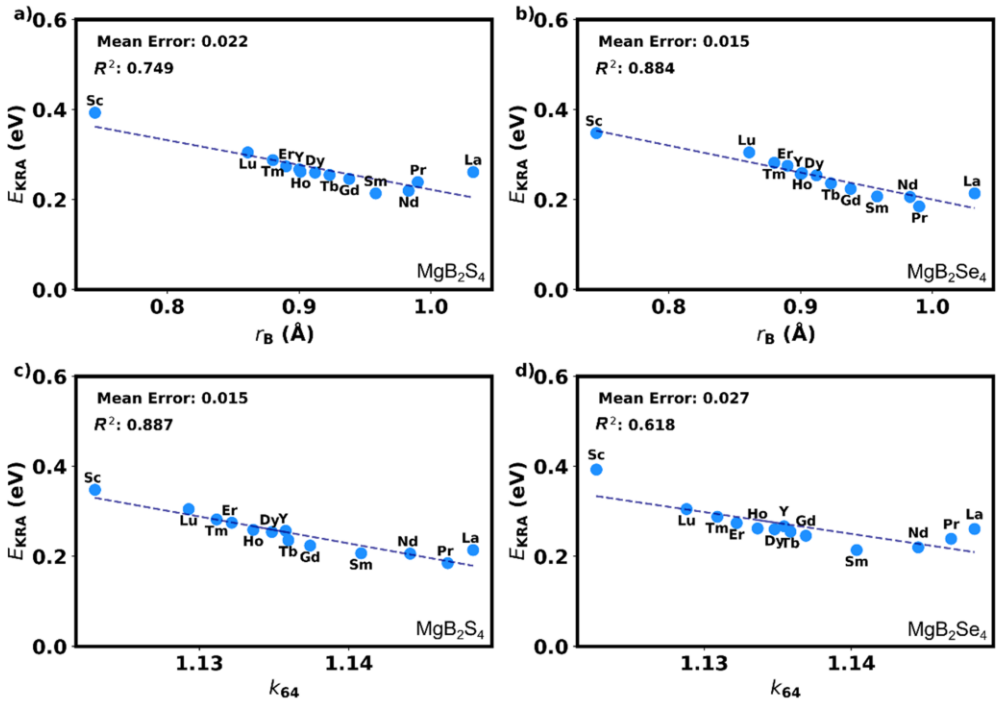

Figure S23. The linear regressions for E_{KRA} as function of the ionic radius r_B of the B metal are shown with dashed lines for a) the MgB_2S_4 sulfide spinels and b) the MgB_2Se_4 selenide spinels including the mean error and R^2 values. The linear regressions for E_{KRA} as function of the ratio of the distance k_{64} including the mean error and R^2 values are shown for c) the MgB_2S_4 sulfide spinels and d) the MgB_2Se_4 selenide spinels.

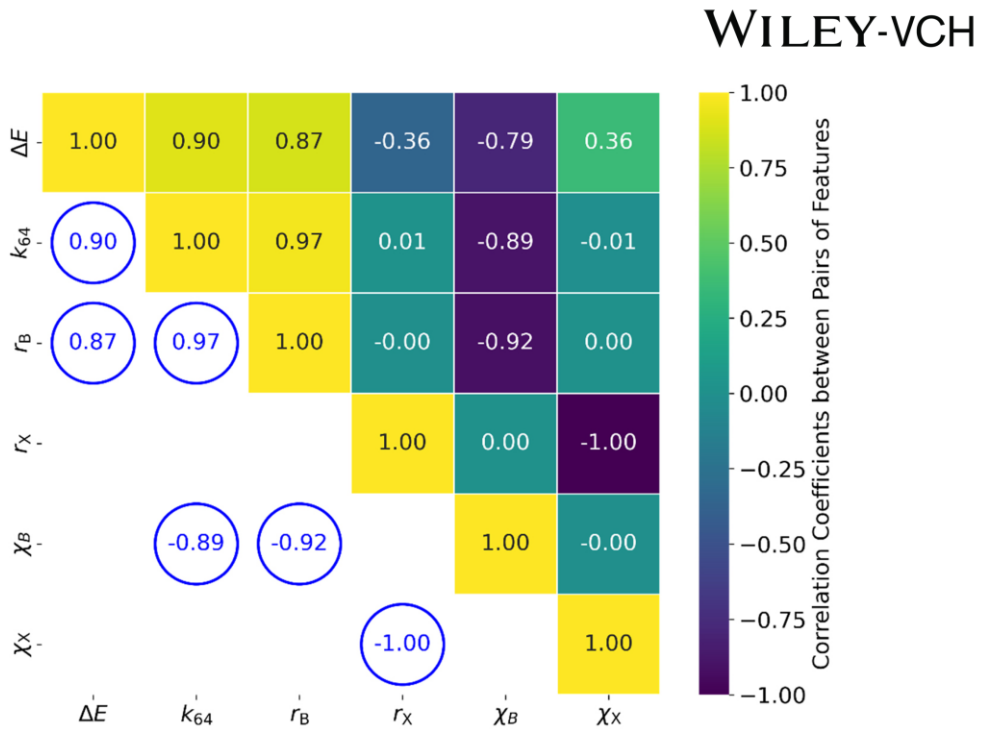

Figure S24. Pair-wise correlation heat map of preprocessed features: A heat map illustrating the correlation coefficients between pairs of features after preprocessing the dataset. Features include ΔE, k_{64}, r_B, r_X, χ_B, and χ_X. Highly correlated feature pairs are emphasized, with blue circles denoting the strength of correlation.

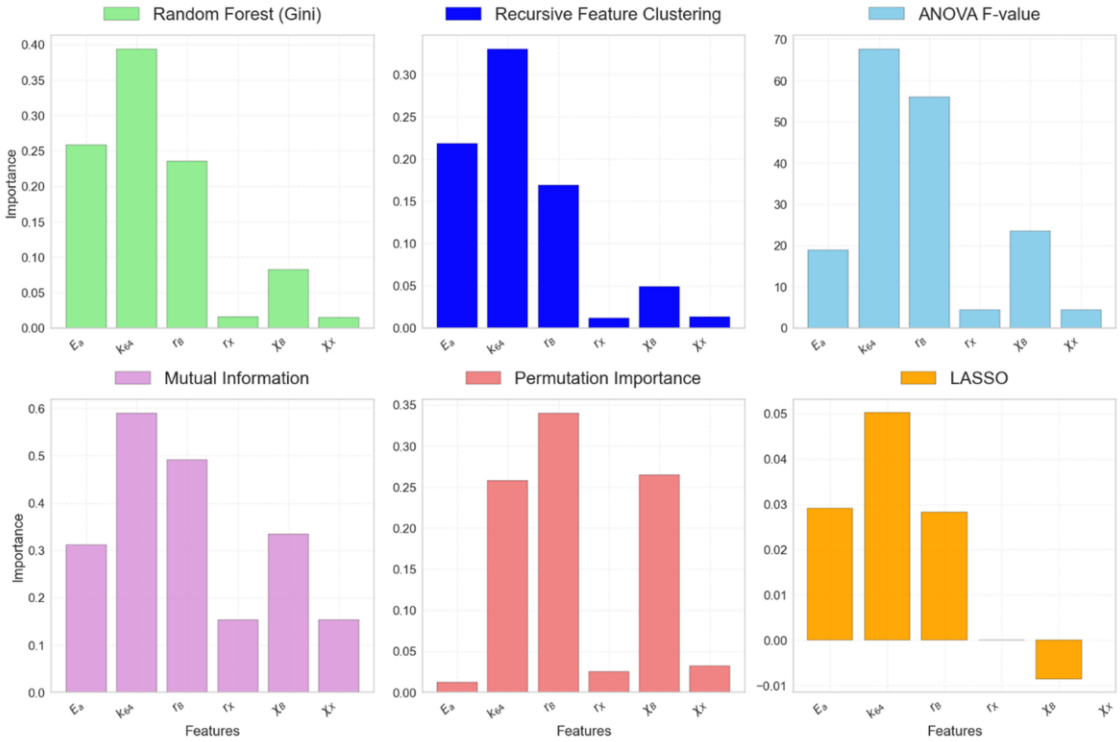

Figure S25. Feature importances for the class of chemical compounds (sulfides and selenides) under investigation, determined by the various techniques: a) Recursive Feature Clustering (RFC) b) Random Forest Gini, c) ANOVA F-value, d) Mutual Information, e) Permutation Importance and f) LASSO (Least Absolute Shrinkage and Selection Operator). The bar plot shows the magnitude and direction of LASSO coefficients or importance for influential features. Non-zero coefficients indicate significant contributions, with positive values suggesting a positive correlation and negative values indicating a negative correlation with ΔE. Color intensity reflects coefficient magnitude.

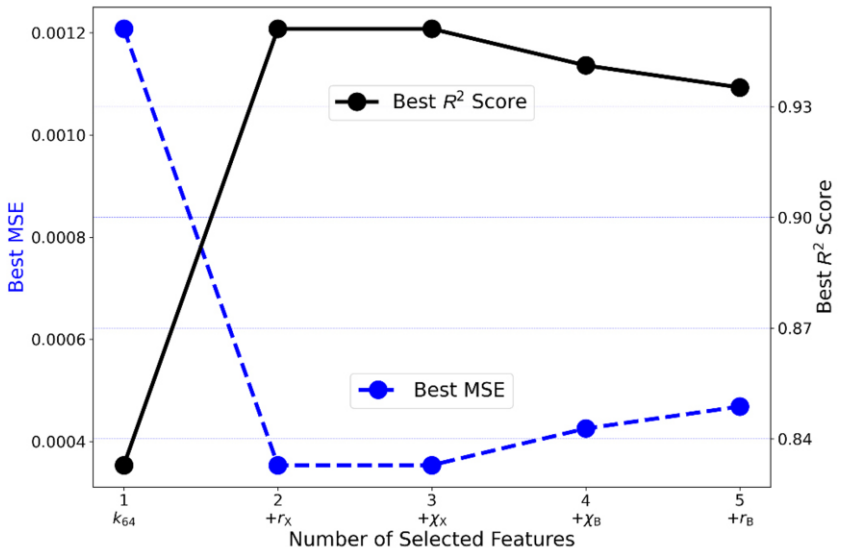

Figure S26. Optimized impact of selected chemical features on linear regression model performance (excluding E_a(th)) for prediction of ΔE: The plot illustrates the trade-off between the number of selected features (excluding E_a(th)) and model performance, showcasing the best mean square error (MSE) and *R*-squared (R^2) scores for each feature subset. The best feature combinations were determined through exhaustive search, showcasing the trade-off between model complexity and predictive accuracy. The results highlight the optimal feature combinations for achieving improved predictive accuracy in the absence of the activation energy E_a(th).

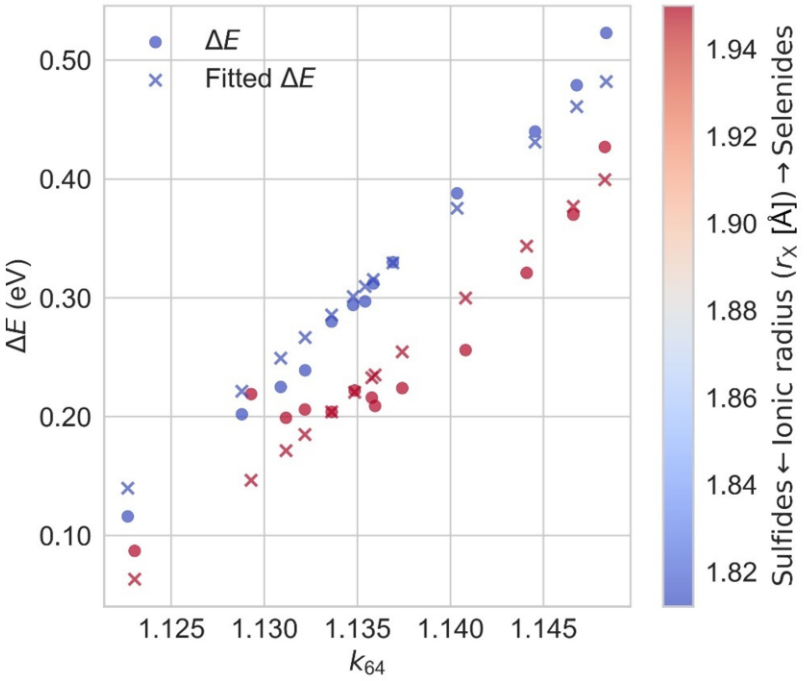

Figure S27. Comparison of actual and fitted ΔE values against r_X and k_{64}. The scatter plot depicts actual ΔE values, with red circles representing selenides and blue circles representing sulfides. Cross marks in corresponding colors represent the fitted data, illustrating the optimized linear regression model's proficiency in capturing the relationship between the target variable (ΔE) and the features r_X and k_{64}.

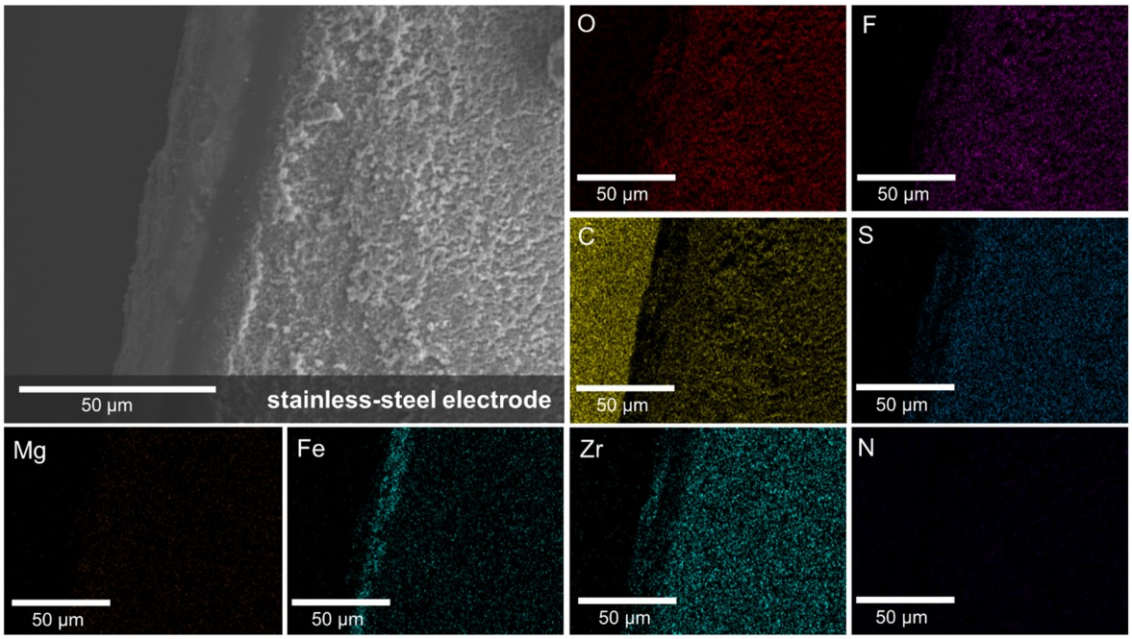

Figure S28. a) Exemplary SEM image of the stainless-steel (SS) electrode after LSV measurements of Mg|UiO66-MgIL|MgB_2Se_4|UiO66-MgIL|SS cells recorded from OCV to –5 V with a scan rate of –0.1 mVs^{-1}. The electrode is completely covered with adherent UiO66-MgIL, which does not allow the detection of possibly deposited Mg.

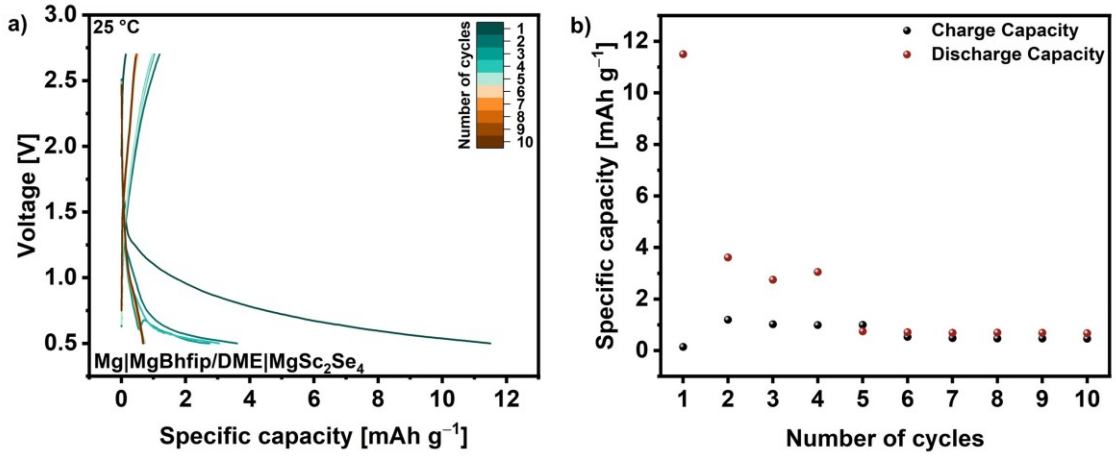

Figure S29. a) Galvanostatic discharge/charge voltage profiles of a cathode with $MgSc_2Se_4$ as active material recorded at room-temperature over ten cycles between 0.5 V and 2.7 V at a current rate of 10 mA g^{-1} and b) the very low specific capacities of discharge and charge steps represent the high redox stability of $MgSc_2Se_4$ in the examined voltage range.

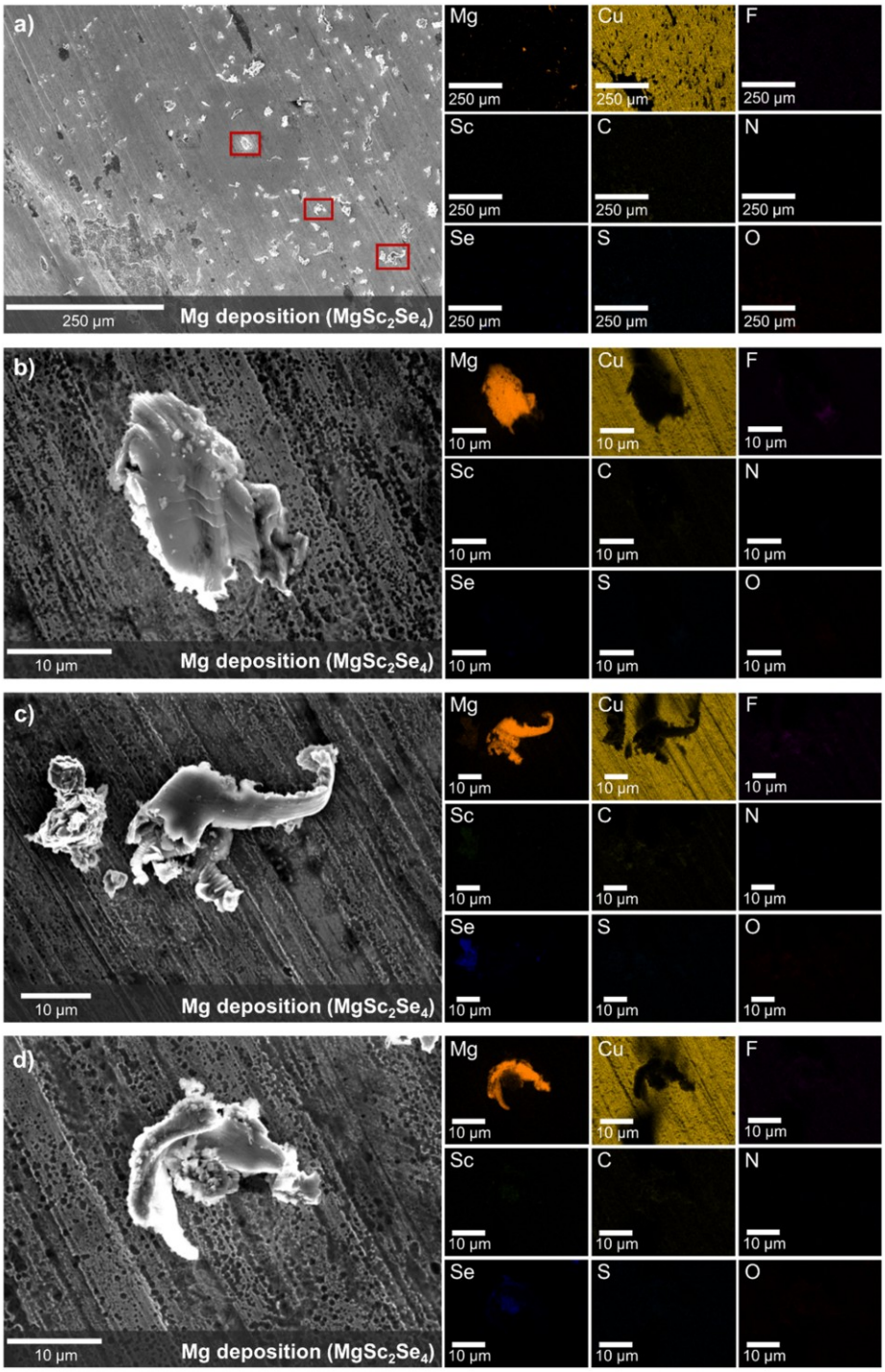

Figure S30. a) Low magnification SEM image (left) and elemental EDS maps (right) of deposited Mg on a Cu foil electrode after performing Mg plating with current of –5 µA for 35 h at 60 °C when using a Mg|UiO66-MgIL|$MgSc_2Se_4$|UiO66-MgIL|Cu cell. Only the particles that show strong intensities in the Mg EDS map are Mg deposits, while the remaining ones are residues of UiO66-MgIL or $MgSc_2Se_4$. b–d) High magnification SEM images and elemental EDS maps of three Mg deposits labeled in a).

Table S1. Crystallographic data for $MgSc_2Se_4$[1] (one-step synthesis) obtained from Rietveld refinement, based on the corresponding XRD pattern measured using Cu K_α radiation.

Crystallographic information	Result
Crystal system	Cubic
Space group	Fd-3m
Lattice parameters	a = b = c = 11.12781 Å
Cell volume	1377.936 Å^3
Density	4.146 g cm^{-3}
X^2	2.18
R_{wp}	11.0
R_{exp}	7.45
Bragg R-factor	5.00
RF-factor	3.74
GoF-index	1.5

Table S2. Crystallographic data for $MgTm_2Se_4$ (one-step synthesis) obtained from Rietveld refinement, based on the corresponding XRD pattern measured using Cu K_α radiation.

Crystallographic information	Result
Crystal system	Cubic
Space group	Fd-3m
Lattice parameters	a = b = c = 11.46260 Å
Cell volume	1506.085 Å^3
Density	5.224 g cm^{-3}
X^2	3.35
R_{wp}	19.6
R_{exp}	10.73
Bragg R-factor	13.6
RF-factor	12.2
GoF-index	1.8

Table S3. Crystallographic data for $MgEr_2Se_4$ (one-step synthesis) obtained from Rietveld refinement, based on the corresponding XRD pattern measured using Cu K_α radiation.

Crystallographic information	**Result**
Crystal system	Cubic
Space group	Fd-3m
Lattice parameters	a = b = c = 11.47062 Å
Cell volume	1509.248 Å^3
Density	5.106 g cm^{-3}
X^2	17.7
R_{wp}	26.5
R_{exp}	6.30
Bragg R-factor	13.7
RF-factor	14.9
GoF-index	4.2

Table S4. Crystallographic data for MgY_2Se_4 (one-step synthesis) obtained from Rietveld refinement, based on the corresponding XRD pattern measured using Cu K_α radiation.

Crystallographic information	**Result**
Crystal system	Cubic
Space group	Fd-3m
Lattice parameters	a = b = c = 11.57293 Å
Cell volume	1549.994 Å^3
Density	4.807 g cm^{-3}
X^2	7.48
R_{wp}	20.6
R_{exp}	7.53
Bragg R-factor	7.97
RF-factor	5.42
GoF-index	2.7

Table S5. Crystallographic data for $MgSc_2Se_4$[1] (two-step synthesis) obtained from Rietveld refinement, based on the corresponding XRD pattern measured using Cu K_α radiation.

Crystallographic information	Result
Crystal system	Cubic
Space group	Fd-3m
Lattice parameters	$a = b = c$ = 11.12973 Å
Cell volume	1378.650 Å^3
Density	4.144 g cm^{-3}
X^2	2.29
R_{wp}	8.56
R_{exp}	5.66
Bragg *R*-factor	3.43
RF-factor	2.17
GoF-index	1.5

Table S6. Crystallographic data for $MgTm_2Se_4$ (two-step synthesis) obtained from Rietveld refinement, based on the corresponding XRD pattern measured using Cu K_α radiation.

Crystallographic information	Result
Crystal system	Cubic
Space group	Fd-3m
Lattice parameters	$a = b = c$ = 11.47505 Å
Cell volume	1510.998 Å^3
Density	6.428 g cm^{-3}
X^2	12.4
R_{wp}	18.2
R_{exp}	5.17
Bragg *R*-factor	10.7
RF-factor	7.13
GoF-index	3.5

Table S7. Crystallographic data for $MgEr_2Se_4$ (two-step synthesis) obtained from Rietveld refinement, based on the corresponding XRD pattern measured using Cu K_α radiation.

Crystallographic information	**Result**
Crystal system	Cubic
Space group	Fd-3m
Lattice parameters	$a = b = c = 11.50949$ Å
Cell volume	1524.643 Å^3
Density	4.790 g cm^{-3}
X^2	4.84
R_{wp}	24.7
R_{exp}	11.23
Bragg *R*-factor	13.0
RF-factor	9.75
GoF-index	2.2

Table S8. Crystallographic data for MgY_2Se_4 (two-step synthesis) obtained from Rietveld refinement, based on the corresponding XRD pattern measured using Cu K_α radiation.

Crystallographic information	**Result**
Crystal system	Cubic
Space group	Fd-3m
Lattice parameters	$a = b = c = 11.57079$ Å
Cell volume	1549.134 Å^3
Density	4.375 g cm^{-3}
X^2	9.61
R_{wp}	16.8
R_{exp}	5.41
Bragg *R*-factor	6.74
RF-factor	3.91
GoF-index	3.1

Table S9. Mass *m* and thickness *d* of the UiO66-MgIL layer in the SS|UiO66-MgIL|SS cells.

cell name	UiO66-MgIL batch	*m*(UiO66-MgIL) [mg]	*d*(UiO66-MgIL) [mm]
MOF1[1]	1	80	0.60
MOF2	2	80	0.59

Table S10. Mass *m* and thickness *d* of MgB_2Se_4 pellets and UiO66-MgIL layers (sum of both layers) in the SS|UiO66-MgIL|MgB_2Se_4|UiO66-MgIL|SS cells and the relative density ρ of the MgB_2Se_4 pellets obtained from pressed spinel powders relative to sintered MgB_2Se_4 pellets [$\rho(MgSc_2Se_4)$ = 3.242 g cm^{-3}, $\rho(MgTm_2Se_4)$ = 4.535 g cm^{-3}, $\rho(MgEr_2Se_4)$ = 4.355 g cm^{-3}, $\rho(MgY_2Se_4)$ = 3.426 g cm^{-3}].

cell name	spinel	*m*(MgB_2Se_4) [mg]	*d*(MgB_2Se_4) [mm]	ρ(MgB_2Se_4) [%]	UiO66-MgIL batch	*m*(UiO66-MgIL) [mg]	*d*(UiO66-MgIL) [mm]
Sc160[1]	$MgSc_2Se_4$	160	0.80	78.6	1	80	0.56
Sc190[1]	$MgSc_2Se_4$	190	0.88	84.8	1	80	0.56
Sc220[1]	$MgSc_2Se_4$	220	1.10	78.6	1	80	0.38
Sc250[1]	$MgSc_2Se_4$	250	1.14	86.1	1	80	0.56
Sc280[1]	$MgSc_2Se_4$	280	1.40	78.6	1	80	0.59
Tm160	$MgTm_2Se_4$	160	0.46	97.7	2	80	0.61
Tm220	$MgTm_2Se_4$	220	0.62	99.6	2	80	0.65
Tm280	$MgTm_2Se_4$	280	1.00	78.6	2	80	0.54
Er160	$MgEr_2Se_4$	160	0.50	93.6	2	80	0.60
Er220	$MgEr_2Se_4$	220	0.68	94.6	2	80	0.58
Er280	$MgEr_2Se_4$	280	0.82	99.8	2	80	0.58
Y160	MgY_2Se_4	160	0.72	82.6	2	80	0.58
Y220	MgY_2Se_4	220	0.86	95.1	2	80	0.55
Y280	MgY_2Se_4	280	1.26	82.6	2	80	0.56

Table S11. Overview of resistances *R* obtained from data fitting ([a]) or due to direct calculation from data points ([b]), exemplarily shown for the room-temperature (25 °C) impedance measurements of all SS|UiO66-MgIL|SS and SS|UiO66-MgIL|MgB_2Se_4|UiO66-MgIL|SS cells. While for the fitting of the SS|UiO66-MgIL|SS cells MOF-1 and MOF-2 the equivalent circuit in **Figure 3b** was applied, the remaining spinel-containing cells were fitted with the equivalent circuit in **Figure 3c**. In addition, for these cells, $R1_{ion}$ and R_{ion}(UiO66-MgIL) were calculated by **Equation S1** ([c]). Note: The electronic resistance $R2_{el}$ is not listed since it is impossible to determine reliable results by the applied equivalent circuit, as described in our earlier work.[1]

cell name	$R1_{ion}$ [Ω]	R_{ion}(UiO66-MgIL) [Ω]	$R2_{ion}$ [Ω]	$R_{ion}(MgB_2Se_4)$ [Ω]	$R1_{ion}+R2_{ion}$ [Ω]	R_{ion}(SEs) [Ω]
MOF1[1]	806[a]	806[b]	-	-	806[a]	806[b]
MOF2	273[a]	274[b]	-	-	273[a]	274[b]
Sc160[1]	752[c]	752[c]	1870[a]	1862[b]	2622[a]	2614[b]
Sc190[1]	752[c]	752[c]	2532[a]	2536[b]	3284[a]	3287[b]
Sc220[1]	510[c]	510[c]	2974[a]	2875[b]	3484[a]	3386[b]
Sc250[1]	752[c]	752[c]	5169[a]	5161[b]	5921[a]	5912[b]
Sc280[1]	792[c]	792[c]	7564[a]	7466[b]	8356[a]	8258[b]
Tm160	283[c]	283[c]	631[a]	592[b]	914[a]	875[b]
Tm220	301[c]	302[c]	1289[a]	1180[b]	1590[a]	1482[b]
Tm280	250[c]	251[c]	3199[a]	3136[b]	3449[a]	3386[b]
Er160	278[c]	279[c]	1282[a]	1003[b]	1560[a]	1282[b]
Er220	269[c]	269[c]	2323[a]	2074[b]	2592[a]	2343[b]
Er280	269[c]	269[c]	2881[a]	2646[b]	3150[a]	2915[b]
Y160	269[c]	269[c]	3534[a]	3530[b]	3803[a]	3799[b]
Y220	254[c]	255[c]	5491[a]	5490[b]	5745[a]	5745[b]
Y280	259[c]	260[c]	11743[a]	11748[b]	12002[a]	12008[b]

Since the total UiO66-MgIL layer thickness in the SS|UiO66-MgIL|MgB_2Se_4|UiO66-MgIL|SS cells (see Table S10) can vary to those used in the SS|UiO66-MgIL|SS reference cells (see Table S9), the impedances of the UiO66-MgIL were adapted to the layer thickness used by Equation S1:

$$R_{ion}(i) = \frac{d(\text{UiO66-MgIL})}{d(\text{UiO66-MgIL-Ref.})} R_{ion}(i\text{-Ref.}) \quad \text{(S1)}$$

i = UiO66-MgIL, $R1_{ion}$

Ref. = MOF1 or MOF2

For the $MgSc_2Se_4$-based cells the reference cell MOF1 was used, while MOF2 was the reference cell for the $MgTm_2Se_4$-, $MgEr_2Se_4$- and MgY_2Se_4-based cells.

Table S12. Comparison of computational migration barriers for spinel compounds $MgSc_2Se_4$, $MgEr_2Se_4$, MgY_2Se_4 and $MgTm_2Se_4$ determined using different exchange-correlation functionals (PBE: Perdew-Burke-Ernzerhof[2]; SCAN: Strongly Constrained and Appropriately Normed[3]) and settings with experimental migration barriers. The supercell volume was either kept fixed (fix) or relaxed (rel) to allow for possible distortion due to the introduction of a vacancy in the system. Moreover, the influence of formal charge compensation due to a uniform background charge (chg) was tested. Overall, the influence of volume relaxation and formal charge compensation were found to be rather limited while SCAN calculations were found to be in better agreement with the experimentally determined migration barriers.

compound	PBE (fix) [meV]	PBE (rel) [meV]	PBE (fix, chg) [meV]	SCAN (fix, chg) [meV]	SCAN (fix) [meV]	experiment [meV]
$MgSc_2Se_4$	336	339	343	367	392	386
$MgTm_2Se_4$	334	362	331	368	381	381
$MgEr_2Se_4$	333	357	330	365	378	382
MgY_2Se_4	348	349	341	361	365	408

References

[1] C. Glaser, Z. Wei, S. Indris, P. Klement, S. Chatterjee, H. Ehrenberg, Z. Zhao‐Karger, M. Rohnke, J. Janek, *Adv. Energy Mater.* **2023**, *13*, 2301980.

[2] J. P. Perdew, K. Burke, M. Ernzerhof, *Phys. Rev. Lett.* **1996**, *77*, 3865.

[3] J. Sun, A. Ruzsinszky, J. P. Perdew, *Phys. Rev. Lett.* **2015**, *115*, 36402.

A.3 Publication 3: "High Room-Temperature Magnesium Ion Conductivity in Spinel-Type $MgYb_2Se_4$ Solid Electrolyte"

High Room-Temperature Magnesium Ion Conductivity in Spinel-Type $MgYb_2Se_4$ Solid Electrolyte

*Clarissa Glaser,[†] Mohsen Sotoudeh,[‡] Manuel Dillenz,[‡] Kanchan Sarkar,[‡] Jasmin S. Bark,[†] Shashwat Singh,[§] Zhixuan Wei,[†] Sylvio Indris,[‖] Riccarda Müller,[⊥] Kerstin Leopold,[⊥] Linda F. Nazar,[§] Axel Groß[‡] and Jürgen Janek[†]**

[†]Institute of Physical Chemistry and Center for Materials Research (ZfM), Justus Liebig University Giessen, Heinrich-Buff-Ring 17, 35392 Giessen, Germany

[‡]Institute of Theoretical Chemistry, Ulm University, Albert-Einstein-Allee 11, 89081 Ulm, Germany

[§]Department of Chemistry and the Waterloo Institute for Nanotechnology, University of Waterloo, Waterloo, Ontario N2L 3G1, Canada

[‖]Institute for Applied Materials-Energy Storage Systems (IAM-ESS), Karlsruhe Institute of Technology (KIT), Hermann-von-Helmholtz-Platz 1, 76344 Eggenstein-Leopoldshafen, Germany

[⊥]Institute of Analytical and Bioanalytical Chemistry, Ulm University, 89081 Ulm, Germany

***Corresponding author:** Juergen.Janek@phys.chemie.uni-giessen.de

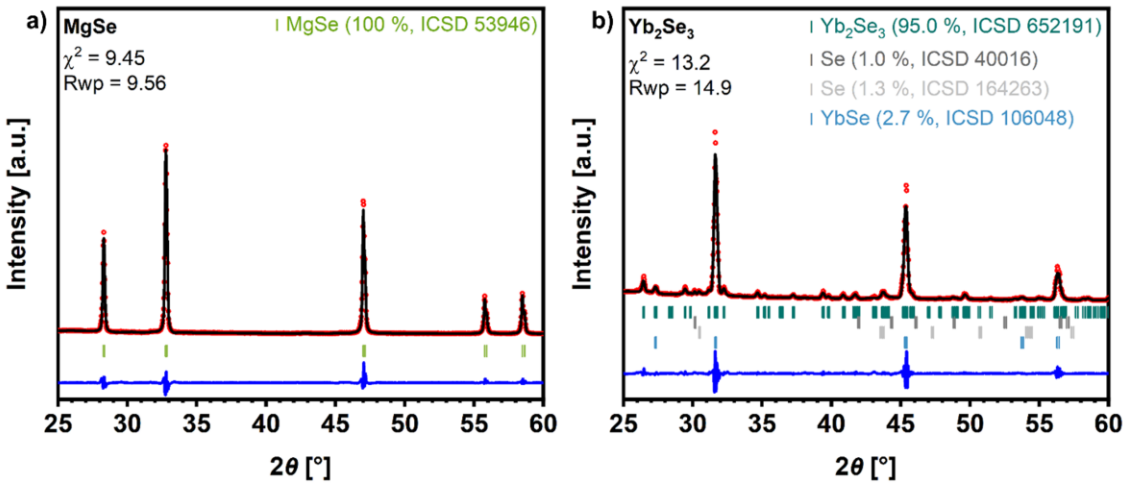

Figure S1. Rietveld refinements based on the XRD data (**Figure 1a**) of a) MgSe and b) Yb_2Se_3. Observed and calculated patterns are shown in red and black, and the difference curves are shown in blue. The refinement with respect to the MgSe sample indicates a phase-pure material without any impurities of possible phases such as Se, Mg or MgO. In the Yb_2Se_3 sample, instead, small fractions of Se (2.3 wt% in total) and YbSe (2.7 wt%) were identified, resulting from an incomplete/non-stoichiometric reaction of Yb and Se, which is expected to continue during the next reaction step ($MgYb_2Se_4$ formation).

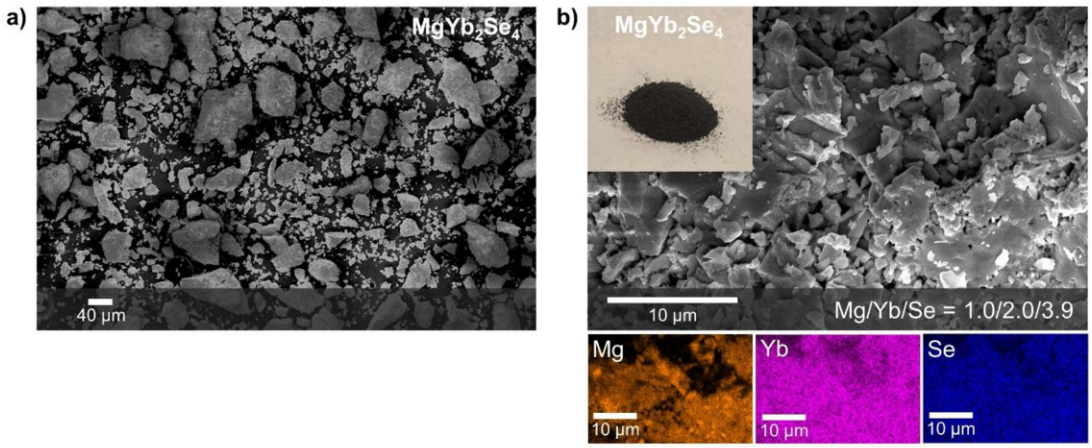

Figure S2. a) Overview SEM image showing sintered fragments of $MgYb_2Se_4$ powder with a typical size of 1–100 µm. b) Light optical image of the dark red $MgYb_2Se_4$ powder and SEM image of a $MgYb_2Se_4$ fragment (consisting of sintered 1–3 µm sized particles) with EDS mapping of the corresponding elements Mg, Yb and Se.

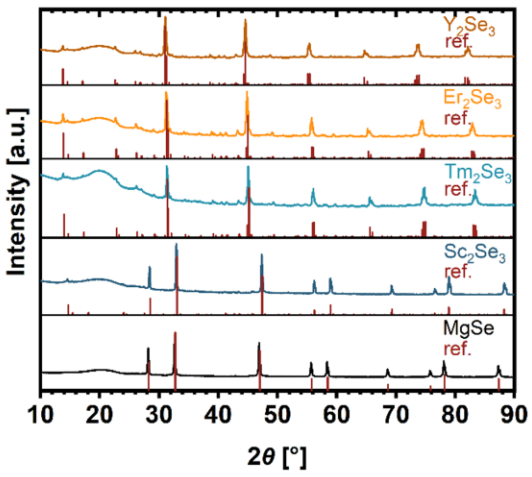

Figure S3. XRD patterns of synthesized MgSe, Sc_2Se_3, Tm_2Se_3, Er_2Se_3 and Y_2Se_3. Reproduced with permission from reference [1]. Copyright 2024, C. Glaser et al.[1]

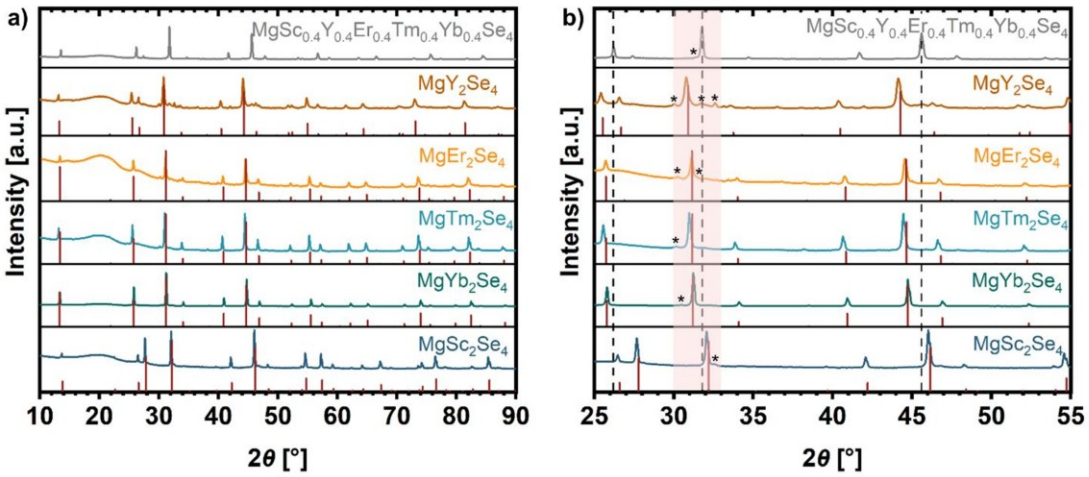

Figure S4. a) XRD patterns of spinels $MgSc_2Se_4$, $MgYb_2Se_4$, $MgTm_2Se_4$, $MgEr_2Se_4$, MgY_2Se_4 and $MgSc_{0.4}Y_{0.4}Er_{0.4}Tm_{0.4}Yb_{0.4}Se_4$ synthesized from corresponding binary selenides. All data for $MgSc_2Se_4$, $MgTm_2Se_4$, $MgEr_2Se_4$ and MgY_2Se_4 reused with permission from references [1,2]. Copyright 2023 and 2024, C. Glaser et al.[1,2] b) Zoomed view of a) showing reflections of impurities in the range of 30° to 33° marked with an asterisk. Among the spinels, $MgYb_2Se_4$ and $MgSc_{0.4}Y_{0.4}Er_{0.4}Tm_{0.4}Yb_{0.4}Se_4$ have the lowest intensities of impurity phases. The XRD pattern of $MgSc_{0.4}Y_{0.4}Er_{0.4}Tm_{0.4}Yb_{0.4}Se_4$ is quite similar to that of MgY_2Se_4 but shifted to larger angles 2θ, which is probably due to the partial substitution of the Y-position by the smaller Sc-, Yb-, Tm- and Er-ions.

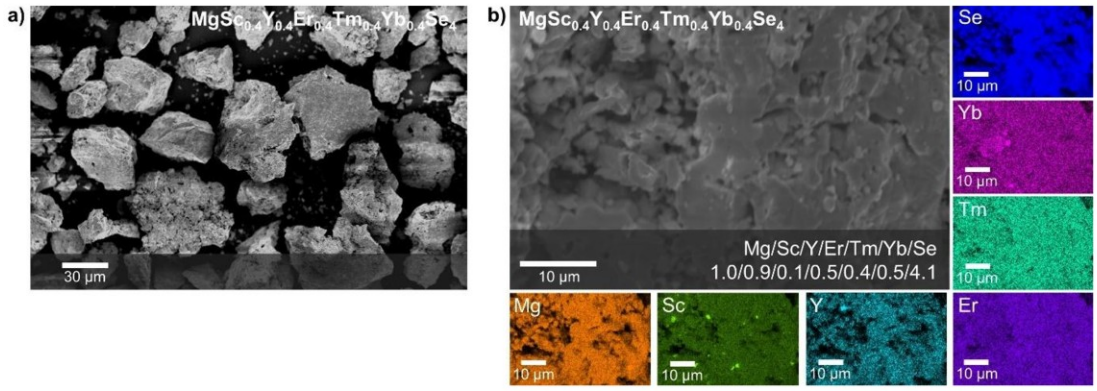

Figure S5. a) Overview SEM image of $MgSc_{0.4}Y_{0.4}Er_{0.4}Tm_{0.4}Yb_{0.4}Se_4$ powder showing sintered fragments with a typically size of 1–80 µm; and b) SEM image of a fragment with EDS mapping of the corresponding elements Mg, Sc, Y, Er, Tm, Yb and Se.

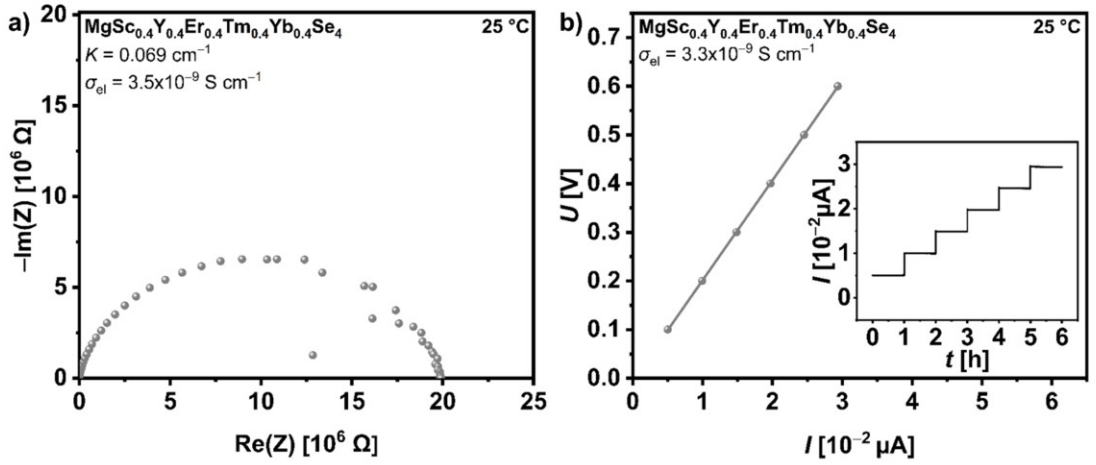

Figure S6. a) Nyquist plot of the C|$MgSc_{0.4}Y_{0.4}Er_{0.4}Tm_{0.4}Yb_{0.4}Se_4$|C press cell in the frequency range of 3 MHz to 100 mHz at 25 °C. b) DC polarization data at 25 °C obtained for the same cell configuration. During the measurement, different voltages (0.1, 0.2, 0.3, 0.4, 0.5 and 0.6 V) were held for 1 h each. The steady-state current at the end of each holding step (shown in the inset) was plotted against the corresponding voltage to calculate the electronic resistance R_{el} of the

multicationic spinel using a linear fit. As a result, $MgSc_{0.4}Y_{0.4}Er_{0.4}Tm_{0.4}Yb_{0.4}Se_4$ shows a similarly low electronic conductivity as the $MgYb_2Se_4$ spinel.

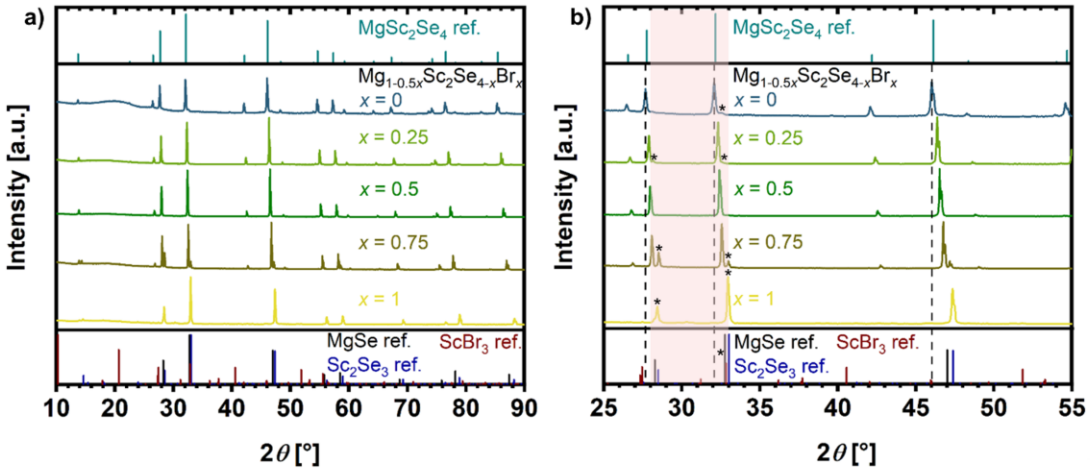

Figure S7. a) XRD patterns of $Mg_{1-0.5x}Sc_2Se_{4-x}Br_x$ compounds (x = 0, 0.25, 0.5, 0.75, 1) synthesized from binary compounds MgSe, Sc_2Se_3 and $ScBr_3$. All data for $MgSc_2Se_4$ reused with permission from reference [2]. Copyright 2023, C. Glaser et al.[2] b) Zoomed view of a) showing reflections of impurities in the range of 28° to 33° marked with an asterisk. Among the spinels, only the $Mg_{0.75}Sc_2Se_{3.5}Br_{0.5}$ spinel shows no impurity phases. The shift of the XRD patterns to larger angles 2θ with increasing x is probably due to the partial substitution of the Se-position by the slightly smaller Br-ions. At $x \geq 0.75$ decomposition to binary compounds is observed.

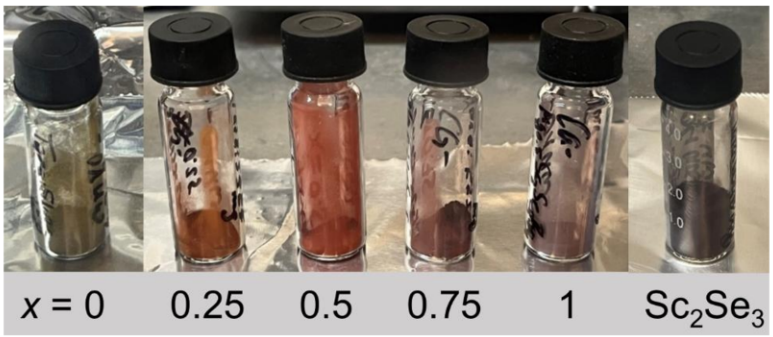

Figure S8. Light optical images of synthesized $Mg_{1-0.5x}Sc_2Se_{4-x}Br_x$ compounds (x = 0, 0.25, 0.5, 0.75, 1) and Sc_2Se_3. The color of the powder changes as x increases from gray-brown to orange, orange-red and dark red to violet. The violet color at x = 1 suggests that decomposition to the dark violet Sc_2Se_3, MgSe (white-grey) and $ScBr_3$ (white) has occurred.

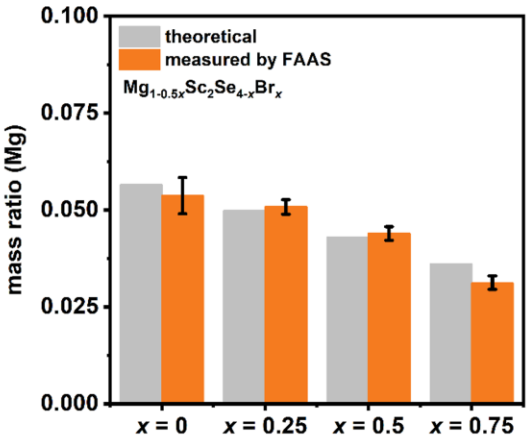

Figure S9. Theoretical mass ratio (grey) and experimentally determined mass ratio of Mg (orange) in $Mg_{1-0.5x}Sc_2Se_{4-x}Br_x$ compounds (x = 0, 0.25, 0.5, 0.75) using FAAS. Error bars represent ±1 SD with n = 3.

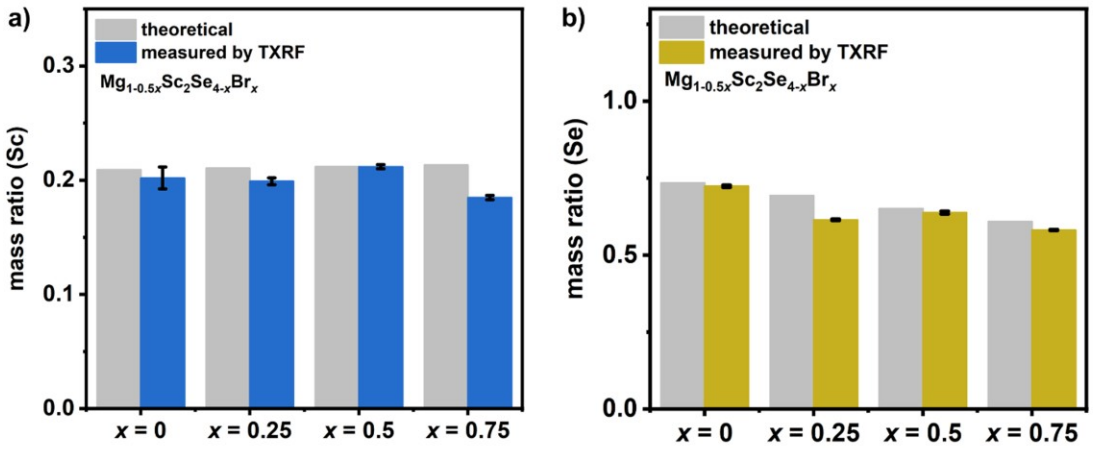

Figure S10. Theoretical mass ratio (grey) and experimentally determined mass ratio of a) Sc (blue) and b) Se (yellow) in $Mg_{1-0.5x}Sc_2Se_{4-x}Br_x$ compounds (x = 0, 0.25, 0.5, 0.75) using TXRF. Error bars represent ±1 SD with n = 3.

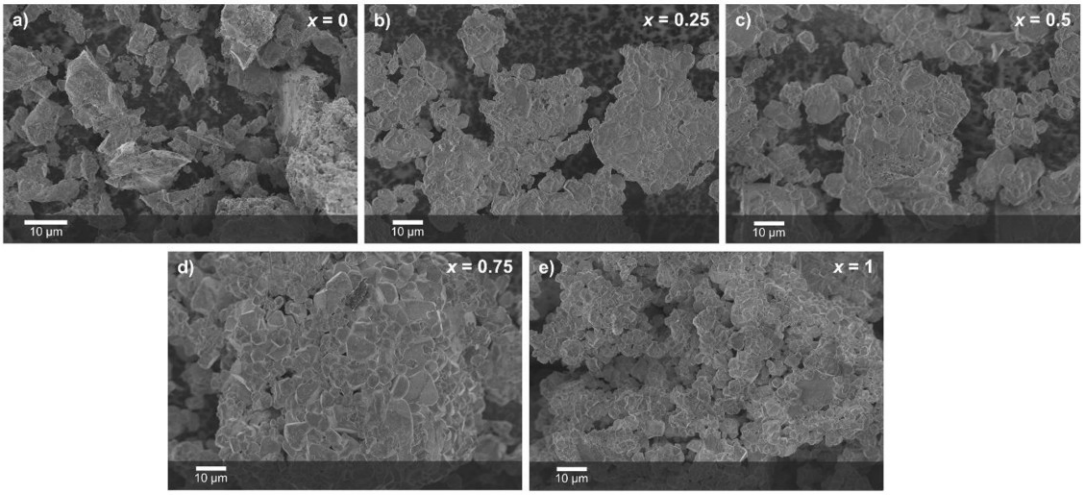

Figure S11. SEM images of $Mg_{1-0.5x}Sc_2Se_{4-x}Br_x$ (x = 0, 0.25, 0.5, 0.75, 1) showing an increase of the size of the sintered particles in the fragments from x = 0 to x = 0.75.

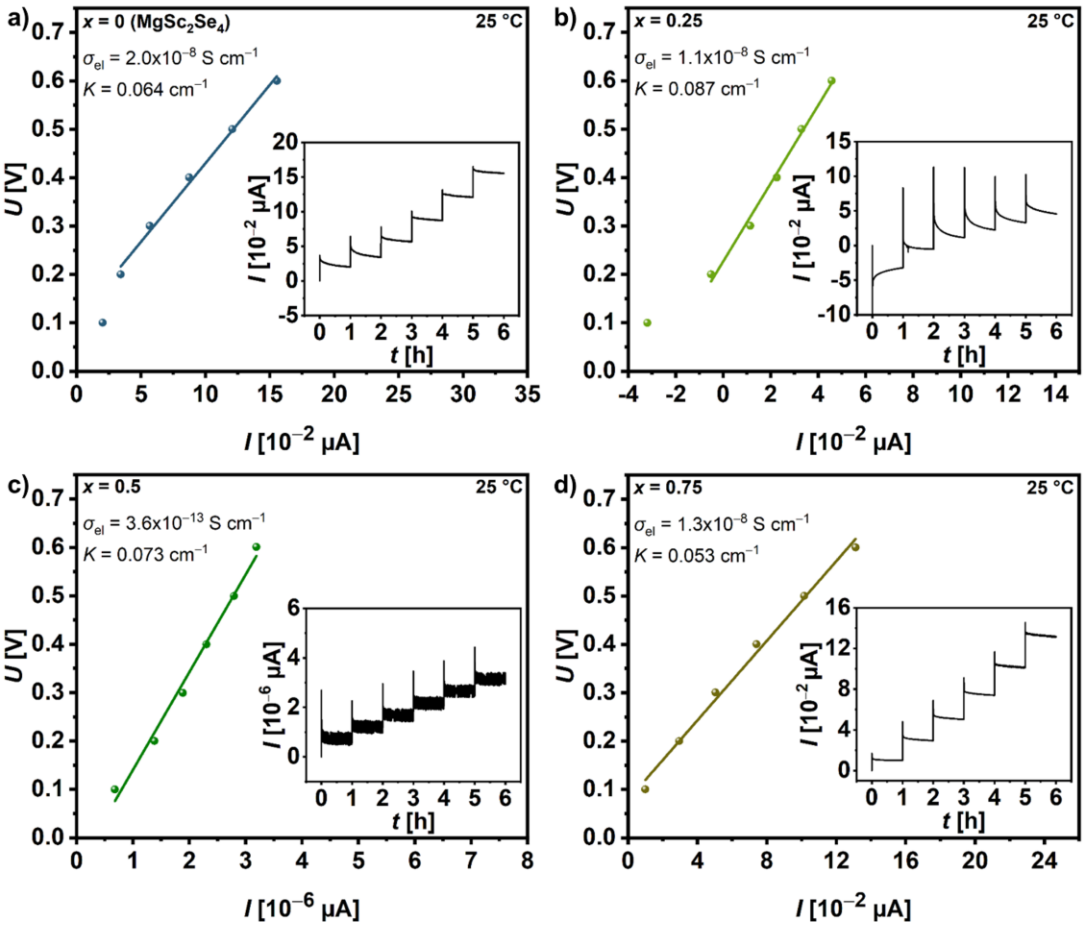

Figure S12. DC polarization data of C|$Mg_{1-0.5x}Sc_2Se_{4-x}Br_x$|C press cells obtained at 25 °C. During the measurement, different voltages (0.1, 0.2, 0.3, 0.4, 0.5 and 0.6 V) were held for 1 h each. The steady-state current at the end of each holding step (shown in the inset) was plotted against the corresponding voltage to calculate the electronic resistance R_{el} of the $Mg_{1-0.5x}Sc_2Se_{4-x}Br_x$ compounds using a linear fit. Among the spinels, $Mg_{0.75}Sc_2Se_{3.5}Br_{0.5}$ shows a five order of magnitude lower electronic conductivity.

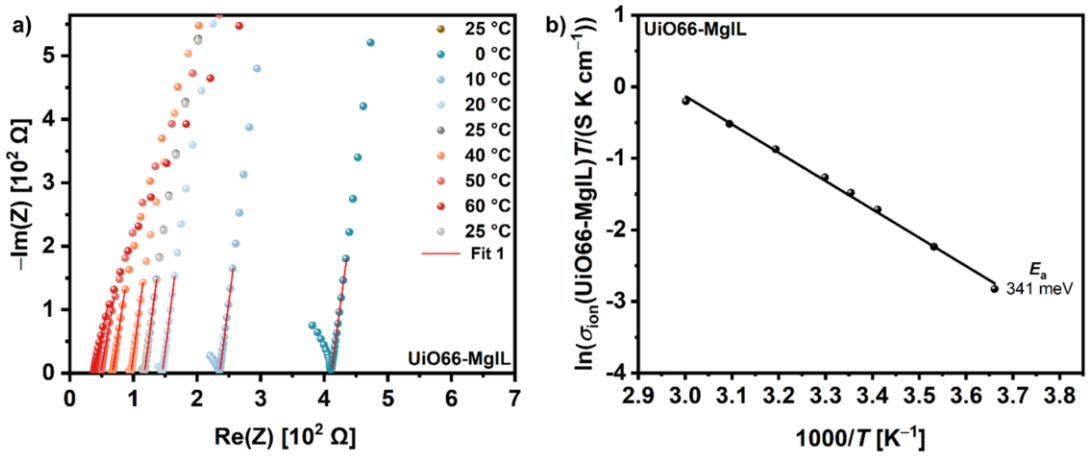

Figure S13. a) Fitted Nyquist plots of a SS|UiO66-MgIL|SS cell at different temperatures ranging from 0 °C to 60 °C and b) corresponding Arrhenius plot showing a Mg^{2+} migration barrier of 341 meV for UiO66-MgIL.

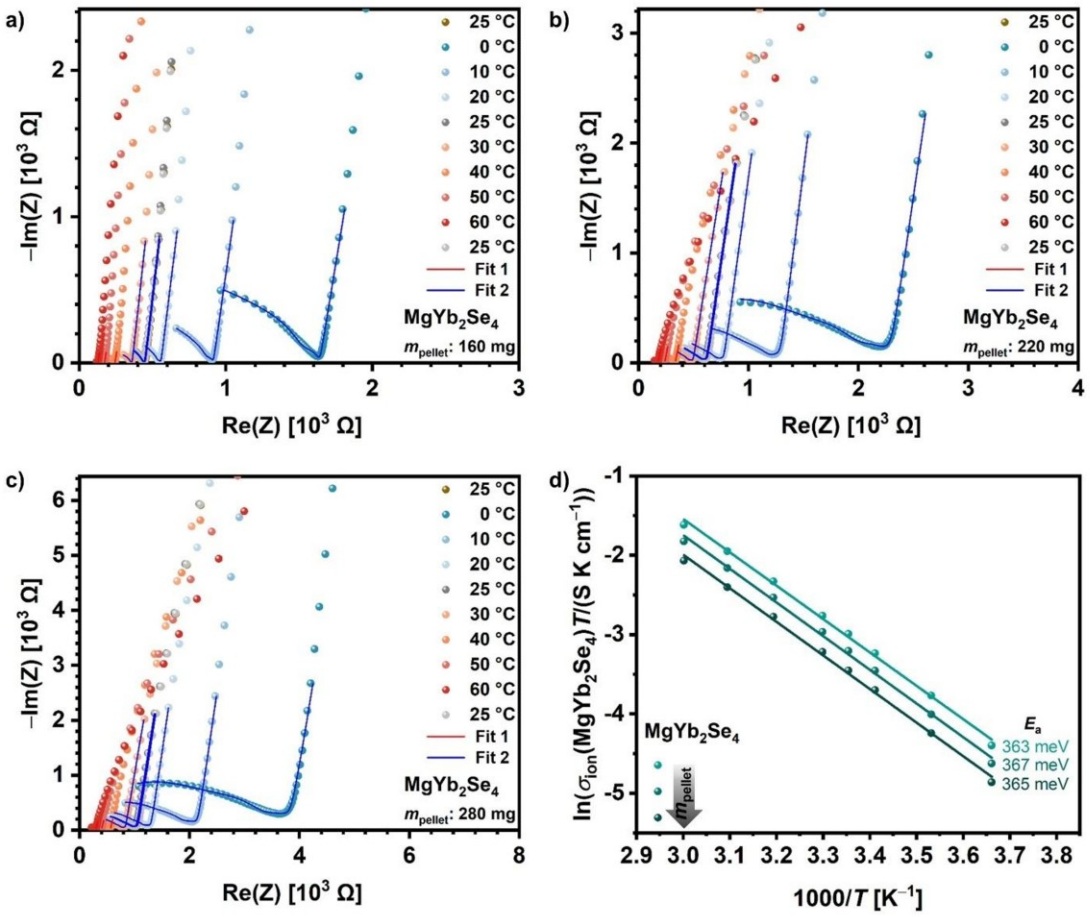

Figure S14. Fitted Nyquist plots of SS|UiO66-MgIL|$MgYb_2Se_4$|UiO66-MgIL|SS cells at different temperatures ranging from 0 °C to 60 °C using a spinel pellet mass/thickness of a) 160 mg/0.46 mm, b) 220 mg/0.54 mm, and c) 280 mg/0.76 mm; and d) Arrhenius plots of the ionic conductivity of $MgYb_2Se_4$ for each cell.

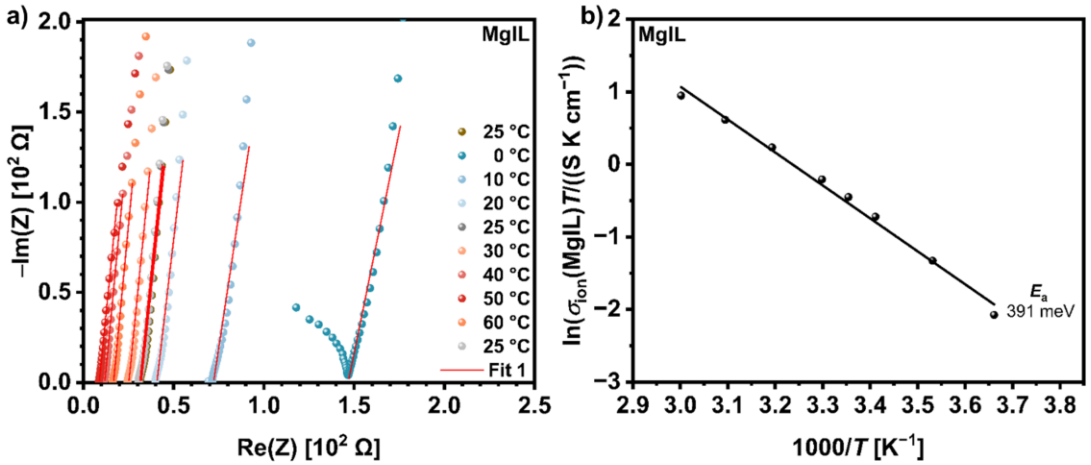

Figure S15. a) Fitted Nyquist plots of a SS|MgIL|SS cell at different temperatures ranging from 0 °C to 60 °C; and b) corresponding Arrhenius plot showing a Mg^{2+} migration barrier of 391 meV for MgIL.

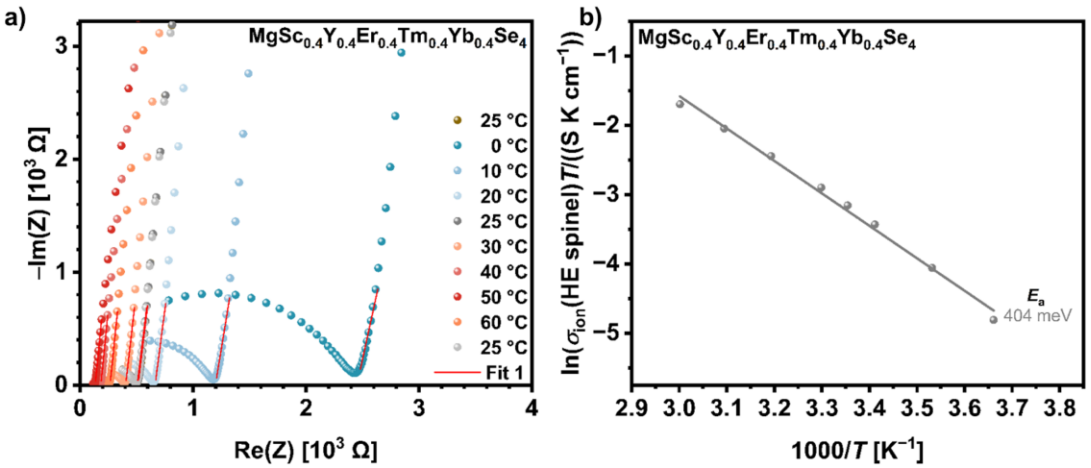

Figure S16. a) Fitted Nyquist plots of the SS|MgIL|$MgSc_{0.4}Y_{0.4}Er_{0.4}Tm_{0.4}Yb_{0.4}Se_4$|MgIL|SS cell at different temperatures ranging from 0 °C to 60 °C using a spinel pellet mass/thickness of 160 mg/0.54 mm; and d) corresponding Arrhenius plot of the ionic conductivity of $MgSc_{0.4}Y_{0.4}Er_{0.4}Tm_{0.4}Yb_{0.4}Se_4$.

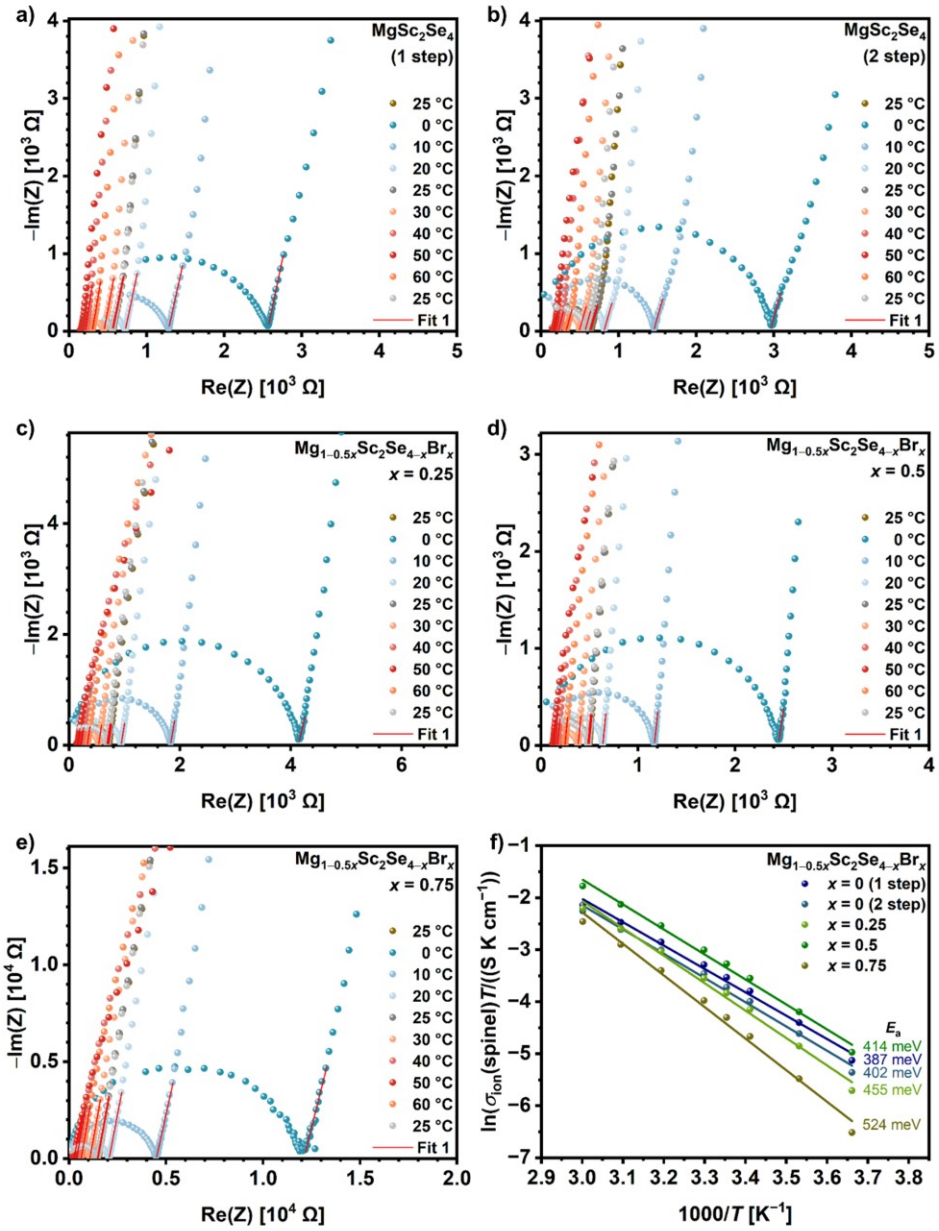

Figure S17. Fitted Nyquist plots of SS|MgIL|$Mg_{1-0.5x}Sc_2Se_{4-x}Br_x$|MgIL|SS cells at different temperatures ranging from 0 °C to 60 °C using a 160 mg spinel pellet with a thickness of a) 0.41 mm, b) 0.38 mm, c) 0.38 mm, d) 46 mm, e) 51 mm; and f) Arrhenius plots of the ionic conductivity of $Mg_{1-0.5x}Sc_2Se_{4-x}Br_x$ for each cell.

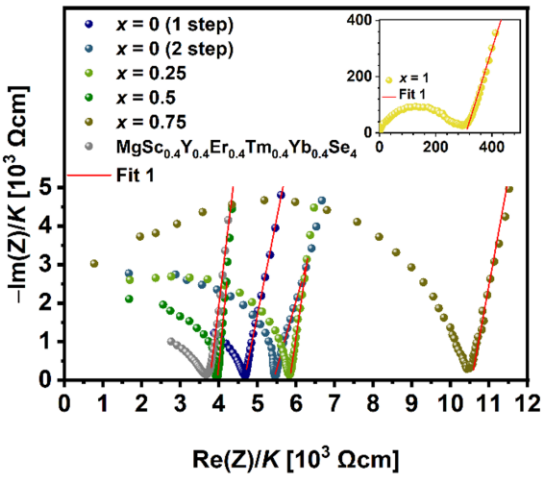

Figure S18. Overview of the fitted Nyquist plots of the SS|MgIL|$Mg_{1-0.5x}Sc_2Se_{4-x}Br_x$|MgIL|SS cells and the SS|MgIL|$MgSc_{0.4}Y_{0.4}Er_{0.4}Tm_{0.4}Yb_{0.4}Se_4$|MgIL|SS cell at 25 °C. The multicationic and multianionic ($x < 0.75$) spinels show comparable ionic resistances to the pristine $MgSc_2Se_4$ samples, while the ionic resistance increases with $x \geq 0.75$ in $Mg_{1-0.5x}Sc_2Se_{4-x}Br_x$ due to the decomposition of the spinel into binary compounds.

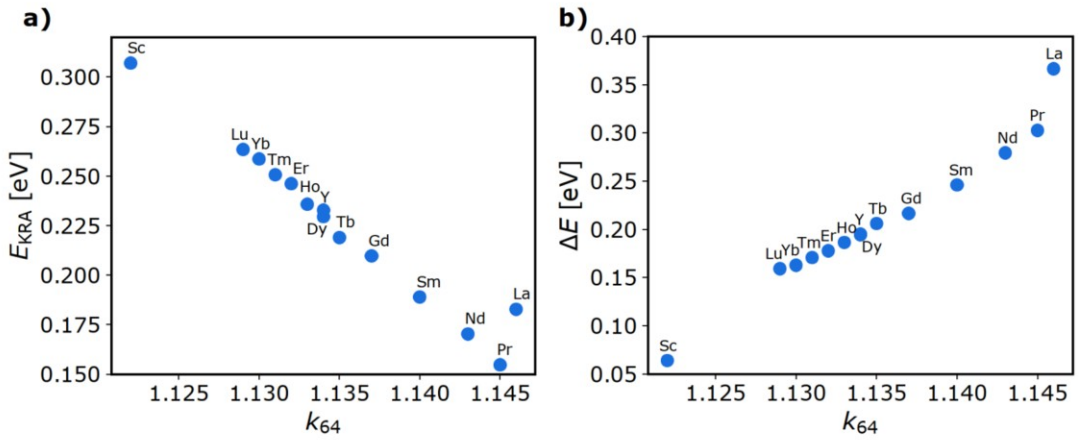

Figure S19. a) The kinetically resolved activation energy (E_{KRA}) and b) the site preference energy (ΔE), both expressed in electron volts (eV), for Mg-ion migration in the MgB_2Se_4 selenide spinel lattice as a function of the k_{64} distance ratio.

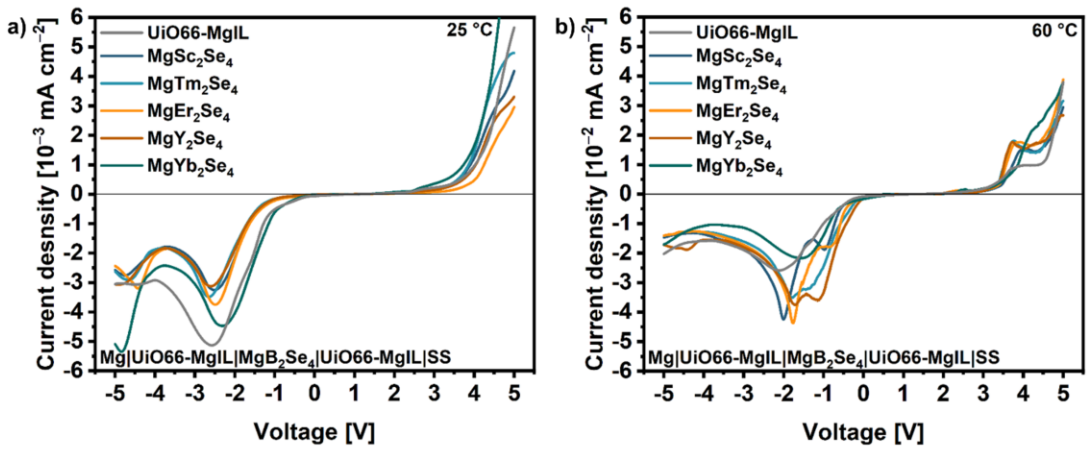

Figure S20. LSV curves of Mg|UiO66-MgIL|SS cell and Mg|UiO66-MgIL|MgB_2Se_4|UiO66-MgIL|SS cells (B = Sc, Tm, Er, Y, Yb) recorded at a scan rate of –0.1 mV s^{-1}/0.1 mV s^{-1} at a) room temperature and b) 60 °C. The current profiles of the sandwich-type cells and the reference cell without spinel layer are quite identical, as the UiO66-MgIL appears to limit the stability window. Data for $MgSc_2Se_4$, $MgTm_2Se_4$, $MgEr_2Se_4$ and MgY_2Se_4 reused with permission from reference [1]. Copyright 2024, C. Glaser et al.[1]

Table S1. Crystallographic data for $MgYb_2Se_4$ obtained from Rietveld refinement, based on the corresponding XRD pattern measured using Cu K_α radiation.

Crystallographic information	**Result**
Crystal system	cubic
Space group	Fd-3m
Lattice parameters	$a = b = c$ = 11.45178 Å
Cell volume	1501.824 Å^3
Density	6.447 g cm^{-3}
Atomic positions of Mg	$X = Y = Z$ = 0.37500
Atomic positions of Yb	$X = Y = Z$ = 0
Atomic positions of Se	$X = Y = Z$ = 0.24456
X^2	6.27
R_{wp}	7.54
R_{exp}	3.01
Bragg *R*-factor	1.20
RF-factor	1.44
GoF-index	2.5

Table S2. Mass *m* and thickness *d* of $MgYb_2Se_4$ pellets and UiO66-MgIL layers (sum of both layers) in the SS|UiO66-MgIL|SS reference cell and the SS|UiO66-MgIL|$MgYb_2Se_4$|UiO66-MgIL|SS cells.

Name of cell	*m*($MgYb_2Se_4$) [mg]	*d*($MgYb_2Se_4$) [mm]	*m*(UiO66-MgIL) [mg]	*d*(UiO66-MgIL) [mm]
MOF3	0	0	80	0.70
Yb160	160	0.46	80	0.58
Yb220	220	0.54	80	0.64
Yb280	280	0.76	80	0.69

Table S3. Overview of the resistances $R1_{ion}$ (for UiO66-MgIL) and $R2_{ion}$ (for $MgYb_2Se_4$) obtained from data fitting of the SS|UiO66-MgIL|SS reference cell using the equivalent circuit in **Figure 3c** and the SS|UiO66-MgIL|$MgYb_2Se_4$|UiO66-MgIL|SS cells using the equivalent circuit in **Figure 3d**, exemplarily shown for the room temperature (25 °C) impedance measurements.

Name of cell	$R1_{ion}$ [Ω]	σ_{ion}(UiO66-MgIL) [10^{-4} S cm^{-1}]	$R2_{ion}$ [Ω]	σ_{ion}(MgB_2Se_4) [10^{-4} S cm^{-1}]
MOF3	117	7.61	-	-
Yb160	97[a]	7.61	348	1.68
Yb220	107[a]	7.61	506	1.36
Yb280	115[a]	7.61	911	1.06

For all spinel-containing cells, $R1_{ion}$ ([a]) of the UiO66-MgIL was calculated by **eq S1**. Note: The electronic resistance $R2_{el}$ of the $MgYb_2Se_4$ is not listed as it is impossible to determine reliable results by the applied equivalent circuit, described in our earlier work.[2]

Since the total UiO66-MgIL layer thickness in the SS|UiO66-MgIL|$MgYb_2Se_4$|UiO66-MgIL|SS cells can vary to those used in the SS|UiO66-MgIL|SS reference cells (see **Table S2**), the impedances of the UiO66-MgIL ($R1_{ion}$ in **Table S3**) were adjusted to the layer thickness used by **eq S1**:

$$R1_{ion} = \frac{d(\text{UiO66-MgIL-}i)}{d(\text{UiO66-MgIL-Ref.})} R1_{ion}(\text{Ref.}) \quad \text{(S1)}$$

i = Yb160, Yb220 and Yb280

Ref. = MOF3

Table S4. Mass m(spinel) and thickness d(spinel) of spinel pellets ($MgSc_2Se_4$, multicationic/multianionic spinels) and thickness d(MgIL) of the glass fiber-MgIL layers (sum of both layers) in the SS|MgIL|SS reference cell and the SS|MgIL|spinel|MgIL|SS cells.

spinel	*m*(spinel) [mg]	*d*(spinel) [mm]	*d*(MgIL) [mm]
-	0	0	0.53
$MgSc_2Se_4$ (1 step)	160	0.41	0.54
$MgSc_2Se_4$ (2 step)	160	0.38	0.53
$Mg_{0.875}Sc_2Se_{3.75}Br_{0.25}$	160	0.38	0.56
$Mg_{0.75}Sc_2Se_{3.5}Br_{0.5}$	160	0.46	0.51
$Mg_{0.625}Sc_2Se_{3.25}Br_{0.75}$	160	0.51	0.58
$Mg_{0.5}Sc_2Se_3Br_1$	160	0.45	0.66
$MgSc_{0.4}Y_{0.4}Er_{0.4}Tm_{0.4}Yb_{0.4}Se_4$	160	0.54	0.53

Table S5. Overview of resistances $R1_{ion}$ (here: total ionic resistance) obtained from data fitting of the SS|MgIL|SS reference cell and the SS|MgIL|spinel|MgIL|SS cells using the equivalent circuit in **Figure 3c**, and the calculated resistances R_{ion}(MgIL) and R_{ion}(spinel), exemplarily shown for the room temperature (25 °C) impedance measurements.

spinel	$R1_{ion}$ [Ω]	R_{ion}(MgIL) [Ω]	σ_{ion}(MgIL) [10^{-4} S cm^{-1}]	R_{ion}(spinel) [Ω]	σ_{ion}(spinel) [10^{-4} S cm^{-1}]
-	32	32	21	-	-
$MgSc_2Se_4$ (1 step)	563	32[a]	21	531	0.98
$MgSc_2Se_4$ (2 step)	628	32 [a]	21	596	0.81
$Mg_{0.875}Sc_2Se_{3.75}Br_{0.25}$	698	33 [a]	21	665	0.73
$Mg_{0.75}Sc_2Se_{3.5}Br_{0.5}$	489	30 [a]	21	459	1.3
$Mg_{0.625}Sc_2Se_{3.25}Br_{0.75}$	1464	35 [a]	21	1429	0.45
$Mg_{0.5}Sc_2Se_3Br_1$	43458	39 [a]	21	43419	0.013
$MgSc_{0.4}Y_{0.4}Er_{0.4}Tm_{0.4}Yb_{0.4}Se_4$	501	31 [a]	21	470	1.5

For all spinel-containing cells, R_{ion}(MgIL) of the glass fiber-MgIL interlayer ([a]) was calculated from $R1_{ion}$ of the SS|MgIL|SS cell analogously to that shown for the UiO66-MgIL interlayer by **eq S1**. R_{ion}(spinel) is determined by the difference of $R1_{ion}$ and R_{ion}(MgIL). Note that σ_{ion}(spinel) may be overestimated as described in context with **Figure 4**.

REFERENCES

(1) Glaser, C.; Dillenz, M.; Sarkar, K.; Sotoudeh, M.; Wei, Z.; Indris, S.; Maile, R.; Rohnke, M.; Müller‐Buschbaum, K.; Groß, A.; Janek, J. MgB2Se4 Spinels (B = Sc, Y, Er, Tm) as Potential Mg‐Ion Solid Electrolytes‐Partial Ionic Conductivity and the Ion Migration Barrier. *Adv. Energy Mater.* **2024**, No. 2402269.

(2) Glaser, C.; Wei, Z.; Indris, S.; Klement, P.; Chatterjee, S.; Ehrenberg, H.; Zhao‐Karger, Z.; Rohnke, M.; Janek, J. To Be or Not to Be‐Is MgSc2Se4 a Mg‐Ion Solid Electrolyte? *Adv. Energy Mater.* **2023**, *13*, No. 2301980.

A.4 Synthesis and Characterization of Further MgB_2X_4 Spinels

The following presents results from additional MgB_2X_4 spinels that were synthesized and partially characterized within the scope of this dissertation. Unless otherwise stated, the same cell concepts, devices, software programs, and measurement settings as in the publications 1 to 3 were used.[43-45] Moreover, all data that supports the findings of the studied MgB_2X_4 spinels are openly available in Zenodo at https://doi.org/10.5281/zenodo.15490069, reference number 15490069.

A.4.1 $MgSc_2S_4$

The solid-state synthesis of $MgSc_2S_4$ was performed via a two-step route. During the first step, MgS and Sc_2S_3 were prepared from stoichiometric amounts of their elements, including magnesium (Sigma Aldrich, ≥99%, powder), scandium (Chempur, 99.9% REO, powder), and sulfur (Sigma Aldrich, 99.998% trace metals basis, powder). For this purpose, according to the synthesis procedure of MgSe and Sc_2Se_3 (publication 1), a mixture of the corresponding powders was pressed into a pellet and heated in an evacuated quartz glass ampule at 500 °C for 96 h (100 °C h^{-1} heating rate).[43] Afterwards, in the second step, a stoichiometric mixture of the prepared binary sulfides was pressed into a pellet with the addition of 90 mol% sulfur. Then, the pellet was placed in an evacuated ampule and heated at 500 °C for 5 h and at 1100 °C for 20 h (100 °C h^{-1} heating rate) to obtain the spinel phase, which was subsequently characterized by XRD, EIS, DC polarization, LSV, and plating/stripping cycling, as demonstrated below.

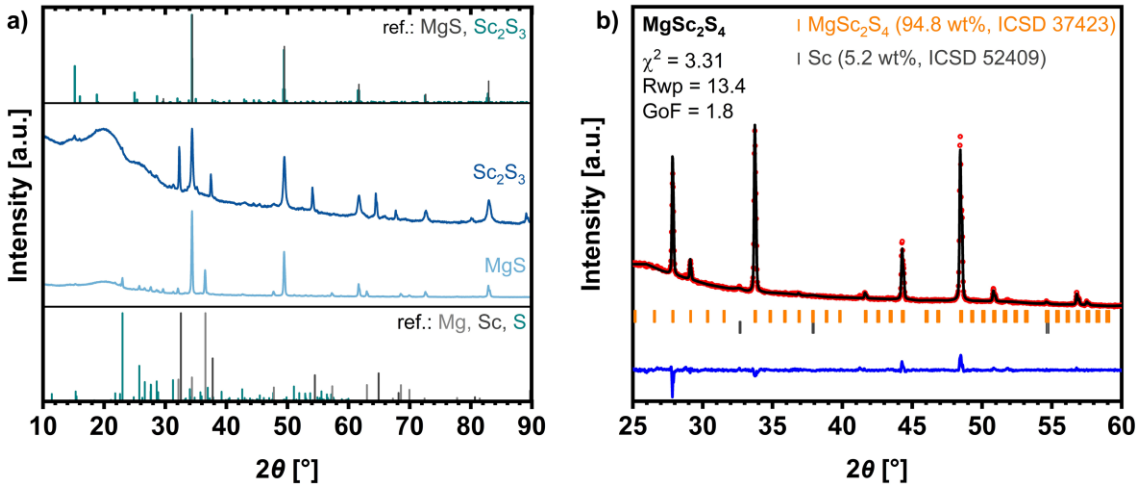

Supporting Figure 1: a) Powder XRD patterns of the MgS and Sc_2S_3 samples compared to the reference patterns of Mg (ICSD 181728), Sc (ICSD 52409), S (ICSD 27840), MgS (ICSD 659124), and Sc_2S_3 (ICSD 22236). Both binary phases were formed during an incomplete reaction of the elemental precursors. This reaction is expected to continue during the next synthesis step at a higher temperature of 1100 °C ($MgSc_2S_4$ formation). b) Rietveld refinement based on the XRD pattern of the $MgSc_2S_4$ sample. The refinement confirms a high purity (94.8 wt%) of the synthesized $MgSc_2S_4$ spinel phase with Fd-3m space group. The observed and calculated patterns are shown in red and black, and the difference curve is shown in blue.

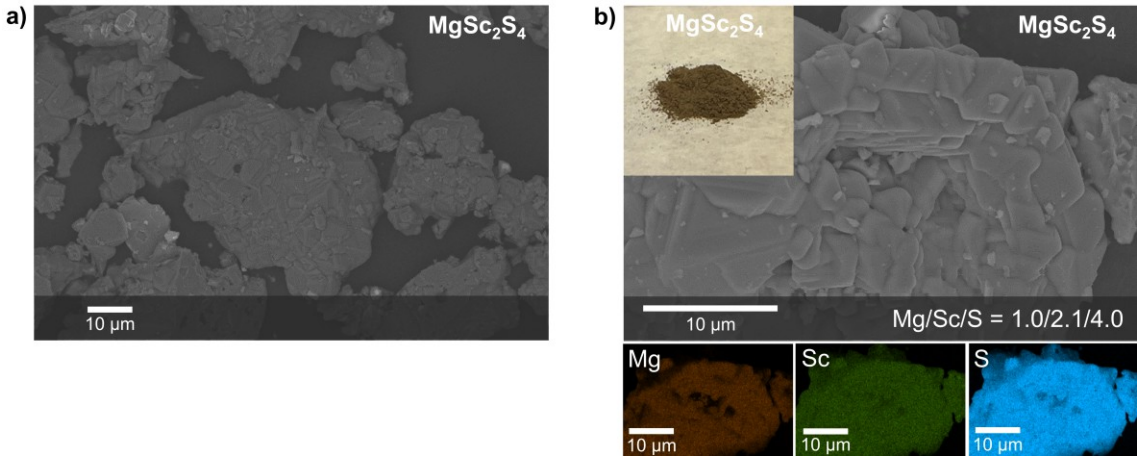

Supporting Figure 2: a) Overview SEM image of $MgSc_2S_4$ powder with a particle size of up to 50 µm. b) SEM image and EDS mapping at higher magnification of the spot in a). The EDS mapping of the brown $MgSc_2S_4$ powder (cf. light optical image top left) confirms that the element stoichiometry (Mg:Sc:S) is 1:2:4, consistent with that of the spinel phase.

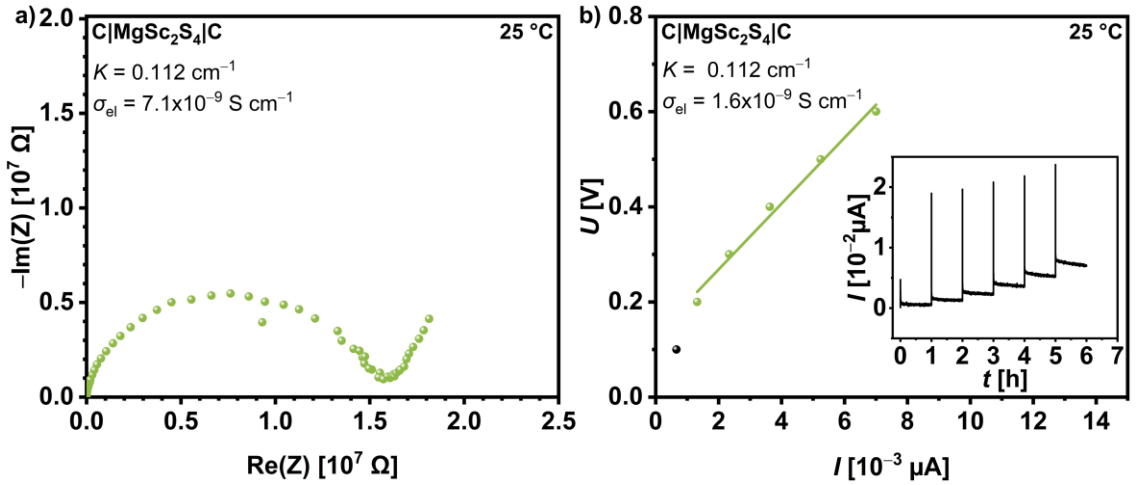

Supporting Figure 3: a) Nyquist plot of the EIS data of a C|$MgSc_2S_4$|C ion-blocking press cell in the frequency range from 3 MHz to 100 mHz at 25 ° with the cell constant represented by K. b) DC polarization data of the C|$MgSc_2S_4$|C press cell at 25 °C. When performing the DC polarization measurement, different voltages (0.1, 0.2, 0.3, 0.4, 0.5, and 0.6 V) were held for 1 h each. The steady-state current at the end of each holding step (cf. inset) was plotted against the corresponding voltage to calculate the electronic conductivity σ_{el} from the linear fit (excluding the first data point in black). As a result, similar to the EIS measurements, an electronic conductivity in the order of 10^{-9} S cm^{-1} was determined for $MgSc_2S_4$, which is about one order of magnitude lower than of $MgSc_2Se_4$ (see publication 1).[43]

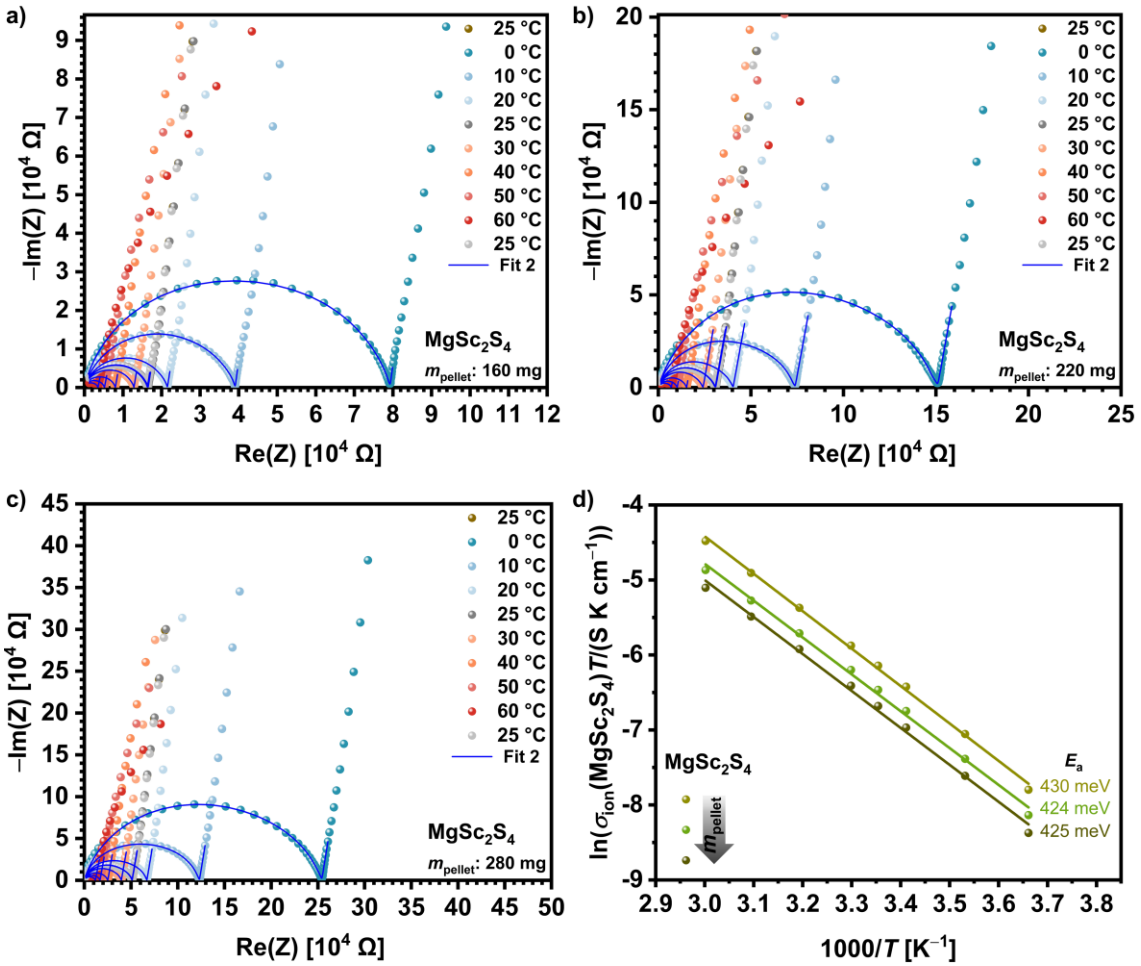

Supporting Figure 4: a-c) Nyquist plots of the EIS data of SS|UiO66-MgIL|$MgSc_2S_4$|UiO66-MgIL|SS press cells with electron-blocking interlayers (UiO66-MgIL, batch of publication 2)[44] and varied spinel pellet mass/thickness (160 mg/0.92 mm, 220 mg/1.26 mm, and 280 mg/1.68mm) collected at temperatures from 0 °C to 60 °C. To determine the ionic conductivity of $MgSc_2S_4$, all Nyquist plots were fitted with an (R)(P)-(R)(RP)(P)-P equivalent circuit model, denoted as Fit 2 (described in publication 1).[43] In this context, an average room-temperature (25 °C) ionic conductivity of $\sigma_{ion} = 5.5 \cdot 10^{-6}$ S cm^{-1} was found for $MgSc_2S_4$, which is about one order of magnitude lower than that of $MgSc_2Se_4$. d) Arrhenius plots of the ionic conductivities obtained from the fitted Nyquist plots in a-c). As a result, these show an average Mg-ion migration barrier of E_a = 426 meV for $MgSc_2S_4$.

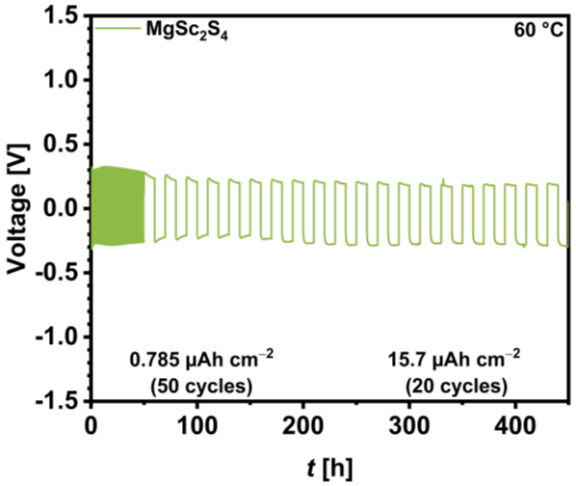

Supporting Figure 5: Long-term cycling performance during Mg plating/stripping of a Mg|UiO66-MgIL|$MgSc_2S_4$|UiO66-MgIL|Mg cell at 60 °C. The cell was first activated over 50 cycles at a current density of 1.57 µA cm^{-2} and a dwell time of 30 min for each plating or stripping step (plated charge amount of 0.785 µAh cm^{-2} ≙ ideally 2 nm of Mg). Then, the plated charge was increased by a factor of 20 (≙ 41 nm of Mg for each step of 10 h) for further 20 cycle, while a stable and reversible plating/stripping cycling was observed.

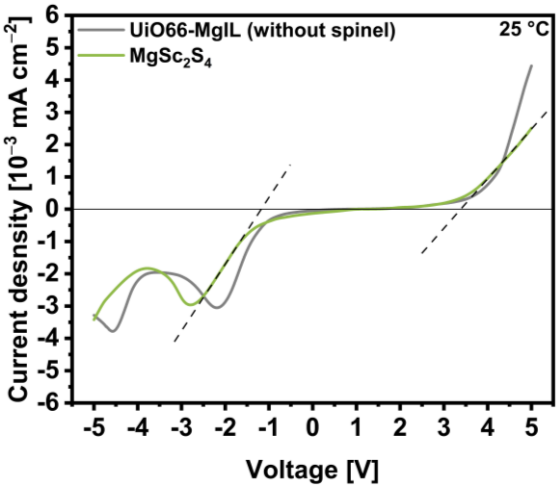

Supporting Figure 6: LSV curves of Mg|UiO66-MgIL|Mg cells and Mg|UiO66-MgIL|$MgSc_2S_4$|UiO66-MgIL|Mg cells at 25 °C recorded at a scan rate of –0.1 mV s^{-1}/0.1 mV s^{-1} from open circuit voltage to 5 V/–5 V. The curves of both cells show a quite similar onset potential of the reduction (value: –1.1 V) and oxidation (range: 3.4-3.5 V) current. This indicates that the electrochemical stability of the cells is possibly limited by the decomposition of the UiO66-MgIL interlayer, while the $MgSc_2S_4$ spinel itself may have a higher stability.

A.4.2 $^{25}MgSc_2S_4$, $^{25}MgSc_2Se_4$, and $^{25}MgY_2Se_4$

To investigate the Mg-ion transport dependent on the MgB_2X_4 spinel composition by ToF-SIMS and ^{25}Mg NMR measurements in future studies (see chapter 5 Outlook), three ^{25}Mg-enriched spinels ($^{25}MgSc_2S_4$, $^{25}MgSc_2Se_4$, and $^{25}MgY_2Se_4$) were synthesized in this work. For this purpose, the spinel syntheses were performed according to the two-step procedures of their non-enriched counterparts $MgSc_2S_4$ (section A.4.1), $MgSc_2Se_4$ (publication 1), and MgY_2Se_4 (publication 2), with exception of the preparation of MgS and MgSe.[43,44] In this case, the corresponding ^{25}Mg-enriched compounds were formed by replacing the usually used Mg powder with 1 mm^2 pieces of a ^{25}Mg foil (buyisotope, 99.10 % ^{25}Mg enrichment, metal foil). This ^{25}Mg metal pieces were mixed in a stoichiometric ratio with sulfur or selenium, respectively. Then, the resulting mixtures were pressed into pellets and sealed separately in evacuated quartz glass ampules. In these, depending on the compound ($^{25}MgSe$ or ^{25}MgS), the corresponding pellets were heated according to an individual temperature protocol. For the synthesis of $^{25}MgSe$, a temperature of 750 °C was used for 48 h (180 °C h^{-1} heating rate), while for ^{25}MgS the pellets were heated for 48 h at 500 °C and for another 48 h at 750 °C (100 °C h^{-1} heating rate). Finally, these binary magnesium chalcogenides were used to continue the aforementioned two-step procedures, resulting in the three ^{25}Mg-enriched spinels $^{25}MgSc_2S_4$, $^{25}MgSc_2Se_4$, and $^{25}MgY_2Se_4$, as confirmed by XRD measurements (Supporting Figure 7).

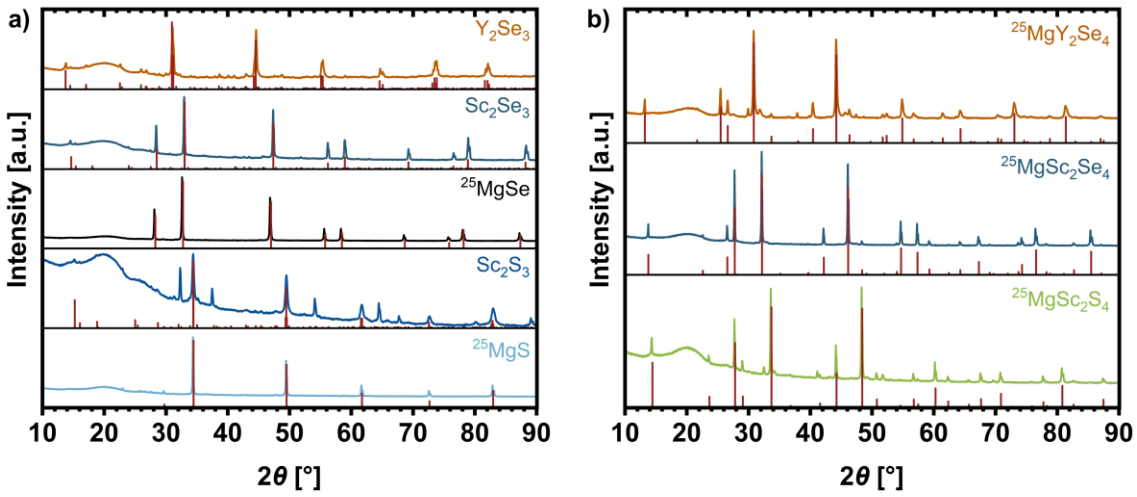

Supporting Figure 7: a) Powder XRD patterns of the ^{25}MgS, Sc_2S_3, $^{25}MgSe$, Sc_2Se_3, and Y_2Se_3 samples compared to their corresponding reference patterns in red (MgS: ICSD 659124, Sc_2S_3: ICSD 2223, MgSe: ICSD 53946, Sc_2Se_3: ICSD 651804, and Y_2Se_3: ICSD 652183). While the binary selenides were obtained in high purity, an incomplete conversion into the binary sulfides occurred. This conversion is expected to continue in the second synthesis step at a much higher temperature of 1100 °C. b) Powder XRD patterns of the $^{25}MgSc_2S_4$, $^{25}MgSc_2Se_4$, and $^{25}MgY_2Se_4$ samples compared to their corresponding reference patterns in red ($MgSc_2S_4$: ICSD 37423, $MgSc_2Se_4$: ICSD 642814, and MgY_2Se_4: ICSD 76052). As a result, all ^{25}Mg-enriched spinel phases were successfully synthesized with minor fractions of impurities.

B Abbreviations and Symbols

B.1 List of Abbreviations

Abbreviation	Definition
AC	Alternating current
BEV	Battery electric vehicle
CE	Counter electrode
CP	Chevrel phase
DC	Direct current
DFT	Density functional theory
EDS	Energy-dispersive X-ray spectroscopy
EIS	Electrochemical impedance spectroscopy
ICSD	Inorganic Crystal Structure Database
IL	Ionic liquid
LE	Liquid electrolyte
LIB	Lithium-ion battery
LSV	Linear sweep voltammetry
LTO	Lithium titanium oxide ($Li_4Ti_5O_{12}$)
MCI	Mixed-conducting interphase
Me	Metal
MIEC	Mixed ionic-electronic conductor
MMA	Magnesium metal anode
MV	Multivalent
NMR	Nuclear magnetic resonance
oct	Octahedral
RE	Reference electrode
RMB	Rechargeable magnesium battery
SE	Solid electrolyte
SEI	Solid electrolyte interphase
SEM	Scanning electron microscopy
SHE	Standard hydrogen electrode
SSB	Solid-state battery
SSC	Steady-state current
TEM	Transmission electron microscopy

tet	Tetrahedral
ToF-SIMS	Time-of-flight secondary ion mass spectrometry
TS	Transition state
WE	Working electrode
XRD	X-ray diffraction

B.2 List of Symbols

Symbol	Description	Unit/value
a_0	Distance (of hopping / migration path)	m
a_0'	Half of Distance a_0	m
C_{geo}	Geometrical capacitance	F
C_{int}	Interfacial capacitance	F
D_R	Random diffusion coefficient	$m^2\ s^{-1}$
D_T	Tracer- or self-diffusion coefficient	$m^2\ s^{-1}$
D_σ	Macroscopic long-range diffusivity	$m^2\ s^{-1}$
d	Number of dimensions	-
E_a	Migration barrier	eV
E_a(th)	Theoretical migration barrier	eV
E_{KRA}	Kinetically resolved activation barrier	eV
E_m	Hopping energy	eV
E_{out}	Output voltage	V
emf	Electromotive force	V
F	Faraday constant	$9.648533 \cdot 10^4$ C mol^{-1}
f	Correlation factor	-
H_R	Haven ratio	-
j_{DC}	Direct current	A
j_{el}	Electronic current	A
j_{ion}	Ionic current	A
k_B	Boltzmann constant	$1.380649 \cdot 10^{-23}$ J K^{-1}
n	Charge carrier density	m^{-3}
q	Quantity of electric charge	C
r	Radius	m
R	Electrical resistance	Ω
R_{el}	Electronic resistance	Ω
R_{ion}	Ionic resistance	Ω
T	Temperature	K
T_1	Spin-lattice relaxation time	s
t_{el}	Electronic transference number	-
t_{ion}	Ionic transference number	-
u	Electrical mobility	$m^2\ V^{-1}\ s^{-1}$
Z	Impedance	Ω

z	Number of transferred electrons	-
ΔE	Site preference energy	eV
$\Delta_r G$	Molar Gibbs free energy of a reaction	J mol^{-1}
ΔH_a	Activation enthalpy	J
$\Delta_f H$	Defect formation enthalpy	J
$\Delta_m H$	Migration enthalpy	J
ΔS_a	Activation entropy	J K^{-1}
μ	Chemical potential	J mol^{-1}
v_0	Hopping frequency	s^{-1}
σ_0	Pre-exponential factor	S K m^{-1}
σ_{el}	Electronic conductivity	S m^{-1}
σ_{ion}	Ionic conductivity	S m^{-1}

C Scientific Contributions

C.1 List of Publications

Published online as of 26.06.2025

2025 **Glaser, C.**; Sotoudeh, M.; Dillenz, M.; Sarkar, K.; Bark, J. S.; Singh, S.; Wei, Z.; Indris, S.; Müller, R.; Leopold, K.; Nazar, L. F.; Groß, A.; Janek, J. High Room-Temperature Magnesium Ion Conductivity in Spinel-Type $MgYb_2Se_4$ Solid Electrolyte. *Chem. Mater.* **2025**, *37*, 3353–3362.[45]

2024 **Glaser, C.**; Dillenz, M.; Sarkar, K.; Sotoudeh, M.; Wei, Z.; Indris, S.; Maile, R.; Rohnke, M.; Müller-Buschbaum, K.; Groß, A.; Janek, J. MgB_2Se_4 Spinels (B = Sc, Y, Er, Tm) as Potential Mg-Ion Solid Electrolytes – Partial Ionic Conductivity and the Ion Migration Barrier. *Adv. Energy Mater.* **2024**, *14*, No. 2402269.[44]

Palacin, M. R.; Johansson, P.; Dominko, R.; Dlugatch, B.; Aurbach, D.; Li, Z.; Fichtner, M.; Lužanin, O.; Bitenc, J.; Wei, Z.; **Glaser, C.**; Janek, J.; Fernández-Barquín, A.; Mainar, A. R.; Leonet, O.; Urdampilleta, I.; Blázquez, J. A.; Tchitchekova, D. S.; Ponrouch, A.; Canepa, P.; Gautam, G. S.; Casilda, R. S. R. G.; Martinez-Cisneros, C. S.; Torres, N. U.; Varez, A.; Sanchez, J.-Y.; Kravchyk, K. V.; Kovalenko, M. V.; Teck, A. A.; Shiel, H.; Stephens, I. E. L.; Ryan, M. P.; Zemlyanushin, E.; Dsoke, S.; Grieco, R.; Patil, N.; Marcilla, R.; Gao, X.; Carmalt, C. J.; He, G.; Titirici, M.-M. Roadmap on Multivalent Batteries. *J. Phys. Energy* **2024**, *6*, No. 031501.[53]

2023 Wei, Z.; Singh, D. K.; Helmbrecht, K.; Sann, J.; Yusim, Y.; Kieser, J. A.; **Glaser, C.**; Rohnke, M.; Groß, A.; Janek, J. In Situ Observation of Room-Temperature Magnesium Metal Deposition on a NASICON/IL Hybrid Solid Electrolyte. *Adv. Energy Mater.* **2023**, *13*, No. 2302525.[62]

Glaser, C.; Wei, Z.; Indris, S.; Klement, P.; Chatterjee, S.; Ehrenberg, H.; Zhao-Karger, Z.; Rohnke, M.; Janek, J. To Be or Not to Be – Is $MgSc_2Se_4$ a Mg-Ion Solid Electrolyte? *Adv. Energy Mater.* **2023**, *13*, No. 2301980.[43]

2022 Dillenz, M.; Sotoudeh, M.; **Glaser, C.**; Janek, J.; Groß, A.; Euchner, H. Unravelling Charge Carrier Mobility in d_0-Metal-Based Spinels. *Batter. Supercaps* **2022**, *5*, No. e202200164.[35]

2021 Werner, S.; **Glaser, C.**; Kasper, T.; Lê, T. N. N.; Gross, S.; Smarsly, B. M. H_2S Dosimetry by CuO: Towards Stable Sensors by Unravelling the Underlying Solid-State Chemistry. *Chem. Eur. J.* **2022**, *28*, No. e202103437.[168]

C.2 List of Conference Contributions

2024 **Glaser, C.**; Dillenz, M.; Sarkar, K.; Sotoudeh, M.; Wei, Z.; Rohnke, M.; Groß, A.; Janek, J. MgB_2Se_4 Spinels (Z = Sc, Y, Er, Tm) as Potential Mg-Ion Solid Electrolytes – Partial Ionic Conductivity and Ion Migration Barrier. *5th International Symposium on Magnesium Batteries (MagBatt V)*, Ulm, Germany, **September 2024**, Oral presentation.

Glaser, C.; Rohnke, M.; Janek, J. MgB_2Se_4 (B = Sc, Er, Tm, Y) Spinels as Promising Mg-Ion Conductors for Almost-Solid-State Mg Batteries. *24th International Conference on Solid State Ionics (SSI-24)*, London, UK, **July 2024**, Oral presentation.

2022 **Glaser, C.**; Wei, Z.; Rohnke, M.; Janek, J. MgZ_2Se_4 (Z = Sc, Er, Tm, Y) Spinels as Promising Mg-Ion Conductors for All-Solid-State Mg Batteries. *4th International Symposium on Magnesium Batteries (MagBatt IV)*, Ulm, Germany, **September 2022**, Oral presentation.

Glaser, C.; Rohnke, M.; Janek, J. Investigation of MgZ_2Se_4 (Z = Sc, Er, Tm, Y) Spinels as Mg-Ion Conductors for All-Solid-State Mg Batteries. *23rd International Conference on Solid State Ionics (SSI-23)*, Boston, MA, USA, **July 2022**, Oral presentation.

2021 **Glaser, C.**; Rohnke, M.; Janek, J. Investigation of MgZ_2Se_4 (Z = Sc, Er, Tm, Y) Spinels as Mg-Ion Conductors for All-Solid-State Mg Batteries. *Post-Lithium Research: Women in Focus (virtual conference)*, **July 2021**, Poster presentation (awarded with best poster award).

Acknowledgements

In this final chapter, I would like to express my gratitude to all those who supported me during my time as a doctoral student:

First of all, I would like to sincerely thank my doctoral supervisor Prof. Jürgen Janek for giving me the opportunity to work and study in his research group. I am deeply grateful for his constant support, the constructive and fruitful discussions with him and his trust in my research, which motivated me through many challenges and helped me grow professionally and personally.

Special thanks also go to Prof. Marcus Rohnke for his continuous support throughout my PhD journey. His door was always open to me and I am truly grateful for his willingness to help me with all sorts of questions and concerns.

Furthermore, I would like to thank Prof. Bernd M. Smarsly for being the second reviewer of this dissertation as well as Prof. Maren Lepple and Prof. Matthias T. Elm for being part of the examination committee of my doctoral defense.

My further thanks go to Dr. Boris Mogwitz, Dr. Klaus Peppler, Dr. Joachim Sann, and Dr. Bjoern Luerssen for their kind assistance with questions regarding scientific equipment (especially to the SEM, XRD, and SPS device), technical problems, and organizational matters.

Additionally, I would like to thank my cooperation partners at KIT, Ulm University, and the University of Waterloo. In this context, special thanks go to Prof. Linda F. Nazar for her supervision and the opportunity to be part of her research group for a couple of months. I am very thankful for the scientific discussions and the open exchange of ideas we had, which have enriched my work enormously. Furthermore, I would also like to thank Dr. Shashwat Singh for the warm welcome in Waterloo and his generous support within and outside the university.

I gratefully acknowledge the financial support of my research by the DFG (German Research Foundation) under the project ID 390874152 (POLiS Cluster of Excellence).

I further thank all of my former and present colleagues in the Janek group for their collegial spirit, supportiveness, and the pleasant working atmosphere. I am especially grateful to Dr. Till Ortmann and Dr. Zhixuan Wei, whose support made the start of my PhD journey much easier. I really appreciate their continued willingness to provide creative input on scientific challenges and to help me with any questions.

Last but not least, I want to express my gratitude to my family and friends who continuously supported me during my time as a PhD student. My special thanks go to my parents Petra Glaser and Ralf Glaser, my brother Felix Glaser, and my fiancé Dr. Christopher Simon. Without their help and encouragement, this work would not have been possible. Thank you for standing by my side through difficult situations and for always believing in me!